Push-pull-based materials for organic photovoltaics

José Maria Andres Castan

THESE DE DOCTORAT DE

L'UNIVERSITE D'ANGERS
COMUE UNIVERSITE BRETAGNE LOIRE

ECOLE DOCTORALE N° 596
Matière Molécules et Matériaux
Spécialité : *Chimie Organique et Sciences des Matériaux*

Par
José María ANDRÉS CASTÁN

Push-pull-based materials for organic photovoltaics

Thèse présentée et soutenue à Angers, le 2 octobre 2020
Unité de recherche : Laboratoire MOLTECH-Anjou – CNRS UMR 6200
Thèse N° : 190403

Rapporteurs avant soutenance :

Renaud Demadrille, Ingénieur-Chercheur HDR, CEA Grenoble
Chantal Andraud, DR CNRS, ENS Lyon

Composition du Jury :

Ángela Sastre, Professeure, Universidad de Elche
Elena Ishow, Professeure, Université de Nantes
Carsten Deibel, Professeur, Technische Universität Chemnitz

Directeur de thèse
Philippe Blanchard, DR CNRS, Université d'Angers
Co-directeur de thèse
Clément Cabanetos, CR HDR CNRS, Université d'Angers

Al camino recto, por el más torcido

Extremoduro

Acknowledgements

After all the ups and downs of these three years, I feel grateful for the opportunity I have had and for the people I have met. I am pretty sure that without the contributions of the following people, this PhD thesis could not have been possible.

First, I would like to thank Renaud Demadrille and Chantal Andraud for accepting the role of reviewers of this PhD thesis and Ángela Sastre, Elena Ishow and Carsten Deibel for their participation as examiners of this work.

I wish to express my deepest gratitude to my supervisors Philippe Blanchard and Clément Cabanetos for the guidance during these three years. I want to thank Philippe for taking time for me anytime I wanted despite his really busy schedule and of course for his infinite kindness, and Clément for his constant support, the scientific discussions… and many more things that could be detailed at this point. Thanks to both of you.

I do not want to forget about the people that had the patience to train me in the first place in Zaragoza, Santiago Franco, Raquel Andreu and Belén Villacampa.

I want to thank all the collaborators we have had in the projects detailed in this PhD thesis and the rest that were not finally included in the manuscript. I would like to highlight the contribution of Olivier Maury, Cyrille Monnereau and Laura Abad Galán from the ENS Lyon for the great photophysical characterization of many products synthesized in our lab. Thanks to Chad Risko of the University of Kentucky for his support regarding computational chemistry. I wish to show my gratitude also to Ivan Ramirez and Karsten Walzer from Heliatek GmbH for the photovoltaic characterization of some of my derivatives. I definitely want to thank Lukasz Baisinger and Karl Leo from the Technische Universität Dresden for the thorough optimization of the solar cells fabrication procedure. I also want to thank Carsten Deibel and all his group for the great welcome during my secondment in the Technische Universität Chemnitz. This appreciation is of course extended to Maria Saladina, for the good times and her inestimable help.

I would also like to express my sincere gratitude to all the people from the lab that have also contributed to this work: Ingrid Freuze and Sonia Jerjir for the mass spectra, Benjamin Siegler for the help with the NMR characterization, Olivier Alévêque for the electrochemistry measurements and Magali Allain for the X-ray analysis. Finally, I'd like to thank Valérie Bonnin and Cécile Mézière for the help in the everyday working life. Thanks also to all the members of the SCL group for all the productive comments and advices during these three years.

I am also grateful to all the people in MOLTECH that have supported or helped me in any way. There are here two friends I would like to highlight at this point. Thanks to Cristina for all the beers, talks and laughs during these three years, Fête de la Musique “without drinking this year” included. Of course I also want to thank Pablo, without whom I probably would not have been able to deal with the ups and downs of the PhD thesis. “Pero co, otra vez Extremoduro? Mejor un poco de Desakato.”

I wish to thank all the people involved in the European SEPOMO project for all the fruitful scientific discussions and all the good moments during these three years. This is of course extended to the ESR students, for all the laughs and beers after our meetings.

I want to thank my lifelong friends from high school for their great welcome in my returns to Zaragoza. This is specially extended to Gustavo and Aitor, without whom the quarantine would have been a total nightmare. We will celebrate it as we deserve it, red flyers and all.

I am particularly grateful to my friends from the University for their support through the distance: Martín, Edu, Clara, Néstor, Miguel Ángel and Isolda. Special thanks to Funes, who has been always there (I mean in Nantes and Paris, not specifically in Angers) to eat “filetits” and cheap cheese every once in a while (1,2…).

I want to thank as well all my friends of Molinos, los exiliadoaks, for the two enjoyable weeks we spend together every summer, even the hangovers in the pool are almost enjoyable.

Last but definitely not least, I want to thank my family for their infinite support during this period. Among all of them, my deepest appreciation goes of course to my brother and my parents. I want to thank my brother for the visits to Angers, his constant support, talks… I could go on for a while. And what to say about my parents… just thank you for all you have fought and everything you have taught me, I certainly would not be here without you. This is a reward for the four of us. Gracias.

Table of contents

Table of contents

List of abbreviations and symbols

A	Electron-accepting block/material
AM	Air mass
BDD	Benzo[1,2-*c*:4,5-*c*']dithiophene-4,8-dione
BDT	Benzo[1,2-*b*:4,5-*b*']dithiophene
BHJ	Bulk heterojunction
BODIPY	Boron-dipyrromethenes
BPA	*N*,*N*-bis(4-biphenylyl)aniline
BTXA	1*H*,3*H*-thioxantheno[2,1,9-*def*]isochromene-1,3-dione
BTXI	2-(alkyl)-1*H*-thioxantheno[2,1,9-*def*]isoquinoline-1,3(2*H*)-dione
BTZ	Benzo[*c*][1,2,5]thiadiazole
CI	Chemical ionization
CV	Cyclic voltammetry
CT	Charge-transfer
D	Electron-donating block/material
DCV	Dicyanovinyl
DFT	Density functional theory
DIO	1,8-diiodooctane
DMA	*N*,*N*-dimethylacetamide
DMF	*N*,*N*-dimethylformamide
DMF-DMA	*N*,*N*-dimethylformamide dimethyl acetal
DPP	Diketopyrrolopyrrole
DSSCs	Dye-sensitized solar cells
EI	Electron impact
E_{ox}	Oxidation potential (V)
E_{pa}	Oxidation peak potential (V)
E_{pc}	Reduction peak potential (V)
E_{red}	Reduction potential (V)
EQE	External quantum efficiency
ESI	Electrospray ionization
Et_3N	Triethylamine
FAB	Fast atomic bombardment
Fc/Fc^+	Ferrocene/ferrocenium redox couple
FF	Fill factor
HOMO	Highest occupied molecular orbital
HRMS	High resolution mass spectrometry
HTM	Hole-transporting material
ICT	Intramolecular charge transfer
IDT	Indacenodithiophene
IDTT	Indacenodithieno[3,2-*b*]thiophene
iPrOH	Isopropanol

List of abbreviations and symbols

ITO	Indium tin oxide
IR	Infrared
J	Current density (mA cm^{-2})
J_{int}	Integrated current density from EQE (mA cm^{-2})
J_{max}	Maximum current density (mA cm^{-2})
J_{sc}	Short-circuit current density (mA cm^{-2})
LUMO	Lowest unoccupied molecular orbital
MALDI	Matrix-assisted laser desorption/ionization
MPTA	*N*-methyl-*N*-phenylthiophen-2-amine
MTTA	*N*-methyl-*N*-(*p*-tolyl)thiophen-2-amine
MS	Mass spectrometry
NDI	Naphthalenediimide
NFA	Non-fullerene acceptor
NIR	Near infrared
NMR	Nuclear magnetic resonance
NOESY	Nuclear Overhauser effect spectroscopy
NTO	Natural transition orbitals
OFET	Organic field-effect transistor
OLED	Organic light-emitting diode
OPV	Organic photovoltaics
OSC	Organic solar cells
P3HT	Poly(3-hexylthiophene-2,5-diyl)
Pc	Phthalocyanine
$PC_{61}BM$	[6,6]-phenyl-C_{61}-butyric acid methyl ester
$PC_{71}BM$	[6,6]-phenyl-C_{71}-butyric acid methyl ester
PCE	Power conversion efficiency (%)
PDI	Perylenediimide
PEDOT	Poly(3,4-ethylenedioxythiophene)
PESA	Photoelectron spectroscopy in air
PHJ	Bilayer/planar heterojunction
P_i	Irradiating power (mW cm^{-2})
P_{max}	Maximum power (mW cm^{-2})
PMDETA	*N*,*N*,*N'*,*N''*,*N''*-pentamethyldiethylenetriamine
PMHJ	Planar mixed heterojunction
PPV	Polyparaphenyle vinylene
PSC	Perovskite solar cells
PSS	Polystyrene sulfonate
PV	Photovoltaics
RPM	Revolutions per minute
SOC	Spin-orbit coupling
T	Thiophene
TAA	Triarylamine derivative

List of abbreviations and symbols

TCNEO	Tetracyanoethylene oxide
TD-DFT	Time-dependent density functional theory
TFA	Trifluoroacetic acid
THF	Tetrahydrofuran
TMS	Trimethylsilyl
TOF	Time-of-flight
TPA	Triphenylamine
UV	Ultraviolet
V	Voltage (V)
V_{max}	Maximum voltage (V)
V_{oc}	Open circuit voltage (V)
ΔE_{opt}	Optical band gap (eV)
ε	Molar absorptivity ($M^{-1}\,cm^{-1}$)
η	Power conversion efficiency (%)
λ	Wavelength (nm)
μ_e	Electron mobility ($cm^2\,V^{-1}\,s^{-1}$)
μ_h	Hole mobility ($cm^2\,V^{-1}\,s^{-1}$)
Φ_f	Fluorescence quantum yield
Φ_Δ	Singlet oxygen quantum yield

SEPOMO project

This PhD thesis was carried out as a part of the Marie Sklodowska-Curie Action (MSCA) *Spin for Efficient Photovoltaic Devices based on Organic Molecules* (SEPOMO). The aim of the project was to train promising *Early Stage Researchers* (ESRs) that can promote the world-wide position of Europe in the field of organic photovoltaics in the coming years. To do so, 15 ESR were thus enrolled in ten host organizations spread through Europe in six different countries (see the map below) and many training activities related to organic solar cells were carried out within the frame of the project.

RUG, The Netherlands

UOXF, United Kingdom

TUC, Germany

UW, Germany

UM, Belgium

TUD, Germany

Heliatek, Germany

EURECAT, Spain

ICMAB, Spain

UA, France

The main scientific aim of the project was to understand and tune the spin dependent mechanisms taking place in the light harvesting of OSCs in order to improve the efficiency of charge generation.

As the ESR 13 and a part of the work package related to materials and samples, my main goals were mostly related to synthesize conjugated donor materials for their application in organic photovoltaics. In addition, I have also been trained in different areas other than organic chemistry, HPLC chromatography, crystallization techniques, thermal characterization and preparation and characterization of thin films and organic solar cells among others. Since the group of the University of Angers (UA) was the only one composed of organic chemists, the main task was to provide our partners with different materials according to their specific needs. To make the most of this opportunity, some of the donor materials synthesized during the frame of this PhD thesis were shipped to Barcelona (EURECAT and ICMAB), Dresden (Heliatek GmbH and TUD) and Groningen (RUG). In addition, a collaboration with the University of Mons (UM)

was set in place in order to obtain a better structure-property relationship from their theoretical calculations. Thus, as the scope of the materials was diverse, only a coherent selection of the molecules and the results was eventually included in this manuscript.

Chapter 1
Introduction to organic solar cells

1.1 Context

Energy has been essential for the development of human activity for a long period of time. It supports economic growth and social progress and is vital to maintain our quality of life. However, there are nowadays several concerns regarding how the current methods of obtaining energy impact the environment.

Over the last years, the energy consumption has continuously increased due to several reasons, such as population growth and a general access to technology. According to a recent study published by the International Energy Agency (IEA), the energy demand would increase up to 1.3% per year until 2040 if the current policies scenario does not change.[1] Although fossil fuels, namely coal or oil, have been the historical and primary sources of energy, they present several drawbacks, such as limited reserves and large generation of greenhouse gas emissions during combustion. Consequently, in light of the above, keeping the same level of fossil fuel consumption would be only postponing the inevitable. That is the reason why different sustainable energy sources are currently emerging.

Photovoltaics is one of them and it stands out due to the high potential of the Sun. The amount of energy it provides the Earth will be more than 1000 times the world energy consumption per year for decades even though the demand will rise.[2] This intrinsically means that by covering only around 0.1% of the surface of the Earth with 10% efficient solar cells would be enough to take care of the whole energy demand.[3] That is why many efforts have been devoted to improving the performance and scalability of these devices in order to make them a real long-standing alternative to conventional energy sources.

1.2 History of photovoltaics

First discovered by Becquerel in 1839,[4-5] the photovoltaic effect corresponds to the generation of electric current and voltage in a material when exposed to light. It is based on the use of a semiconductor that is excited under irradiation, thus creating an electron-hole pair, the so-called exciton, due to the absorption of a photon. Eventually, the dissociation of this exciton in two different charges and their collection by two different electrodes lead to the generation of an electric current.

However, the fabrication of the first solar cell prototype, made out of silicon, came quite later, i.e., in 1954.[6] This started the first generation of devices based on silicon with a power conversion efficiency (PCE) of around 6%. Since this first demonstration, the PCE has constantly improved and this first generation of devices currently generates 93% of the solar energy production.[7] However, it is noteworthy that their performance greatly depends on the quality of silicon, which is directly related to its price. The most efficient devices, which are made of monocrystalline silicon, exhibit a PCE of 27.6%, but it decreases respectively to 23.2% and 14.0% when multi-crystalline and amorphous silicon are used instead.[8] Moreover, and even if commercially available, they present additional drawbacks, such as their extremely energy-demanding fabrication and high weight, impacting for instance the ease of installation on roof tops. In view of the foregoing, different types of solar cells have been developed afterwards (Figure 1.1).[9]

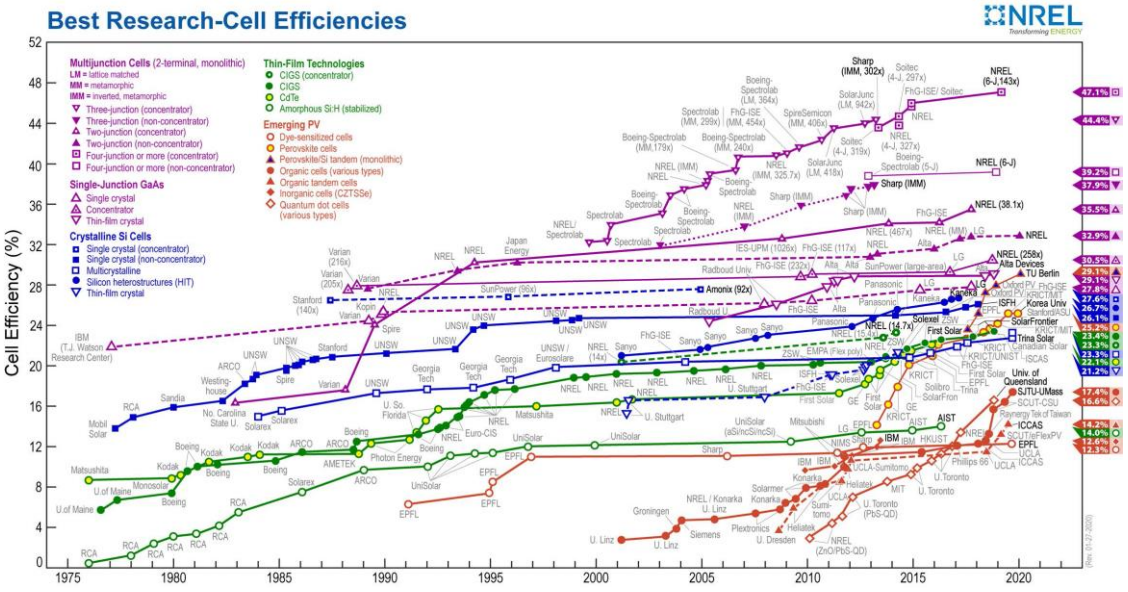

Figure 1.1. Best research-cell efficiencies chart from the National Renewable Energy Laboratory (NREL).[9]

Hence, the second generation of solar cells is based on inorganic semiconductors. Among other materials, GaAs (gallium arsenide), CIGS (copper indium gallium diselenide) and CdTe (cadmium

telluride) stand out with efficiencies of 30.5%, 23.4% and 22.1% respectively. Their improved optical properties in comparison to the silicon-based devices allow the use of thinner layers, decreasing the required weight and enabling their deposition on top of flexible substrates. The main hurdles for their large-scale implementation are the toxicity and low availability of the involved materials.

Besides, a more recent third generation of solar cells has been developed to overcome the major issues of all the previous systems, and particularly their high production cost. The main difference composition-wise is the implementation of organic materials. This generation of hybrid solar cells includes different types of devices, such as dye-sensitized solar cells (DSSCs), perovskite solar cells (PSCs) and the so-called organic solar cells or organic photovoltaics (OSCs/OPV).

DSSCs were largely developed by Grätzel[10] and they are mainly composed of a dye-sensitized wide-bandgap inorganic semiconductor, a counter electrode and an electrolyte which allows the electron transfer. The dye or sensitizer carries out the light harvesting and, through its excited state, it is able to inject electrons into the conduction band of the n-type semiconductor. The electrolyte subsequently regenerates the sensitizer and is, in turn, reduced by the counter electrode, resulting in the generation of photocurrent. These devices can reach efficiencies over 14%.[11]

The keys for the success of PSCs are the great charge mobility and the outstanding optical properties of the perovskite. This inorganic network based on an ABX_3 structure, where A is an organic cation, B a metallic cation and X a halide, was first used in a photovoltaic device in 2009 as a sensitizer for DSSCs.[12] Although this result was already promising, the major breakthrough came in 2012, when it was proved that this material can efficiently transport the electronic charges to the electrodes in the total absence of the detrimental liquid electrolyte,[13] reaching a PCE of 10.9%.[14] Since then, this topic has attracted considerable research attention resulting in an impressive enhancement of the performances reaching 25.2% at this moment.[9, 15] However, the main drawback of these devices comes from their lack of stability, since the perovskite is water-soluble and moisture greatly spoils their performance. It is noteworthy that their air stability has improved from minutes to thousands of hours but it is still far from being enough for a real application.[16] In addition, another big concern is the toxicity of lead, which has led to several studies aiming to replace it by another cation. However, the efficiencies of these lead-free PSCs are still lagging behind the conventional ones.[17]

Eventually, unlike the other types of solar cells, the active layer of OSCs is composed of organic semiconductors sandwiched between two electrodes. As this PhD thesis will be related to this type of devices, their working principle and their recent progress will be thoroughly detailed along this chapter.

1.3 Organic solar cells

The first example of OPV was reported in 1958.[18] The active layer was made of two different components, i.e., magnesium phthalocyanine and oxidized tetramethyl *p*-phenylenediamine. However, the following examples were usually based on active layers of just one material in the so-called Schottky devices. Although different organic semiconductors were tested for many years,[19-21] the intrinsic lack of charge separation completely hindered the development of this type of devices.

Thus, to solve this problem, active layers made of two components with different electron affinities were re-introduced. The electron-donating (D) material carries out the transport of holes and the electron-accepting (A) material the transport of electrons. Then, depending on how both materials are combined, two structures have been most widely employed, namely the bilayer or planar heterojunction (PHJ) and the bulk heterojunction (BHJ).

1.3.1 Planar heterojunction solar cells

In this architecture, the D and A materials are deposited separately in two superimposed layers (Figure 1.2). The first PHJ device was reported in 1986 by Tang and reached a PCE of 0.95%. In this device, copper phthalocyanine (**CuPc**) and 3,4,9,10-perylenetetracarboxylic bisbenzimidazole (**PTCBI**) were used as D and A materials respectively.[22] The main advantage over the elder examples comes from the existence of a D/A interface, which allows a better exciton separation. However, this improvement is still limited to significantly increase the performance of the devices. In addition, the exciton diffusion length is usually between 5 and 10 nm for amorphous materials,[23] thus impacting the thickness of the layers and consequently the absorbing capability of the active layer. Although this architecture presents several drawbacks, it remains a great breakthrough in the OPV research and an accessible way of evaluating the photovoltaic performances of new semiconductors.

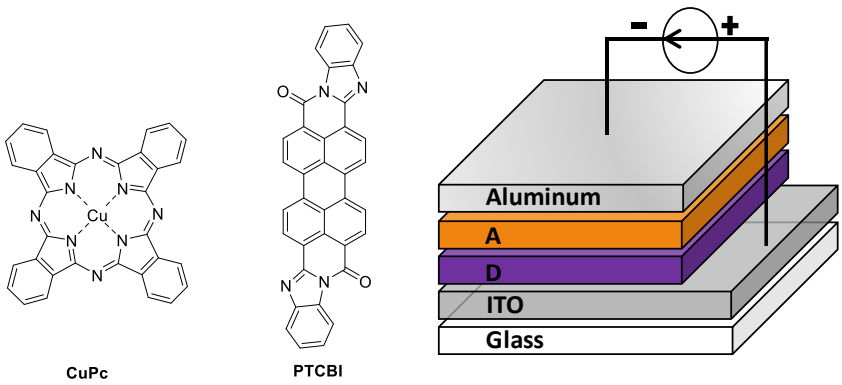

Figure 1.2. Representation of a PHJ OSC and the D/A couple used in the first device.

1.3.2 Bulk heterojunction solar cells

Based on the limitations previously stated, the concept of bulk heterojunction was introduced in 1995.[24-25] In these devices, both components of the active layer are mixed together in the same film instead of processed separately. This modification intrinsically increases the D/A interface area facilitating the exciton dissociation (Figure 1.3). In addition, larger thicknesses can now be used resulting in a highly improved absorption potential of the devices. However, in this structure, the phase segregation was found to be a key parameter that needs to be controlled, since it deeply affects the degree of interpenetration between nano-domains and also their size.[26] In the ideal case, a mixture of pure domains of D and A with sizes in the order of the exciton diffusion length would be regularly distributed along the active layer. In contrast, extremely large domains would indeed lead to the recombination of the excitons since they would not be able to reach the interface, as well as to a poor exciton dissociation due to a limited interface area. Besides, controlling this phenomenon is not straightforward and turns out to be empirical and time-consuming, since the morphology differs significantly from one D/A couple to another. To date, the most-studied active materials in BHJ OSCs are poly(3-hexylthiophene-2,5-diyl) (**P3HT**) and [6,6]-phenyl-C_{61}-butyric acid methyl ester (**$PC_{61}BM$**).[27]

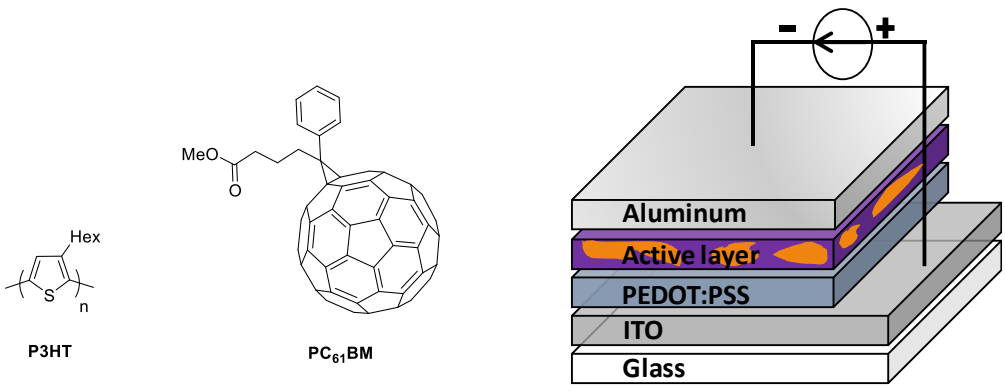

Figure 1.3. Representation of a BHJ OSC and the most studied D/A couple in this type of devices.

1.3.3 Working principle of OSCs

The electronic processes occurring in both PHJ and BHJ OSCs that lead to a photocurrent are depicted in Figure 1.4. First, the light reaches the active layer through the transparent electrode (1). Photons are then absorbed by the constituting materials, both the donor and the acceptor. Although for simplification and clarification purposes only the contribution of the donor will be fully detailed, an analogous process can take place in the acceptor domains also leading to the separation of free charges to produce an electric current (right diagram of Figure 1.5).[22] Hence, the light absorption by the donor produces the electronic transition between its highest occupied molecular orbital (HOMO) and its lowest unoccupied molecular orbital (LUMO). This generates an exciton (2) that only can be dissociated at the D/A interface. In addition, although for years an energy offset of approximately 0.3 eV between the LUMO of D and the LUMO of A was thought to be required, recent publications report that charge separation can also take place despite a negligible driving force.[28] Then, if all of this is accomplished, in order to separate the charges, it is believed that an intermediate charge-transfer state (CT state) has to be reached (3).[29-30] Finally, as a consequence of the internal electric field, the electron goes through the acceptor towards the cathode (4) and the hole through the donor towards the anode (5).

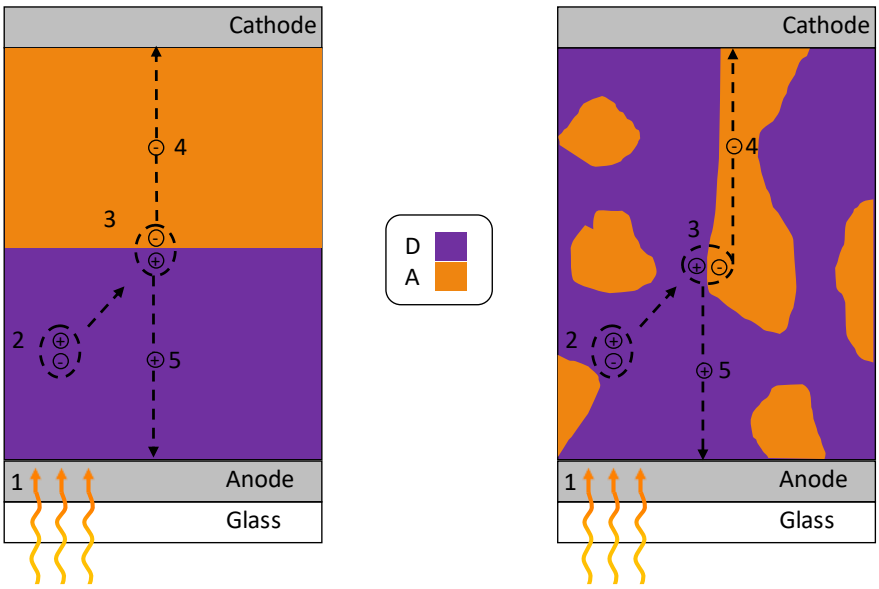

Figure 1.4. Schematic representation of the working principle of PHJ (left) and BHJ (right) OSCs.

On the other hand, several detrimental processes can impact the performances of the devices, such as the charge recombination, in which hole and electron come together to go back to their initial state, resulting from different radiative and non-radiative pathways. The former are inevitable in this type of devices but not that unfavorable since they are intrinsically related to

the new emission of photons that can be reabsorbed. However, non-radiative recombination is completely detrimental and it has to be avoided as much as possible as state-of-the-art OSCs usually suffer from high energy losses, which significantly limit their performance.[31] According to a recent publication, one solution could be the use of non-fullerene acceptors (NFA), since their electroluminescence quantum yields are relatively higher than those of fullerenes and this could hinder such detrimental processes.[28, 32-33]

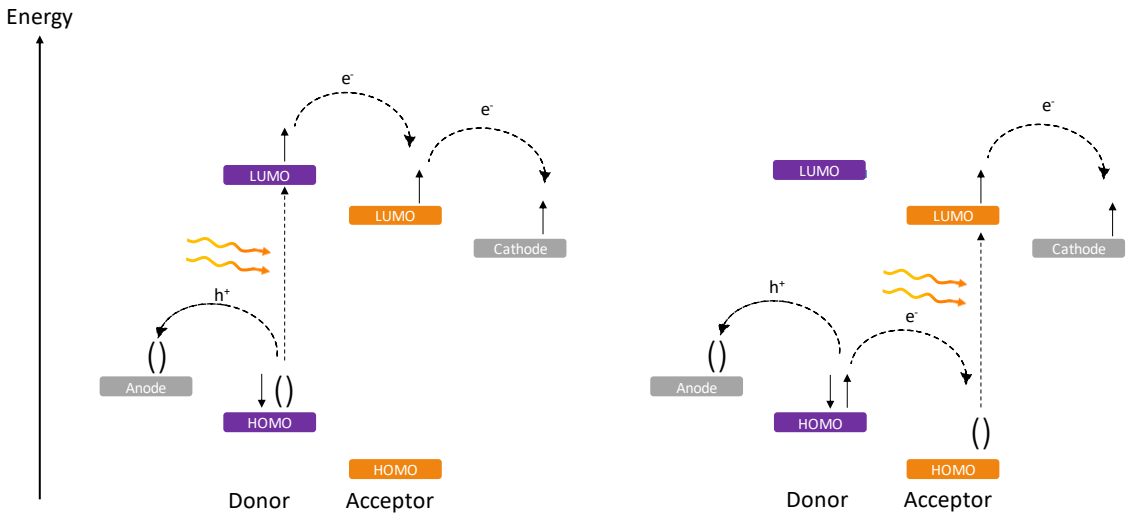

Figure 1.5. Energetic diagram of charge generation in OSCs as consequence of donor (left) or acceptor (right) absorption.

1.3.4 Characterization of OSCs

Prior to discussing the composition and evolution of the active layer, this section describes the analytical tools usually used to characterize a solar cell. It turns out that most of the key characteristics can be extracted from a current density-voltage (J-V) curve recorded in the dark and under illumination (Figure 1.6). On the one hand, the photovoltaic parameters that are related to the PCE can be obtained directly from the illuminated curves, i.e., the open circuit voltage (V_{oc}), the short-circuit current density (J_{sc}) and the fill factor (*FF*). On the other hand, the shapes of both dark and illuminated curves can provide hints about the possible pitfalls of the cells.[34-36]

- J_{sc} corresponds to the current density at illuminated conditions when the applied voltage is equal to zero. It depends on many parameters related to the active layer, among others, its thickness, the mobilities of holes and electrons, the charge separation capability and the absorption properties.

- V_{oc} is the voltage at a neutral current density. Its maximum theoretical value is related to the energy difference between the HOMO level of the donor and the LUMO of the acceptor.[37-38] However, this value cannot be achieved in actual devices due to detrimental processes, such as charge generation losses and charge recombination.[31]
- *FF* corresponds to the quotient of the maximum power delivered by the cell by the maximum theoretical power, in other words, the blue area divided by the gray area in Figure 1.6, which is calculated through the following equation:

$$FF = \frac{Area_{blue}}{Area_{gray}} = \frac{P_{max}}{J_{sc} \cdot V_{oc}} = \frac{J_{max} \cdot V_{max}}{J_{sc} \cdot V_{oc}}$$

This parameter can be affected by the quality of the charge transport and the recombination rate that takes place in the solar cell.[39]

- Eventually, the PCE can be directly obtained by means of all the already mentioned photovoltaic parameters and the following equation (for a specific intensity of incident light P_i):

$$PCE = \frac{P_{max}}{P_i} = \frac{J_{sc} \cdot V_{oc} \cdot FF}{P_i}$$

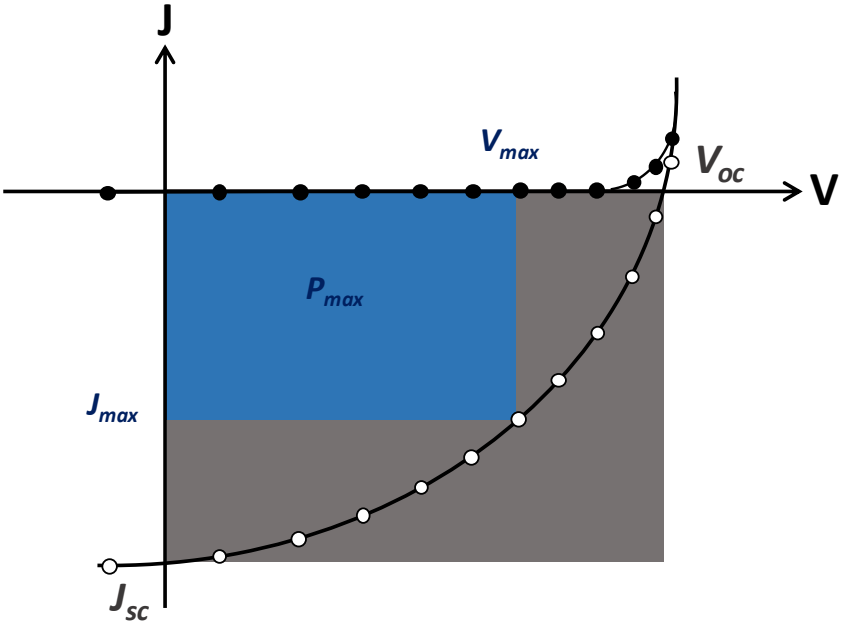

Figure 1.6. Representation of a J-V curve under illuminated (white dots) and dark conditions (black dots).

A second characterization technique is routinely used, namely the external quantum efficiency (EQE) also known as the incident photon-to-current conversion efficiency (IPCE). This measurement provides the percentage of incident photons converted into electrons for each wavelength (Figure 1.7). The integration of the area below the curve provides the J_{int} value, which should match the J_{sc} obtained by means of J-V curves.

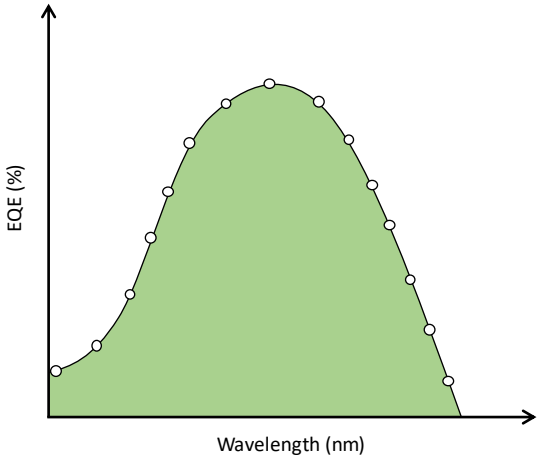

Figure 1.7. Representation of an EQE curve.

Eventually, for comparative purposes, every photovoltaic characterization has to be carried out under standard experimental conditions. Hence, simulated light sources have to be calibrated in terms of wavelength and power. To do so, a general agreement was adopted through the air mass coefficient (AM), in an attempt to simulate the solar spectrum taking into consideration the interaction of the light with several atmospheric species, such as ozone, H_2O and CO_2 in its way to the surface of the Earth.[40] Moreover, usual experimental measurements are carried out under an AM 1.5 illumination, corresponding to an incident simulated light power of 1000 W m^{-2} with a deviation angle of 48.2°, as illustrated in Figure 1.8.[41]

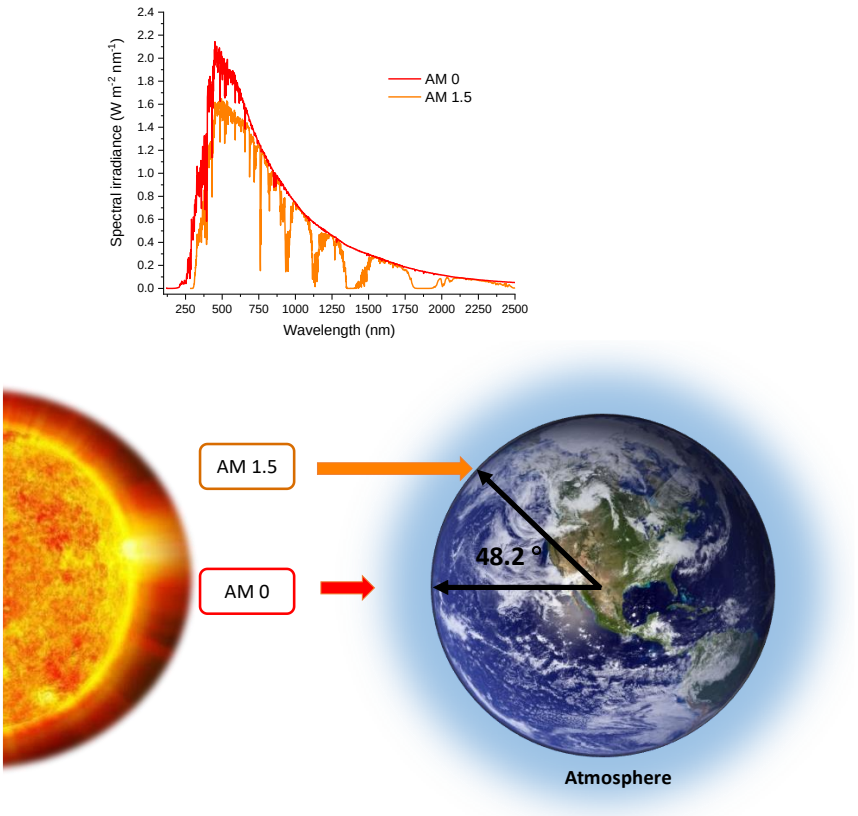

Figure 1.8. Solar emission spectra depending on the position: AM 0 (before entering the atmosphere) and the widely used irradiating source in OSCs AM 1.5 (on the Earth's surface and 48.2 ° tilted).[41-42]

1.3.5 Evolution of the active layer

In order to improve their performance, all the aspects of the cells have to be optimized in parallel. The structure of the devices is extremely crucial and it has been subjected to constant modifications, such as the followings:

- There are two general architectures for single junction devices, i.e., direct and inverted, depending on the direction in which the electrons and the holes are extracted from the device.[43] In the direct (or standard) configuration, the holes are going towards the transparent electrode, generally made of indium tin oxide (ITO), and the electrons away from it and vice versa for the inverted solar cells (Figure 1.9).
- In addition to PHJ and BHJ, both approaches can be combined in the so-called planar-mixed heterojunction (PMHJ) (Figure 1.9). In that way, a bulk heterojunction is sandwiched between layers of donor and acceptor. This configuration ensures both the low resistance to charge transport of a PHJ and the high exciton diffusion efficiency of a BHJ.[44-45]
- In contrast to single junctions, multi-junction solar cells, which are composed of stacked active layers (Figure 1.9), can minimize the low charge mobility of

organic materials and a higher overall thickness can be used. In addition, complementary active layers can be used to cover the light spectrum as much as possible.[46] Another advantage is that the V_{oc} of a multi-junction solar cell is ideally the sum of the V_{oc} of its sub-cells.[47] Although the fabrication procedure is more challenging, this strategy historically has led to higher efficiencies than those recorded with single junctions.[48]

- Ternary blends are another useful strategy in OPV. Their active layer is composed of a donor, an acceptor and a third D or A material. The idea is to use an additional complementary material that produces a synergic effect to improve the overall performance.[49-50]

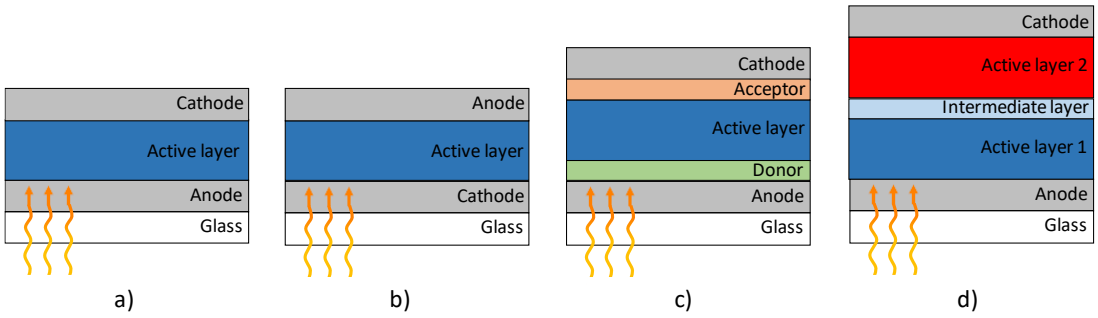

Figure 1.9. Schematic structure of direct (a), inverted (b), PMHJ (c) and multi-junction (d) devices.

Moreover, and common to the above described architectures, several modifications within the fabrication procedure can also been carried out:

- The deposition of the active layer onto heated substrates is sometimes an effective approach in order to impact the morphology of the active layer ending up, in some cases, with a significant performance enhancement.[51]
- The use of extra interlayers is another critical point that has attracted a lot of interest since it can play an important role in several parameters, such as the morphology and/or the carrier recombination/extraction.[52]
- Post-treatments (thermal or solvent annealing) carried out on the active layer can drastically enhance the performance of the devices. In these processes, the cell is exposed to the vapor of a solvent[53] or to a higher temperature[54-55] resulting in changes in the morphology of the active layer.
- The use of solvent additives in the blend can also induce a positive effect in the morphology of the active layer.[56] Several molecules have been tested for this purpose, such as 1,8-diiodooctane (DIO),[57] different alkanedithiols,[58] 1-chloronaphthalene[59] or *N*-methyl-2-pyrrolidone.[60]

Finally, since this PhD thesis will be primarily related to synthesis, a special emphasis will be placed on the key donor and acceptor materials reported in the field.

1.3.5.1 Donors materials

1.3.5.1.1 Macromolecular architectures

The first types of donor polymers used in OSCs were mainly polyparaphenyle vinylene- (PPV) or polythiophene-based (PT).[24] They had been thoroughly studied and their properties could be easily tuned by modifying their synthetic procedure.[61] Among the most well-known polymers of those series, the **P3HT** holds a special place.[27] However, their photovoltaic performances have been spoiled by their large bandgap that prevents the absorption of 70% of the solar radiation.[62] Thus, in order to maximize the number of absorbed photons, the synthesis of low-bandgap polymers became of substantial importance.[63]

To achieve this goal, the most common approach corresponds to the copolymerization of an electron-donating and an electron-accepting block. In that way, the optical bandgap of the resulting polymer is narrowed due to the orbit coupling between these two blocks along the polymer backbone.[64] So far, a myriad of combinations of several monomers have been reported and some examples are illustrated in Figure 1.10.

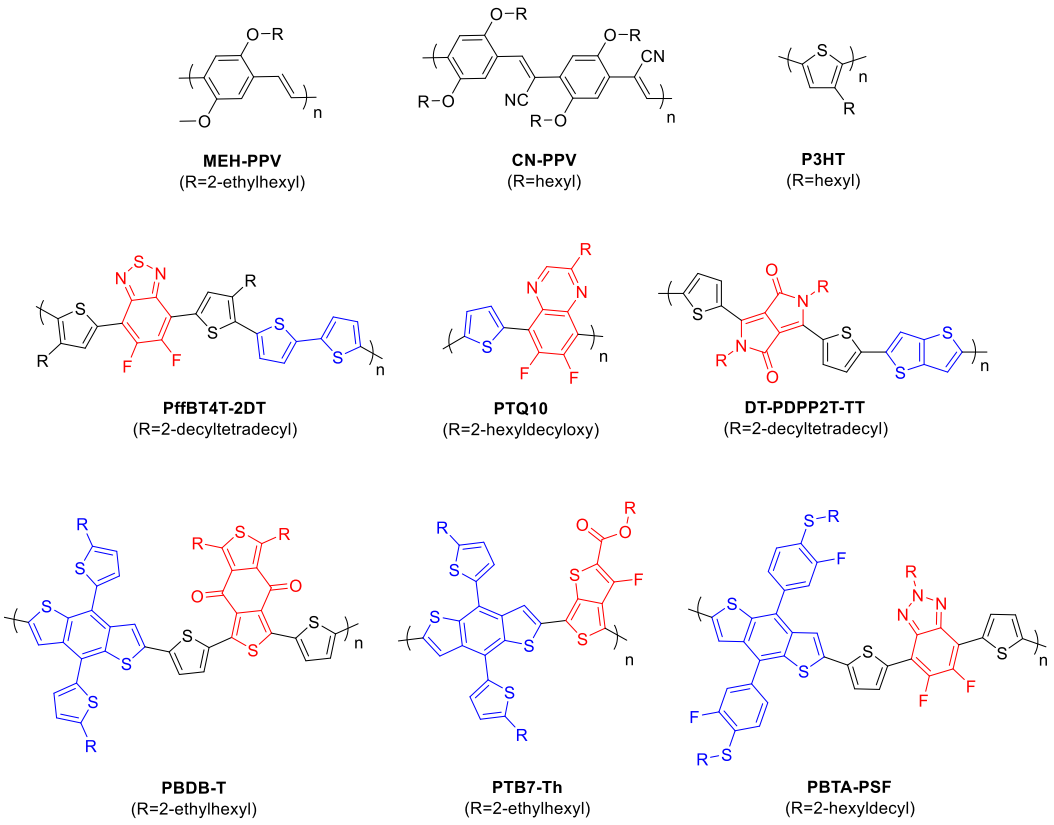

Figure 1.10. Examples of donor polymers used in OPV (D and A blocks highlighted in blue and red respectively).

Among the most common moieties used as donor monomers, thiophene (T), 2,2'-bithiophene, thieno[3,2-*b*]thiophene, benzo[1,2-*b*:4,5-*b*']dithiophene (BDT) and fluorene stand out.[63, 65] On the other hand, benzo[2,1,3]thiadiazole, thieno[3,4-*b*]thiophene, 2*H*-benzo[*d*][1,2,3]triazole, diketopyrrolopyrrole (DPP), thieno[3,4-*c*]pyrrole-4,6-dione, quinoxaline and benzo[1,2-*c*:4,5-*c*']dithiophene-4,8-dione (BDD) can be cited as examples of commonly used accepting blocks.[66-69]

Although highly performing, these materials present several drawbacks, such as the batch-to-batch variations, which impact their polydispersity index, or the usual difficulty to obtain a high degree of purity. In this context, the development of molecular donors has attracted considerable attention.

1.3.5.1.2 Molecular architectures

The main advantage of this class of materials comes from their discrete structure that avoids the molecular weight dependence, thus enabling a better structure-properties relationship. Although used in the first OPV devices, they did not trigger a great interest until the mid-2000s. At this point, the first materials were mainly meant to be deposited by evaporation. For instance, acene-based donors as tetracene, pentacene and rubrene were really popular since they exhibited promising PCEs between 2 and 3% (Figure 1.11).[70-72] Oligothiophenes have been as well employed due to their outstanding charge transport properties,[73] either by themselves or substituted by short alkyl chains or end-capped with dicyanovinyl groups (DCV).[74] Besides, more complex molecules based on macrocycles, such as porphyrines and phthalocyanines, have been also used as donor materials due to their suitable absorption and charge transport properties.[75-76]

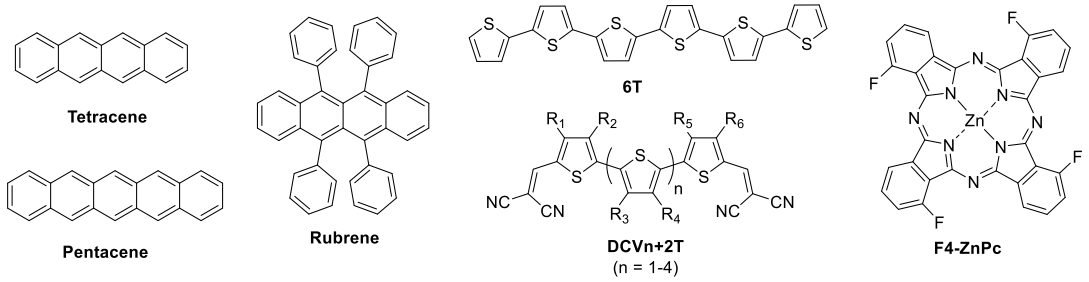

Figure 1.11. Examples of donor molecular architectures for vacuum-processed OSCs.

Afterwards, the introduction of solubilizing groups was strongly considered as a further step towards solution-processed solar cells based on small molecules. Roncali et al. published one of the pioneer papers in which a home-made soluble small molecule consisting of a tetrahedral oligothiophene donor was reported.[77] The three-dimensional structure of this molecule allowed

an isotropic charge transport but its narrow absorption limited the efficiency resulting in a modest PCE of 0.3%. Although the devices were not highly performing, this publication paved the way for the development of molecular architectures in OPV. Since then, countless structures have been studied and reported: from the soluble version of the above stated molecular donors[78-79] to the use of materials based on different organic dyes, such as merocyanines,[80] squaraines,[81-82] boron-dipyrromethenes (BODIPYs)[83] and DPPs.[84-85]

Linear small D-π-A push-pull molecules have also been used as D materials due to their ease of synthesis, tunability, suitable absorption in the visible spectrum[86-87] and usual compatibility with both solution and vacuum deposition processes. In view of the great potential of these materials, their development, with particular emphasis on arylamine-based push-pull molecules, has been one of the main focuses of the reaserch developped by the SCL group of MOLTECH-Anjou over the last decade.[88-89] This electron-rich block exhibits relatively good hole transport properties[90] and a high versatility, since subtle chemical modifications can indeed deeply affect the optical, electrochemical, self-assembling and therefore photovoltaic properties of the materials. Among other promising and performing molecules (Figure 1.12),[90-94] **DTDCPB** can be highlighted, since impressive PCEs of 9.8% and 15.0% were reported when combined with **C_{70}** in single- and multi-junction stacks respectively.[95]

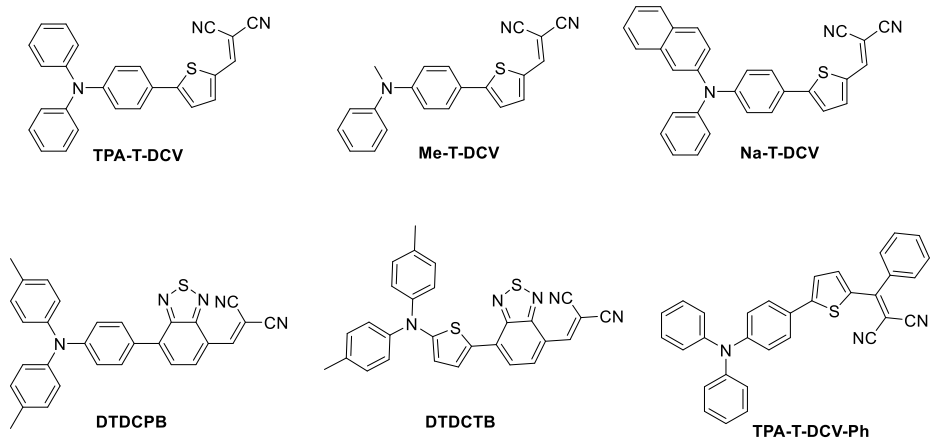

Figure 1.12. Examples of arylamine-based push-pull donor materials used in OPV.

Eventually, in a further attempt to reduce the gap in performance between small molecules and polymers as donor materials in OPV, more extended structures have been designed.[96] Hence, one approach deals with the synthesis of oligomers to combine the properties of both chemical architectures, i.e., the mono-dispersity of the molecular systems and the good film-forming capabilities of the polymers. Consequently, these molecules usually include blocks that come directly from the most performing D polymers, as illustrated in the structure of **PBDB-T** or

DR3TBDD (Figure 1.13). These BDT- and BDD-based donors reached efficiencies of 9.2% and 11.3% when blended with **$PC_{71}BM$** in simple device architectures.[97-98] In addition, many soluble molecules based on π-conjugated macrocycles have been synthesized,[99] such as the **DPPEZnP-BzTBO**, which exhibits a PCE of 9.1% once blended with **$PC_{61}BM$**.[100]

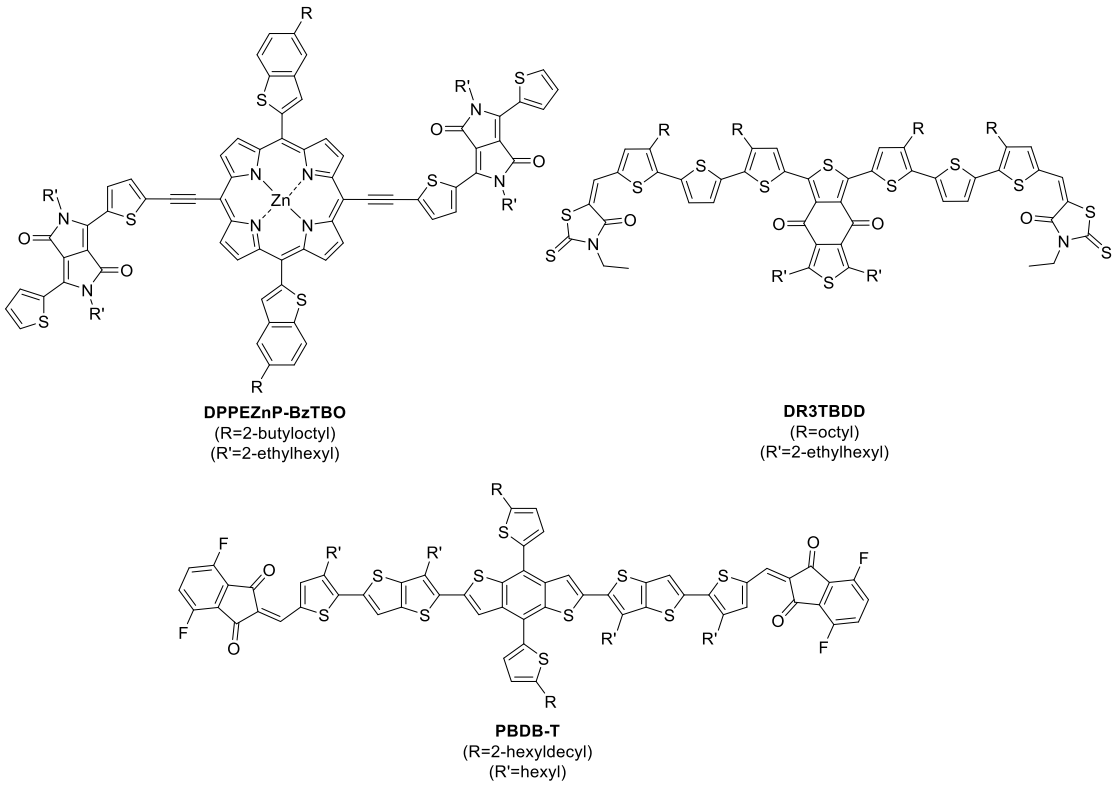

Figure 1.13. Examples of highly performing small molecule donor materials used in OPV.

1.3.5.2 Acceptor materials

1.3.5.2.1 Fullerene derivatives

Since the discovery of the fullerenes in 1985,[101] **C_{60}** and **C_{70}** (Figure 1.14) have been widely employed as acceptor materials in organic solar cells.[102] There are several reasons to justify their long reign as reference compounds in the field of OPV. First, they are characterized by a great electron-withdrawing capability, as the photoinduced electron transfer from the donor takes place in the sub-picosecond time scale.[103] In addition, they can reversibly accept up to six electrons depending on the fullerene derivative.[104] In order to favor the good functioning of the solar cells, it is also possible to limit their high tendency to form nano-domains through π-π stacking by using different solvent additives or techniques, such as thermal or vapor annealing.[105-106] These features, along with their outstanding electron mobility and their isotropic charge transport,[107-108] are the main reasons for their great success in OPV for many years, and that is why a myriad of donors have been synthesized according to their energy levels.

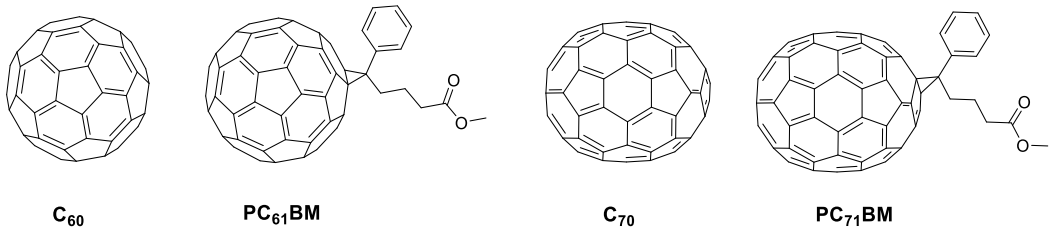

*Figure 1.14. Chemical structures of **C_{60}** and **C_{70}** and their soluble derivatives **$PC_{61}BM$** and **$PC_{71}BM$**.*

On the other hand, several structural modifications have been carried out to make them compatible with the different solution processing technologies. Obtained by means of the respective cyclopropanation reactions of **C_{60}** and **C_{70}**, **$PC_{61}BM$** and **$PC_{71}BM$** are amongst the most commonly used soluble fullerenes. This additional functionalization was also found to tune the morphological, optical and electrochemical properties of the fullerene-based materials.[106-107, 109] Another well-known example is the indene-C_{60} bisadduct (**ICBA**),[110-111] which presents a higher LUMO level that can lead to larger V_{oc} values and therefore to improved performances in comparison to the conventional **$PC_{61}BM$**.

Even though they exhibit quite suitable properties for their use as acceptors in OPV, their tridimensional structure is a double-edged sword as it is also responsible for their main drawbacks. First, the high symmetry of **C_{60}** hinders many electronic transitions leading to an almost negligible visible absorption. This effect is less intense in the case of **C_{70}** due to its lower degree of symmetry, which results in an improved absorption in the 400-600 nm range, but still with a limited contribution in the harvesting process in comparison to the donor.[112-113] In addition, it is possible to modify the properties of the fullerenes via different approaches, such as the use of fulleropyrrolidines,[114] open-cage fullerenes,[115-116] penta(organo)fullerenes[117] or different substituents other than the phenyl ring in PCBM.[118] However, the delocalization of the orbitals limits the room for maneuver in terms of efficient energy tuning. Consequently, many efforts have been devoted to tune the donor materials instead. In addition, their apparently fruitful aggregation seems not to be that beneficial if it is not controlled, since their crystallization can also lead to a detrimental phase segregation.[105] There are also many concerns regarding their stability towards oxygen and light since several adverse processes can take place. For instance, in the presence of the former, fullerenes suffer from photo-oxidation reactions,[119] thus producing epoxides and carbonyl groups in the fullerene cage.[120-121] In addition, dimerization processes can also take place in the presence of the latter.[122]

1.3.5.2.2 Non-fullerene acceptors

All these drawbacks are the main reasons for the current increasing interest in the synthesis of non-fullerene acceptors. Although their efficiencies were not comparable to those of fullerenes at the beginning, they became highly competitive and are currently part of the renewal occurring in the field, resulting in a countless number of related publications. Their main advantages are their improved absorption properties and their easier electrochemical tunability.[123]

Rylene derivatives[124] (Figure 1.15) have been one of the most common NFAs used in OPV. In fact, one acceptor of this family was used in the seminal PHJ solar cell reported by Tang in 1986. Their optical and electrochemical properties, i.e., great absorption coefficients, mobility and electronic affinity, together with their electron-withdrawing character, charge transport properties and high thermal and chemical stabilities make them really suitable for this application.[125]

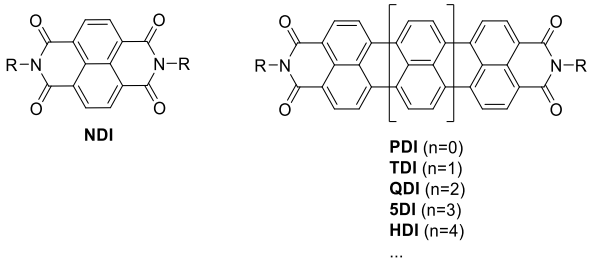

Figure 1.15. Structures of the most common rylene diimides.

However, their main weakness is their excessive π-stacking induced by their intrinsic planarity. This phenomenon leads to a better charge transport but can also result in extremely large domains that reduce the exciton dissociation thus limiting their film-forming capabilities. Considering that the intensity of this effect increases along with the length of the rylene core, the most common derivatives for OPV rely on the use of naphthalene diimide (**NDI**) and especially perylene diimide (**PDI**) derivatives.

Different strategies have been developed to synthesize more sterically hindered structures in an attempt to avoid their excessive aggregate formation without jeopardizing their outstanding properties.[126] Although the functionalization of the nitrogen atoms constituting the imide groups can already limit this π-stacking, high performances have been mainly reached with multimeric structures ranging from homo-multimers[127-128] to hetero-multimers with several building blocks (Figure 1.16).[129-131]

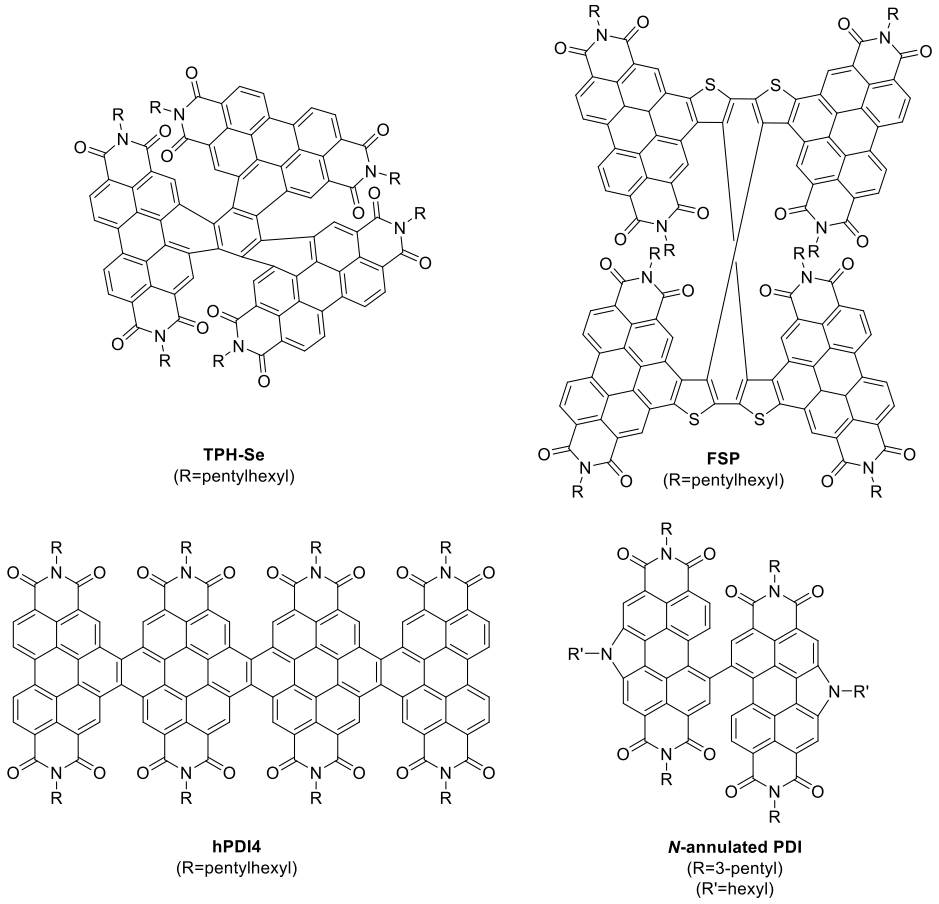

*Figure 1.16. Examples of **PDI** derivatives used as acceptors in OPV.*

On the other hand, whereas small molecules derived from **NDI**, such as **NDI-TR**, have not been that successful in OPV,[132] **NDI**-based polymers (**N2200** derivatives)[123, 133] are among the reference compounds used for the fabrication of all-polymer solar cells with PCEs of 10% (Figure 1.17).

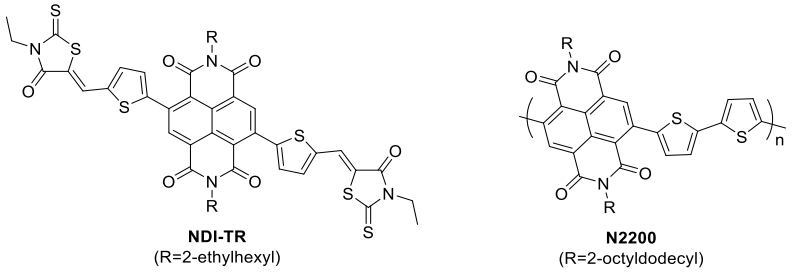

*Figure 1.17. Examples of **NDI** derivatives used as acceptors in OPV.*

In addition to the rylene family, most of the highly efficient NFAs are based on an A-D-A configuration. One of the first reported derivatives, namely **FEHIDT**, was based on a fluorene core substituted with two 1,3-indanediones connected through thiophene spacers.[134] This NFA

was able to reach an efficiency of ca. 2.4% when it was blended with **P3HT**. Afterwards, the replacement of this core by an indacenodithiophene (IDT) increased the PCE up to 3.7%.[135] Eventually, the substitution of the IDT by the extended indacenodithieno[3,2-*b*]thiophene (IDTT) was a major breakthrough, as the new reported material (**ITIC**) was the first high performing NFA of this series of acceptors to outperform the fullerenes.[136] The structural modification of these systems has been a hot topic ever since, being always related to the highest performances in the field.[137] Among other successful examples, **IT-4F** and **CO$_i$8DFIC** stand out, since they both have been able to reach efficiencies of ca. 14% (Figure 1.18). The main advantages of this type of NFAs lie in their narrow bandgaps and higher molar extinction coefficients. In addition, their rigid backbone enhances their crystallinity both in pure and blend films, thus leading to high electron mobilities (ca. 10^{-4} to 10^{-3} cm^2 $V^{-1}s^{-1}$).[138]

Finally, the low-bandgap acceptor **Y6** has been recently established as the new cornerstone for the fabrication of high-performing solar cells.[139] Reported in 2019, this NFA recently set up a world record for a single junction solar cell with a PCE of 18.22%.[140] The active layer consisted of a blend of **Y6** and a wide-bandgap DTBT-based copolymer, whose combination was found to efficiently harvest all the visible and a significant part of the NIR spectrum. Some modifications of this structure have already been reported in an attempt to improve its performance.[141]

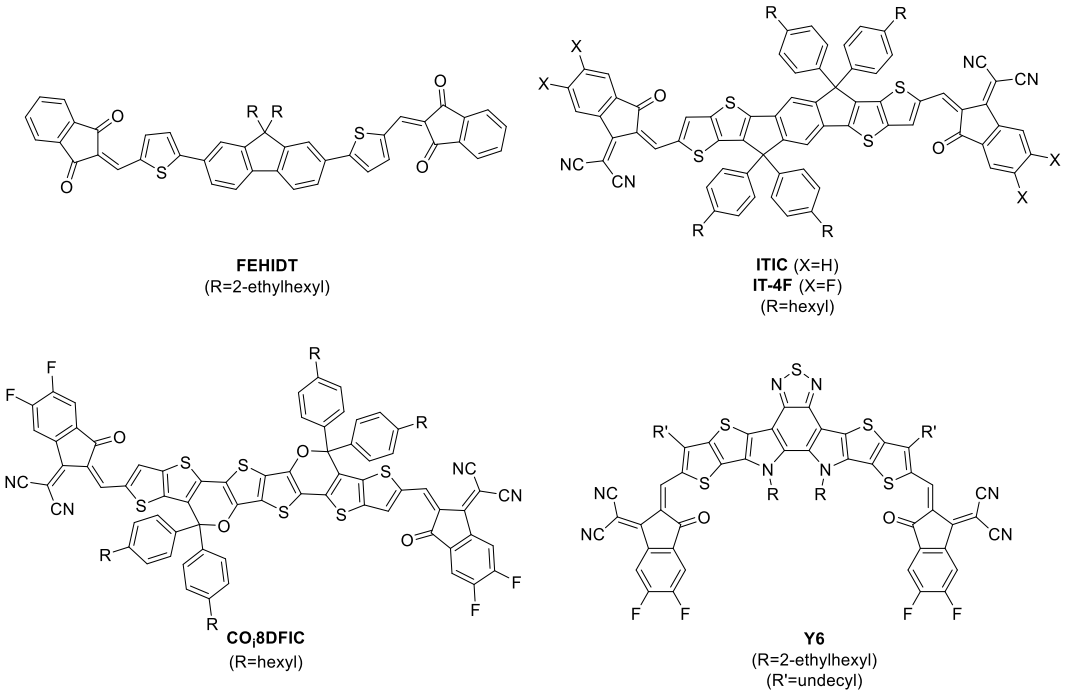

Figure 1.18. Examples of A-D-A derivatives used as NFAs in OPV.

Although not fully detailed herein, additional types of acceptor materials have been reported, including subphthalocyanine,[142-143] porphyrin[144] or DPP[145-146] derivatives.

1.4 Objectives of the thesis

Even if performances of OSCs are getting closer to those of other photovoltaic technologies (silicon or perovskites), a critical vision of the state-of-the-art publications highlights that the highest efficiencies are generally paired with an enhancement of the synthetic complexity of both the materials and the fabrication procedure. Hence, the large-scale production of efficient OSCs is currently not realistic and thus the research on their actual applicability is of substantial importance.

In the recent years, continuous efforts have been devoted to optimize the scalability of the fabrication process. Owing to its industrial optimization, roll-to-roll printing techniques have become a real alternative for the fabrication of actual modules and could reduce the existing efficiency gap between them and the demonstrators built in laboratories.[147] This technique also presents several additional advantages that could lead to several milestones, such as the possibility of fabricating efficient devices under air and using harmless solvents.

However, most performing materials are not compatible with these large-scale processing technics and do not fulfill the basic requirements for their commercialization, namely to be low-cost (Figure 1.19).

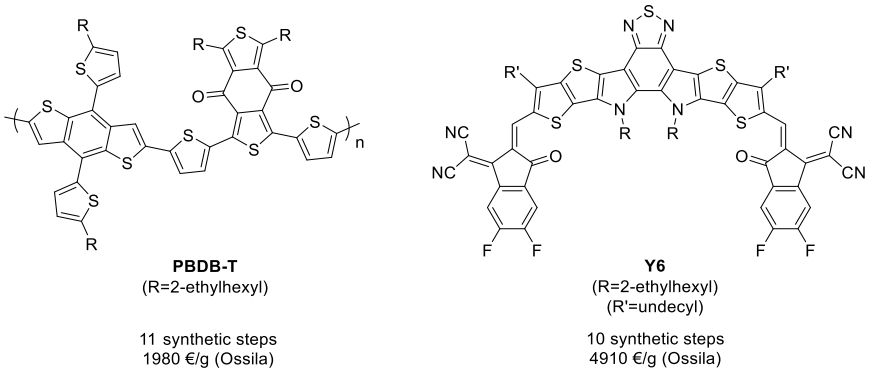

Figure 1.19. Synthetic length and cost of a highly performing D/A couple: ***PBDB-T/Y6****.*

Their syntheses are indeed very long, tedious, require the use of toxic reagents and their purifications are expensive and generate a huge amount of waste. Several studies have been already reported regarding many aspects of the scalability of the synthesis of highly performing materials, e.g., donor polymers[148-149] or NFAs.[150] In view of these results, it seems that the complexity required to improve the performance of the devices has outweighed the goal to produce affordable scalable devices, which is the final aim of this technology. Thus, in pursuit of a real commercialization, a compromise between the photovoltaic performances and the

production cost has to be reached, and that is the reason why the preparation of simpler and less expensive materials is that crucial.

In this context, the aim of this PhD thesis will be to minimize the synthetic cost by decreasing the number of steps and using non-expensive starting materials. Hence, based on this approach, different donor molecules based on a push-pull configuration will be synthesized, characterized and tested in devices (Figure 1.20).

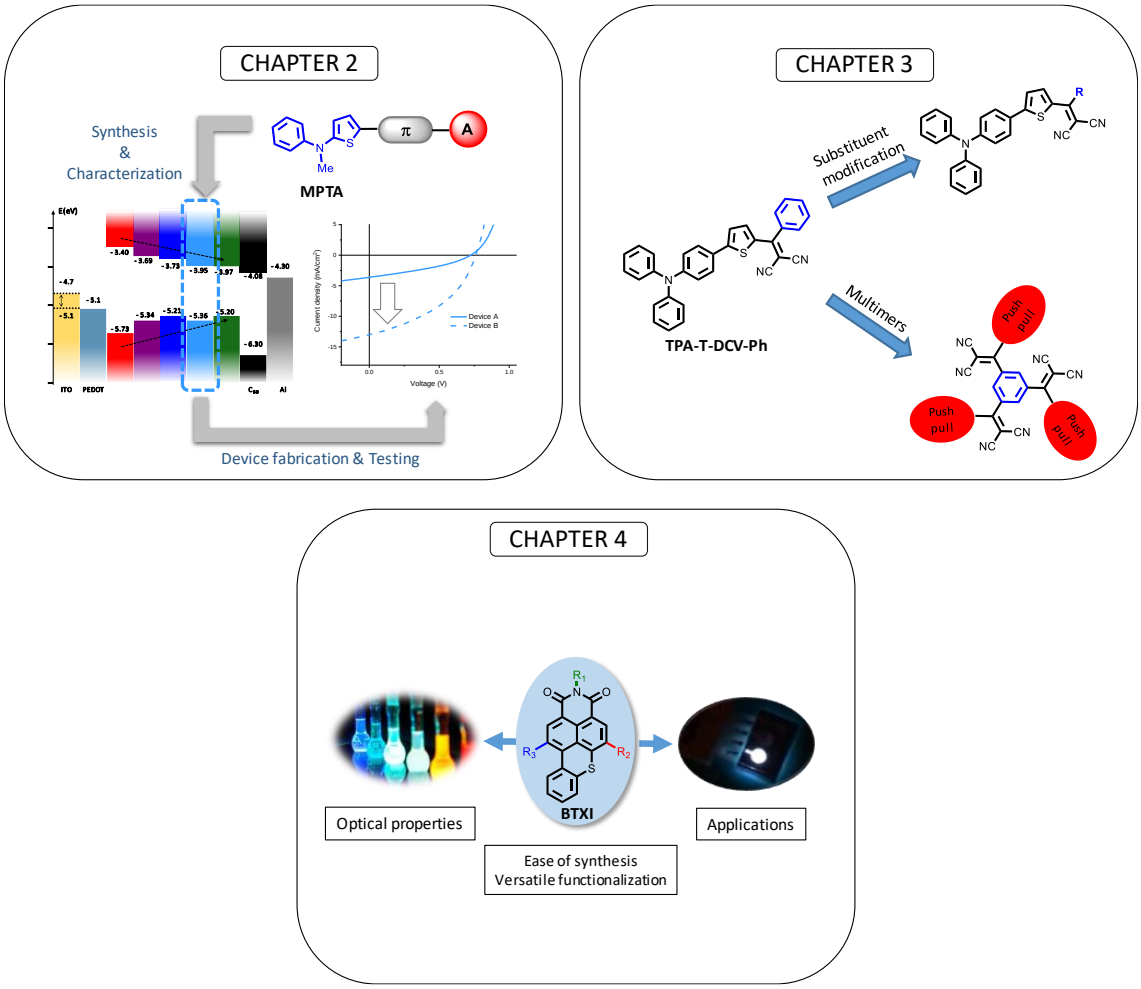

Figure 1.20. Graphical abstracts of chapters 2, 3 and 4 of this PhD thesis.

Chapter 2 will be focused on the synthesis of D-π-A molecules based on the *N*-methyl-*N*-phenylthiophen-2-amine (MPTA) donor unit, which has not yet been explored in the field. A series of derivatives will be synthesized by modulating the π-spacer and the electron-withdrawing group, and the impact on the optical, electrochemical and photovoltaic properties will be naturally investigated.

Chapter 3 will be related to the structural modification of a recently reported push-pull molecule, namely **TPA-T-DCV-Ph** (Figure 1.20). The latter includes an additional phenyl ring in

its accepting moiety compared to the well-known **TPA-T-DCV**. This change results in a higher exciton diffusion length and therefore PCE. Hence, two different structural modifications of this donor will be reported.

Eventually, chapter 4 will be related to the functionalization of a promising and unexplored rylene, namely the benzothioxanthene imide (**BTXI**), whose most attractive features are its low synthetic cost and outstanding optical and electrochemical properties. Thus, its reactivity will be explored in a deeper level and the properties of the new derivatives will be studied.

References

[1] https://www.iea.org World Energy Outlook 2019
[2] https://www.iea.org Solar Energy Perspectives 2011
[3] Grätzel, M., *Inorganic Chemistry* **2005**, *44*, 6841-6851.
[4] Becquerel, A. E., *Comptes Rendus de L'Academie des Sciences* **1839**, *9*, 145-149.
[5] Becquerel, A. E., *Comptes Rendus de L'Academie des Sciences* **1839**, *9*, 561-567.
[6] Chapin, D. M., Fuller, C. S. and Pearson, G. L., *Journal of Applied Physics* **1954**, *25*, 676-677.
[7] Photovoltaics Report, Fraunhofer Institute for Solar Energy Systems, ISE, February 2018
[8] Green, M. A., Dunlop, E. D., Hohl-Ebinger, J., Yoshita, M., Kopidakis, N. and Ho-Baillie, A. W. Y., *Progress in Photovoltaics: Research and Applications* **2020**, *28*, 3-15.
[9] https://www.nrel.gov Best Research-Cell Efficiency Chart 2020
[10] O'Regan, B. and Grätzel, M., *Nature* **1991**, *353*, 737-740.
[11] Kakiage, K., Aoyama, Y., Yano, T., Oya, K., Fujisawa, J. and Hanaya, M., *Chemical Communications* **2015**, *51*, 15894-15897.
[12] Kojima, A., Teshima, K., Shirai, Y. and Miyasaka, T., *Journal of the American Chemical Society* **2009**, *131*, 6050-6051.
[13] Kim, H.-S., Lee, C.-R., Im, J.-H., Lee, K.-B., Moehl, T., Marchioro, A., Moon, S.-J., Humphry-Baker, R., Yum, J.-H., Moser, J. E., Grätzel, M. and Park, N.-G., *Scientific Reports* **2012**, *2*, 591.
[14] Lee, M. M., Teuscher, J., Miyasaka, T., Murakami, T. N. and Snaith, H. J., *Science* **2012**, *338*, 643-647.
[15] Zhang, F. and Zhu, K., *Advanced Energy Materials* **2020**, *10*, 1902579.
[16] Wang, R., Mujahid, M., Duan, Y., Wang, Z.-K., Xue, J. and Yang, Y., *Advanced Functional Materials* **2019**, *29*, 1808843.
[17] Kour, R., Arya, S., Verma, S., Gupta, J., Bandhoria, P., Bharti, V., Datt, R. and Gupta, V., *Global Challenges* **2019**, *3*, 1900050.
[18] Kearns, D. and Calvin, M., *The Journal of Chemical Physics* **1958**, *29*, 950-951.
[19] Ghosh, A. K., Morel, D. L., Feng, T., Shaw, R. F. and Jr., C. A. R., *Journal of Applied Physics* **1974**, *45*, 230-236.
[20] Tang, C. W. and Albrecht, A. C., *Nature* **1975**, *254*, 507-509.
[21] Merritt, V. Y. and Hovel, H. J., *Applied Physics Letters* **1976**, *29*, 414-415.
[22] Tang, C. W., *Applied Physics Letters* **1986**, *48*, 183-185.
[23] Mikhnenko, O. V., Blom, P. W. M. and Nguyen, T.-Q., *Energy & Environmental Science* **2015**, *8*, 1867-1888.
[24] Halls, J. J. M., Walsh, C. A., Greenham, N. C., Marseglia, E. A., Friend, R. H., Moratti, S. C. and Holmes, A. B., *Nature* **1995**, *376*, 498-500.
[25] Yu, G., Gao, J., Hummelen, J. C., Wudl, F. and Heeger, A. J., *Science* **1995**, *270*, 1789-1791.

[26] Lu, L., Zheng, T., Wu, Q., Schneider, A. M., Zhao, D. and Yu, L., *Chemical Reviews* **2015**, *115*, 12666-12731.
[27] Dang, M. T., Hirsch, L. and Wantz, G., *Advanced Materials* **2011**, *23*, 3597-3602.
[28] Liu, J., Chen, S., Qian, D., Gautam, B., Yang, G., Zhao, J., Bergqvist, J., Zhang, F., Ma, W., Ade, H., Inganäs, O., Gundogdu, K., Gao, F. and Yan, H., *Nature Energy* **2016**, *1*, 16089.
[29] Vandewal, K., *Annual Review of Physical Chemistry* **2016**, *67*, 113-133.
[30] Brédas, J.-L., Norton, J. E., Cornil, J. and Coropceanu, V., *Accounts of Chemical Research* **2009**, *42*, 1691-1699.
[31] Menke, S. M., Ran, N. A., Bazan, G. C. and Friend, R. H., *Joule* **2018**, *2*, 25-35.
[32] Baran, D., Kirchartz, T., Wheeler, S., Dimitrov, S., Abdelsamie, M., Gorman, J., Ashraf, R. S., Holliday, S., Wadsworth, A., Gasparini, N., Kaienburg, P., Yan, H., Amassian, A., Brabec, C. J., Durrant, J. R. and McCulloch, I., *Energy & Environmental Science* **2016**, *9*, 3783-3793.
[33] Cheng, P., Zhang, M., Lau, T.-K., Wu, Y., Jia, B., Wang, J., Yan, C., Qin, M., Lu, X. and Zhan, X., *Advanced Materials* **2017**, *29*, 1605216.
[34] Tress, W., Petrich, A., Hummert, M., Hein, M., Leo, K. and Riede, M., *Applied Physics Letters* **2011**, *98*, 063301.
[35] Hegedus, S., Desai, D. and Thompson, C., *Progress in Photovoltaics: Research and Applications* **2007**, *15*, 587-602.
[36] Tress, W., Leo, K. and Riede, M., *Advanced Functional Materials* **2011**, *21*, 2140-2149.
[37] Brabec, C. J., Cravino, A., Meissner, D., Sariciftci, N. S., Fromherz, T., Rispens, M. T., Sanchez, L. and Hummelen, J. C., *Advanced Functional Materials* **2001**, *11*, 374-380.
[38] Scharber, M. C., Mühlbacher, D., Koppe, M., Denk, P., Waldauf, C., Heeger, A. J. and Brabec, C. J., *Advanced Materials* **2006**, *18*, 789-794.
[39] Kim, M.-S., Kim, B.-G. and Kim, J., *ACS Applied Materials & Interfaces* **2009**, *1*, 1264-1269.
[40] Hagfeldt, A., Boschloo, G., Sun, L., Kloo, L. and Pettersson, H., *Chemical Reviews* **2010**, *110*, 6595-6663.
[41] Bird, R. E., Hulstrom, R. L. and Lewis, L. J., *Solar Energy* **1983**, *30*, 563-573.
[42] https://www.nasa.gov.
[43] Glatthaar, M., Niggemann, M., Zimmermann, B., Lewer, P., Riede, M., Hinsch, A. and Luther, J., *Thin Solid Films* **2005**, *491*, 298-300.
[44] Xue, J., Rand, B. P., Uchida, S. and Forrest, S. R., *Advanced Materials* **2005**, *17*, 66-71.
[45] Xue, J., Rand, B. P., Uchida, S. and Forrest, S. R., *Journal of Applied Physics* **2005**, *98*, 124903.
[46] Li, G., Chang, W.-H. and Yang, Y., *Nature Reviews Materials* **2017**, *2*, 17043.
[47] Di Carlo Rasi, D. and Janssen, R. A. J., *Advanced Materials* **2019**, *31*, 1806499.
[48] Meng, L., Zhang, Y., Wan, X., Li, C., Zhang, X., Wang, Y., Ke, X., Xiao, Z., Ding, L., Xia, R., Yip, H.-L., Cao, Y. and Chen, Y., *Science* **2018**, *361*, 1094-1098.
[49] Lu, L., Chen, W., Xu, T. and Yu, L., *Nature Communications* **2015**, *6*, 7327.
[50] Lee, J., Lee, S. M., Chen, S., Kumari, T., Kang, S. H., Cho, Y. and Yang, C., *Advanced Materials* **2019**, *31*, e1804762.
[51] Pfuetzner, S., Mickel, C., Jankowski, J., Hein, M., Meiss, J., Schuenemann, C., Elschner, C., Levin, A. A., Rellinghaus, B., Leo, K. and Riede, M., *Organic Electronics* **2011**, *12*, 435-441.
[52] Lai, T.-H., Tsang, S.-W., Manders, J. R., Chen, S. and So, F., *Materials Today* **2013**, *16*, 424-432.
[53] Huang, Y., Kramer, E. J., Heeger, A. J. and Bazan, G. C., *Chemical Reviews* **2014**, *114*, 7006-7043.
[54] Peumans, P., Uchida, S. and Forrest, S. R., *Nature* **2003**, *425*, 158-162.
[55] Verploegen, E., Mondal, R., Bettinger, C. J., Sok, S., Toney, M. F. and Bao, Z., *Advanced Functional Materials* **2010**, *20*, 3519-3529.
[56] Liao, H.-C., Ho, C.-C., Chang, C.-Y., Jao, M.-H., Darling, S. B. and Su, W.-F., *Materials Today* **2013**, *16*, 326-336.
[57] Ye, L., Zhang, S., Ma, W., Fan, B., Guo, X., Huang, Y., Ade, H. and Hou, J., *Advanced Materials* **2012**, *24*, 6335-6341.
[58] Peet, J., Kim, J. Y., Coates, N. E., Ma, W. L., Moses, D., Heeger, A. J. and Bazan, G. C., *Nature Materials* **2007**, *6*, 497-500.

[59] Cabanetos, C., El Labban, A., Bartelt, J. A., Douglas, J. D., Mateker, W. R., Fréchet, J. M. J., McGehee, M. D. and Beaujuge, P. M., *Journal of the American Chemical Society* **2013**, *135*, 4656-4659.
[60] Guo, X., Cui, C., Zhang, M., Huo, L., Huang, Y., Hou, J. and Li, Y., *Energy & Environmental Science* **2012**, *5*, 7943-7949.
[61] Roncali, J., *Chemical Reviews* **1997**, *97*, 173-206.
[62] Nunzi, J.-M., *Comptes Rendus Physique* **2002**, *3*, 523-542.
[63] Cui, C. and Li, Y., *Energy & Environmental Science* **2019**, *12*, 3225-3246.
[64] Xu, T. and Yu, L., *Materials Today* **2014**, *17*, 11-15.
[65] Hou, J., Chen, H.-Y., Zhang, S., Chen, R. I., Yang, Y., Wu, Y. and Li, G., *Journal of the American Chemical Society* **2009**, *131*, 15586-15587.
[66] Li, W., Hendriks, K. H., Roelofs, W. S. C., Kim, Y., Wienk, M. M. and Janssen, R. A. J., *Advanced Materials* **2013**, *25*, 3182-3186.
[67] Li, X., Huang, G., Zheng, N., Li, Y., Kang, X., Qiao, S., Jiang, H., Chen, W. and Yang, R., *Solar RRL* **2019**, *3*, 1900005.
[68] Wadsworth, A., Ashraf, R. S., Abdelsamie, M., Pont, S., Little, M., Moser, M., Hamid, Z., Neophytou, M., Zhang, W., Amassian, A., Durrant, J. R., Baran, D. and McCulloch, I., *ACS Energy Letters* **2017**, *2*, 1494-1500.
[69] Sun, C., Pan, F., Bin, H., Zhang, J., Xue, L., Qiu, B., Wei, Z., Zhang, Z.-G. and Li, Y., *Nature Communications* **2018**, *9*, 743.
[70] Chu, C.-W., Shao, Y., Shrotriya, V. and Yang, Y., *Applied Physics Letters* **2005**, *86*, 243506.
[71] Yoo, S., Domercq, B. and Kippelen, B., *Applied Physics Letters* **2004**, *85*, 5427-5429.
[72] Pandey, A. K. and Nunzi, J.-M., *Advanced Materials* **2007**, *19*, 3613-3617.
[73] Mishra, A., Ma, C.-Q. and Bäuerle, P., *Chemical Reviews* **2009**, *109*, 1141-1276.
[74] Fitzner, R., Mena-Osteritz, E., Mishra, A., Schulz, G., Reinold, E., Weil, M., Körner, C., Ziehlke, H., Elschner, C., Leo, K., Riede, M., Pfeiffer, M., Uhrich, C. and Bäuerle, P., *Journal of the American Chemical Society* **2012**, *134*, 11064-11067.
[75] Walter, M. G., Rudine, A. B. and Wamser, C. C., *Journal of Porphyrins and Phthalocyanines* **2010**, *14*, 759-792.
[76] Meiss, J., Merten, A., Hein, M., Schuenemann, C., Schäfer, S., Tietze, M., Uhrich, C., Pfeiffer, M., Leo, K. and Riede, M., *Advanced Functional Materials* **2012**, *22*, 405-414.
[77] Roncali, J., Frère, P., Blanchard, P., de Bettignies, R., Turbiez, M., Roquet, S., Leriche, P. and Nicolas, Y., *Thin Solid Films* **2006**, *511-512*, 567-575.
[78] Lin, Y., Li, Y. and Zhan, X., *Chemical Society Reviews* **2012**, *41*, 4245-4272.
[79] Mishra, A. and Bauerle, P., *Angewandte Chemie International Edition* **2012**, *51*, 2020-2067.
[80] Steinmann, V., Kronenberg, N. M., Lenze, M. R., Graf, S. M., Hertel, D., Meerholz, K., Bürckstümmer, H., Tulyakova, E. V. and Würthner, F., *Advanced Energy Materials* **2011**, *1*, 888-893.
[81] Yang, D., Sasabe, H., Sano, T. and Kido, J., *ACS Energy Letters* **2017**, *2*, 2021-2025.
[82] Zimmerman, J. D., Lassiter, B. E., Xiao, X., Sun, K., Dolocan, A., Gearba, R., Vanden Bout, D. A., Stevenson, K. J., Wickramasinghe, P., Thompson, M. E. and Forrest, S. R., *ACS Nano* **2013**, *7*, 9268-9275.
[83] Srinivasa Rao, R., Bagui, A., Hanumantha Rao, G., Gupta, V. and Singh, S. P., *Chemical Communications* **2017**, *53*, 6953-6956.
[84] Gao, K., Jo, S. B., Shi, X., Nian, L., Zhang, M., Kan, Y., Lin, F., Kan, B., Xu, B., Rong, Q., Shui, L., Liu, F., Peng, X., Zhou, G., Cao, Y. and Jen, A. K.-Y., *Advanced Materials* **2019**, *31*, 1807842.
[85] Wang, J.-L., Wu, Z., Miao, J.-S., Liu, K.-K., Chang, Z.-F., Zhang, R.-B., Wu, H.-B. and Cao, Y., *Chemistry of Materials* **2015**, *27*, 4338-4348.
[86] Malytskyi, V., Simon, J.-J., Patrone, L. and Raimundo, J.-M., *RSC Advances* **2015**, *5*, 354-397.
[87] Bures, F., *RSC Advances* **2014**, *4*, 58826-58851.
[88] Roncali, J., Leriche, P. and Blanchard, P., *Advanced Materials* **2014**, *26*, 3821-3838.
[89] Cabanetos, C., Blanchard, P. and Roncali, J., *The Chemical Record* **2019**, *19*, 1-9.

[90] Jiang, Y., Cabanetos, C., Allain, M., Liu, P. and Roncali, J., *Journal of Materials Chemistry C* **2015**, *3*, 5145-5151.
[91] Mohamed, S., Demeter, D., Laffitte, J.-A., Blanchard, P. and Roncali, J., *Scientific Reports* **2015**, *5*, 9031.
[92] Kozlov, O. V., Luponosov, Y. N., Solodukhin, A. N., Flament, B., Douhéret, O., Viville, P., Beljonne, D., Lazzaroni, R., Cornil, J., Ponomarenko, S. A. and Pshenichnikov, M. S., *Organic Electronics* **2018**, *53*, 185-190.
[93] Choi, J. W., Kim, C.-H., Pison, J., Oyedele, A., Tondelier, D., Leliège, A., Kirchner, E., Blanchard, P., Roncali, J. and Geffroy, B., *RSC Advances* **2014**, *4*, 5236-5242.
[94] Lin, L.-Y., Chen, Y.-H., Huang, Z.-Y., Lin, H.-W., Chou, S.-H., Lin, F., Chen, C.-W., Liu, Y.-H. and Wong, K.-T., *Journal of the American Chemical Society* **2011**, *133*, 15822-15825.
[95] Che, X., Li, Y., Qu, Y. and Forrest, S. R., *Nature Energy* **2018**, *3*, 422-427.
[96] Ilmi, R., Haque, A. and Khan, M. S., *Organic Electronics* **2018**, *58*, 53-62.
[97] Deng, D., Zhang, Y., Zhang, J., Wang, Z., Zhu, L., Fang, J., Xia, B., Wang, Z., Lu, K., Ma, W. and Wei, Z., *Nature Communications* **2016**, *7*, 13740.
[98] Zhang, H., Liu, Y., Sun, Y., Li, M., Kan, B., Ke, X., Zhang, Q., Wan, X. and Chen, Y., *Chemical Communications* **2017**, *53*, 451-454.
[99] Mahmood, A., Hu, J.-Y., Xiao, B., Tang, A., Wang, X. and Zhou, E., *Journal of Materials Chemistry A* **2018**, *6*, 16769-16797.
[100] Liang, T., Xiao, L., Gao, K., Xu, W., Peng, X. and Cao, Y., *ACS Applied Materials & Interfaces* **2017**, *9*, 7131-7138.
[101] Kroto, H. W., Heath, J. R., O'Brien, S. C., Curl, R. F. and Smalley, R. E., *Nature* **1985**, *318*, 162-163.
[102] Krätschmer, W., Lamb, L. D., Fostiropoulos, K. and Huffman, D. R., *Nature* **1990**, *347*, 354-358.
[103] Sariciftci, N. S., Smilowitz, L., Heeger, A. J. and Wudl, F., *Science* **1992**, *258*, 1474-1476.
[104] Xie, Q., Perez-Cordero, E. and Echegoyen, L., *Journal of the American Chemical Society* **1992**, *114*, 3978-3980.
[105] Campoy-Quiles, M., Ferenczi, T., Agostinelli, T., Etchegoin, P. G., Kim, Y., Anthopoulos, T. D., Stavrinou, P. N., Bradley, D. D. C. and Nelson, J., *Nature Materials* **2008**, *7*, 158-164.
[106] Li, C.-Z., Yip, H.-L. and Jen, A. K. Y., *Journal of Materials Chemistry* **2012**, *22*, 4161-4177.
[107] He, Y. and Li, Y., *Physical Chemistry Chemical Physics* **2011**, *13*, 1970-1983.
[108] Guldi, D. M., *Chemical Communications* **2000**, 321-327.
[109] Deng, L.-L., Xie, S.-Y. and Gao, F., *Advanced Electronic Materials* **2018**, *4*, 1700435.
[110] He, Y., Chen, H.-Y., Hou, J. and Li, Y., *Journal of the American Chemical Society* **2010**, *132*, 1377-1382.
[111] Zhao, G., He, Y. and Li, Y., *Advanced Materials* **2010**, *22*, 4355-4358.
[112] Wienk, M. M., Kroon, J. M., Verhees, W. J. H., Knol, J., Hummelen, J. C., van Hal, P. A. and Janssen, R. A. J., *Angewandte Chemie International Edition* **2003**, *42*, 3371-3375.
[113] Pfuetzner, S., Meiss, J., Petrich, A., Riede, M. and Leo, K., *Applied Physics Letters* **2009**, *94*, 223307.
[114] Matsumoto, K., Hashimoto, K., Kamo, M., Uetani, Y., Hayase, S., Kawatsura, M. and Itoh, T., *Journal of Materials Chemistry* **2010**, *20*, 9226-9230.
[115] Chen, C.-P., Lin, Y.-W., Horng, J.-C. and Chuang, S.-C., *Advanced Energy Materials* **2011**, *1*, 776-780.
[116] Murata, M., Morinaka, Y., Murata, Y., Yoshikawa, O., Sagawa, T. and Yoshikawa, S., *Chemical Communications* **2011**, *47*, 7335-7337.
[117] Niinomi, T., Matsuo, Y., Hashiguchi, M., Sato, Y. and Nakamura, E., *Journal of Materials Chemistry* **2009**, *19*, 5804-5811.
[118] Kooistra, F. B., Knol, J., Kastenberg, F., Popescu, L. M., Verhees, W. J. H., Kroon, J. M. and Hummelen, J. C., *Organic Letters* **2007**, *9*, 551-554.
[119] Yamane, S., Mizukado, J., Suzuki, Y., Sakurai, M., Chen, L. and Suda, H., *Chemistry Letters* **2015**, *44*, 339-341.

[120] Xiao, Z., Yao, J., Yang, D., Wang, F., Huang, S., Gan, L., Jia, Z., Jiang, Z., Yang, X., Zheng, B., Yuan, G., Zhang, S. and Wang, Z., *Journal of the American Chemical Society* **2007**, *129*, 16149-16162.
[121] Lee, H. K. H., Telford, A. M., Röhr, J. A., Wyatt, M. F., Rice, B., Wu, J., de Castro Maciel, A., Tuladhar, S. M., Speller, E., McGettrick, J., Searle, J. R., Pont, S., Watson, T., Kirchartz, T., Durrant, J. R., Tsoi, W. C., Nelson, J. and Li, Z., *Energy & Environmental Science* **2018**, *11*, 417-428.
[122] Fraga Domínguez, I., Distler, A. and Lüer, L., *Advanced Energy Materials* **2017**, *7*, 1601320.
[123] Sun, H., Chen, F. and Chen, Z.-K., *Materials Today* **2019**, *24*, 94-118.
[124] Zhao, X., Xiong, Y., Ma, J. and Yuan, Z., *The Journal of Physical Chemistry A* **2016**, *120*, 7554-7560.
[125] Feng, J., Jiang, W. and Wang, Z., *Chemistry – An Asian Journal* **2018**, *13*, 20-30.
[126] Nowak-Krol, A., Shoyama, K., Stolte, M. and Wurthner, F., *Chemical Communications* **2018**, *54*, 13763-13772.
[127] Hendsbee, A. D., Sun, J.-P., Law, W. K., Yan, H., Hill, I. G., Spasyuk, D. M. and Welch, G. C., *Chemistry of Materials* **2016**, *28*, 7098-7109.
[128] Zhong, Y., Trinh, M. T., Chen, R., Purdum, G. E., Khlyabich, P. P., Sezen, M., Oh, S., Zhu, H., Fowler, B., Zhang, B., Wang, W., Nam, C.-Y., Sfeir, M. Y., Black, C. T., Steigerwald, M. L., Loo, Y.-L., Ng, F., Zhu, X. Y. and Nuckolls, C., *Nature Communications* **2015**, *6*, 8242.
[129] Yan, C., Barlow, S., Wang, Z., Yan, H., Jen, A. K. Y., Marder, S. R. and Zhan, X., *Nature Reviews Materials* **2018**, *3*, 18003.
[130] Zhang, J., Li, Y., Huang, J., Hu, H., Zhang, G., Ma, T., Chow, P. C. Y., Ade, H., Pan, D. and Yan, H., *Journal of the American Chemical Society* **2017**, *139*, 16092-16095.
[131] Duan, L., Elumalai, N. K., Zhang, Y. and Uddin, A., *Solar Energy Materials and Solar Cells* **2019**, *193*, 22-65.
[132] Sung, M. J., Huang, M., Moon, S. H., Lee, T. H., Park, S. Y., Kim, J. Y., Kwon, S.-K., Choi, H. and Kim, Y.-H., *Solar Energy* **2017**, *150*, 90-95.
[133] Fan, B., Ying, L., Zhu, P., Pan, F., Liu, F., Chen, J., Huang, F. and Cao, Y., *Advanced Materials* **2017**, *29*, 1703906.
[134] Winzenberg, K. N., Kemppinen, P., Scholes, F. H., Collis, G. E., Shu, Y., Birendra Singh, T., Bilic, A., Forsyth, C. M. and Watkins, S. E., *Chemical Communications* **2013**, *49*, 6307-6309.
[135] Bai, H., Wang, Y., Cheng, P., Wang, J., Wu, Y., Hou, J. and Zhan, X., *Journal of Materials Chemistry A* **2015**, *3*, 1910-1914.
[136] Lin, Y., Wang, J., Zhang, Z.-G., Bai, H., Li, Y., Zhu, D. and Zhan, X., *Advanced Materials* **2015**, *27*, 1170-1174.
[137] Suman and Singh, S. P., *Journal of Materials Chemistry A* **2019**, *7*, 22701-22729.
[138] Zhang, J., Tan, H. S., Guo, X., Facchetti, A. and Yan, H., *Nature Energy* **2018**.
[139] Yuan, J., Zhang, Y., Zhou, L., Zhang, G., Yip, H.-L., Lau, T.-K., Lu, X., Zhu, C., Peng, H., Johnson, P. A., Leclerc, M., Cao, Y., Ulanski, J., Li, Y. and Zou, Y., *Joule* **2019**, *3*, 1140-1151.
[140] Liu, Q., Jiang, Y., Jin, K., Qin, J., Xu, J., Li, W., Xiong, J., Liu, J., Xiao, Z., Sun, K., Yang, S., Zhang, X. and Ding, L., *Science Bulletin* **2020**, *65*, 272-275.
[141] Zhou, Z., Liu, W., Zhou, G., Zhang, M., Qian, D., Zhang, J., Chen, S., Xu, S., Yang, C., Gao, F., Zhu, H., Liu, F. and Zhu, X., *Advanced Materials* **2020**, *32*, 1906324.
[142] Cnops, K., Rand, B. P., Cheyns, D., Verreet, B., Empl, M. A. and Heremans, P., *Nature Communications* **2014**, *5*, 3406.
[143] Cnops, K., Zango, G., Genoe, J., Heremans, P., Martinez-Diaz, M. V., Torres, T. and Cheyns, D., *Journal of the American Chemical Society* **2015**, *137*, 8991-8997.
[144] Guo, Y., Zhang, A., Li, C., Li, W. and Zhu, D., *Chinese Chemical Letters* **2018**, *29*, 371-373.
[145] Zhao, C., Guo, Y., Zhang, Y., Yan, N., You, S. and Li, W., *Journal of Materials Chemistry A* **2019**, *7*, 10174-10199.
[146] Josse, P., Dalinot, C., Jiang, Y., Dabos-Seignon, S., Roncali, J., Blanchard, P. and Cabanetos, C., *Journal of Materials Chemistry A* **2016**, *4*, 250-256.

[147] Carlé, J. E., Helgesen, M., Hagemann, O., Hösel, M., Heckler, I. M., Bundgaard, E., Gevorgyan, S. A., Søndergaard, R. R., Jørgensen, M., García-Valverde, R., Chaouki-Almagro, S., Villarejo, J. A. and Krebs, F. C., *Joule* **2017**, *1*, 274-289.
[148] Po, R., Bernardi, A., Calabrese, A., Carbonera, C., Corso, G. and Pellegrino, A., *Energy & Environmental Science* **2014**, *7*, 925-943.
[149] Marzano, G., Ciasca, C. V., Babudri, F., Bianchi, G., Pellegrino, A., Po, R. and Farinola, G. M., *European Journal of Organic Chemistry* **2014**, *2014*, 6583-6614.
[150] Wadsworth, A., Moser, M., Marks, A., Little, M. S., Gasparini, N., Brabec, C. J., Baran, D. and McCulloch, I., *Chemical Society Reviews* **2019**, *48*, 1596-1625.

Chapter 2

N-methylarylamine-based electron-donors for organic solar cells

2.1 Introduction

Triarylamine derivatives (TAAs) represent a major class of building blocks for the synthesis of hole-transporting materials (HTMs) used in various optoelectronic applications, such as organic light-emitting diodes (OLEDs) or organic/hybrid solar cells. During the past decades, and considering that the chemistry of active materials related to OSCs has witnessed an increasing interest, TAA-based materials have been widely used for the preparation of molecular electron-donor materials due to their strong electron-donating properties and high hole-mobility. One of the first examples for OPV was reported in 2006 by our laboratory group, when the usual donor polymer was replaced by a soluble D-(π-A)$_3$ push-pull molecule composed of a TPA substituted by electron-withdrawing T-DCV branches in each *para* position of its constituting phenyl rings (**TPA-(T-DCV)$_3$**, Figure 2.1).[1]

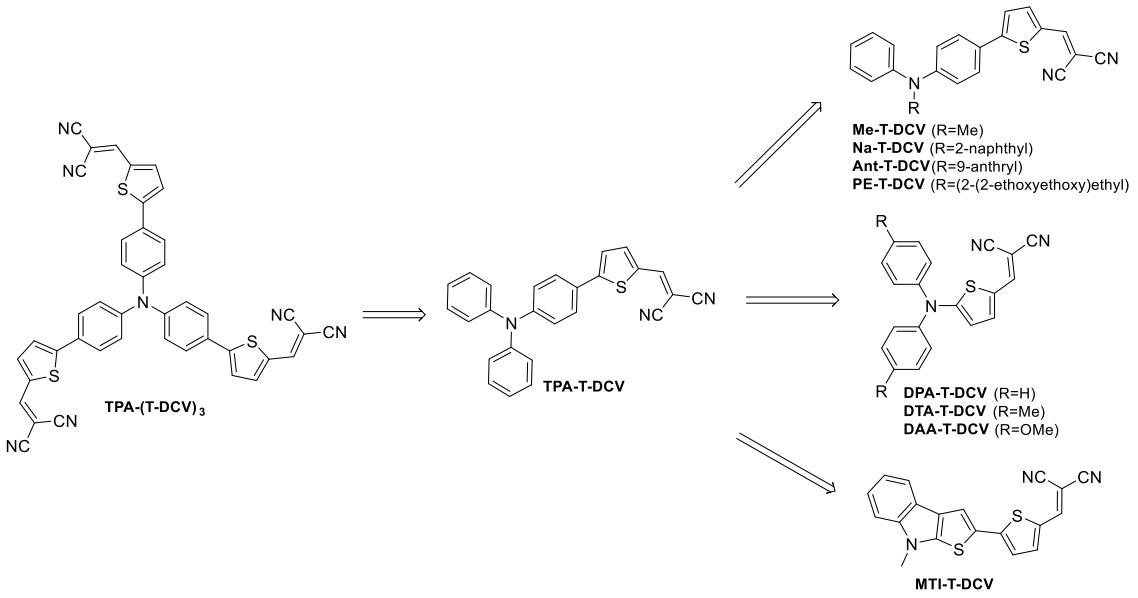

Figure 2.1. Evolution of the chemical structure of the TAA-based D materials from our laboratory group.

Since then, several types of molecular donors based on TAA units have been developed through various configurations and combinations with different π-spacers and acceptor moieties. However, it is noteworthy that our interest has been mainly related to the preparation of simple, accessible and affordable donor materials. To that end, two T-DCV branches of **TPA-(T-DCV)$_3$** were removed, ending up in the mono-substituted **TPA-T-DCV** (Figure 2.1).[2] First, the gram-scale synthesis of the latter was thoroughly optimized and it can currently be obtained in only two "green" steps in an overall yield of 87% from affordable and commercially available materials.[3] **TPA-T-DCV** was then embedded as a donor material in solution-processed OSCs revealing promising power conversion efficiencies of 2.5% and 3.0% in PHJ and BHJ respectively.[4-5] The

photovoltaic performances were thereafter improved by reaching a 4.0% PCE through the development of co-evaporated devices.[6] Hence, these results contributed in demonstrating promising efficiencies for a quite affordable couple of materials and devices.

Afterwards, the latter has been subjected to several chemical modifications that, in some cases, exerted a considerable and specific impact on the properties of the materials (Figure 2.1). For instance, one strategy consisted in substituting one of the outer phenyl rings of the TPA by different groups. Hence, the replacement by a polyether chain (**PE-T-DCV**) led to original and unexpected mechano-fluoro-NLO-chromic properties.[7] On the other hand, the substitution by an 9-anthryl (**Ant-T-DCV**), a 2-naphthyl (**Na-T-DCV**) or even a methyl group (**Me-T-DCV**) led to a three-, five- and fifty-fold increase of the hole mobility respectively and therefore to better photovoltaic performances.[2, 8-10] Another strategy has been the substitution of the phenyl ring that connects the nitrogen atom with the π-spacer by a thiophene (**DPA**, **DTA** and **DAA** donors, Figure 2.1).[11] This modification led to an electron-rich D unit with a higher donating capability responsible for redshifted absorptions and higher HOMO levels. This approach has been combined with additional cyclizations to afford the 8-methyl-8*H*-thieno[2,3-*b*]indole that also showed promising results (**MTI-T-DCV**, Figure 2.1).[12-13]

Another highly performing push-pull molecule from the literature that can be cited is **DTDCTB** (Figure 1.12). With an associated PCE of 5.8% when used as donor material, this molecule is characterized by a great evaporability, broad absorption and suitable phase segregation with fullerene derivatives.[14]

In that way, by combining these reported results with our background and experience, the synthesis and characterization of *N*-methyl-*N*-phenylthiophen-2-amine- (MPTA) based push-pull molecules was carried out during this chapter. Hence, different structures resulting from the combination of the aforementioned donor unit with different π-spacers and accepting blocks were considered (Figure 2.2).

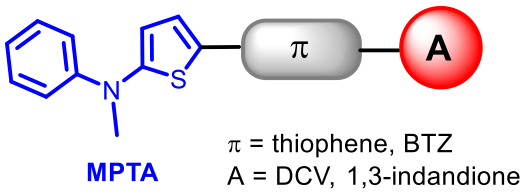

Figure 2.2. General structure of the MPTA-based target molecules of this chapter.

Due to their good performance in multiple applications related to organic electronics, thiophene[15-16] and benzothiadiazole[17-18] (BTZ) will thus be employed as spacers and dicianovinyl[19] and 1,3-indandione[20] as A units. Once isolated, the optical, electrochemical and photovoltaic characterizations of the new D materials will be discussed to rationalize the structure-property relationships.

2.2 Synthesis of the MPTA-based molecular donors

The electron-rich **MPTA** block was synthesized using a procedure from the literature[21] via a Buchwald-Hartwig cross-coupling between the commercially available *N*-methylaniline and 2-bromothiophene (Scheme 2.1).[21]

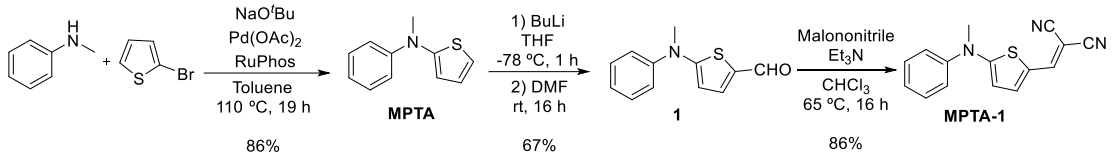

*Scheme 2.1. Synthetic pathway followed to obtain **MPTA-1**.*

Then, the smallest push-pull molecule of the series was first synthesized. To that end, **MPTA** was selectively formylated at the α position of the thiophene by means of a lithiation with *n*-butyllithium (*n*-BuLi) in THF followed by an electrophilic quench with DMF. The resulting compound **1** was finally engaged in a Knoevenagel condensation with malononitrile in chloroform to afford the target push-pull **MPTA-1**. In parallel, a π-spacer was introduced between the D and A units. Since the pinacol derivative of **MPTA** was not stable enough, a tributyltin group was consequently introduced on the constituting thiophene (**MPTA-Sn**). This stannane derivative was directly engaged in two Stille couplings with the bromocarboxaldehyde derivatives of thiophene and BTZ to afford aldehydes **2** and **3** respectively (Scheme 2.2).

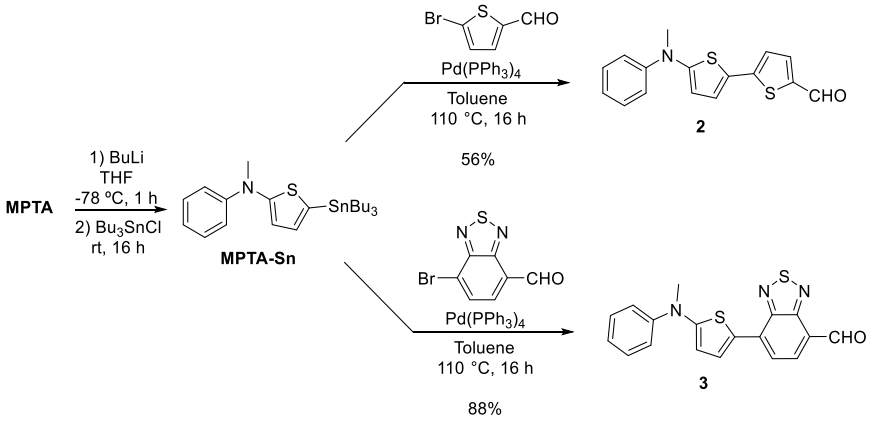

*Scheme 2.2. Synthetic pathway towards aldehydes **2** and **3**.*

Eventually, Knoevenagel condensations involving aldehydes **2** and **3** were finally carried out in acetonitrile for 2-4 hours at room temperature and protected from light (Scheme 2.3). All crudes were purified using a recycling preparative HPLC (see experimental section for details) except for **MPTA-5**. Due to its solubility issues, the crude was dissolved in chloroform and precipitated with pentane to obtain the pure product after thoroughly washing with distilled pentane.

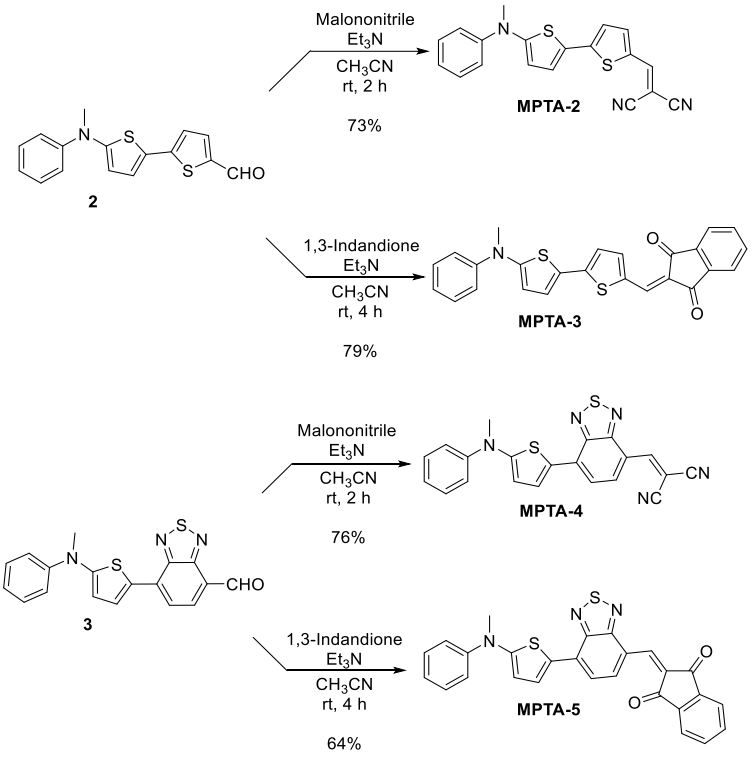

*Scheme 2.3. Knoevenagel conditions used for the synthesis of **MPTA-2**, **MPTA-3**, **MPTA-4** and **MPTA-5**.*

The change in the solvent for the Knoevenagel condensations from chloroform, i.e., to prepare **MPTA-1**, to acetonitrile for the rest of the series was not arbitrary. When **2** and **3** reacted in standard conditions with malononitrile in chloroform, reactions were highly problematic as the products decomposed and only some byproducts were recovered upon purification. For instance, during the reaction of aldehyde **3** with malononitrile, the color of the solution changed from purple to red (blueshifted absorption) instead of going towards the expected blue color (redshift), in consistency with the usual effect of adding such electron-withdrawing moiety. The only isolated structure, which was investigated by ^{1}H NMR and mass spectroscopy (Figure 2.3), was the result of the hydrogenation of the vinylene group constituting of the DCV moiety. The ^{1}H NMR spectrum revealed the complete disappearance of the characteristic deshielded proton of the double bond of DCV derivatives (blue arrow in Figure 2.3) giving rise to a system of a doublet and a triplet integrating for one proton each at 3.8 and 4.7 ppm respectively (red arrows in Figure 2.3).

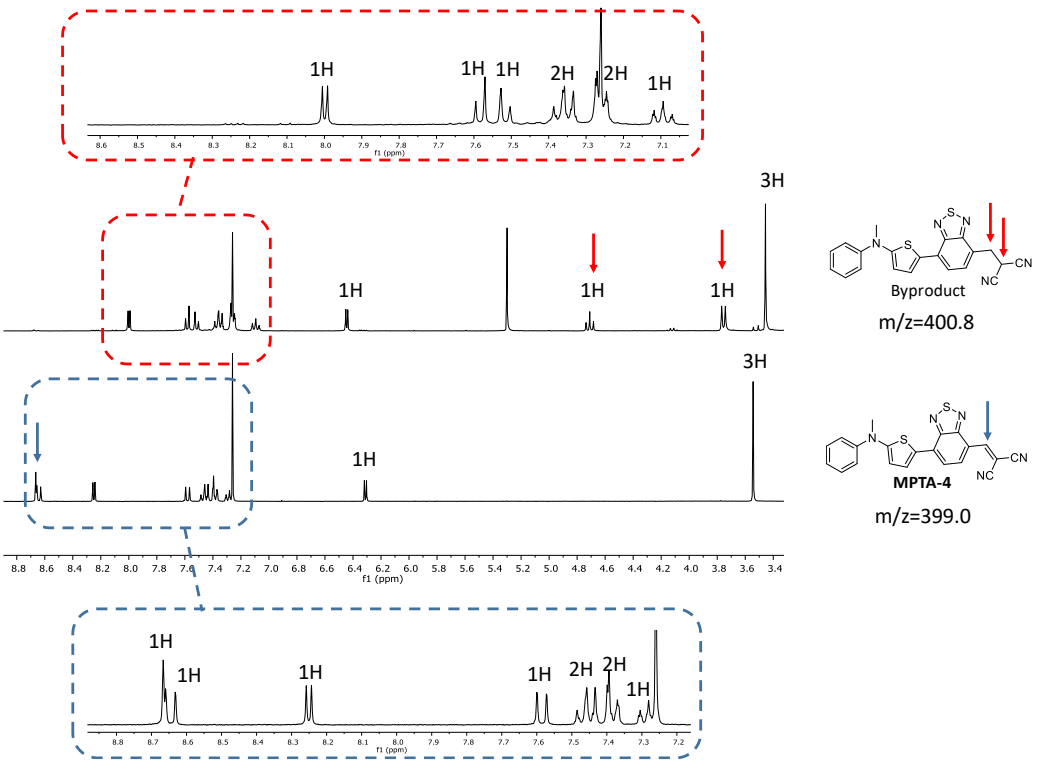

*Figure 2.3. ^{1}H NMR ($CDCl_3$) and MS comparison between the products obtained in the Knoevenagel condensation of **3** with malononitrile in chloroform (byproduct, up) and acetonitrile (**MPTA-4**, down).*

This new triplet appeared more deshielded, in agreement with its closer position to the DCV accepting group. Moreover, with a broken conjugation, this result was consistent with the blueshifted absorption observed during the reaction.

2.3 Optical properties in solution

Once all the compounds were isolated and purified, their optical properties were first evaluated by means of UV-Vis spectroscopy in CH_2Cl_2 solutions. The spectra and the summary of their optical properties are gathered in Figure 2.4 and Table 2.1 respectively.

Table 2.1. Optical properties of the MPTA-based push-pull molecules in CH_2Cl_2 solutions.

Molecule	λ_{abs} (nm)	ε (M^{-1} cm^{-1})	λ_{em} (nm)	Stokes Shift (cm^{-1})	Φ_f[a]
MPTA-1	463	56500	527	2,623	0.3
MPTA-2	562	30000	657	2,573	26.2
MPTA-3	597	40100	699	2,444	4.8
MPTA-4	657	30000	756	1,993	0.0
MPTA-5	663	42200	776	2,196	0.0

[a] Measured with an integrating sphere.

As expected, all of them presented an intense and broad band in the visible ranging from 460 to 660 nm and attributed to an intramolecular charge transfer (ICT) from the donor to the electron-withdrawing moiety (D to A).

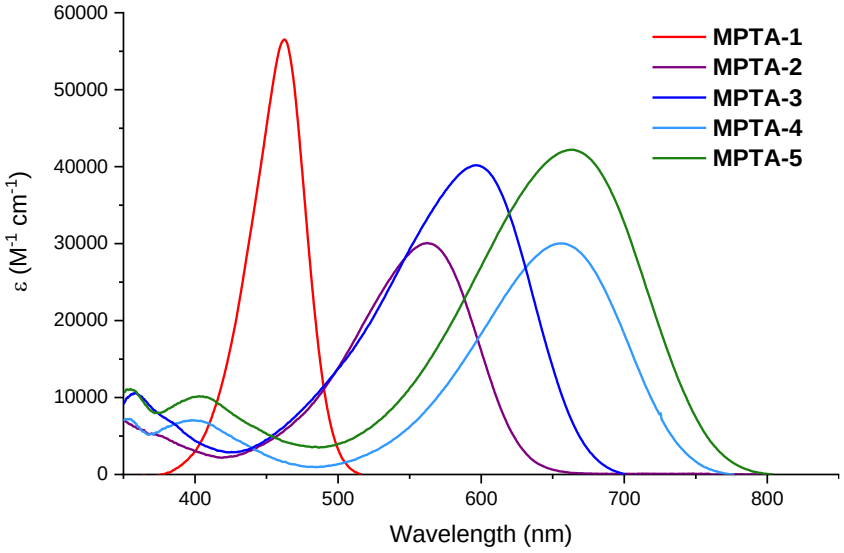

Figure 2.4. UV-Vis absorption spectra of the MPTA-based donors in CH_2Cl_2 solutions.

Due to its shortest conjugated structure, **MPTA-1** exhibited the narrowest absorption band with a maximum at 463 nm and a molar absorptivity (ε) of 56500 M^{-1} cm^{-1}. Then, a 100 nm redshift was observed for **MPTA-2** by extending the conjugated chain with a single thienyl spacer. An extra 100 nm redshift was witnessed when replacing the latter by a BTZ (**MPTA-4**) due to its stronger electron-withdrawing capability. Although the ε of both derivatives, of ca. 30000 M^{-1} cm^{-1}, were lower than that of **MPTA-1**, the bands significantly broadened, thus covering a wider range of the visible spectrum. Eventually, when DCV was replaced by 1,3-indandione, the bands were slightly redshifted, broader and their molar absorptivity was enhanced by ca. 30%.

The emissive properties of the series of molecules were subsequently explored in CH_2Cl_2 solutions (Figure 2.5 and Table 2.1).

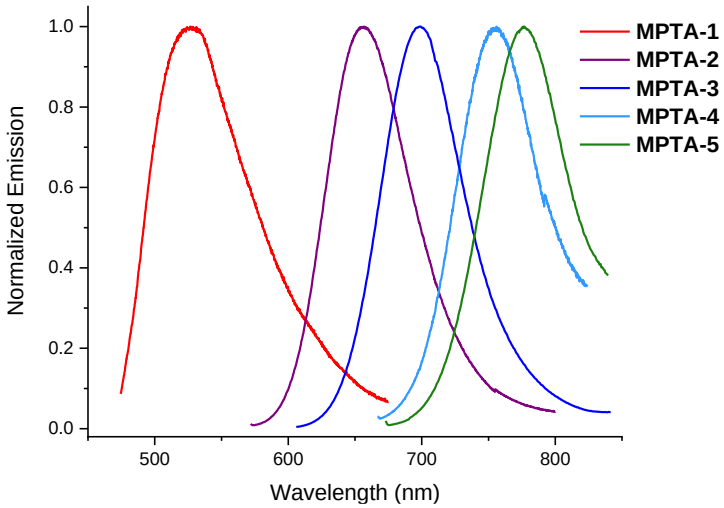

Figure 2.5. Normalized emission spectra of the MPTA-based donors in CH_2Cl_2 solutions.

As it can be observed, they all exhibited complementary bands along the spectrum. In addition, it is noteworthy that the emission bands of both BTZ derivatives even reached the Near Infrared (NIR) region (up to 900 nm for **MPTA-5**). However, the quantification of their fluorescence quantum yields (Φ_f), performed in the same conditions on a fluorimeter equipped with an integrating sphere, revealed almost negligible emissions (<0.5%) except for **MPTA-2** and **MPTA-3** (26.2 and 4.8% respectively). The fact that **MPTA-4** and **MPTA-5** were not emissive was not really surprising since NIR emitting organic dyes typically suffer from low photoluminescence quantum yields due to the energy gap law.[22]

2.4 Electrochemical properties in solution

The electrochemical properties of all the donors were subsequently evaluated by means of cyclic voltammetry (CV) (Figure 2.6). To do so, 1 mM solutions of each donor were prepared in a 0.1 M Bu_4NPF_6 buffer in CH_2Cl_2. Platinum electrodes were used as working and auxiliary electrodes and a saturated calomel electrode (SCE) as the reference. Finally, potentials were calibrated against the ferrocene/ferrocenium couple.

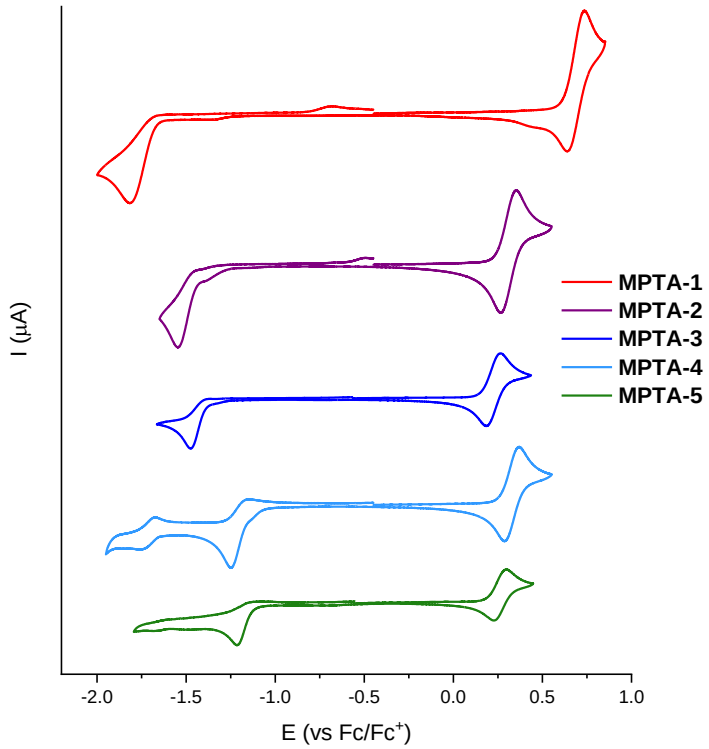

Figure 2.6. Cyclic voltammograms of the MPTA-based donors in CH_2Cl_2 (1 mM) vs Fc/Fc^+. WE (Pt), AE (Pt), RE (SCE) and 100 mV/s scan rate (buffer: 0.1 M Bu_4NPF_6 in CH_2Cl_2).

Table 2.2. Electrochemical properties of the MPTA-based donors obtained by CV. WE (Pt), AE (Pt), RE (SCE) and 100 mV/s scan rate (buffer: 0.1 M Bu_4NPF_6 in CH_2Cl_2).

Molecule	E_{pa} ($V_{/Fc/Fc^+}$)	E_{pc} ($V_{/Fc/Fc^+}$)	E_{HOMO} (eV)[a]	E_{LUMO} (eV)[b]	ΔE^{elec} (eV)
MPTA-1	0.73	-1.82	-5.42	-3.13	2.29
MPTA-2	0.35	-1.55	-5.03	-3.37	1.66
MPTA-3	0.26	-1.47	-4.95	-3.42	1.54
MPTA-4	0.37	-1.25	-5.06	-3.66	1.40
MPTA-5	0.30	-1.21	-4.99	-3.67	1.32

[a]E_{HOMO} (eV) = -(E_{ox}^{onset} + 4.8). [b]E_{LUMO} (eV) = -(E_{red}^{onset} + 4.8).

First, the cyclic voltammogram of **MPTA-1** exhibited a quasi-reversible oxidation at E_{pa} = 0.73 V and an irreversible reduction at E_{pc} = -1.82 V resulting in the widest electrochemical band gap of the series. Indeed, the insertion of a π-spacer between the donor and the acceptor resulted in a significant reduction of the latter. Whereas both thiophene derivatives (**MPTA-2** and **MPTA-3**) presented also a reversible oxidation and an irreversible reduction, **MPTA-4** and **MPTA-5** were characterized by an additional reduction peak attributed to the reduction of the BTZ spacer. Although prepared at the same concentration, the lower intensity observed in both indandione derivatives may be related to their inherent lower solubility, which can also explain the difference in their reduction patterns.

An overview and comparison of the oxidation and reduction potentials revealed that replacing a thiophene spacer by a BTZ significantly affected the E_{pc} (ca. 0.28 V shifted to higher potentials) while E_{pa} remained almost unaffected, highlighting that the LUMO level was partially delocalized on the acceptor-spacer moieties.

Hence, frontier energy levels, namely the HOMO and LUMO, were estimated through the experimental E_{ox}^{onset} and E_{red}^{onset} and the following equations: HOMO (eV) = - (E_{ox}^{onset} (vs Fc/Fc^+) + 4.8) and LUMO (eV) = - (E_{red}^{onset} (vs Fc/Fc^+) + 4.8).[23] These values are gathered in Table 2.2 and revealed that the electrochemical band gap can be gradually tuned from 2.29 to 1.32 eV by developing simple chemical modifications. Furthermore, according to these data, it turns out that all of them could be potentially used as donor materials in OSCs if complementarily used with a fullerene derivative ($LUMO_{D-\pi-A}$ > - 4 eV).

2.5 Properties in solid state

The properties of the new donor materials were subsequently investigated by spun-casting the respective $CHCl_3$ solutions on glass sheets (Table 2.3).

First, the UV-Vis spectra appeared significantly broadened due to the aggregation in solid state (Figure 2.7).

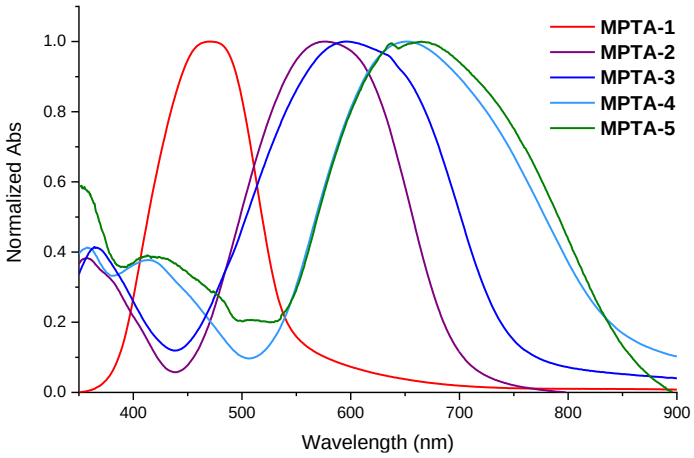

Figure 2.7. UV-Vis absorption spectra of the spun-casted films on glass of the new MPTA derivatives.

While the spectra of **MPTA-1**, **MPTA-2** and **MPTA-5** showed a bathochromic effect upon aggregation, the spectra of **MPTA-3** and **MPTA-4** were characterized by an antagonist behaviour with blueshifted maxima, which could be attributed to the formation of J- and H-aggregates respectively.[24] It is also noteworthy that BTZ-based derivatives showed absorptions ranging from 500 to 900 nm, being thus active in part of the NIR. This not so common property, particularly for small molecules, is interesting since it could be useful for the preparation of semi-transparent solar cells.

The optical band gap (E_g^{opt}) of each material was thereafter estimated from their respective absorption spectra (Table 2.3). To do so, the Planck equation (E_g^{opt} (eV) = hc/λ = 1240/λ (nm)) was applied to the low-energy absorption edge. In parallel, the HOMO levels were estimated on thin films from the ionization energy measured by photoelectron spectroscopy in air (PESA) (Figure 2.8) and then the LUMO levels were deduced from the equation LUMO = HOMO + E_g^{opt}.

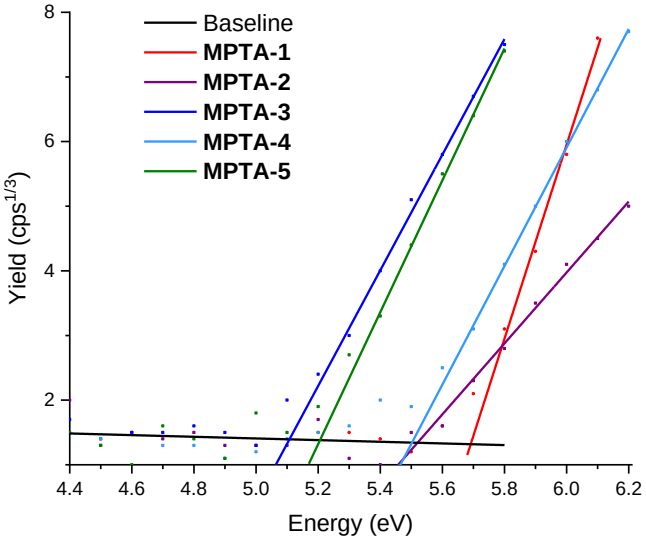

Figure 2.8. PESA spectra of the new MPTA derivatives.

It thus turned out that the trend observed for the band gaps in solution remained the same. However, while the HOMO energies in solution were similar for the four extended molecules, the use of 1,3-indandione instead of DCV led to ca. 0.4 eV higher HOMO and LUMO levels in thin films. As a result, the LUMO level of **MPTA-4** was very close in energy to that of the fullerene derivatives, which could be problematic for the preparation of OSCs.

Table 2.3. Summary of the optical and energetic properties of the five MPTA donors as spun-casted films.

Molecule	λ_{abs} (nm)	λ_{edge} (nm)[a]	HOMO (eV)[b]	E_g^{opt} (eV)[c]	LUMO (eV)[d]
MPTA-1	470	548	-5.70	2.26	-3.44
MPTA-2	577	718	-5.49	1.73	-3.76
MPTA-3	596	749	-5.08	1.66	-3.42
MPTA-4	651	862	-5.58	1.44	-4.14
MPTA-5	665	865	-5.17	1.43	-3.74

[a] Low-energy absorption edge (ICT bands). [b] HOMO energy in solid state determined by PESA. [c] Optical band gap estimated through the low-energy absorption edge. [d] Obtained through the equation: LUMO = HOMO + E_g^{opt}.

2.6 Organic solar cells

2.6.1 Solution-processed solar cells

Eventually, the photovoltaic properties of the new donors were firstly evaluated in the laboratory in solution-processed OSCs (Figure 2.9).

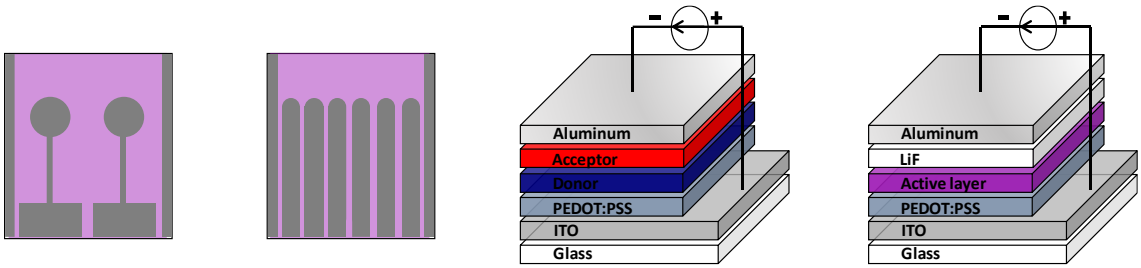

Figure 2.9. Diagram of the solution-processed OSCs: actual devices (active area = 27 mm^2) (a-b), PHJ structure (c) and BHJ structure (d).

The three DCV derivatives, **MPTA-1**, **MPTA-2** and **MPTA-4**, were initially assessed in solution-processed PHJ OSCs to rapidly evaluate the photovoltaic performance of the new series using an ITO/PEDOT:PSS/D/C_{60}/Al architecture. First, a commercial solution of PEDOT:PSS and a solution of each donor (10 mg/mL in chloroform) were sequentially spun-casted (at 5000 and 6000 rpm respectively). Then, the fullerene and aluminum layers, of 30 and 100 nm respectively, were evaporated under vacuum. Although these PHJ devices usually improve their performance after a thermal annealing procedure, in this case almost negligible PCEs were obtained for the three molecules even after the annealing at 80 °C (Figure 2.10 and Table 2.4).

*Table 2.4. Photovoltaic parameters obtained in solution-processed PHJ solar cells using **MPTA-1**, **MPTA-2** and **MPTA-4** as donors and C_{60} as acceptor (AM1.5 conditions, 100 mW/cm^2).*

Donor	J_{sc} (mA cm^{-2})	V_{oc} (V)	*FF* (%)	PCE (%)
MPTA-1	-0.47	0.40	29	0.05
MPTA-2	-2.76	0.25	31	0.21
MPTA-4	-1.50	0.24	34	0.12

It can be observed that the respective J-V curves exhibited strong S-shapes resulted from detrimental resistive processes.

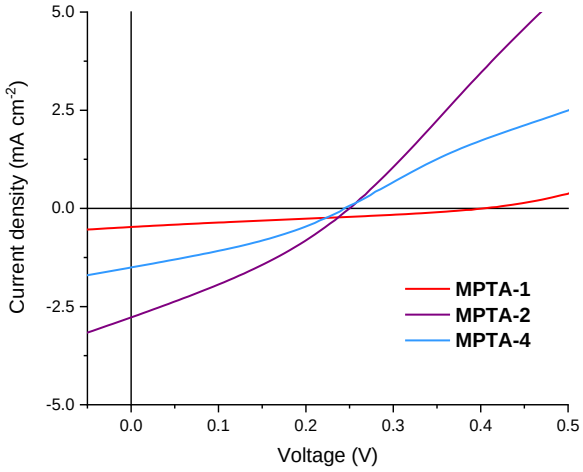

*Figure 2.10. Photovoltaic parameters obtained in solution-processed PHJ solar cells using **MPTA-1**, **MPTA-2** and **MPTA-4** as donors and C_{60} as acceptor.*

Consequently, in an attempt to understand these poor performances, the morphology of the active layers was investigated (after the annealing process) with an optical microscope mounted with a polarized light (Figure 2.11).

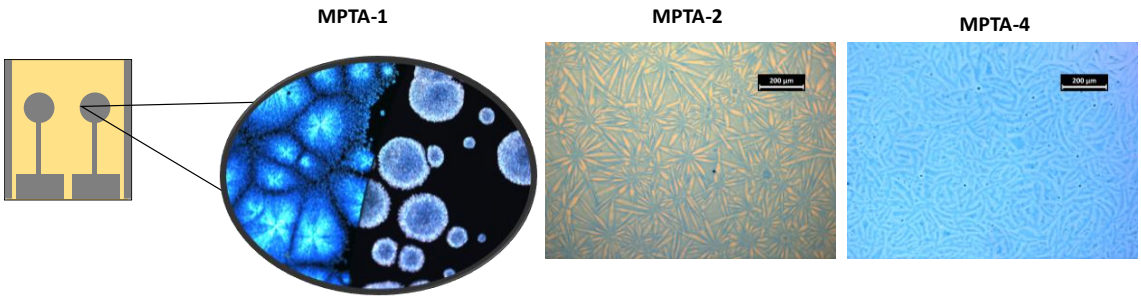

*Figure 2.11. Optical microscopy images of solution-processed PHJ solar cells made of **MPTA-1**, **MPTA-2** and **MPTA-4** as donors and C_{60} as acceptor.*

Photographs revealed massive formations of crystals all over the devices and even under the aluminum contact in the case of **MPTA-1**. This huge phase segregation significantly affected the separation and transport of the free charges, thus impacting the photovoltaic performances.

Consequently, with a limited absorption and a high crystallinity, **MPTA-1** was no longer considered for the preparation of solar cells.

Thereafter, the most performing donor in PHJ, **MPTA-2**, was naturally selected to study the effect of using different accepting materials ($PC_{61}BM$, $PC_{71}BM$ and ICBA) in BHJ OSCs (ITO/PEDOT:PSS/D:A/LiF/Al). LiF was deposited as an interlayer to improve the contact between the active layer and the aluminum-made electrode. Hence, after the deposition of PEDOT:PSS, blends of D and A at a 1:1 weight to weight (w/w) ratio in chloroform (10 mg/mL in total) were spun-casted at 1300 rpm prior to the subsequent evaporation of LiF (1 nm) and aluminum (100 nm). It turned out that all photovoltaic parameters were significantly improved, resulting at least in modest PCEs (Figure 2.12 and Table 2.5).

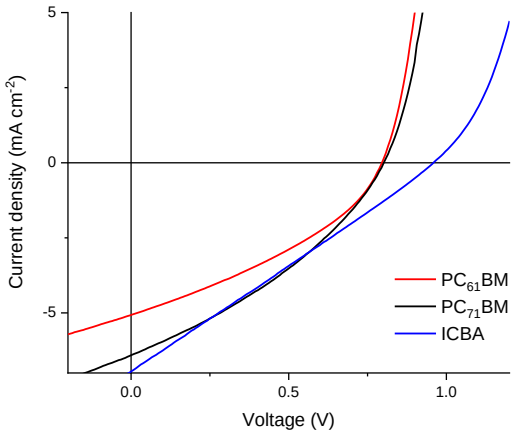

*Figure 2.12. J-V curves of solution-processed BHJ solar cells using **MPTA-2** as donor and $PC_{61}BM$, $PC_{71}BM$ and ICBA as acceptors (1:1 w/w ratio).*

*Table 2.5. Photovoltaic parameters of solution-processed BHJ solar cells using **MPTA-2** as donor and $PC_{61}BM$, $PC_{71}BM$ and ICBA as acceptors (1:1 w/w ratio).*

Acceptor	J_{sc} (mA cm^{-2})	V_{oc} (V)	*FF* (%)	PCE (%)
$PC_{61}BM$	-5.06	0.79	36	1.44
$PC_{71}BM$	-6.40	0.80	35	1.77
ICBA	-6.93	0.96	26	1.72

$PC_{61}BM$-based devices exhibited the lowest efficiencies mainly due to their low J_{sc}. This was slightly improved in the case of $PC_{71}BM$, in agreement with its better absorbing properties. Finally, the main difference came from the use of ICBA, which is characterized by the highest LUMO level thus resulting, as expected, in the highest V_{oc} (0.96 V). However, a high decrease in *FF* was also produced, therefore impacting the PCE.

Consequently, $PC_{71}BM$ turned out to be the best compromise to test the rest of the series. Moreover, the D:A ratio of the active layer was optimized for each donor, in an attempt to

improve the photovoltaic performances. Three different w/w D:A ratios were thus evaluated, i.e., 1:1, 1:2 and 1:3. The best curves and the best photovoltaic data for each donor are gathered in Figure 2.13 and Table 2.6.

*Table 2.6. Photovoltaic parameters of the best solution-processed BHJ solar cells using **MPTA-2**, **MPTA-3**, **MPTA-4** and **MPTA-5** as donors and $PC_{71}BM$ as acceptor.*

Donor	Ratio (D:A)	J_{sc} (mA cm^{-2})	V_{oc} (V)	*FF* (%)	PCE (%)
MPTA-2	1:1	-6.40	0.80	35	1.77
MPTA-3	1:2	-4.41	0.64	37	1.05
MPTA-4	1:3	-3.61	0.72	35	0.91
MPTA-5	1:3	-3.89	0.65	32	0.81

While **MPTA-2**-based OSCs still exhibited the best PCE (1.77%), several general conclusions can be drawn from these results. On the one hand, it is noticeable that the PCEs recorded for thiophene derivatives were higher than for their BTZ analogues. Although the latter could theoretically achieve higher V_{oc} values due to their lower lying HOMO energy levels, the opposite trend was unfortunately observed. In addition, BTZ-based derivatives exhibited, in every case, a lower LUMO energy that may decrease the driving force of the photoinduced electron transfer towards the LUMO of the fullerene. Eventually, although they exhibited broader EQE curves since they are active in the NIR (up to 900 nm), their contribution was significantly lower than that of the thiophene derivatives.

On the other hand, the comparison of the impact of the accepting moieties revealed that DCV-based molecules exhibited better performances than their indandione counterparts. The reason may be related to the higher HOMO levels of indandione-based donors which led to lower V_{oc} values. In addition, even though their absorption was redshifted in comparison to the DCV-based derivatives, they did not lead to broader EQEs. Eventually, since indandione-based donors exhibited a lower solubility, this could have led to deposition issues and therefore to a less optimized morphology.

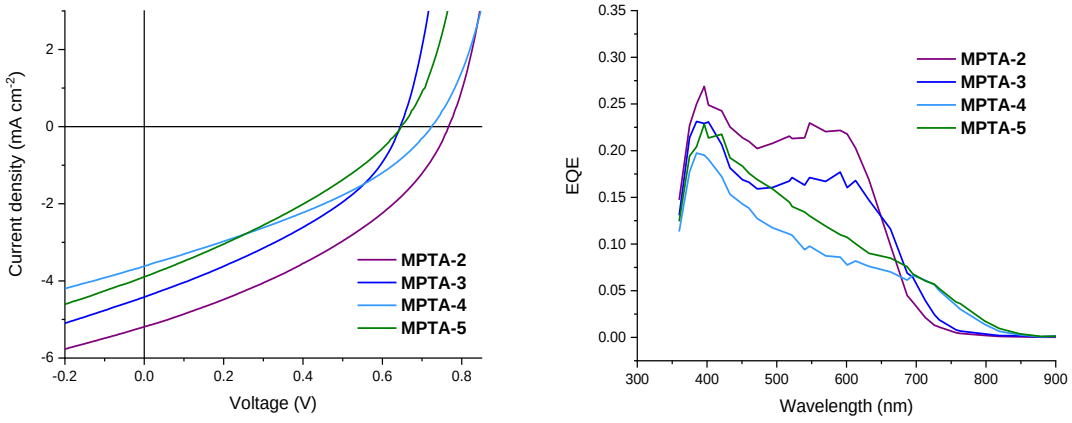

*Figure 2.13. J-V (left) and EQE curves (right) of the best solution-processed BHJ solar cells using **MPTA-2**, **MPTA-3**, **MPTA-4** and **MPTA-5** as donors and $PC_{71}BM$ as acceptor.*

2.6.2 Vacuum-processed solar cells

In parallel to the solution-processed OSCs from Angers, vacuum-deposited organic solar cells were also fabricated. However, it is noteworthy that materials with a higher purity are usually required and thus an additional purification step, namely the sublimation, is often carried out. Consequently, **MPTA-3**, **MPTA-4** and **MPTA-5** were sent to the German company Heliatek GmbH. First, an evaporability study was carried out consisting in measuring the percentage of residue after an evaporation process. While an empty crucible was recovered for **MPTA-4**, **MPTA-3** and **MPTA-5** produced a ca. 26% and 60% of residue respectively. These values highlight the modest stability of indandione accepting moieties during vacuum depositions. In addition to these results, **MPTA-4** was also selected for its NIR absorbing properties, a key parameter barely investigated in all-small-molecule OSCs.

Hence, two preliminary devices were fabricated at Heliatek using the following inverted planar architecture: ITO/C_{60}/**MPTA-4**/BPAPF/BPAPF:NDP9(1:1)/NDP9/Al (active area = 2.76 mm^2). In these devices, 9,9-bis(4-(*N*,*N*-bis-biphenyl-4-yl-amino)phenyl)-9*H*-fluorene (BPAPF) and the commercial NDP9 (by Novaled) played the role of hole-transporting material and p-dopant respectively.

Surprisingly, negligible PCEs were obtained mainly due to the lack of collected current (Table 2.7).

*Table 2.7. Photovoltaic parameters of PHJ solar cells fabricated in Heliatek using **MPTA-4** and C_{60}.*

Donor thickness (nm)	J_{sc} (mA cm^{-2})	V_{oc} (V)	*FF* (%)	PCE (%)
6	-0.0	0.65	16	0.0
10	-0.0	0.63	15	0.0

These poor performances highlight the difficulty in finding the most suitable processing conditions for this kind of molecules.

Though these results were simply baffling, **MPTA-4** was studied in parallel by the group of Karl Leo at the Technische Universität Dresden (TUD). First evaluated in PHJ OSCs with a standard configuration, i.e., ITO/MoO_3 (3 nm)/**MPTA-4**/C_{60} (15 nm)/Bathophenanthroline (BPhen) (8 nm)/Ag (100 nm) (active area = 6.44 mm^2), a photocurrent, though modest, was detected in stark contrast with the results obtained by Heliatek (Table 2.8 and Figure 2.14).

*Table 2.8. Photovoltaic parameters of vacuum-processed PHJ solar cells using **MPTA-4** and C_{60}.*

Donor thickness (nm)	J_{sc} (mA cm^{-2})	V_{oc} (V)	*FF* (%)	PCE (%)
6	-2.08	0.85	48	0.85
9	-1.79	0.76	48	0.65
12	-1.78	0.76	49	0.66

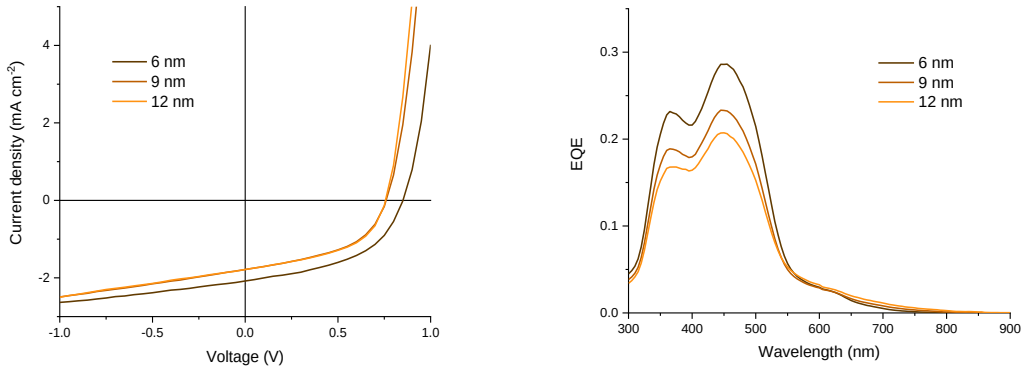

*Figure 2.14. J-V (left) and EQE curves (right) of vacuum-processed PHJ solar cells using **MPTA-4** and C_{60}.*

According to the EQE spectra, the low J_{sc} can be correlated to the almost negligible contribution of the donor resulting in the unique participation of C_{60}. Moreover, considering that the thinner devices (6 nm) led to slightly better performances, exciton diffusion issues and/or limited hole transporting properties can partially contribute to these modest efficiencies.

In an attempt to improve the performance of **MPTA-4**, vacuum-processed BHJ OSCs were fabricated using C_{60} as the complementary co-evaporated acceptor material (Table 2.9 and Figure 2.15). Standard (ITO/MoO_3 (3 nm)/D:A/BPhen (8 nm)/Ag (100 nm)) and inverted (ITO/Bis-HFl-NTCDI:W_2(hpp)$_4$ (5 nm)/A:D/MoO_3 (3 nm)/Ag (100 nm)) configurations were assessed, as well as the D:A ratio, the thickness of the active layer, the deposition over heated substrates and the use of a PMHJ architecture (active layer sandwiched between a pure layer of donor and one acceptor, Figure 1.9). *N*,*N*-Bis(fluoren-2-yl)-naphthalenetetracarboxylic diimide (Bis-HFl-NTCDI) doped with W_2(hpp)$_4$ plays the role of electron-transporting layer in inverted devices.[25]

*Table 2.9. Photovoltaic parameters of the optimization of **MPTA-4** in vacuum-processed BHJ solar cells using C_{60} as acceptor.*

Configuration	Thickness (nm)	Ratio (D:A)	Deposition T (°C)	J_{sc} (mA cm^{-2})	V_{oc} (V)	*FF* (%)	PCE (%)
Standard	30	1:1	rt	-6.94	0.69	48	2.31
Standard	30	1:2	rt	-6.07	0.55	41	1.37
Standard	30	1:1	80	-7.87	0.65	47	2.43
Inverted	30	1:1	rt	-5.28	0.60	54	1.71
Inverted	30	1:1	80	-6.20	0.53	60	1.97
Standard	40	1:1	rt	-8.17	0.68	46	2.65
Standard PMHJ	50	1:1	rt	-10.13	0.78	48	3.79
Standard PMHJ	60	1:1	rt	-9.71	0.78	48	3.64

In stark contrast to the previous devices, the contribution of the donor in the EQE (band between 550 and 900 nm) was at last comparable to that of C_{60}, thus substantially enhancing the J_{sc} values. Moreover, it was observed that the 1:2 D:A ratio led to substantially lower J_{sc}, V_{oc}, *FF* and thus PCE. Therefore, the 1:1 ratio was used thereafter.

While slightly better results were obtained using a standard architecture, particularly on pre-heated substrates, it is difficult to draw a general conclusion on the real gain with respect to inverted solar cells. Indeed, and although the latter exhibited higher *FF*, especially in heated substrates, the notable decrease in V_{oc} and J_{sc} significantly impacted the PCEs.

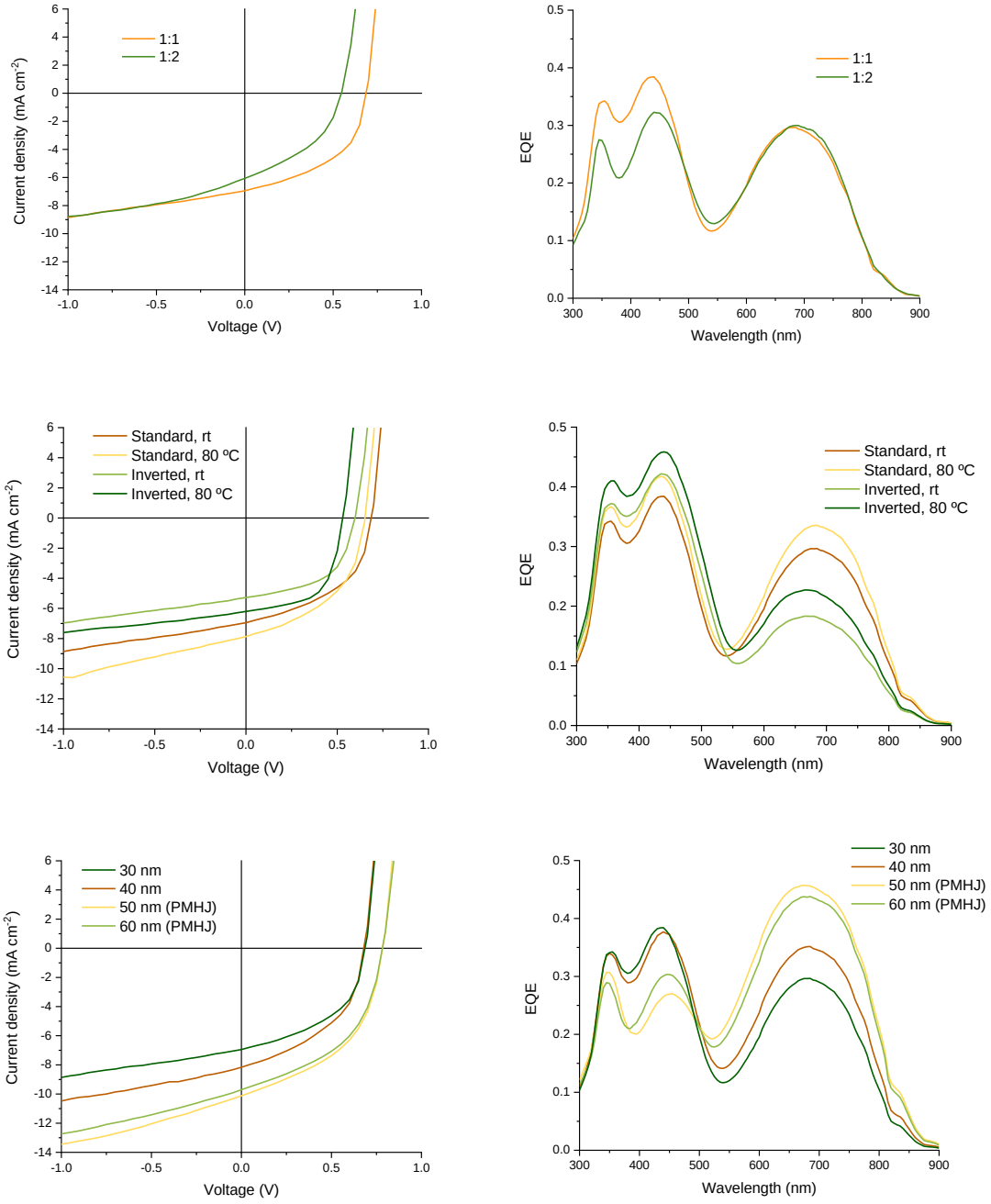

*Figure 2.15. J-V (left) and EQE (right) curves resulted from the optimization of the D:A ratio (top), architecture (center) and thickness (bottom) of vacuum-processed BHJ solar cells using **MPTA-4** and C_{60}.*

Eventually, the thickness of the active layer was gradually increased from 30 to 60 nm (bottom part of Figure 2.15). First, the increase from 30 to 40 nm resulted in a slightly higher J_{sc} and therefore PCE since the other parameters (V_{oc} and *FF*) remained constant. A major breakthrough

in efficiency was reached when the thickness was increased to 50 and 60 nm using a PMHJ configuration. It turned out that all the photovoltaic parameters were improved resulting in PCEs over 3.6%. This PMHJ structure thus minimized the intrinsic issue of low V_{oc} inherent to the high HOMO level of **MPTA-4**. Moreover, the improved contribution of the donor, highlighted by the EQE, resulted in a ca. 2 mA cm^{-2} increase in J_{sc}, which was clearly beneficial for the PCE. Finally, considering that a higher J_{sc} and thus PCE were obtained with the 50-nm-thick active layer, these parameters will be set and used for further optimizations.

Indeed, using those conditions, the replacement of C_{60} by C_{70} was subsequently evaluated as well as the use of different ETL combinations (Table 2.10 and Figure 2.16).

*Table 2.10. Photovoltaic parameters of vacuum-processed PMHJ solar cells using **MPTA-4** as donor, C_{60} and C_{70} as acceptors and two different ETLs (active layers of 50 nm).*

Acceptor	ETL	J_{sc} (mA cm^{-2})	V_{oc} (V)	*FF* (%)	PCE (%)
C_{60}	BPhen (8 nm)	-10.13	0.78	48	3.79
	BPhen:C_{60} (8 nm)/BPhen (5 nm)	-10.08	0.78	48	3.53
C_{70}	BPhen (8 nm)	-12.84	0.75	42	3.95
	BPhen:C_{60} (8 nm)/BPhen (5 nm)	-13.38	0.75	44	4.27

First, although the modification of the ETL did not really affect the photovoltaic parameters in the C_{60}-based devices, a slightly different behavior was observed in their C_{70} counterparts. A higher J_{sc} (-13.38 mA cm^{-2}) was indeed achieved thus leading to the highest efficiencies with a champion device exhibiting a PCE of ca. 4.27%. Interestingly, the increase in J_{sc} can be correlated with the EQE of ca. 50% from 400 to 800 nm, thus demonstrating the synergic effect between donor and acceptor. One of the reasons was the improved absorption properties of C_{70}, which led to a more efficient photo-generation between 500 and 600 nm thus producing a more homogeneous EQE curve without the previously observed valley at ca. 540 nm.

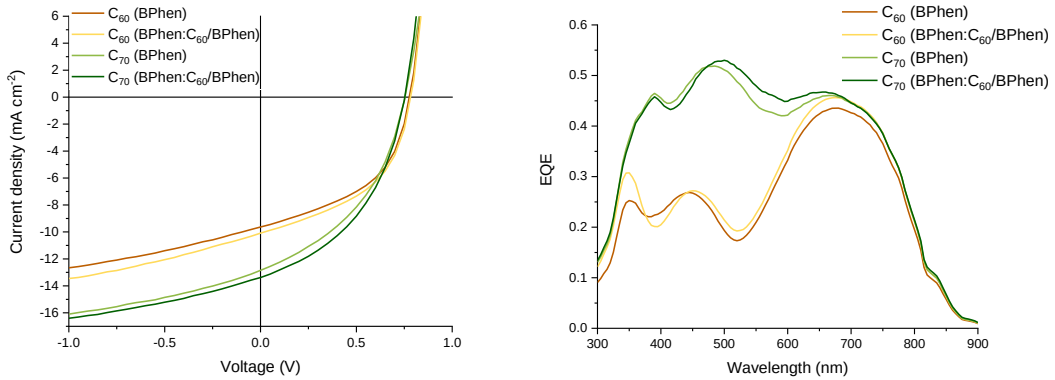

*Figure 2.16. J-V (left) and EQE (right) obtained in PMHJ solar cells using **MPTA-4** as donor, C_{60} and C_{70} as acceptors and two different ETLs (active layers of 50 nm).*

Since this was the first test with C_{70}, it would be expected to enhance the obtained PCE after additional optimization tests that have been already planned in the short term.

2.7 Conclusions and perspectives

A series of small push-pull molecules based on the *N*-methyl-*N*-phenylthiophen-2-amine donor unit, which had not been used previously in the field of OPV, was synthesized. To do so, this arylamine was combined with two different heterocyclic spacers and two acceptor moieties, thus leading to a fine tuning of the optical and electrochemical properties of these new materials. Though relatively small, the latter indeed presented complementary absorption covering the whole visible spectrum and part of the NIR. Moreover, according to the data recorded both in solution and in solid state, their energy levels have been chemically tuned leading to a progressive reduction of the band gap from ca. 2.3 to 1.4 eV.

Finally, they all have been tested as donor materials in solution-processed OSCs mostly leading to modest efficiencies due to their high crystallinity. **MPTA-4** has been selected to be evaluated in vacuum-processed OSCs due to its low band gap and better evaporability. While PHJ devices prepared at Heliatek were not performing, the fabrication of BHJ and PMHJ OSCs in Karl Leo's group led to a significant improvement of the PCE, reaching a maximum value of 4.27% in the preliminary measurements with C_{70}. These photovoltaic results clearly highlight the enormous and empirical processing dependence of this type of materials.

In addition, even though further optimizations will be carried out in the short term, the PCE of 5.8% reported in single junction organic solar cells with **DTDCTB** probably will not be reached. Consequently, the chemical structures of **MPTA-2** and **MPTA-4** were recently modified by substituting their outer phenyl ring by a *p*-tolyl moiety, affording **MTTA-2** and **MTTA-4** respectively (Figure 2.17).

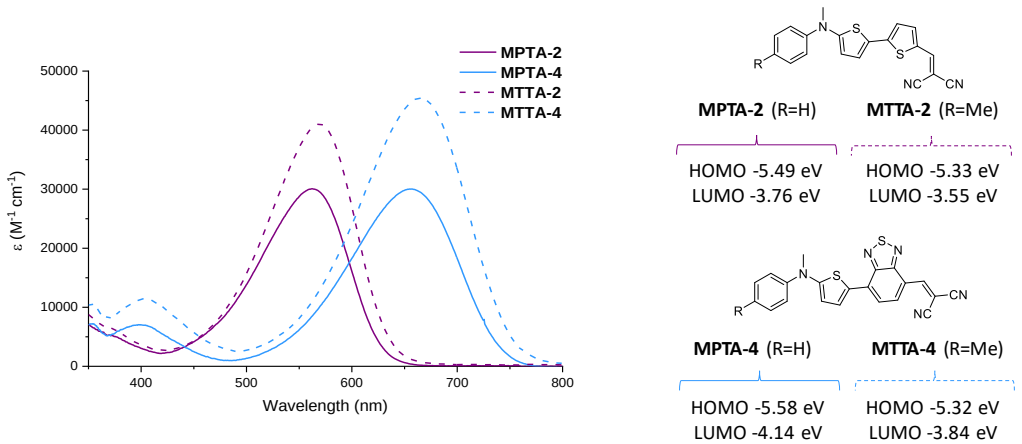

Figure 2.17. UV-Vis absorption spectra in CH_2Cl_2 solutions (left) and energy levels in solid state (right) of the MPTA and MTTA analogues.

With higher HOMO and LUMO levels, MTTA derivatives significantly improved the molar extinction coefficients of their MPTA counterparts. Hence, they present the enhanced

absorptivity of the indandione-based push-pull molecules without, hopefully, their evaporability issues. Consequently, **MTTA-2** and **MTTA-4** were recently sent to the Technische Universität Dresden for optimized device fabrication.

References

[1] Roquet, S., Cravino, A., Leriche, P., Alévêque, O., Frère, P. and Roncali, J., *Journal of the American Chemical Society* **2006**, *128*, 3459-3466.
[2] Leliege, A., Regent, C.-H. L., Allain, M., Blanchard, P. and Roncali, J., *Chemical Communications* **2012**, *48*, 8907-8909.
[3] Grolleau, J., Gohier, F., Allain, M., Legoupy, S., Cabanetos, C. and Frère, P., *Organic Electronics* **2017**, *42*, 322-328.
[4] Leliège, A., Grolleau, J., Allain, M., Blanchard, P., Demeter, D., Rousseau, T. and Roncali, J., *Chemistry – A European Journal* **2013**, *19*, 9948-9960.
[5] Labrunie, A., Jiang, Y., Baert, F., Leliège, A., Roncali, J., Cabanetos, C. and Blanchard, P., *RSC Advances* **2015**, *5*, 102550-102554.
[6] Choi, J. W., Kim, C.-H., Pison, J., Oyedele, A., Tondelier, D., Leliège, A., Kirchner, E., Blanchard, P., Roncali, J. and Geffroy, B., *RSC Advances* **2014**, *4*, 5236-5242.
[7] Jiang, Y., Gindre, D., Allain, M., Liu, P., Cabanetos, C. and Roncali, J., *Advanced Materials* **2015**, *27*, 4285-4289.
[8] Jiang, Y., Cabanetos, C., Allain, M., Liu, P. and Roncali, J., *Journal of Materials Chemistry C* **2015**, *3*, 5145-5151.
[9] Mohamed, S., Demeter, D., Laffitte, J.-A., Blanchard, P. and Roncali, J., *Scientific Reports* **2015**, *5*, 9031.
[10] Jiang, Y. PhD Thesis, Université d'Angers, **2015**.
[11] Jeux, V., Demeter, D., Leriche, P. and Roncali, J., *RSC Advances* **2013**, *3*, 5811-5814.
[12] Baert, F. PhD thesis, Université d'Angers, **2015**.
[13] Baert, F., Cabanetos, C., Allain, M., Silvestre, V., Leriche, P. and Blanchard, P., *Organic Letters* **2016**, *18*, 1582-1585.
[14] Lin, L.-Y., Chen, Y.-H., Huang, Z.-Y., Lin, H.-W., Chou, S.-H., Lin, F., Chen, C.-W., Liu, Y.-H. and Wong, K.-T., *Journal of the American Chemical Society* **2011**, *133*, 15822-15825.
[15] Jia, X. e., Chen, Z., Duan, C., Wang, Z., Yin, Q., Huang, F. and Cao, Y., *Journal of Materials Chemistry C* **2019**, *7*, 314-323.
[16] Zhu, J., Zheng, X., Tan, H., Tan, H., Yang, J., Yu, J. and Zhu, W., *Chemical Physics Letters* **2019**, *726*, 7-12.
[17] Keles, D., Erer, M. C., Bolayir, E., Cevher, S. C., Hizalan, G., Toppare, L. and Cirpan, A., *Renewable Energy* **2019**, *139*, 1184-1193.
[18] Wang, M., Lin, J., Hsiao, Y.-C., Liu, X. and Hu, B., *Nature Communications* **2019**, *10*, 1614.
[19] Che, X., Li, Y., Qu, Y. and Forrest, S. R., *Nature Energy* **2018**, *3*, 422-427.
[20] Revoju, S., Biswas, S., Eliasson, B. and Sharma, G. D., *Physical Chemistry Chemical Physics* **2018**, *20*, 6390-6400.
[21] Charles, M. D., Schultz, P. and Buchwald, S. L., *Organic Letters* **2005**, *7*, 3965-3968.
[22] Lo, Y. C., Yeh, T. H., Wang, C. K., Peng, B. J., Hsieh, J. L., Lee, C. C., Liu, S. W. and Wong, K. T., *ACS Applied Materials & Interfaces* **2019**, *11*, 23417-23427.
[23] Cardona, C. M., Li, W., Kaifer, A. E., Stockdale, D. and Bazan, G. C., *Advanced Materials* **2011**, *23*, 2367-2371.
[24] Würthner, F., Kaiser, T. E. and Saha-Möller, C. R., *Angewandte Chemie International Edition* **2011**, *50*, 3376-3410.
[25] Meerheim, R., Körner, C., Oesen, B. and Leo, K., *Applied Physics Letters* **2016**, *108*, 103302.

Chapter 3

Linear and multimeric triphenylamine-based donors for OPV

3.1 Introduction

The benefits of using accessible TAA-based materials for OPV have been already stated and demonstrated. In recent years, different design strategies were reported to reach higher performances. Among them, Kozlov et al. reported in 2018 the effect of substituting the hydrogen atom of the DCV moiety by a simple phenyl, affording the **TPA-T-DCV-Ph** derivative, whose structure is depicted in Figure 3.1. While this chemical modification was found to barely affect the optical and electrochemical properties in comparison to its **TPA-T-DCV** analogue,[1] **TPA-T-DCV-Ph** showed higher thermal stability and longer exciton diffusion length (ca. 25 nm), resulting in improved OPV performances (PCE= 5.11% in BHJ co-evaporated with C_{70}).

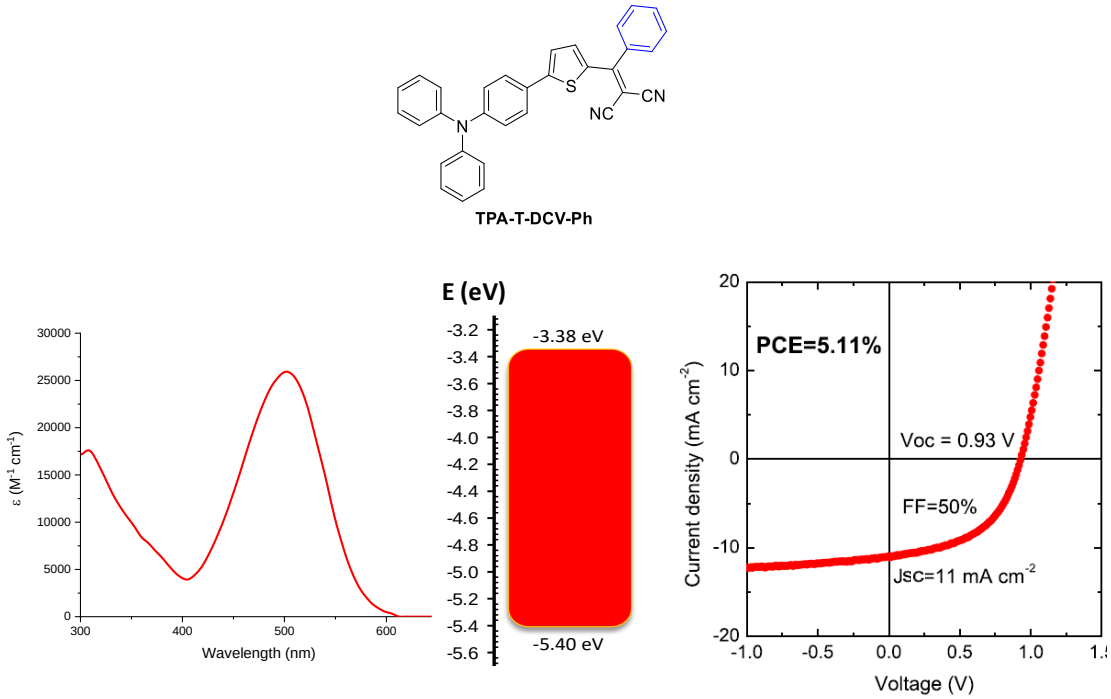

*Figure 3.1. Summary of the most relevant properties of **TPA-T-DCV-Ph**: UV-Vis absorption spectrum in CH_2Cl_2 (left), energetic levels obtained by CV in CH_3CN/o-$C_6H_4Cl_2$ 1:4 (center) and J-V curve and photovoltaic parameters of an ITO/MoO_3/**TPA-T-DCV-Ph**:C_{70}/BCP/Al device (right).*

Consequently, in view of these advantages, the idea was to synthesize analogues functionalized with different aryl substituents on the DCV accepting group. However, prior to that, the already reported synthetic route towards **TPA-T-DCV-Ph** has to be reconsidered (Scheme 3.1), particularly for large-scale synthesis.

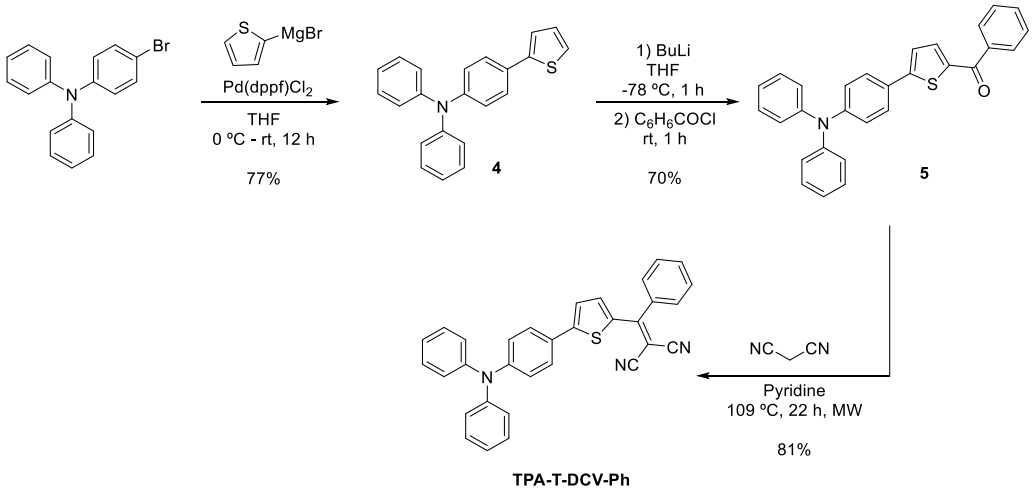

*Scheme 3.1. Reported synthesis for **TPA-T-DCV-Ph**.*[1]

Indeed, it is noteworthy that **4** can be obtained by means of a Suzuki coupling in a higher yield than that of the reported Kumada coupling involving a Grignard reagent. Moreover, even if afforded in good yield, **TPA-T-DCV-Ph** resulted in the paper from the Knoevenagel condensation of ketone **5** with malononitrile under harsh conditions (microwave irradiation for 22 h). Consequently, a simpler, mild and scalable pathway will be explored. Starting with the preparation of **TPA-T-DCV-Ph**, the viability of the new synthetic procedure will be transposed to other **TPA-T-DCV-Ar** derivatives (Figure 3.2) to evaluate the impact of these structural modifications on the optical, electrochemical and photovoltaic properties.

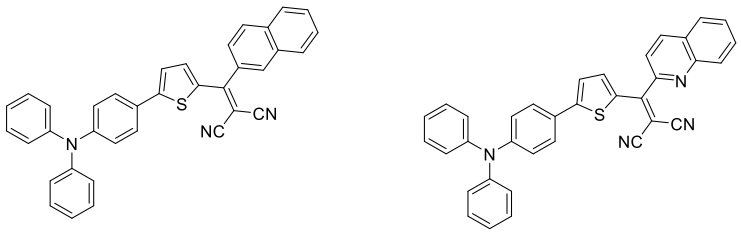

Figure 3.2. Structure of the targeted push-pull molecules.

In parallel, another approach, still based on the **TPA-T-DCV** structure that showed interesting features, including a promising PCE (4.0 %), deals with the preparation of push-pull-based multimers. This simple strategy was recently applied by the group to prepare the **Tetra-T** (Figure 3.3) from a cheap and commercially available pentaerythritol central core.[2-3]

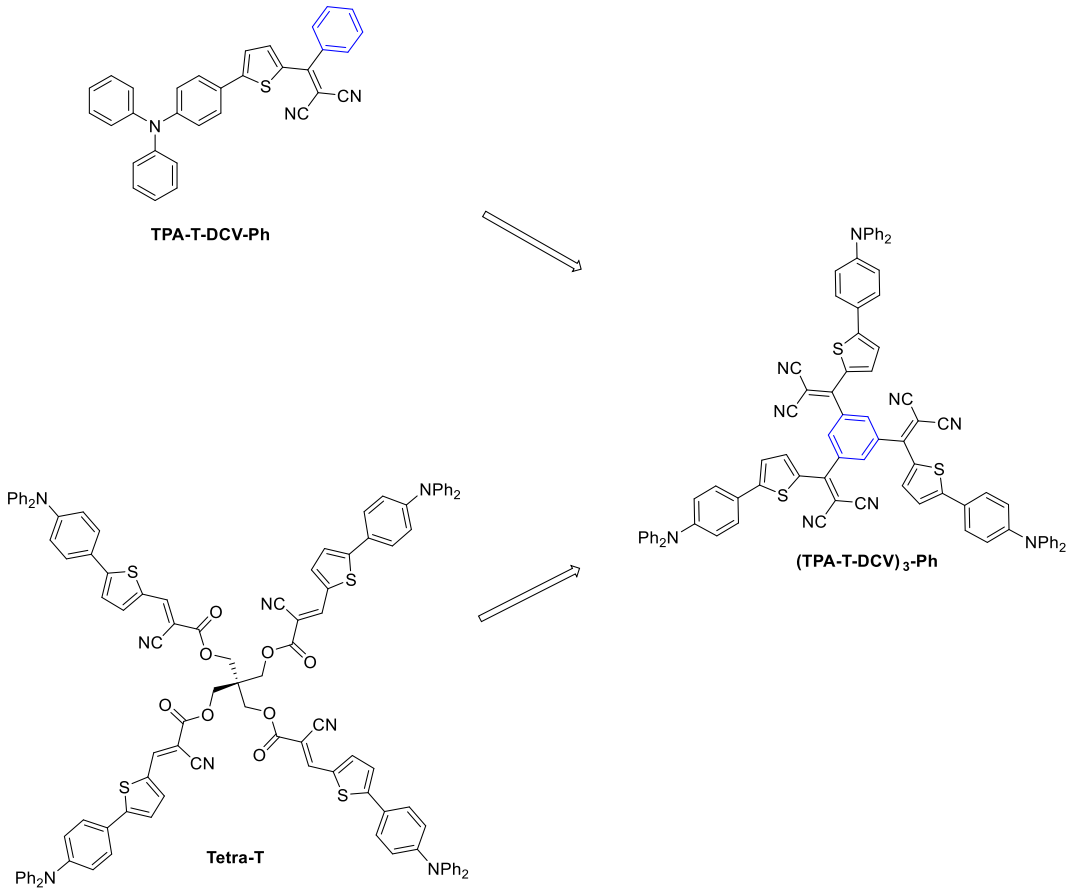

Figure 3.3. Structure of the targeted trimer.

Consequently, the combination of this multimeric-based strategy with the good results reached by **TPA-T-DCV-Ph** led to the design of **(TPA-T-DCV)$_3$-Ph**, whose synthetic pathway and the optical, electrochemical and photovoltaic properties will be explored in this chapter.

3.2 Synthesis

3.2.1 Synthesis of **TPA-T-DCV-N**

The reported synthetic procedure to prepare **TPA-T-DCV-Ph** was first reconsidered (Scheme 3.2).

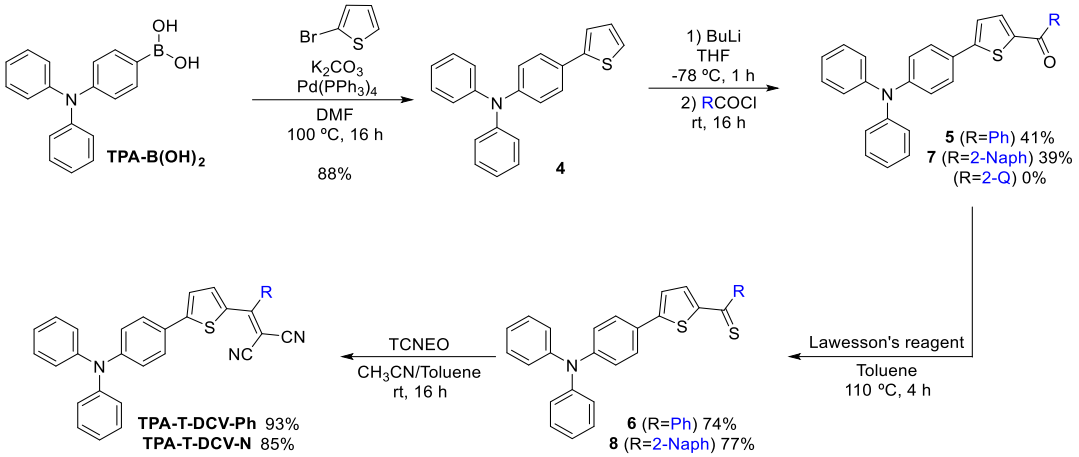

*Scheme 3.2. Adapted synthetic pathway to obtain **TPA-T-DCV-Ph** and **TPA-T-DCV-N**.*

Hence, as mentioned above, the new pathway started with a Suzuki coupling reaction between the commercially available **TPA-B(OH)$_2$** and bromothiophene, leading to molecule **4** in a better yield than that of the initial report (88% vs 77% respectively). As in the publication, the latter was then lithiated and subsequently quenched with benzoyl chloride to afford ketone **5** in a moderate yield before being engaged in the Knoevenagel condensation.

Considering that the reactivity of ketones in Knoevenagel condensations can be quite poor, especially for the ones with low electrophilicity, it was not surprising that harsh conditions were required and reported. Indeed, ketone **5** did not react with malononitrile even though different solvents, temperatures and bases were used. To tackle this issue, a two-step alternative consisting in converting the ketone in a highly reactive thione was carried out.[4] To that end, ketone **5** successfully reacted with Lawesson's reagent to afford compound **6** that in turn reacted with tetracyanoethylene oxide (TCNEO) to eventually obtain **TPA-T-DCV-Ph** in a good yield.

All in all, this new pathway allowed to obtain the desired product in a lower overall yield (25% instead of 43%) but avoiding this energy and time consuming microwave-assisted step. However, additional precautions have to be taken into consideration since thione derivatives can easily face some stability issues in solution in the presence of light.

Afterwards, this new pathway was applied to the synthesis of two other derivatives, either functionalized with a 2-naphthyl or a 2-quinolyl group (Scheme 3.2). However, the fact that both acyl chlorides were solids (unlike benzoyl chloride), hindered the reaction as the addition of the pure reagent over the lithium derivative of **4** was not possible in the same manner. This protocol difference completely changed the outcome of the reaction, since the fast addition of concentrated solutions of both acyl chlorides in dry THF over the lithium derivative of **4** only led

to traces of the desired products. Therefore, to avoid this problem, this step was performed the other way around and the lithium derivative was slowly added to a solution of each acyl chloride. On the one hand, ketone **7** was obtained in a comparable yield to that of ketone **5**, but demonstrating that this new synthetic route allows the synthesis of this type of derivatives based on the use of solid acyl chlorides. While the rest of the synthetic route to afford **TPA-T-DCV-N** was carried out in the same way as in the case of the phenyl derivative, the lower solubility of quinaldoyl chloride in the conventional solvents used for lithiations, such as THF and diethyl ether, totally prevented the reaction resulting in the absence of formation of the target ketone.

3.2.2 Synthesis of the trimer **(TPA-T-DCV)$_3$-Ph**

Different approaches were considered for the synthesis of the trimer **(TPA-T-DCV)$_3$-Ph** (Scheme 3.3).

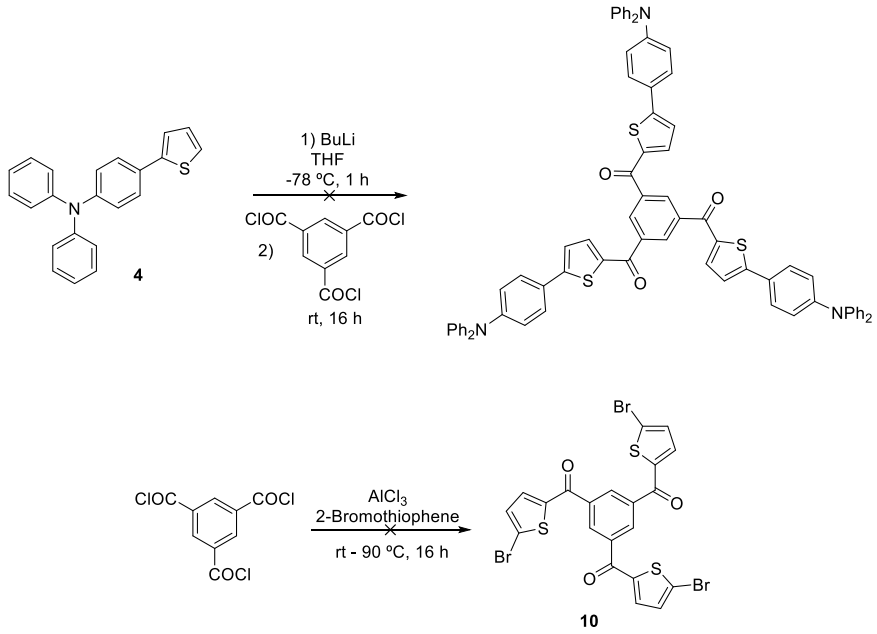

*Scheme 3.3. Unsuccessful approaches towards the conjugated trimer **(TPA-T-DCV)$_3$-Ph**.*

The first one was naturally based on the protocol developed for **TPA-T-DCV-Ph**, i.e., reaction of the lithiated derivative of **4** with the respective acyl chloride, namely benzene-1,3,5-tricarbonyl trichloride (Scheme 3.3). However, considering that the reaction did not take place in a really good yield for the monomer, it was not surprising to detect only traces of the triketone in the reaction mixture. Then, the same tricarbonyl trichloride was engaged in a Friedel-Crafts acylation with 2-bromothiophene to obtain the tri-bromide **10** but, once again, the reaction was not successful. Eventually, a different pathway was considered. Adapting a procedure found in

the literature,[5-6] the commercially available 2-acetyl-5-bromothiophene reacted at 160 °C in an excess of *N*,*N*-dimethylformamide dimethyl acetal (DMF-DMA) to first afford the enaminone **9** almost in a quantitative yield (Scheme 3.4). The latter was then engaged in a reaction with lactic acid at 90 °C in water yielding the tri-brominated central core **10** in a good yield and a column-free way.

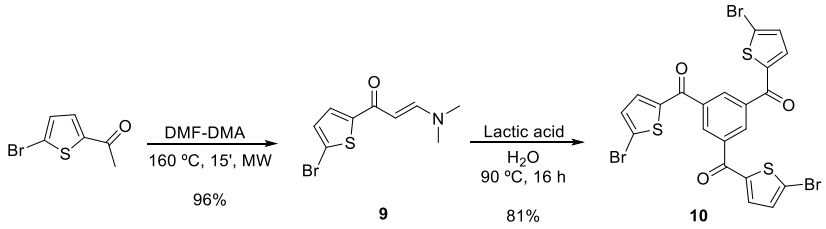

*Scheme 3.4. Synthetic pathway used to obtain the tri-brominated central core **10**.*

Afterwards, **10** reacted with **TPA-B(OH)$_2$** under Suzuki-Miyaura palladium-catalyzed cross-coupling conditions to afford ketone **11** in a moderate yield (Scheme 3.5).

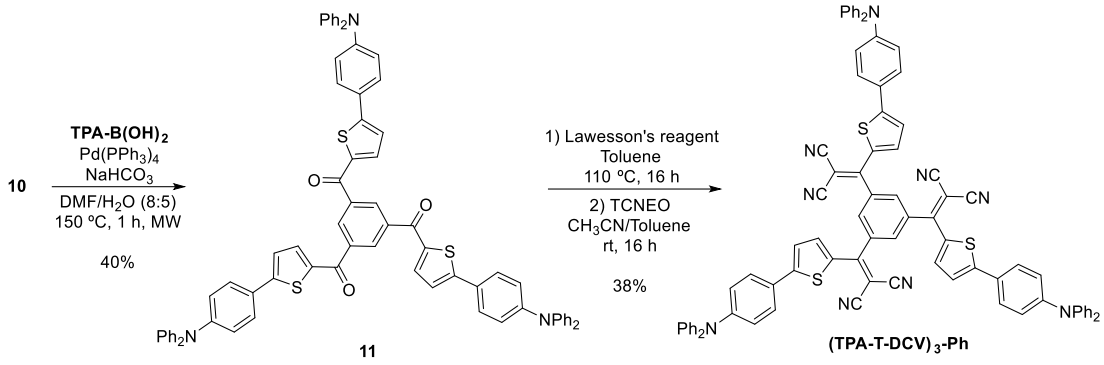

*Scheme 3.5. Synthetic pathway towards **(TPA-T-DCV)$_3$-Ph**.*

Finally, the procedure used to obtain **TPA-T-DCV-Ph** was thus adapted since ketone **11** was converted into thione **12** that was subsequently engaged in a reaction with TCNEO to obtain the target trimer **(TPA-T-DCV)$_3$-Ph**. The yields of these reactions were comparable to those obtained with the monomers, especially taking into consideration that three reactions took place per molecule.

3.3 Optical properties in solution

Hence, the two new compounds, namely **TPA-T-DCV-N** and **(TPA-T-DCV)$_3$-Ph**, were isolated, purified and compared to the reference compound **TPA-T-DCV-Ph**. Starting with their UV-Vis profiles recorded in CH_2Cl_2 solutions, it turns out that both monomers exhibited comparable patterns and absorption ranges even though a slight redshift was recorded in the case of **TPA-**

T-DCV-N. However, it is noteworthy that the latter was characterized by a higher ε which could be beneficial once embedded in OSCs (Figure 3.4 and Table 3.1).

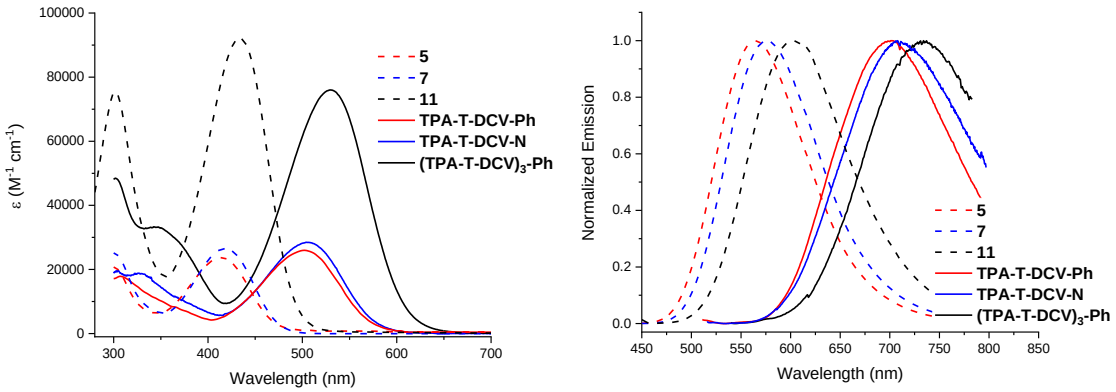

*Figure 3.4. UV-Vis absorption (left) and normalized emission (right) spectra of **TPA-T-DCV-Ph**, **TPA-T-DCV-N**, **(TPA-T-DCV)$_3$-Ph** and their respective ketones **5**, **7** and **11** in CH_2Cl_2 solutions.*

The main difference was found when the properties of the trimer were compared to those of its single counterpart **TPA-T-DCV-Ph**, since a threefold ε was obtained due to the effect induced by the three push-pull structures within the same molecule. In addition, its absorption spectrum was ca. 25 nm redshifted, probably due to the extension of the conjugation within the structure.

*Table 3.1. Summary of the optical properties of **TPA-T-DCV-Ph**, **TPA-T-DCV-N**, **(TPA-T-DCV)$_3$-Ph** and their respective ketones **5**, **7** and **11** in CH_2Cl_2 solutions.*

Molecule	λ_{abs} (nm)	ε (M^{-1} cm^{-1})	λ_{em} (nm)	Stokes shift (cm^{-1})	Φ_f[a]
5	414	23696	565	6,455	99.4
TPA-T-DCV-Ph	502	25950	701	5,655	0.7
7	418	26511	575	6,532	92.3
TPA-T-DCV-N	505	28448	708	5,678	0.3
11	434	92181	603	6,458	47.9
(TPA-T-DCV)$_3$-Ph	530	76000	734	5,244	0.3

[a] Measured with an integrating sphere.

Eventually, the emission spectra of the three DCV-based push-pull molecules were subsequently recorded and their Φ_f values measured revealing significant Stokes shifts (ca. 5,400 cm^{-1}) but negligible quantum yields (Figure 3.4 and Table 3.1).

On the other hand, the intriguing emission properties of ketones **5**, **7** and **11**, highlighted even with naked eyes, were also investigated in CH_2Cl_2 solutions (Figure 3.4 and Table 3.1). In addition to significant Stokes shifts of ca. 6,500 cm^{-1}, the latter were indeed characterized by impressive fluorescence quantum yields (almost quantitative for the monomers **5** and **7**). Consequently, in view of these outstanding properties, these ketones turned out to be potential candidates for optoelectronic applications such as OLEDs.

3.4 Electrochemical properties in solution

The electrochemical properties of the two new donors were compared to those of the reference **TPA-T-DCV-Ph** by means of cyclic voltammetry using the same experimental conditions already detailed in Chapter 2. The collected spectra and the most relevant electrochemical data are gathered in Figure 3.5 and Table 3.2.

*Table 3.2. Electrochemical properties of **TPA-T-DCV-Ph**, **TPA-T-DCV-N** and **(TPA-T-DCV)$_3$-Ph** obtained by CV. WE (Pt), AE (Pt), RE (SCE), 100 mV/s scan rate (buffer: 0.1 M Bu_4NPF_6 in CH_2Cl_2).*

Molecule	E_{pa} (V/$_{Fc/Fc^+}$)	E_{pc}^1 (V/$_{Fc/Fc^+}$)	E_{pc}^2 (V/$_{Fc/Fc^+}$)	E_{HOMO} (eV)[a]	E_{LUMO} (eV)[b]	ΔE^{elec} (eV)
TPA-T-DCV-Ph	0.60	-1.53	-1.84	-5.29	-3.40	1.89
TPA-T-DCV-N	0.50	-1.48	-1.61	-5.17	-3.45	1.72
(TPA-T-DCV)$_3$-Ph	0.61	-1.75	-	-5.29	-3.31	1.98

[a] E_{HOMO} (eV) = -(E_{ox}^{onset} + 4.8). [b] E_{LUMO} (eV) = -(E_{red}^{onset} + 4.8).

The three donors showed one reversible oxidation wave that could be assigned to the formation of a radical cation localized on the TPA-thiophene branch, as previously observed in other TPA-based push-pull derivatives. In comparison to **TPA-T-DCV-Ph**, the position of the peak was subjected to a 100 mV negative shift upon substitution of the phenyl by a naphthyl group although remained unaffected in the case of the trimer. In addition, when scanning towards negative potentials, a different behavior was observed. Whereas the CV of **TPA-T-DCV-Ph** showed two reduction waves, being the first of them reversible and the second irreversible, the one of **TPA-T-DCV-N** showed two quasi-successive reversible waves. In stark contrast, the CV of **(TPA-T-DCV)$_3$-Ph** only showed one non-reversible reduction wave at E_{pc}= -1.75 V.

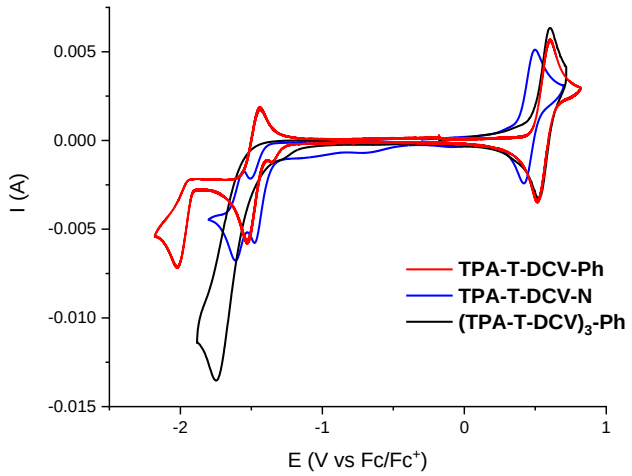

*Figure 3.5. Cyclic voltammograms of **TPA-T-DCV-Ph** (1 mM), **TPA-T-DCV-N** (1 mM) and **(TPA-T-DCV)$_3$-Ph** (0.5 mM). WE (Pt), AE (Pt), RE (SCE), 100 mV/s scan rate (buffer: 0.1 M Bu_4NPF_6 in CH_2Cl_2).*

Regarding their estimated energy levels (calculated as detailed in Chapter 2), whereas the trimer presented the same HOMO energy as the reference **TPA-T-DCV-Ph** (-5.29 eV), the one of **TPA-T-DCV-N** was slightly higher (-5.17 eV). In addition, while the substitution of the phenyl by a naphthyl led to a lower LUMO, **(TPA-T-DCV)$_3$-Ph** exhibited the highest LUMO (-3.31 eV) due to its greater band gap ΔE^{elec}.

3.5 Properties in solid state

The properties of the new donors as spun-casted thin films were compared to those of the reference **TPA-T-DCV-Ph** prior to their use in OSCs (Table 3.3). Following the procedure already detailed in Chapter 2, both HOMO and LUMO energies were estimated from PESA and the absorption spectra in solid state.

*Table 3.3. Summary of the optical and energetic properties of **TPA-T-DCV-Ph**, **TPA-T-DCV-N** and **(TPA-T-DCV)$_3$-Ph** as spun-casted films.*

Molecule	λ_{abs} (nm)	λ_{edge} (nm)[a]	HOMO (eV)[b]	E_g^{opt} (eV)[c]	LUMO (eV)[d]
TPA-T-DCV-Ph	529	630	-5.66	1.97	-3.69
TPA-T-DCV-N	528	617	-5.59	2.01	-3.58
(TPA-T-DCV)$_3$-Ph	552	657	-5.69	1.89	-3.80

[a] Low-energy absorption edge. [b] HOMO energy in solid state determined by PESA. [c] Optical gap estimated through the low-energy absorption edge (ICT bands). [d] Obtained through the equation: LUMO = HOMO + E_g^{opt}.

The UV-Vis spectra in solid state (Figure 3.6) followed the trend observed in solution but they appeared slightly broadened and redshifted (ca. 30 nm) due to aggregation phenomena.

Although the HOMO levels estimated by PESA (Figure 3.6 and Table 3.3) matched the tendency previously obtained by CV, a different trend was observed for the LUMOs. While the monomers presented a similar E_g^{opt} (1.97 and 2.01 eV), both the HOMO and LUMO energies of the naphthyl derivative turned out to be less stabilized. In addition, the HOMO level of the trimer **(TPA-T-DCV)$_3$-Ph** was found to be almost the same as for **TPA-T-DCV-Ph**, but its shorter estimated band gap led to a lower LUMO. Thus, according to these data, both new donors could be potentially used as donors for OSCs since their LUMO energies were higher than the ones of the main fullerene derivatives (ca. 4 eV).

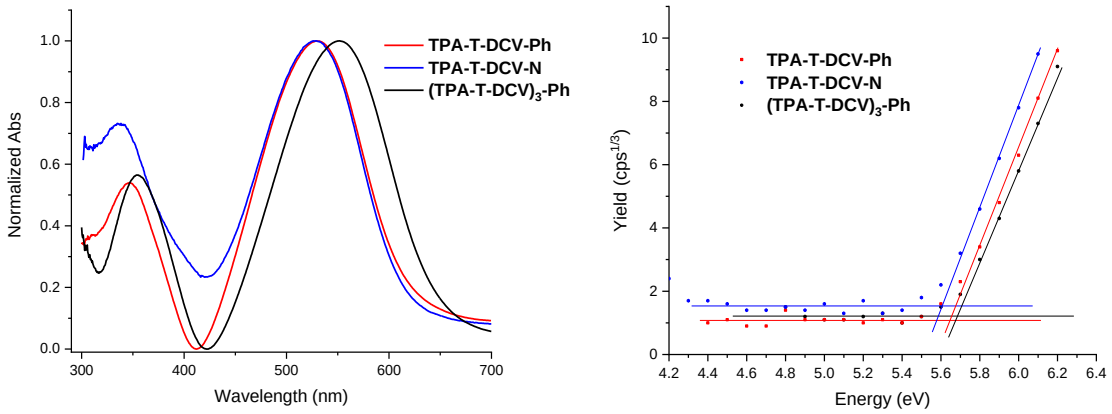

*Figure 3.6. Normalized UV-Vis absorption (left) and PESA (right) spectra of **TPA-T-DCV-Ph**, **TPA-T-DCV-N** and **(TPA-T-DCV)$_3$-Ph** in solid state.*

3.6 Organic solar cells

3.6.1 **TPA-T-DCV-N**

In view of the great photovoltaic performance of **TPA-T-DCV-Ph** in vacuum-processed OSCs, **TPA-T-DCV-N** was directly tested in such devices by our partners of the Technische Universität Dresden. First, standard (ITO/MoO_3/**TPA-T-DCV-N**/C_{60}/BPhen/Ag) and inverted (ITO/Bis-HFl-NTCDI:$W_2(hpp)_4$/C_{60}/**TPA-T-DCV-N**/MoO_3/Ag) PHJ OSCs were fabricated using three different donor thicknesses (6, 9 and 12 nm) (Figure 3.7 and Table 3.4).

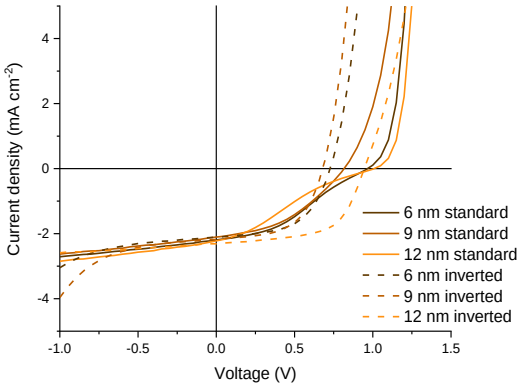

*Figure 3.7. J-V curves of vacuum-processed PHJ solar cells using **TPA-T-DCV-N** and C_{60}.*

*Table 3.4. Photovoltaic parameters of vacuum-processed PHJ solar cells using **TPA-T-DCV-N** and C_{60}.*

D thickness (nm)	Configuration	J_{sc} (mA cm^{-2})	V_{oc} (V)	*FF* (%)	PCE (%)
6	Standard	-2.19	0.97	35	0.74
	Inverted	-2.11	0.73	55	0.85
9	Standard	-2.11	0.82	41	0.71
	Inverted	-2.18	0.68	60	0.83
12	Standard	-2.22	1.01	24	0.54
	Inverted	-2.31	0.95	60	1.31

On the one hand, it can be clearly observed that J-V curves recorded on devices of standard configuration exhibited strong S-kinks, potentially related to injection/extraction barriers or an unbalance between the electron and hole mobilities, which highly spoiled the performances. On the other hand, inverted PHJ OSCs showed suitable curves even though the performances were not really high due to their moderate J_{sc}. In addition, the device fabricated with the thickest donor layer (12 nm) led to the best performance due to its higher V_{oc} and *FF*, thus indicating that the diffusion of the excitons was not hindered in thicker layers.

To improve the performance of the donor, BHJ OSCs were then fabricated using C_{60} as the complementary acceptor material. Several parameters of the fabrication procedure were modulated using once again standard (ITO/MoO_3/D:A/BPhen/Ag) and inverted (ITO/Bis-HFl-NTCDI:$W_2(hpp)_4$/A:D/MoO_3/Ag) configurations, such as the D:A ratio, the thickness of the active layer, the deposition over heated substrates (80 °C) and the use of a PMHJ architecture (Table 3.5 and Figure 3.8). In addition, the last two strategies were tested at the same time in an attempt to observe a synergic effect.

The outcome of this sequential modulation of parameters will be fully detailed but it has to be firstly highlighted that these devices were significantly more performing than their PHJ counterparts mainly due to the improvement of the J_{sc} resulting from a better extraction of the charges.

*Table 3.5. Photovoltaic parameters obtained in the optimization of vacuum-processed BHJ solar cells using **TPA-T-DCV-N** and C_{60}.*

Entry	Configuration	Thickness (nm)	Ratio (D:A)	Deposition T (°C)	J_{sc} (mA cm^{-2})	V_{oc} (V)	*FF* (%)	PCE (%)
1	Standard	20	1:2	rt	-4.12	0.91	44	1.64
2	Standard	20	1:2	80	-4.05	0.89	46	1.67
3	Standard PMHJ	20	1:2	rt	-4.36	0.96	42	1.76
4	Standard PMHJ	20	1:2	80	-4.62	0.95	45	1.99
5	Inverted	20	1:2	rt	-3.57	0.81	49	1.40
6	Standard	30	1:2	rt	-4.88	0.94	45	2.08
7	Standard	30	1:1	rt	-5.08	0.98	47	2.33
8	Standard	30	2:1	rt	-4.99	1.04	45	2.32

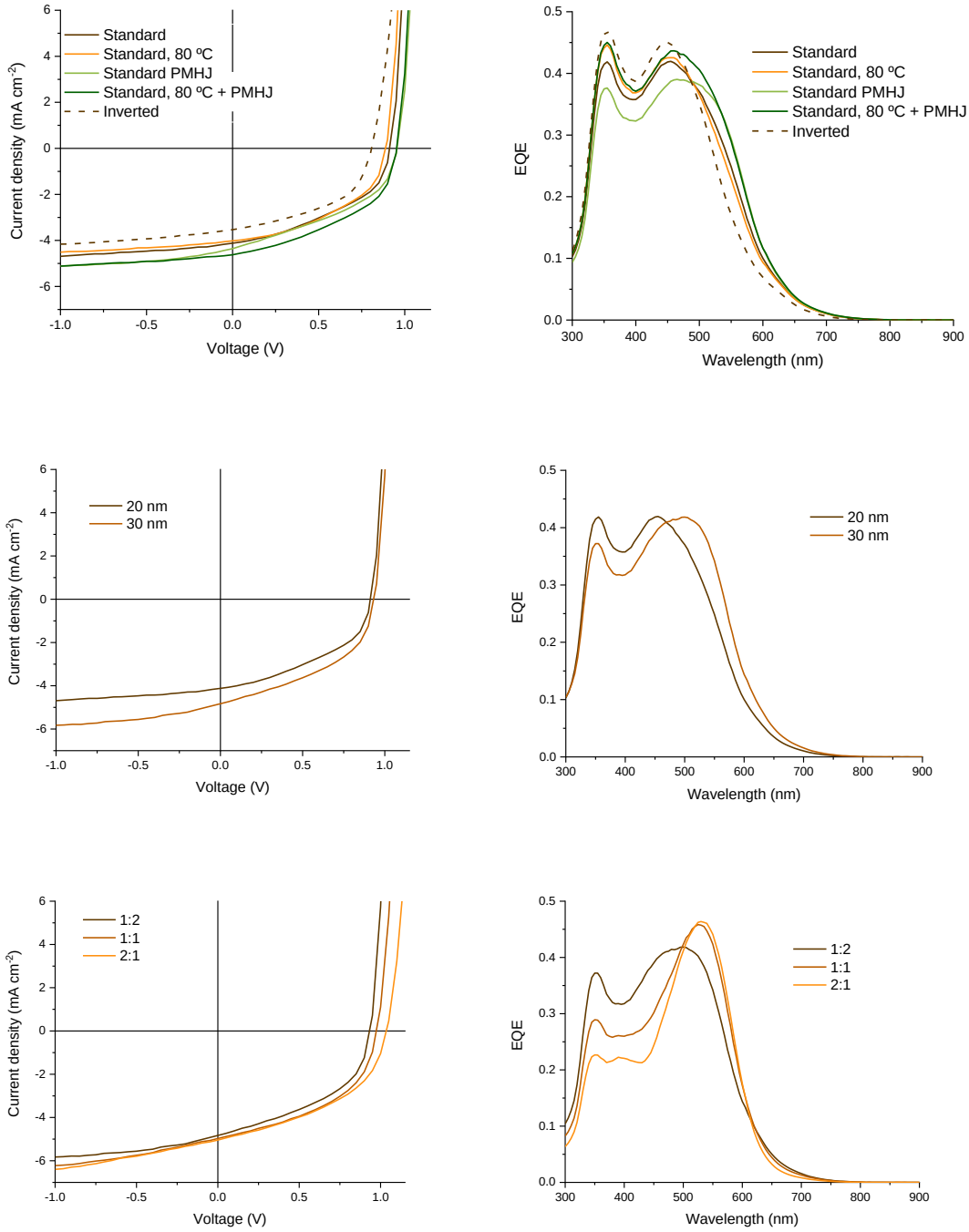

Figure 3.8. J-V (left) and EQE (right) curves obtained in the optimization of the architecture (top, Table 3.5, entries 1-5), thickness (center, Table 3.5, entries 1 and 6) and D:A ratio (bottom, Table 3.5, entries 6-8) of vacuum-processed BHJ solar cells fabricated with ***TPA-T-DCV-N*** *and* C_{60}.

First, in stark contrast to PHJ OSCs, BHJ fabricated with an inverted configuration (entry 5, Table 3.5) were less performing than the corresponding standard devices (entry 1, Table 3.5) despite their substantially higher *FF*. In addition, it is noteworthy that for active layers of 20 nm, PMHJ structures (entry 3, Table 3.5) led to slightly higher performances due to their higher J_{sc} and V_{oc}. Then, while deposition over heated substrates (entry 2, Table 3.5) did not give rise to a better

efficiency on its own, a synergic effect was observed when combined with the PMHJ architecture leading to an increase of the J_{sc}.

In addition, all the photovoltaic parameters were substantially improved simply by increasing the thickness of the active layer from 20 to 30 nm (entries 1 and 6, Table 3.5). The improvement in the J_{sc} was especially noteworthy since this parameter was clearly spoiling the performance of the devices up to this point. Consequently, thicker active layers are currently being tested in an attempt to boost the generated photocurrent.

Finally, three different D:A ratios (2:1, 1:1 and 1:2) were compared, still for active layers of 30 nm (entries 6-8, Table 3.5). Although there was not much difference between the overall performances when the ratio was modulated, several conclusions can be drawn. First, it was noticeable that the V_{oc} seems to be ratio-dependent. Thus, additional experiments with thicker active layers would be required to unequivocally conclude whether the 1:1 D:A ratio performs better than its 1:2 counterpart.

In parallel, C_{70} was used as the complementary acceptor material since it is known to enhance the absorption properties usually leading to improved PCEs. To check if this assumption can be extended to this new donor, devices with a direct configuration were fabricated using a 1:2 D:A ratio in active layers of 20 and 30 nm (Figure 3.9 and Table 3.6).

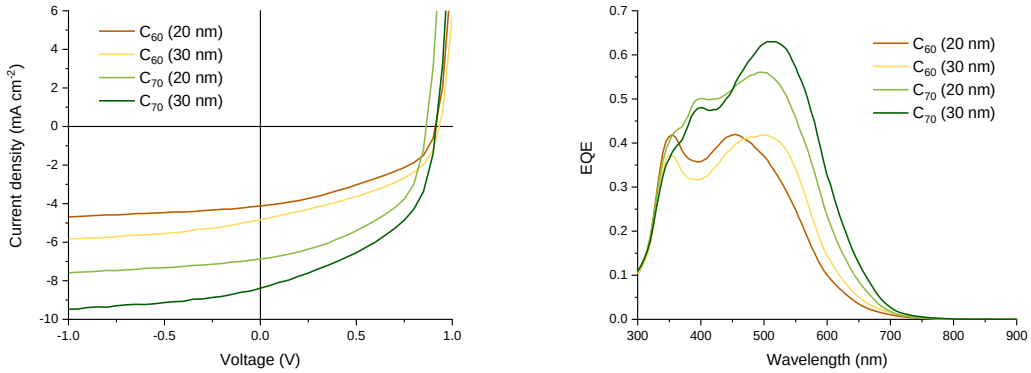

*Figure 3.9. J-V (left) and EQE (right) curves of vacuum-processed BHJ solar cells using **TPA-T-DCV-N** as donor and C_{60} and C_{70} as acceptors.*

*Table 3.6. Photovoltaic parameters of vacuum-processed BHJ solar cells using **TPA-T-DCV-N** as donor and C_{60} and C_{70} as acceptors.*

Acceptor	Thickness (nm)	J_{sc} (mA cm^{-2})	V_{oc} (V)	*FF* (%)	PCE (%)
C_{60}	20	-4.12	0.91	44	1.64
	30	-4.89	0.94	45	2.08
C_{70}	20	-6.91	0.87	50	3.01
	30	-8.45	0.91	48	3.72

According to the preliminary results, despite the slight decrease in the V_{oc}, the use of C_{70} counterbalanced the low J_{sc} of C_{60}-based devices since the highest value (-8.45 mA cm^{-2}) was obtained up to this point. In addition, the EQE spectra showed an improved photogeneration all along the visible spectrum with a maximum of ca. 65% at 505 nm. It is also noteworthy that just the contribution of the donor (peak at 500 nm) was improved when the thickness was increased from 20 to 30 nm. Therefore, C_{70} seems to be a more appropriate complement for **TPA-T-DCV-N** as it helps to enhance the most limited parameter, namely the J_{sc}.

All in all, although the optimization process was not completed by our partner by the time this manuscript was submitted, **TPA-T-DCV-N** achieved quite decent *FF* and V_{oc} values but suffered from low J_{sc}. Therefore, the idea would be to keep optimizing the device fabrication by using a PMHJ architecture combined with the deposition over heated substrates but also with optimized thickness, D:A ratio (between 2:1 and 1:1) and of course acceptor (C_{70} instead of C_{60}). Indeed, in view of these preliminary results, there is still room to improve the 3.72% PCE obtained up to this point.

3.6.2 **(TPA-T-DCV)$_3$-Ph**

Considering that the high molecular weight of the trimer **(TPA-T-DCV)$_3$-Ph** (1282.6 g mol^{-1}) may hinder its evaporation, a preliminary evaluation was performed through the fabrication of solution-processed BHJ OSCs of architecture ITO/PEDOT:PSS/DA/LiF/Al. Hence, **(TPA-T-DCV)$_3$-Ph** was solubilized in chloroform and blended with either $PC_{61}BM$ and $PC_{71}BM$ in a 1:1 ratio (10 mg/mL in total) and spun-casted at 1300 rpm (Figure 3.10 and Table 3.7).

*Table 3.7. Photovoltaic parameters of solution-processed BHJ solar cells using **(TPA-T-DCV)$_3$-Ph** as donor and $PC_{61}BM$ and $PC_{71}BM$ as acceptors in a 1:1 D:A ratio.*

Acceptor	J_{sc} (mA cm^{-2})	V_{oc} (V)	*FF* (%)	PCE (%)
$PC_{61}BM$	-2.43	0.40	28	0.27
$PC_{71}BM$	-3.16	0.64	27	0.55

As it can be observed, the performance of the trimer blended with both acceptors was rather modest. The devices indeed suffered from really low *FF* (only ca. 28%) but also V_{oc} and J_{sc}. As usual, PCEs were slightly enhanced when the expensive but better absorbing $PC_{71}BM$ was used due to the higher J_{sc} and especially V_{oc} (+0.24 V). Although the only apparent advantage of this material with respect to the monomer was its slightly broader absorption range, it did not lead to a significant improvement due to the low intensity of the EQE.

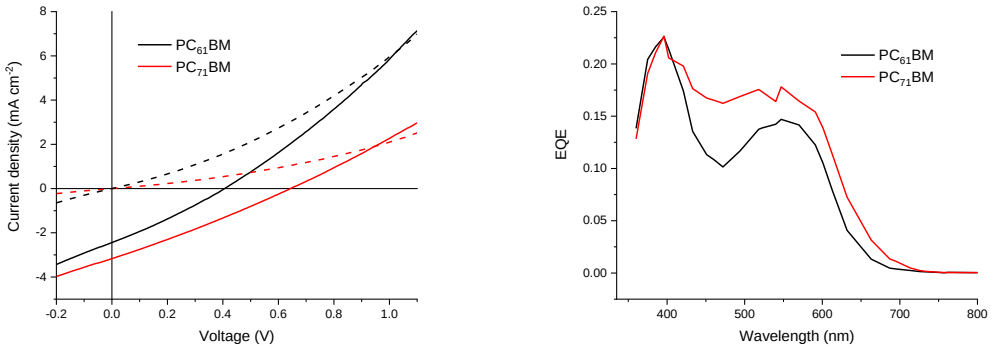

Figure 3.10. J-V (left) and EQE (right) of solution-processed BHJ solar cells using ***(TPA-T-DCV)$_3$-Ph*** *as donor and PC$_{61}$BM and PC$_{71}$BM as acceptors.*

To improve these preliminary measurements, an optimization process should be carried out later on in order to evaluate, for instance, the use of different additives, D:A ratios, thicknesses of the active layer and also configurations of the devices (standard vs inverted). In parallel, **(TPA-T-DCV)$_3$-Ph** was sent to a collaborator (Prof. Gregory Welch, University of Calgary) to be tested in ternary organic solar cells.

3.7 Conclusions

First of all, the synthetic procedure for the synthesis of **TPA-T-DCV-Ph** has been adapted and a naphthyl analogue, namely **TPA-T-DCV-N**, has been synthesized as a proof of concept with comparable synthetic yields. The substitution of the phenyl ring by a naphthyl did not impact the optical and electrochemical properties of the reference molecule in a great manner. Then, the new **TPA-T-DCV-N** was evaluated as a donor material in vacuum-processed OSCs. Although the optimization process was not fully completed within the frame of this thesis, a significant improvement of PCE was observed, reaching a promising value of 3.72%. It was found that the use of C_{70} drastically increased the *FF* and especially the J_{sc}, reaching a notable maximum EQE of 65% at 505 nm. Therefore, with additional optimizations, it is expected to significantly improve its PCE. In addition, the ketone intermediates of both donor materials (**5** and **7**) were found to be highly emissive with almost quantitative fluorescence quantum yields, opening doors to other applications.

Thus, in view of the notable photovoltaic performances of **TPA-T-DCV-Ph** and **TPA-T-DCV-N**, the synthesis of different analogues is envisioned in the short term. The most evident way to improve the photovoltaic performance is to broaden the absorption range of the molecules, which has led so far to low J_{sc}. To that end, the use of better electron-donating blocks, such as MPTA or MTTA, will be considered in order to redshift the absorbance and take advantage of photons of lower energy.

Additionally, a new strategy to synthesize conjugated trimers of push-pull molecules with a benzene moiety as a central core has been designed and applied for the preparation of **(TPA-T-DCV)$_3$-Ph**. While the latter exhibited interesting optical and electrochemical properties, further device optimizations have to be carried out to evaluate the potential of such architectures in OSCs.

From the synthetic point of view, more soluble arylamine-based electron-rich moieties are currently considered in order to exploit this new synthetic strategy. For instance, we recently reported the synthesis of two simple donor materials for OPV based on a *N*,*N*-bis(4-biphenylyl)aniline (BPA) donor unit that exhibited high hole mobility and fill factors over 73%, which have been barely achieved in all-small-molecule OSCs.[7] Hence, in an attempt to improve the results obtained by **(TPA-T-DCV)$_3$-Ph**, an additional trimer, namely **(BPA-T-DCV)$_3$-Ph**, was recently synthesized following the same synthetic pathway but using a BPA donor unit (Figure 3.11). Thus, this new trimer, with similar electrochemical properties but improved absorptivity, will be soon tested in solution-processed BHJ solar cells.

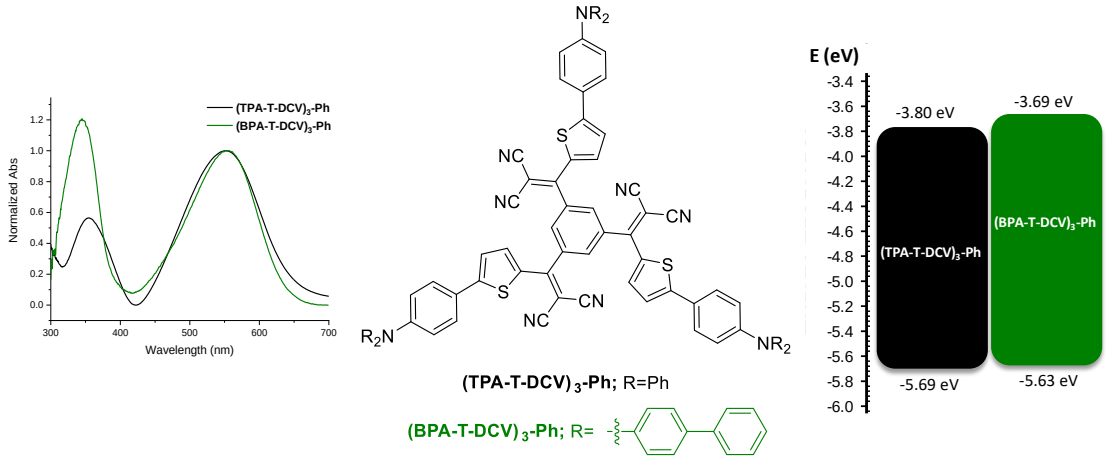

Figure 3.11. UV-Vis absorption spectra (left) and HOMO/LUMO levels (right) of ***(TPA-T-DCV)$_3$-Ph*** *and* ***(BPA-T-DCV)$_3$-Ph*** *in solid state.*

References

[1] Kozlov, O. V., Luponosov, Y. N., Solodukhin, A. N., Flament, B., Douhéret, O., Viville, P., Beljonne, D., Lazzaroni, R., Cornil, J., Ponomarenko, S. A. and Pshenichnikov, M. S., *Organic Electronics* **2018**, *53*, 185-190.

[2] Labrunie, A., Josse, P., Dabos-Seignon, S., Blanchard, P. and Cabanetos, C., *Sustainable Energy & Fuels* **2017**, *1*, 1921-1927.

[3] Malacrida, C., Habibi, A. H., Gámez-Valenzuela, S., Lenko, I., Marqués, P. S., Labrunie, A., Grolleau, J., López Navarrete, J. T., Ruiz Delgado, M. C., Cabanetos, C., Blanchard, P. and Ludwigs, S., *ChemElectroChem* **2019**, *6*, 4215-4228.

[4] Baert, F. PhD thesis, Université d'Angers, **2015**.

[5] Castillo, J.-C., Tigreros, A. and Portilla, J., *The Journal of Organic Chemistry* **2018**, *83*, 10887-10897.
[6] Wan, J.-P., Lin, Y., Hu, K. and Liu, Y., *RSC Advances* **2014**, *4*, 20499-20505.
[7] Marqués, P. S., Andrés Castán, J. M., Josse, P., Blais, M., Habibi, A. H., Ramirez, I., Walzer, K., Roncali, J., Blanchard, P. and Cabanetos, C., *New Journal of Chemistry* **2020**.

Chapter 4

Nitration of the benzothioxanthene core: towards new functionalization strategies

4.1 Introduction

Among other simple, affordable and absorbing molecules, dyes have clearly a special place. Several architectures, such as BODIPY, porphyrin, phthalocyanine, diketopyrrolopyrrole or rylene imide derivatives, have been already synthesized, functionalized and used in organic photovoltaics. One intriguing example is *N*-(alkyl)benzothioxanthene-3,4-dicarboximide (**BTXI**), whose most distinctive feature is the push-pull effect created along its conjugated core through the interaction between the electron-donating sulfur atom and the imide group. Its structure is compared to that of the well-known **PDI** in Figure 4.1.

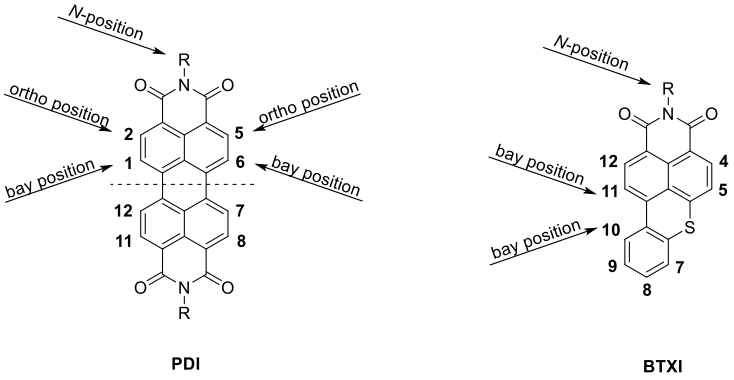

*Figure 4.1. Structures of **PDI** and **BTXI**.*

In stark contrast to the reference and symmetrical **PDI**, which has been extensively employed due to its redox, electron-withdrawing and charge-carrier transport properties as well as its excellent chemical, thermal and photochemical stabilities,[1-4] **BTXI** has been scarcely studied since its discovery in 1974.[5-6] Indeed, just a few publications related to its application in bioimaging[7-9] or antitumor therapeutics[10] were reported before 2018.

First fully investigated by our group, **BTXI** revealed interesting optical properties with an absorption in the visible and an associated emission characterized by an almost quantitative fluorescence quantum yield (Figure 4.2).

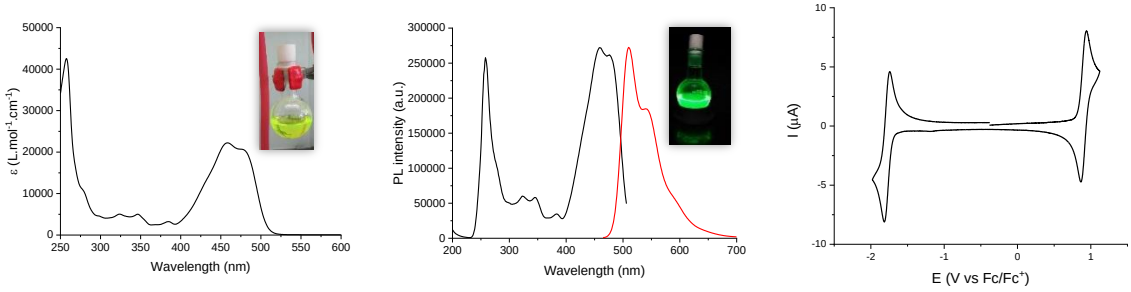

*Figure 4.2. UV-Vis absorption (left) and emission (center) spectra in CH_2Cl_2 and cyclic voltammogram (right) in 0.1 M Bu_4NPF_6/CH_2Cl_2 (100 mV/s scan rate, Pt working electrode) of **BTXI**.*

In addition, the exploration of its redox properties highlighted two fully reversible and stable one-electron processes in both the anodic and cathodic regions with an impressive electrochemical gap of ca. 2.5 V.

As a step forward to its use in the preparation of extended π-conjugated systems, the synthetic pathway to obtain the bare **BTXI** in gram-scale was first optimized (Scheme 4.1).

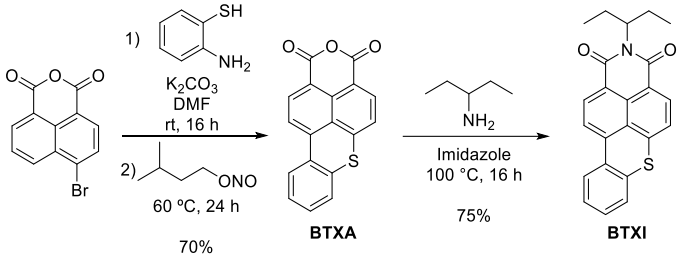

*Scheme 4.1. Optimized synthetic pathway used to obtain **BTXI**.*

To do so, two already reported routes were combined to afford the anhydride **BTXA** from 4-bromo-1,8-naphthalic anhydride and 2-aminothiophenol through a one-pot reaction with isopentyl nitrite prior to the introduction of the alkyl chain in molten imidazole. Eventually, this 2-step synthesis was upscaled allowing the column-free production of **BTXI** in a 52% yield and using less expensive starting materials.

Indeed, unlike **PDI**, whose chemical functionalization in the bay, ortho and *N* positions had been widely studied,[11] **BTXI** had been only functionalized in the latter (imide) for post-grafting or solubility purposes.[10, 12-13] Hence, it is important to note that the reactivity of the 8 available positions of its conjugated backbone was still unexplored. Consequently, the selective mono-bromination of the core was investigated by our group.[14] It turned out that the structural elucidation of the product was not straightforward, since only X-ray diffraction provided the exact position (5) of this efficient and selective functionalization. This new **BTXI-Br** was proven to be fully compatible with the most commonly used palladium-catalyzed cross-coupling reactions, i.e., Stille, Suzuki-Miyaura, Sonogashira and direct arylation (Scheme 4.2).

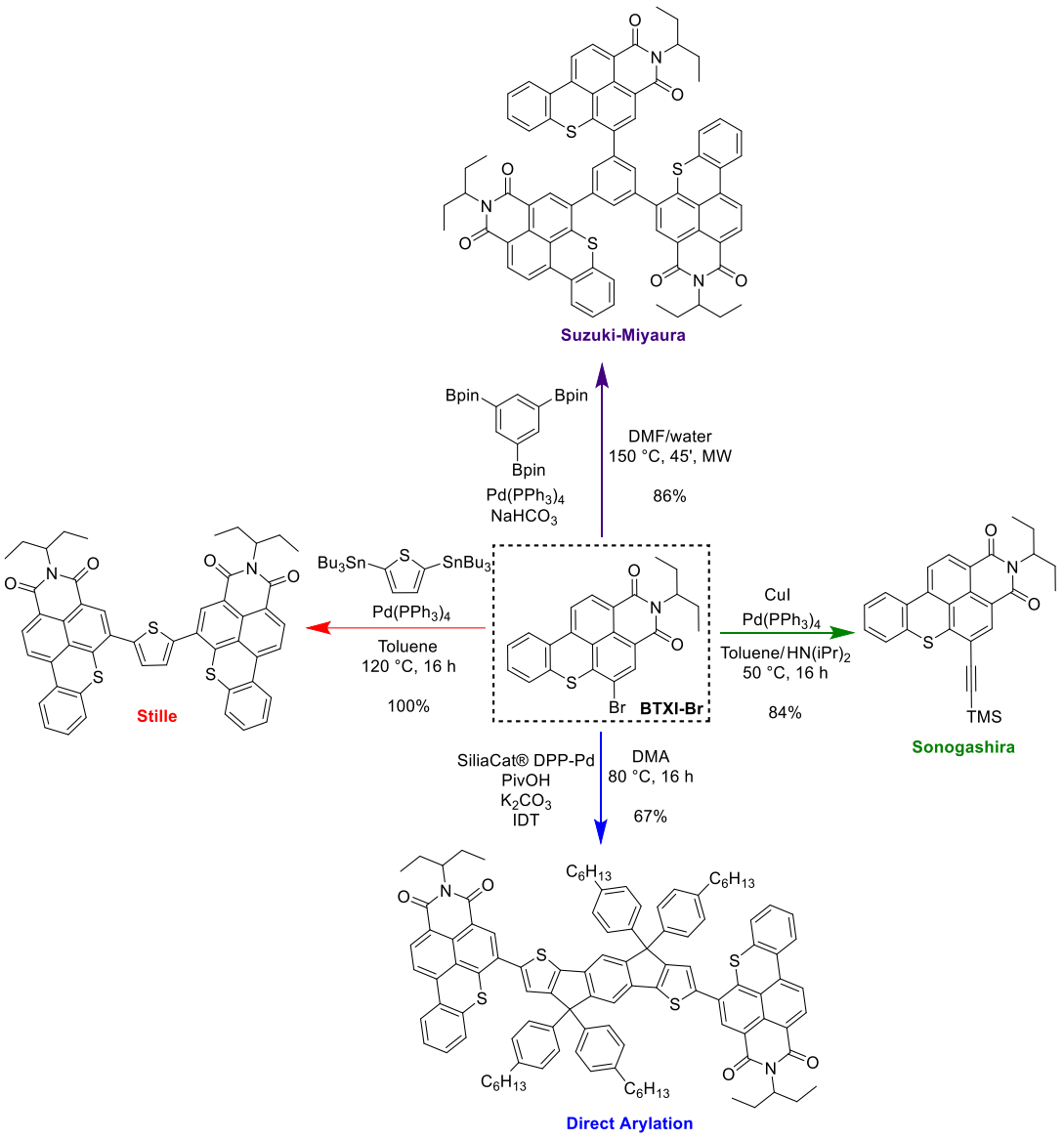

*Scheme 4.2. Illustration of the synthetic versatility of **BTXI-Br**.*

Following this approach, several π-conjugated systems were prepared and evaluated in different applications of organic electronics with great results in, for instance, OPV,[14] OTFT[15] and supercapacitors[16] (Figure 4.3).

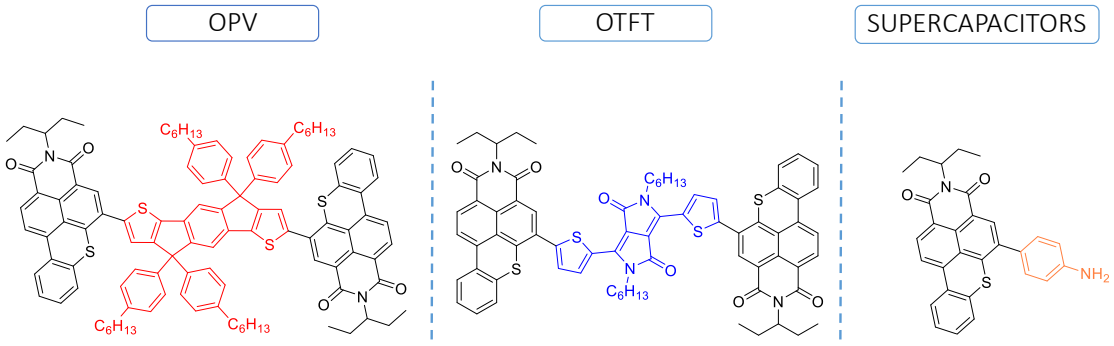

Figure 4.3. Examples of BTXI-based materials for organic electronics.

On the other hand, it is noteworthy that the nitration of other rylenes, particularly in the case of **PDI**, has gained attention over the bromination over the last few years, especially due to two main reasons. The first one is related to the ease of synthesis and purification of nitro derivatives.[17] The second deals with the potential compatibility of this group with different cyclizations in the bay area through Cadogan-type reactions in order to incorporate diverse heteroatoms, namely sulfur,[17] oxygen,[18] nitrogen[19] or even more complex structures, such as azaborine-[20] or pyran-based[21] moieties. Considering that there are no examples of this reaction over **BTXI** in the literature, the experimental conditions will be first optimized and then the susceptible positions to react in this non-symmetric block will be evaluated. Then, the reactivity of the nitro group will be studied and afterwards the optical and electrochemical properties of the new synthesized derivatives will be naturally investigated.[22]

Eventually, the ultimate goal would be to develop a methodology to nitrate a bay position of **BTXI** in order to study the viability of different cyclizations through Cadogan reactions to obtain new extended BTXI-based systems.

4.2 Synthesis and characterization of **BTXI-NO_2** and **NO_2-BTXI-NO_2**

In view of the high reactivity of **BTXI** with bromine, the former was subjected to one molar equivalent of fuming nitric acid under air at room temperature (Scheme 4.3).

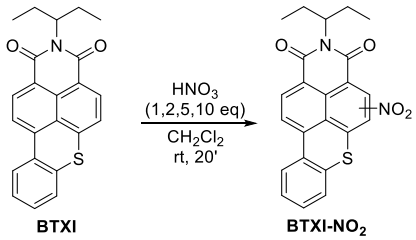

*Scheme 4.3. Reactive conditions used for the nitration of **BTXI**.*

However, regardless of the reaction time, the full conversion of the starting material was not reached, resulting in the addition of different equivalents of HNO_3, i.e., 2, 5 and 10. As an illustration, the NMR of the unpurified crudes after reactions of 20 minutes are gathered in Figure 4.4.

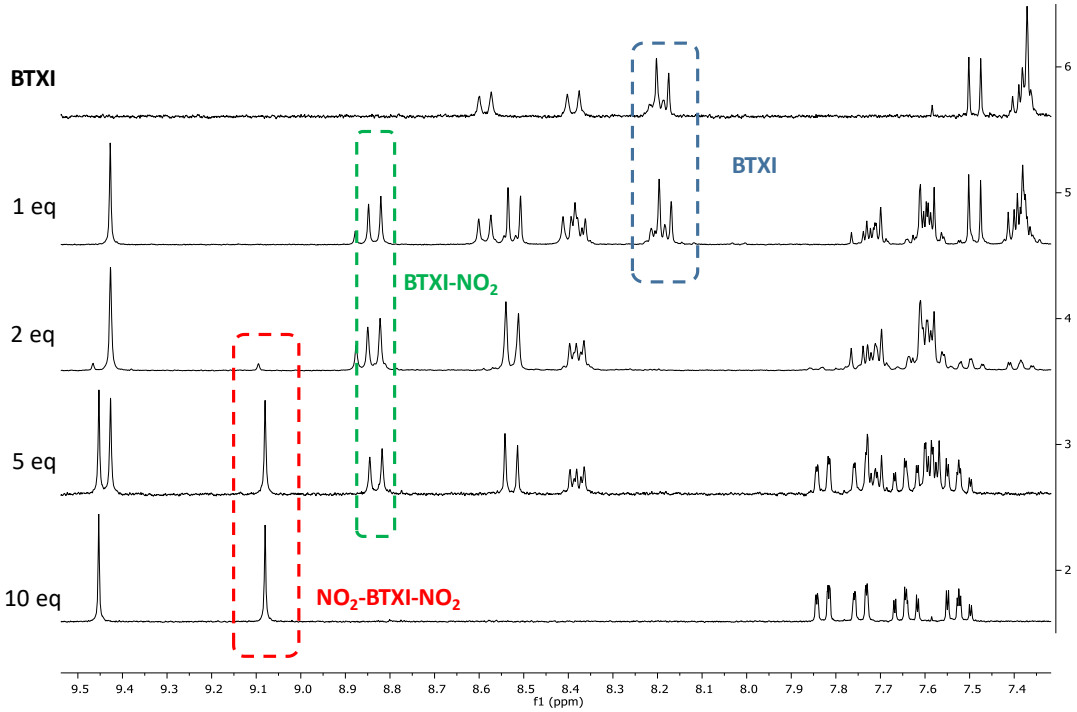

*Figure 4.4. ^{1}H NMR in $CDCl_3$ of **BTXI** and the reaction crudes obtained after the nitration of **BTXI** with different equivalents of HNO_3 in CH_2Cl_2 at rt during 20 minutes.*

It turns out that the full conversion of **BTXI** was already achieved with two equivalents, even though it already started to generate traces of a secondary product. In these conditions, the mono-nitrated **BTXI-NO$_2$** directly precipitated from the reaction after approximately 20 minutes and was directly recovered by a simple filtration. The rest of the product was purified by recrystallization from CH_2Cl_2, meaning that **BTXI-NO$_2$** is less soluble than its multi-nitrated counterparts in chlorinated solvents. Then, when 5 eq were added, a mixture of **BTXI-NO$_2$** and a di-nitrated product was obtained according to the NMR spectrum. Eventually, when 10 equivalents were added, the di-nitrated derivative **NO$_2$-BTXI-NO$_2$** was obtained in a high yield without additional impurities. Both products were also confirmed by mass spectroscopy. However, the addition of more equivalents, i.e., 20 or 30, provided mixtures of **NO$_2$-BTXI-NO$_2$** and more than one multi-nitrated product that could not be separated by column chromatography. Thus, the reactivity of this block towards nitric acid just allows the selective synthesis of **BTXI-NO$_2$** and **NO$_2$-BTXI-NO$_2$**. Hence, as in the case of **BTXI-Br**, the next step was to precisely identify the functionalized positions.[14]

To that end, the mono-nitrated product was first fully characterized by NMR, even if complicated due to its modest solubility (Figure 4.5).

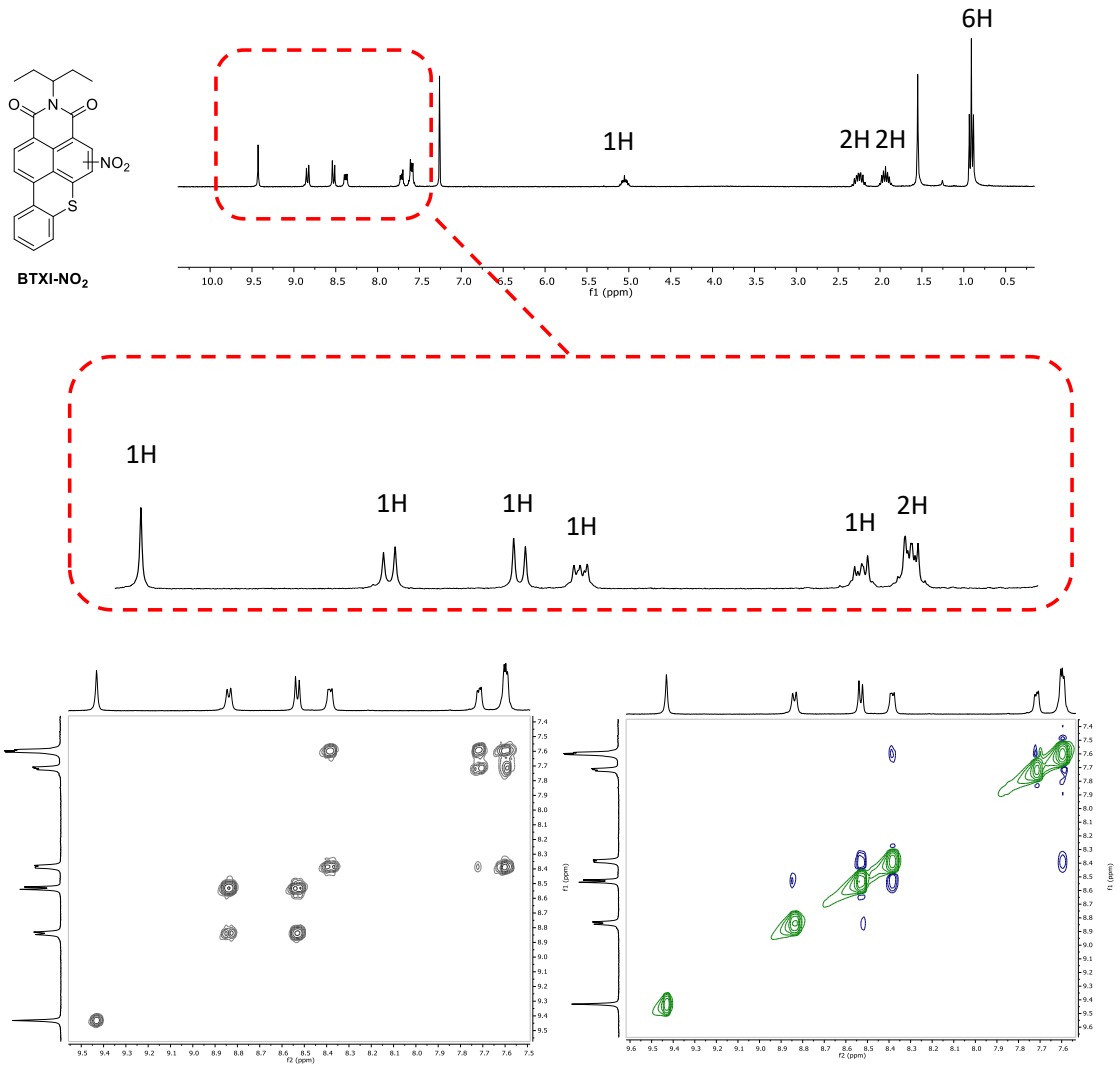

*Figure 4.5. ^{1}H NMR (top), ^{1}H-^{1}H COSY (bottom-left) and ^{1}H-^{1}H NOESY (bottom-right) spectra of **BTXI-NO$_2$** in $CDCl_3$.*

By means of its COSY spectrum, 3 systems of aromatic protons were confirmed: 1 singlet (1H at 9.43 ppm), 2 doublets (1H each at 8.84 and 8.53 ppm) and 3 multiplets (4H in total, at 8.39, 7.72 and 7.59 ppm), demonstrating that the -NO_2 group was grafted on the naphthyl ring, i.e., positions 4, 5, 11 and 12. Then, NOESY experiments confirmed the interaction between protons 11 (doublet, 8.53 ppm) and 10 (multiplet, 8.39 ppm) thus highlighting that the nitro group was located either on position 4 or 5. However, unlike for **BTXI-Br**, the crystal growth process was unfortunately unsuccessful even if different techniques were tested.

Consequently, density functional theory (DFT) calculations were carried out at the OT-ωB97X-D/6-31g(d,p) level of theory to determine the low-energy nitro-substitution site for each unique and potential **BTXI-NO$_2$** derivative. It is noteworthy that geometries were optimized with methyl groups instead of ethylpropyl side chains to reduce the computational cost. As illustrated in

Figure 4.6, the mono-nitrated isomer with the lowest energy was found to be the one functionalized on the position labeled 9.

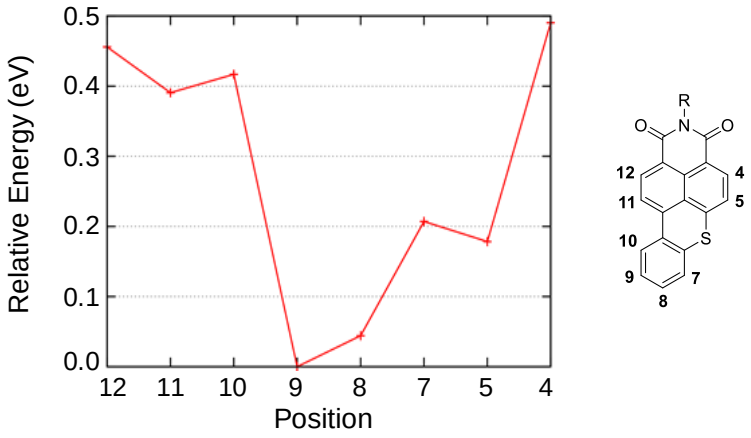

*Figure 4.6. Relative energy of every possible mono-nitrated isomer of **BTXI**.*

These results, in disagreement with those deduced from the NMR experiments, suggested that the isolated **BTXI-NO$_2$** did not correspond to the thermodynamic product but to the kinetic one. Moreover, although computational chemistry revealed that isomer 5 was substantially more stable than its counterpart functionalized on position 4, a different approach was required to unequivocally assign the right substitution. Indeed, an indirect synthetic strategy was subsequently considered, consisting in the preparation and comparison of two structural isomers obtained from **BTXI-Br**, whose functionalized position was known and confirmed (5), and **BTXI-NO$_2$** (approaches A and B respectively of Scheme 4.4).

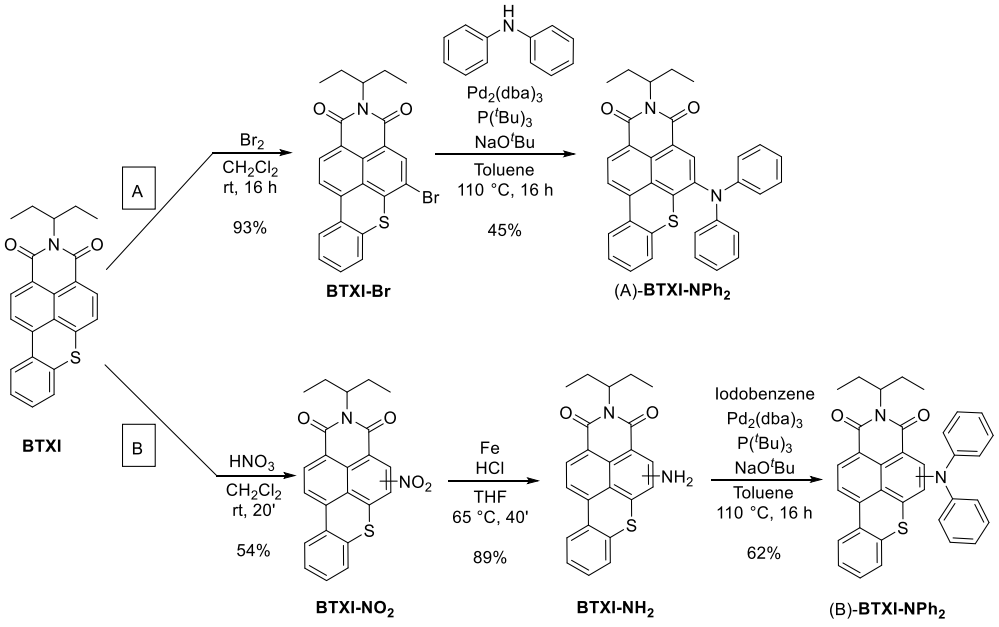

*Scheme 4.4. Synthetic route towards **BTXI-NPh$_2$** using two different approaches (A and B).*

Hence, **BTXI-Br** was involved in a Buchwald-Hartwig cross-coupling reaction with diphenylamine to afford the reference compound (A)-**BTXI-NPh$_2$**. In parallel, the nitro group of **BTXI-NO$_2$** was first reduced into a primary amine (**BTXI-NH$_2$**) with iron powder and hydrochloric acid in a high yield before being engaged in a double Buchwald-Hartwig coupling with iodobenzene to obtain (B)-**BTXI-NPh$_2$**. Once isolated and purified by column chromatography, both molecules revealed a perfect superimposition of their ^{1}H NMR spectra (Figure 4.7), thus confirming the nitro substitution in position 5.

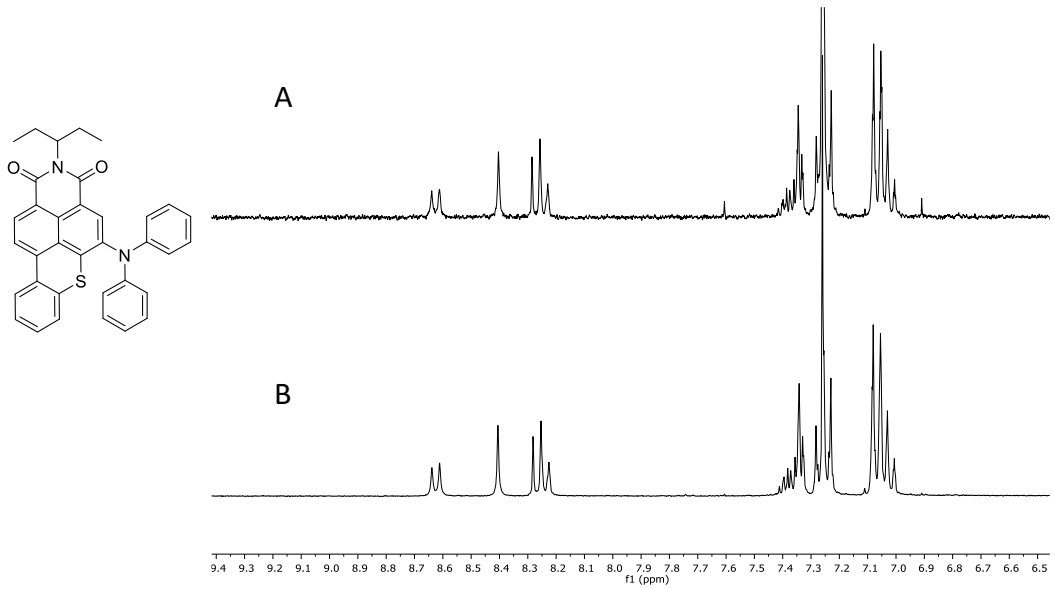

*Figure 4.7. ^{1}H NMR in $CDCl_3$ of **BTXI-NPh$_2$** obtained by approaches A and B.*

Eventually, to unequivocally confirm the right substitution in position 5, single crystals of (B)-**BTXI-NPh$_2$** were successfully grown via slow evaporation of a CH_2Cl_2/petroleum ether mixture (Figure 4.8).

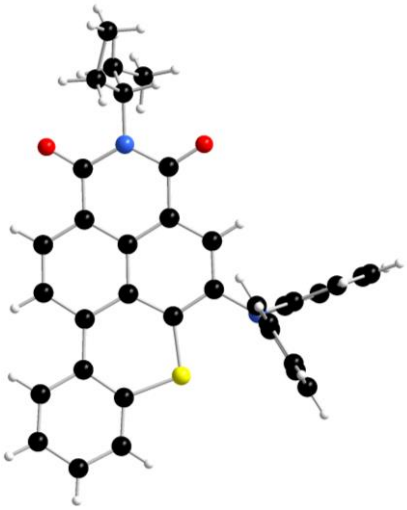

*Figure 4.8. Molecular structure of **BTXI-NPh$_2$** obtained by X-ray diffraction.*

On the contrary, the elucidation was straightforward in the case of **NO_2-BTXI-NO_2**, since single crystals were successful grown via slow evaporation of toluene. X-ray analysis showed that the nitro groups were located in positions 5 and 11 (Figure 4.9).

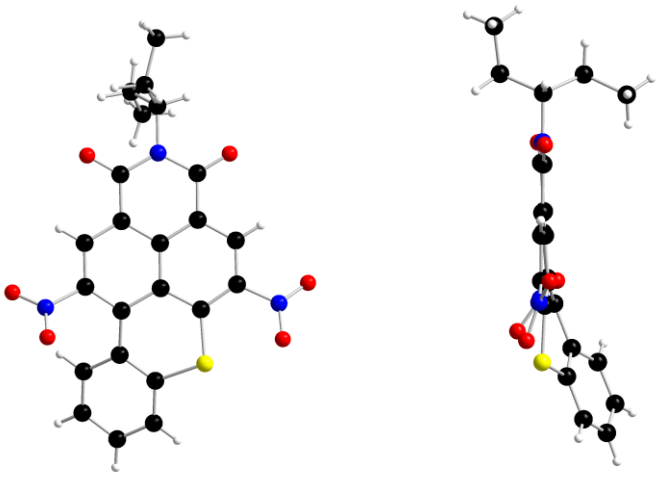

*Figure 4.9. Molecular structure of **NO_2-BTXI-NO_2** obtained by X-ray diffraction.*

As it can be observed, the planar structure of the core is lost due to the higher torsion induced by the functionalization in the bay position 11. Another conformation, in which the phenyl ring is twisted towards the other face of the molecule was also found in the crystal structure. This higher torsion may decrease the strength of the π-stacking thus explaining the higher solubility of **NO_2-BTXI-NO_2** in comparison to the mono-functionalized **BTXI-NO_2** and the bare **BTXI**. This is also the reason why the mono-nitrated product was obtained via precipitation in the presence of **NO_2-BTXI-NO_2**.

4.3 Properties of the *N*-functionalized BTXI derivatives

4.3.1 Electrochemical properties in solution

In order to compare the electronic effect of incorporating D and A moieties to the BTXI core, the electrochemical properties of **BTXI-NO_2**, **BTXI-NH_2** and **BTXI-NPh_2** were studied. The cyclic voltammetry measurements were carried out in CH_2Cl_2 using a 0.10 M Bu_4NPF_6 solution as supporting electrolyte and the experimental conditions detailed in previous chapters (Figure 4.10 and Table 4.1).

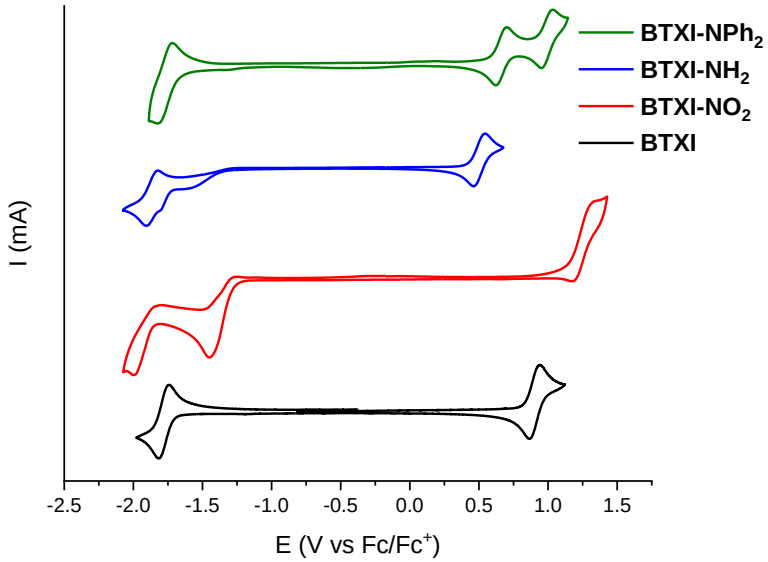

*Figure 4.10. Cyclic voltammograms of **BTXI, BTXI-NO₂, BTXI-NH₂** and **BTXI-NPh₂** (1 mM) in 0.1 M Bu_4NPF_6 in CH_2Cl_2 using a 100 mV/s scan rate. WE (Pt), AE (Pt), RE (SCE).*

The cyclic voltammogram of **BTXI**, used herein as a reference, exhibits two perfectly reversible processes in both positive and negative regions with a gap of 2.53 V. It turns out that the substitution of the core led, in all the cases, to lower electrochemical gaps regardless of the electronic nature of the grafted moiety.

On the one hand, the CV of **BTXI-NO₂** showed a single irreversible oxidation and two irreversible reduction peaks. In addition, the functionalization with this electron-withdrawing group destabilized both the HOMO and LUMO levels ending up in a narrower gap of ca. 2.41 eV. On the other hand, the voltammograms of both amines exhibited reversible oxidation processes and quasi-reversible reduction peaks. The second oxidation wave of **BTXI-NPh₂** could be attributed to the oxidation of the diphenylamine moiety. Besides, while both electron-donating groups led to substantially higher HOMO energies in comparison to **BTXI**, the LUMO levels were not really impacted, thus leading to lower band gaps of 2.23 and 2.09 eV for **BTXI-NPh₂** and **BTXI-NH₂** respectively.

Table 4.1. Electrochemical data of the BTXI derivatives at a concentration of 1 mM. 0.10 M Bu_4NPF_6/CH_2Cl_2, 100 mV/s scan rate. WE (Pt), AE (Pt), RE (SCE).

Molecule	E_{pa}^1 (V_{Fc/Fc^+})	E_{pa}^2 (V_{Fc/Fc^+})	E_{pc}^1 (V_{Fc/Fc^+})	E_{pc}^2 (V_{Fc/Fc^+})	E_{HOMO} (eV)[a]	E_{LUMO} (eV)[b]	ΔE^{elec} (eV)
BTXI	0.94	-	-1.82	-	-5.63	-3.10	2.53
BTXI-NO₂	1.33	-	-1.45	-2.00	-5.93	-3.52	2.41
BTXI-NH₂	0.54	-	-1.91	-	-5.23	-3.14	2.09
BTXI-NPh₂	0.70	1.04	-1.82	-	-5.37	-3.14	2.23

[a] E_{HOMO} (eV) = -(E_{ox}^{onset} + 4.8). [b] E_{LUMO} (eV) = -(E_{red}^{onset} + 4.8).

4.3.2 Optical properties

Considering that i) rylene derivatives are prone to exhibit interesting photophysical properties and ii) that there was not much information related to **BTXI**, the spectroscopic features of the series synthesized above were thus investigated and compared to the previously reported **BTXI** and **BTXI-Br** in collaboration with our partners of the ENS Lyon. In addition to the absorption and emission profiles (Figure 4.11), the fluorescence lifetimes (τ_{obs}) and quantum yields (Φ_f) were determined in dichloromethane solutions (Table 4.2). Eventually, due to the presence of heavy heteroatoms in the molecules (S and in one instance Br) that are expected to increase the spin-orbit coupling (SOC),[23] the potential of these derivatives to generate singlet oxygen (Φ_Δ) based on their triplet excited states was also quantified.

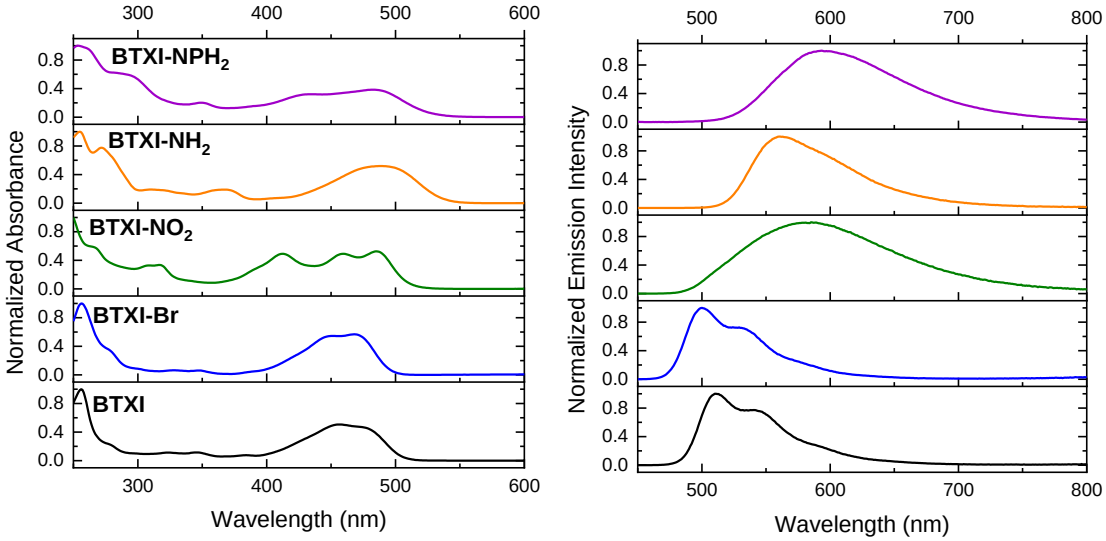

Figure 4.11. Normalized absorption (left) and emission (right) spectra of the BTXI derivatives in CH_2Cl_2 solutions at rt.

Table 4.2. Photophysical data of the BTXI derivatives in CH_2Cl_2 solutions.

Molecule	λ_{abs} (nm)	λ_{em} (nm)	Stokes Shift (cm^{-1})	Φ_f[a]	τ_{obs} (ns)	Φ_Δ[b]	$E_{Triplet}$ (cm^{-1}) [c]
BTXI	455	510	2,370	0.99	7.48	0.00	-
BTXI-Br	469	500	1,322	0.78	6.49	0.11	14,925
BTXI-NO_2	486	585	3,482	0.01	8.14	0.42	15,870
BTXI-NH_2	490	555	2,390	0.67	11.17	0.00	-
BTXI-NPh_2	483	600	4,037	0.33	10.68	0.46	14,600

[a] Measured using coumarine-153 as reference (Φ_f = 0.45 in MeOH); [b] Measured using phenalenone as reference (Φ_f = 0.95 in CH_2Cl_2).[12] [c] Calculated at the first phosphorescence band maximum.

While **BTXI** and its brominated counterpart exhibited structured absorption and emission spectra involving a main transition (at ca. 480 nm) ascribed to a localized π-π* transition of the polyaromatic core, the optical signatures of **BTXI-NH_2**, **BTXI-NPh_2** and **BTXI-NO_2** were more complex and required a deeper analysis to understand their different behavior, starting with a solvatochromic study (Figure 4.12).

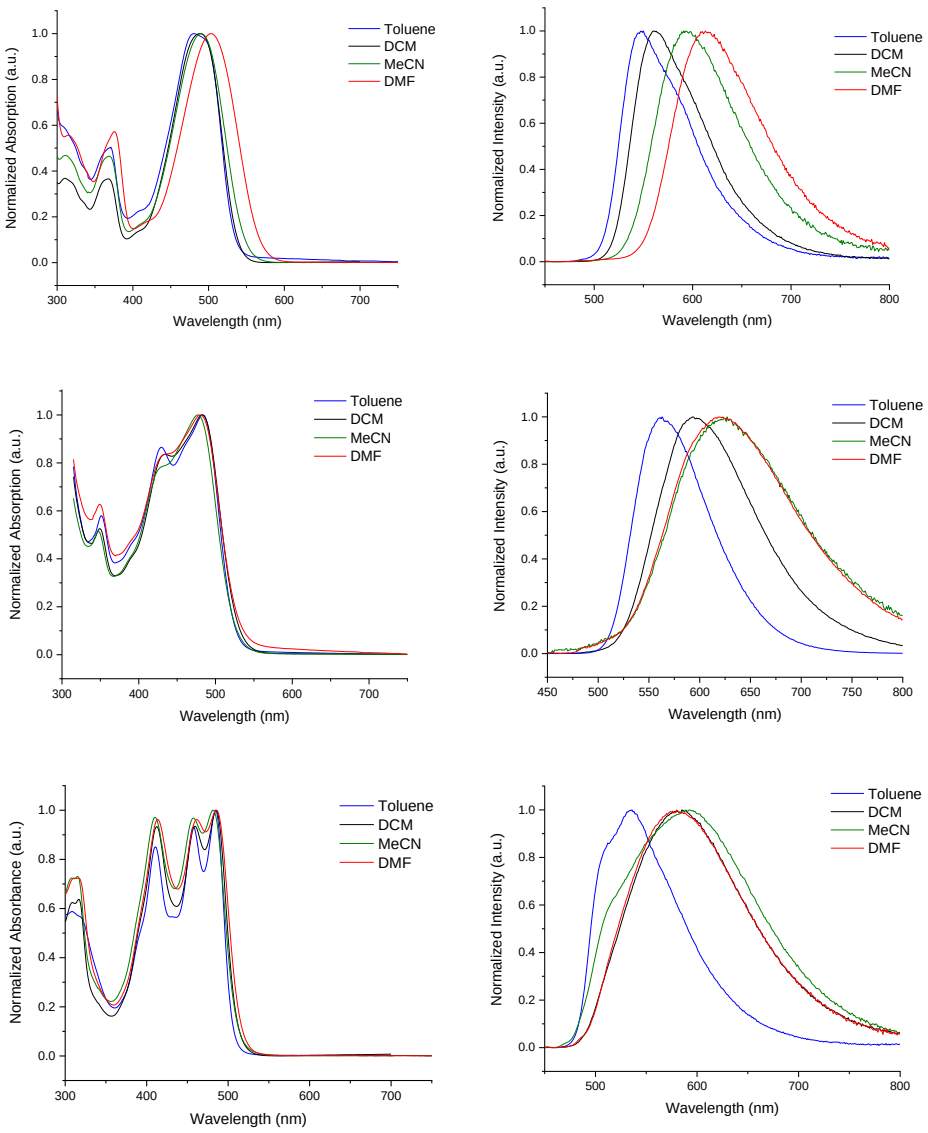

*Figure 4.12. Normalized absorption (left) and emission (right) spectra in toluene, DCM, acetonitrile (MeCN) and DMF of **BTXI-NH$_2$** (top), **BTXI-NPh$_2$** (middle) and **BTXI-NO$_2$** (bottom).*

While no significant solvatochromic behavior was observed for **BTXI**, **BTXI-NH$_2$** did show broad and structureless solvent dependent absorption and emission bands that appeared significantly redshifted when compared to other **BTXI** derivatives. Moreover, a clear linear tendency with positive slope was found when plotting the energy of the Stokes shift against the solvent polarizability following the Lippert-Mataga equation (Figure 4.13). All these features are consistent with an assignment of this band to a charge-transfer (CT) transition, indicative of a push-pull effect between the amine and the naphthalimide. With an even more redshifted emission spectrum, **BTXI-NPh$_2$** also exhibited similar features. This observation can be assigned to a greater reorganization between a more distorted ground state (produced by the steric hindrance of the diphenylamine) and a more planar excited state. According to the natural transition orbitals (NTOs) derived from the TD-DFT calculations, the transitions with significant

oscillator strength are the ones taking place between the amino and naphthalimide moieties, thus confirming the CT-like character.

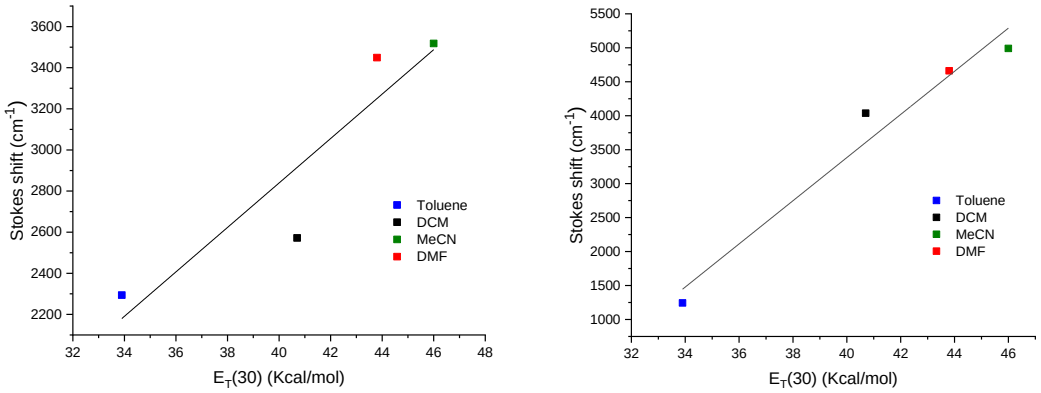

Figure 4.13. Stokes shift versus solvent polarizability following the Lippert-Mataga equation for ***BTXI-NH₂*** *(left) and* ***BTXI-NPh₂*** *(right).*

On the other hand, although **BTXI-NO₂** also exhibited a redshifted, broad and structureless emission band, it did not follow a solvatochromic behavior.

Thereafter, the emission spectra of all the derivatives was recorded at 77 K in a 1:4 MeOH/EtOH mixture (Figure 4.14 and Table 4.2). In the case of **BTXI-NO₂**, an emission band at 650 nm assigned to a triplet-centered phosphorescence was observed. Afterwards, by applying a delay of 0.05 ms, the phosphorescence band could be observed and an energy at zero-phonon transition of 15,870 cm^{-1} was recorded. This long-lived triplet state even at room temperature confirmed both efficient SOC and ISC, which can be the reason for the broader and redshifted pattern.

Contrarily to the reference **BTXI** dye, **BTXI-Br** and **BTXI-NPh₂** also showed phosphorescent behavior. As expected, the presence of a heavy bromine atom induced SOC thus facilitating the spin-forbidden S1-T1 intersystem crossing. However, surprisingly the intensity was lower than in the case of the nitro derivative. Regarding **BTXI-NPh₂**, the distortions of the π-conjugated backbone induced by the phenyl moieties resulted in an improvement of the SOC characterized by a triplet state energy of 14,600 cm^{-1}.

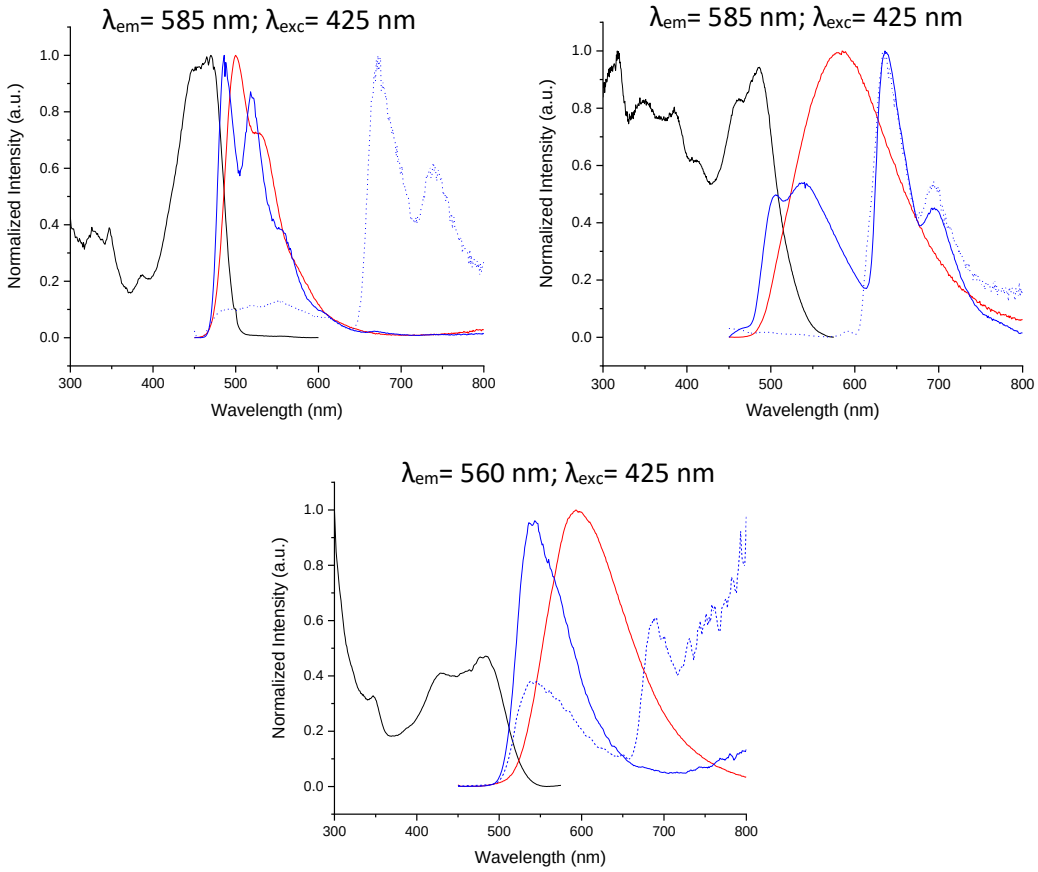

Figure 4.14. Normalized excitation (black trace), emission at rt (red trace) and 77 K in a MeOH:EtOH mixture (1:4) without (blue solid trace) and with a 0.05 ms delay (blue dotted trace) of ***BTXI-Br*** *(top-left),* ***BTXI-NO$_2$*** *(top-right) and* ***BTXI-NPh$_2$*** *(bottom).*

The fluorescence quantum yields were subsequently determined for all the molecules using coumarine-153 as reference. While for **BTXI** almost a quantitative quantum yield was obtained, the addition of the different substituents efficiently quenched the emission (Table 4.2). The CT character observed for **BTXI-NH$_2$** and **BTXI-NPh$_2$** could explain this difference since the lower recorded emission energy can enhance the non-radiative deactivations via vibronic couplings between the ground and excited electronic states (energy gap law). The more efficient ISC, which quenches the emission from the singlet state, seems to be the reason for the lower quantum yields of **BTXI-Br** and **BTXI-NO$_2$**. This fact was further confirmed by their notable Φ_Δ efficiencies, i.e., 0.11 and 0.42 respectively. Although the higher value measured for **BTXI-NO$_2$** seems counterintuitive, this effect in nitro-polyaromatic cores has already been reported.[24-26] This phenomenon can be attributed to a lowest lying emitting $^3\pi$-π^* state as well as to a more energetic ^{3}n-π^* state centered on the nitroaromatic part. The latter state, which is comparatively closer in energy to the $^1\pi$-π^* state and involves a change in the electronic configuration ($^1\pi$-$\pi^* \rightarrow {}^3$n-π^*), can substantially favor the SOC effect.

4.4 Towards new extended BTXI-based rylenes

Once the first series of nitrogen-functionalized molecules was fully characterized, the development of new extended **BTXI** derivatives via Cadogan cyclizations was thereafter considered. Being conscious that the nitration can be performed in a bay position (11), the reactivity of a BTXI functionalized in position 5 was assessed in an attempt to obtain a derivative compatible with the cyclizations. Among others, **BTXI-Br** stood out for two reasons. Firstly, it could enable the reactivity through palladium-catalyzed cross-couplings or be potentially removed afterwards, i.e., being used as a protecting group for position 5. Secondly, the heavy bromine atom could potentially provide interesting optical properties to the final product.

Consequently, the same conditions used for the mono-nitration, i.e., 2 equivalents of fuming nitric acid at room temperature for 20 minutes under air (Scheme 4.5), were used over **BTXI-Br** and turned out to be enough to reach a total conversion of the starting material into a new compound that was easily purified by column chromatography on silica gel.

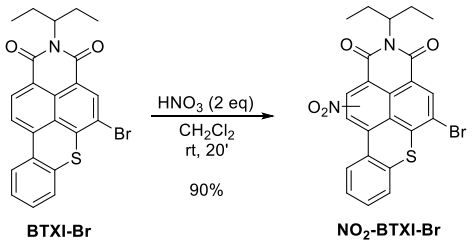

*Scheme 4.5. Nitration conditions used to synthesize **NO_2-BTXI-Br**.*

The position of the nitro group was then confirmed by X-ray diffraction analyses (Figure 4.15) after a successful crystal growth via slow evaporation of toluene. As expected, the substituted position (11) was the same as for **NO_2-BTXI-NO_2**.

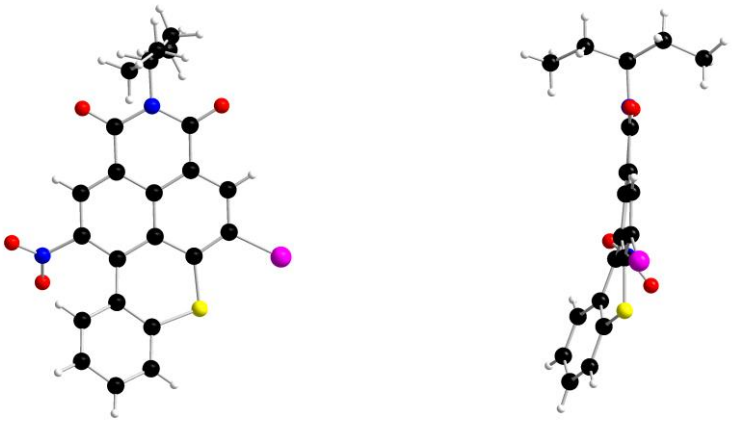

*Figure 4.15. Molecular structure of **NO_2-BTXI-Br** obtained by X-ray diffraction.*

Then, the new **NO_2-BTXI-Br** was used as the starting material in several Cadogan-type reactions already reported for the cyclization of the nitrated PDI (Scheme 4.6).[17, 20-21]

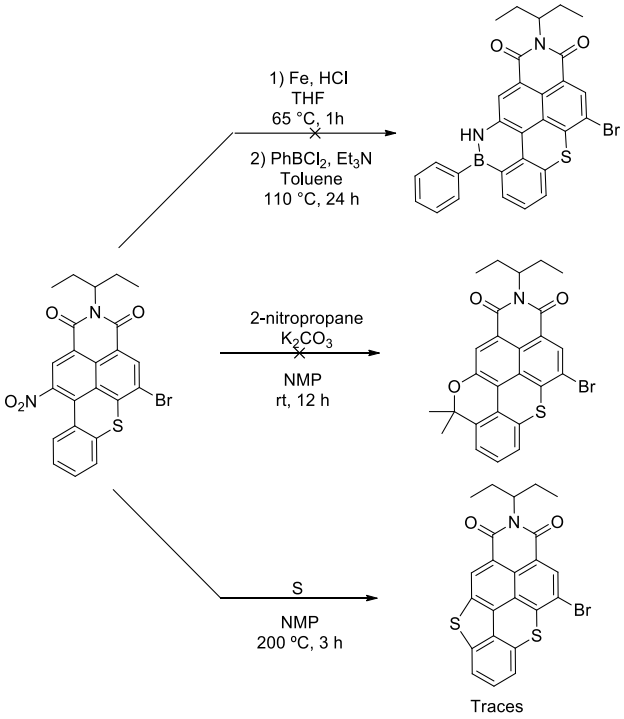

*Scheme 4.6. Unsuccessful cyclization tests on **NO_2-BTXI-Br**.*

As illustrated, the described conditions for the incorporation of azaborine- and pyran-based moieties were completely unsuccessful. On the other hand, even if properly crystallized via slow evaporation of chloroform and therefore structurally confirmed, the S-cyclization only led to traces of the desired product (Figure 4.16).

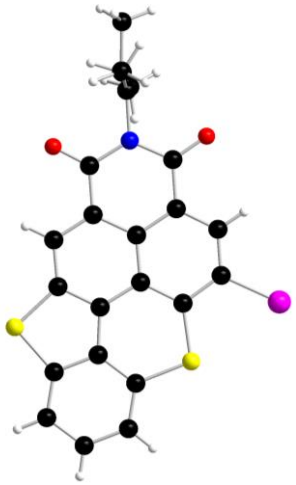

*Figure 4.16. Molecular structure of the brominated S-annulated **BTXI** obtained by X-ray diffraction.*

These poor yields highlight the tremendous difference in reactivity between **BTXI** and **PDI**. At this point, the fact that the bromine atom could be detrimental for the reactivity was considered. However, even though position 5 was also protected with an alkyl side chain, the outcome of the reactions turned out to be the same.

In a further attempt to perform a cyclization, the procedure used for the synthesis of the *N*-annulated PDI was subsequently adapted for **NO_2-BTXI-Br** (Scheme 4.7).[19] Interestingly, the latter successfully reacted with PPh_3 in DMF thus affording carbazole **13** in a good yield. Then, the alkylation was performed with 1-bromohexane and potassium carbonate in DMF. Note that the resulting **TCCI-Br** was already set to be used in palladium-catalyzed cross-couplings for the synthesis of different materials. However, for comparative purposes, the bromine atom was removed by means of a catalytic reaction with a NHC palladium complex in isopropyl alcohol in the presence of sodium *tert*-butoxide to afford the unreported 1*H*-thiochromeno[5,4,3,2-*cdef*]carbazole imide (**TCCI**).[27]

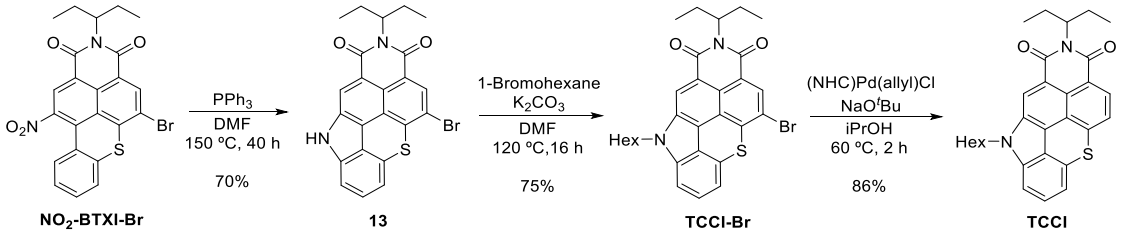

*Scheme 4.7. Synthetic pathway towards **TCCI**.*

Once the first block was synthesized, larger conjugated structures were thereafter considered. To do so, the first step was to design a synthetic route for the functionalization of the outer phenyl ring which was, up to that moment, unexplored and consequently unreported. Considering that the functionalization of the precursor 2-aminobenzenethiol is tedious and the commercial availability of such analogues is scarce, the synthesis of different amine-thiol derivatives was investigated. It turns out that the latter can be easily obtained from their benzothiazole counterparts once engaged under simple basic conditions in ethylene glycol.[28] To test this strategy, 2-methylnaphtho[1,2-*d*]thiazole was used as the starting material and its thiazole ring was successfully opened according to a reported procedure (Scheme 4.8).[29] Eventually, the synthesis of the new dibenzo[*a*,*kl*]thioxanthene imide (**DBTXI**), was carried out using the same procedure as for **BTXI** but using the resulting 1-aminonaphthalene-2-thiol instead of 2-aminobenzenethiol.

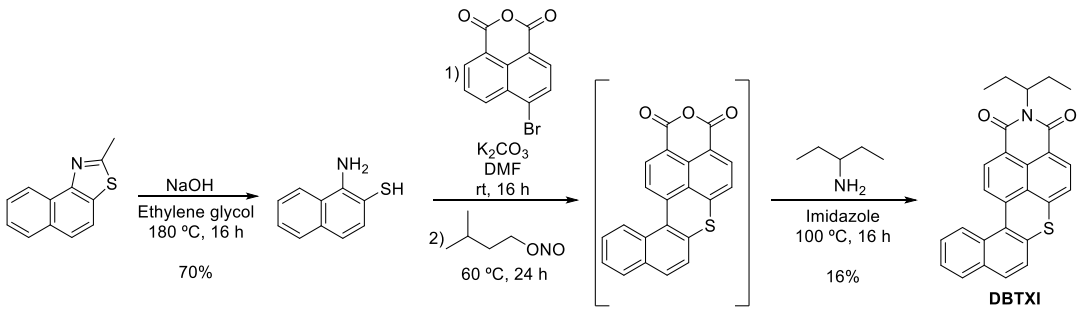

*Scheme 4.8. Synthetic pathway towards **DBTXI**.*

It is noteworthy that the anhydride was not isolated due to the lack of solubility that hindered its purification and characterization. However, once alkylated, the resulting compound was easily purified and isolated. Then, the reactivity of this new derivative was investigated using the methodology previously described for **BTXI** (Scheme 4.9).

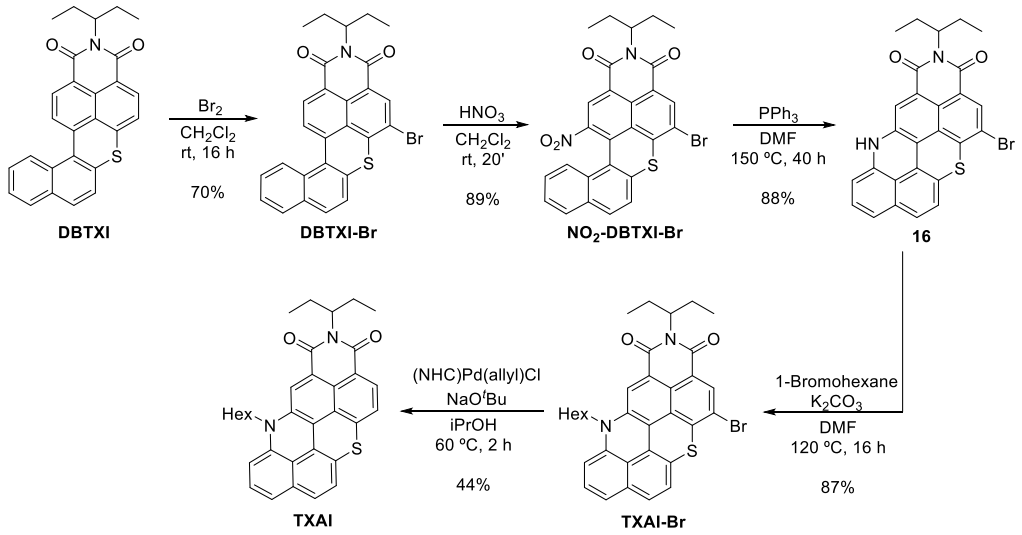

*Scheme 4.9. Synthetic pathway towards **TXAI**.*

Interestingly, **DBTXI** was also mono-brominated in position 5 using similar conditions than those used for **BTXI** (molecular structure in Figure 4.17). Then, 2 equivalents of fuming nitric acid were added to a solution of **DBTXI-Br** in CH_2Cl_2 at room temperature under air and the mono-nitrated compound **NO_2-DBTXI-Br**, whose structure was confirmed by X-ray analyses (Figure 4.17), was isolated in a high yield.

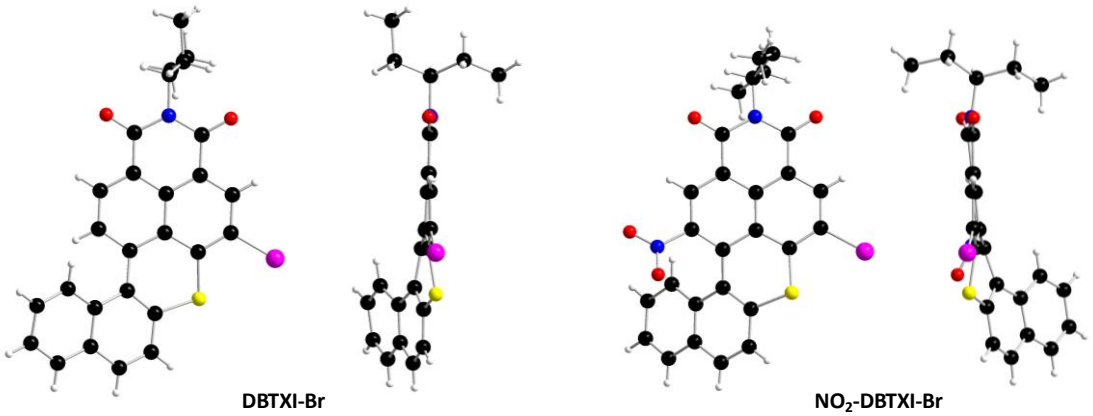

*Figure 4.17. Molecular structures of **DBTXI-Br** (left) and **NO$_2$-DBTXI-Br** (right) obtained by X-ray diffraction.*

As the nitro group was placed once again in a bay position, **NO$_2$-DBTXI-Br** was then subjected to similar *N*-annulation conditions thus affording an unknonw new product. As in the case of **TCCI**, the new carbazole was alkylated with 1-bromohexane and the protecting bromine atom removed. Luckily, crystals of the isolated blue molecule were successfully grown revealing and confirming the structure of the expected 12*H*-thioxantheno[2,1,9,8-*klmna*]acridine imide (**TXAI**) (see X-ray crystallography and theoretical calculations section).

4.4.1 Optical and electrochemical properties

The optical properties of the three new blocks were evaluated both in solution and as spun-casted films and compared to the ones of **BTXI** (Figures 4.18-4.19 and Table 4.3).

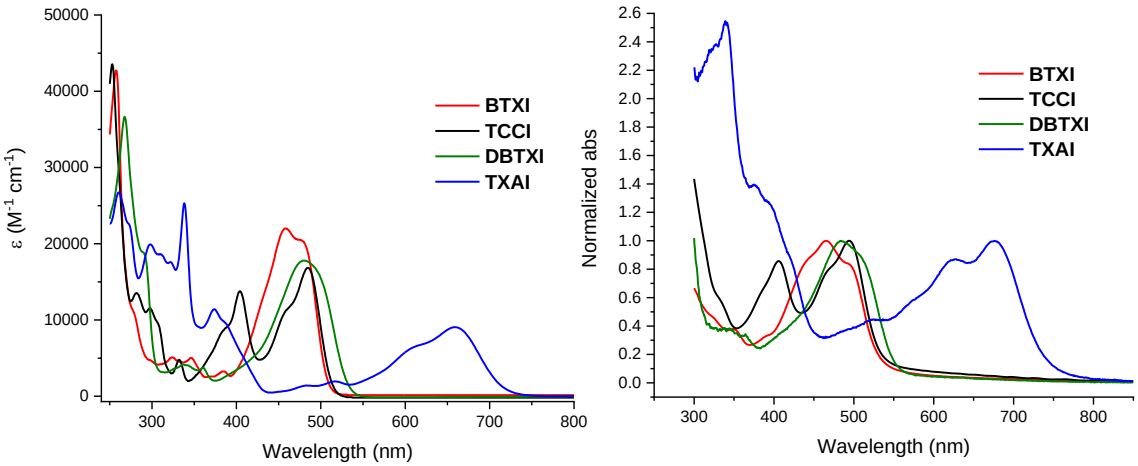

*Figure 4.18. UV-Vis spectra of **BTXI**, **TCCI**, **DBTXI** and **TXAI** in CH_2Cl_2 solutions (left) and as spun-casted films (right).*

Regarding the UV-Vis absorption spectra, it is noteworthy that the absorption ranges of **BTXI**, **DBTXI** and **TCCI** (ca. 350-500 nm) and their ε (ca. 15000-20000 M^{-1} cm^{-1}) were very similar. However, and contrarily to **BTXI** and **DBTXI**, the *N*-annulated **TCCI** exhibited two main bands

resulting in a broader absorption. On the other hand, with a similar pattern in comparison to **BTXI**, the main band of **TXAI** became considerably broader and redshifted, but presented a lower epsilon. In that way, the extended structure of **TXAI** enabled for the first time the absorption beyond 550 nm, even reaching the NIR, only with a BTXI-based block.

Their spectra in solid state followed the same trend although they were redshifted in comparison to those in solution.

*Table 4.3. Optical properties of **BTXI**, **TCCI**, **DBTXI** and **TXAI** in CH_2Cl_2 solutions and as spun-casted films.*

Molecule	$\lambda_{abs\ sol}$ (nm)	ε (M^{-1} cm^{-1})	$\lambda_{abs\ film}$ (nm)	λ_{em} (nm)	Φ_f[a]	τ_{obs} (ns)	Φ_Δ[b]	$E_{Triplet}$ (cm^{-1})[c]
BTXI	477 458 257	20000 22000 42500	493 465	541 511	0.99	7.48	0.00	-
TCCI	485 404 332 253	17000 14000 5000 44000	494 406	520	0.80	9.61	0.14	-
DBTXI	480 268	18000 37000	483	574 542	0.08	<1[d]	1.00	14,250
TXAI	659 374 338 260	9000 11000 25000 27000	676 628 339	733	0.05	2.88	0.00	-

[a] Measured using coumarin-153 as reference (Φ_f = 0.45 in methanol). [b] Measured using phenalenone as reference (Φ_f = 0.95 in dichloromethane). [c] Calculated at the first phosphorescence band maximum. [d] Lifetime below the limit measured using a nanoLED-390 nm.

Then, the emission properties of the four blocks were investigated. First, **TCCI** exhibited a comparable emission to the one of **BTXI** despite its lower Φ_f, which was countered with an improvement in the singlet oxygen generation properties (Φ_Δ = 0.14). However, the extension of the conjugation in **DBTXI** resulted in a significant drop in the fluorescence quantum yield and a slight redshift. Since a high distortion was found for its molecular structure (see X-ray crystallography and theoretical calculations section), this favored, as previously demonstrated for other BTXI derivatives, triplet instead of singlet emission as an outstanding Φ_Δ of 1 was recorded. Eventually, according to its absorption properties, the emission of **TXAI** was found in the NIR but its Φ_f and Φ_Δ were almost negligible.

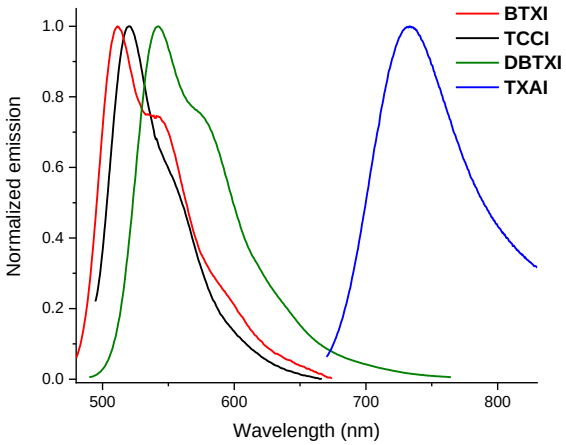

*Figure 4.19. Normalized emission spectra of **BTXI**, **TCCI**, **DBTXI** and **TXAI** in CH_2Cl_2 solutions.*

In order to compare the electrochemical properties of the three new blocks to those of **BTXI**, cyclic voltammograms at a concentration of 10^{-3} M were recorded in a glovebox using a 0.1 M Bu_4NPF_6 solution in CH_2Cl_2 as the supporting electrolyte, a glassy carbon electrode and a 100 mV/s scan rate (Figure 4.20).

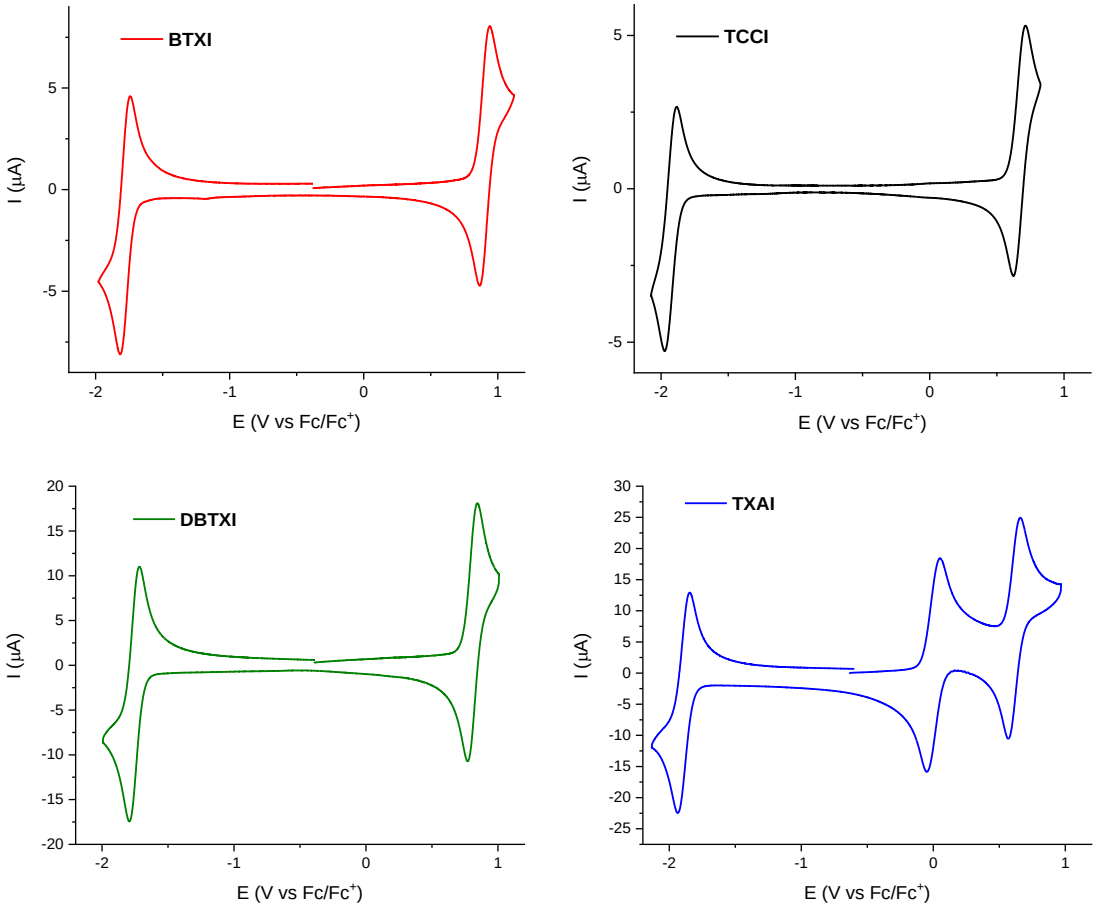

*Figure 4.20. Cyclic voltammograms of **BTXI**, **TCCI**, **DBTXI** and **TXAI** (1 mM) in 0.1 M Bu_4NPF_6 in CH_2Cl_2 using a 100 mV/s scan rate and a glassy carbon electrode (WE).*

On the one hand, both **TCCI** and **DBTXI** exhibited similar voltammograms to that of **BTXI** with perfectly reversible single oxidation and reduction peaks (Figure 4.20 and Table 4.4). Nonetheless, although the profiles of **BTXI** and **DBTXI** were almost superimposable, a ca. 0.2 V shift towards negative potentials was monitored for **TCCI**. On the other hand, although a similar effect was observed for **TXAI**, it surprisingly exhibited two reversible oxidation peaks and just one reversible reduction thus leading to a substantially shorter ΔE^{elec}.

The frontier orbital energy levels of the four blocks (Table 4.4) were investigated both in solution, by means of CV (Figure 4.20), and as spun-casted films, by means of PESA (Figure 4.21) and UV-Vis spectroscopy (Figure 4.18).

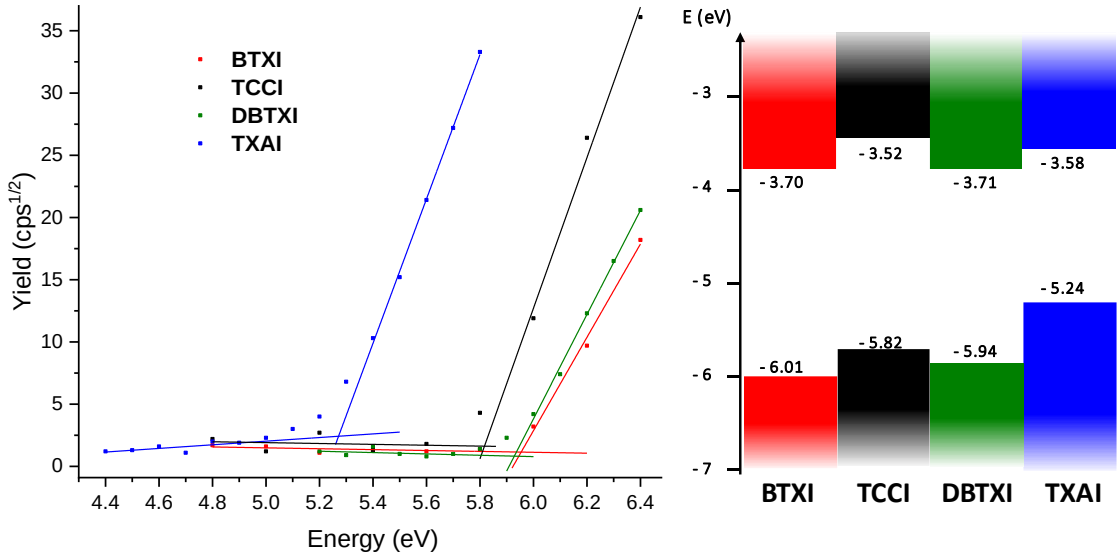

*Figure 4.21. PESA spectra (left) and energy levels (right) of **BTXI**, **TCCI**, **DBTXI** and **TXAI** as spun-casted films.*

The same trend was observed for both states although the obtained gaps in solid state were slightly narrower. In comparison to **BTXI**, the insertion of an extra phenyl ring in **DBTXI** did not have a real effect on the recorded HOMO and LUMO energy levels. On the contrary, their respective *N*-annulated counterparts exhibited both higher HOMO and LUMO energies. However, while in the case of **TCCI** this just led to slightly higher levels without affecting the band gap, the substantial increase in the HOMO level of **TXAI** led to a much narrower band gap, in agreement with the optical characteristics of this new molecule.

*Table 4.4. Electrochemical properties obtained by CV using a glassy carbon electrode (buffer: 0.1 M Bu_4NPF_6 in CH_2Cl_2) and estimated energy levels in CH_2Cl_2 solutions and as spun-casted films of **BTXI**, **TCCI**, **DBTXI** and **TXAI**.*

Molecule	E_{pa}^1 (V_{Fc/Fc^+})	E_{pa}^2 (V_{Fc/Fc^+})	E_{pc} (V_{Fc/Fc^+})	E_{HOMO} (eV)[a]	E_{LUMO} (eV)[b]	ΔE^{elec} (eV)[c]	HOMO (eV)[d]	E_g^{opt} (eV)[e]	LUMO (eV)[f]
BTXI	0.94	-	-1.82	-5.63	-3.10	2.53	-6.01	2.31	3.70
TCCI	0.71	-	-1.97	-5.39	-2.94	2.45	-5.82	2.30	-3.52
DBTXI	0.84	-	-1.79	-5.53	-3.12	2.41	-5.94	2.23	-3.71
TXAI	0.05	0.66	-1.93	-4.71	-2.99	1.72	-5.24	1.66	-3.58

[a] E_{HOMO} (eV) = -(E_{ox}^{onset} + 4.8). [b] E_{LUMO} (eV) = -(E_{red}^{onset} + 4.8). [c] Obtained through the equation: $\Delta E^{elec} = E_{LUMO} - E_{HOMO}$. [d] HOMO energy in solid state determined by PESA. [e] Optical gap estimated through the low-energy absorption onset. [f] Obtained through the equation: LUMO = HOMO + E_g^{opt}.

4.4.2 X-ray crystallography and theoretical calculations

As a further step into a better understanding of the obtained properties, X-ray data were gathered and analyzed. It is important to highlight at this point that although many of the intermediate compounds were crystallized with ease, it was way more challenging in the case of the final materials, particularly for the *N*-annulated blocks. First, single crystals of **DBTXI** were obtained via slow evaporation of chloroform. Then, whereas single crystals of **TXAI** were obtained via vapor diffusion using CH_2Cl_2 and heptane as solvents, attempts to crystalize **TCCI** with such long alkyl chain systematically failed. Thus, its methyl derivative **15** was synthesized under similar conditions to solve this issue (Scheme 4.10).

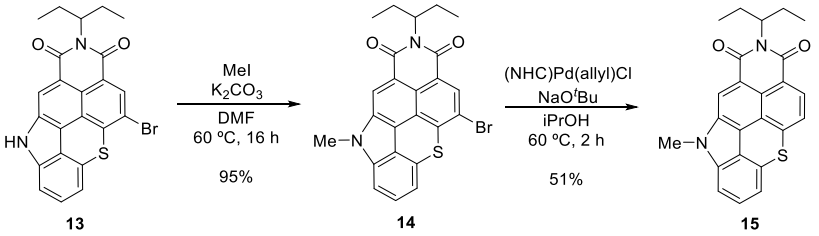

*Scheme 4.10. Synthetic pathway towards the methylated **TCCI** (molecule **15**).*

Luckily, single crystals of this methylated **TCCI** were successfully grown via vapor diffusion using CH_2Cl_2 and pentane as solvents. The X-ray structures of the four blocks are gathered in Figure 4.22.

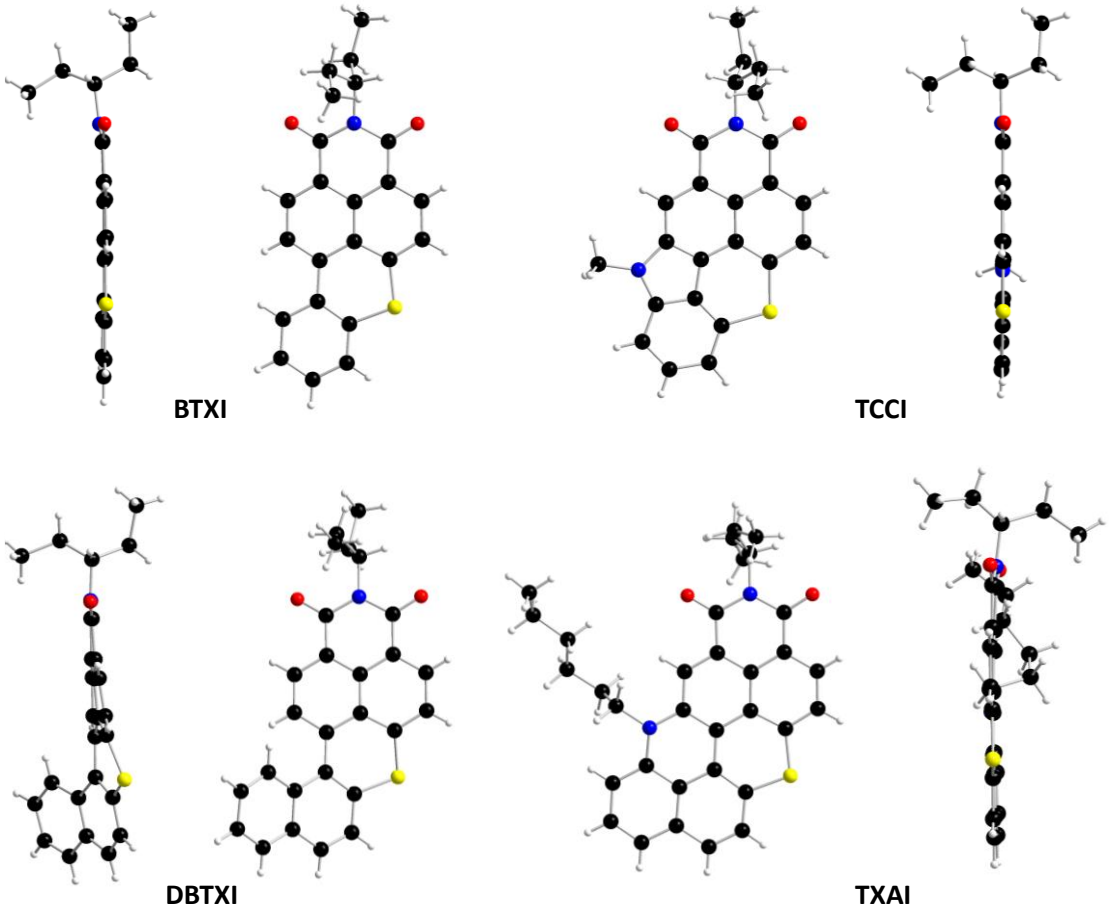

*Figure 4.22. Molecular structures of **BTXI**, **DBTXI**, the methylated **TCCI** and **TXAI** obtained by X-ray diffraction.*

In parallel, the obtained X-ray structures were compared to the optimized geometries calculated at the DFT/ωB97-XD/6-31G(d,p) level of theory. The molecules of solvent (dichloromethane) were treated as a polarizable continuum (PCM). Moreover, to reduce the computational cost, geometries were optimized with methyl groups instead of ethylpropyl and hexyl alkyl chains. Hence, the most highlightable parameters of the experimental and computational molecular structures (**a**, **b** and **θ**) are gathered in Table 4.5, where it can be observed that the calculations were extremely accurate for the four molecules.

*Table 4.5. Most highlightable parameters of the experimental and computational molecular structures of **BTXI**, **TCCI**, **DBTXI** and **TXAI**.*

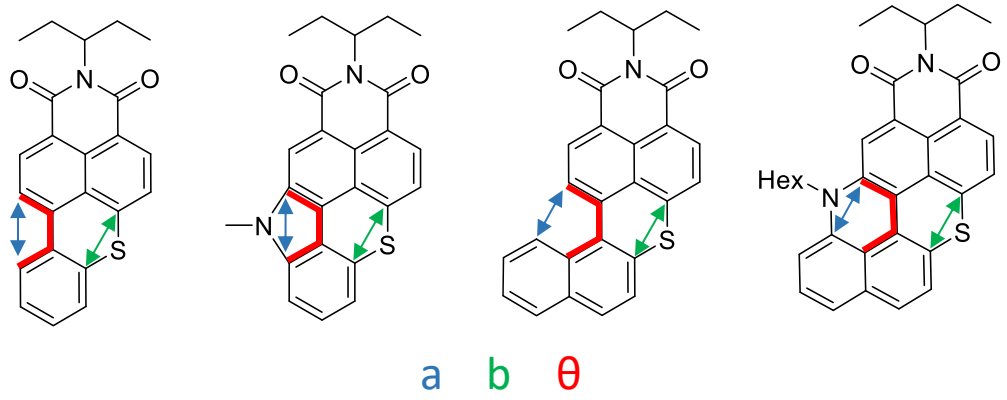

Molecule	a (Å)		b (Å)		θ (°)	
	Exp.	Comp.	Exp.	Comp.	Exp.	Comp.
BTXI	2.88	2.88	2.74	2.74	2	2
TCCI	2.27	2.27	2.83	2.85	1	0
DBTXI	2.98	2.97	2.75	2.75	28	28
TXAI	2.44	2.43	2.74	2.76	1 (4)*	5

*Two different conformations were obtained in the crystal mainly differing in their θ angle.

As depicted, parameter **a** stands for the distance between the carbon atoms directly involved in the carbazole formation, **b** is the distance between the carbon atoms adjacent to the sulfur atom and **θ** is the dihedral induced by the four carbons forming the bay area of **BTXI**. The latter denotes the angle between the naphthalimide and the phenyl/naphthyl below, and thus the degree of torsion of the molecule.

The molecular structure obtained for **TCCI** showed a highly planar conformation as for **BTXI** with even a lower **θ** (Figure 4.22). However, in order to allow the formation of the five-membered ring of **TCCI**, a substantial reorganization of the phenyl ring away from the imide group is produced. Thus, distance **a** becomes substantially lower (from 2.88 to 2.27 Å), thus impacting distance **b**, which is significantly increased, resulting in a lower charge transfer interaction between the sulfur atom and the rest of the block. This effect was not observed in the other derivatives. In the case of **DBTXI**, the conformation dramatically changes due to the steric hindrance induced by its extra phenyl ring resulting in a recorded dihedral angle **θ** of 28°, which is the highest torsion angle experimentally obtained for any BTXI derivative. The sulfur atom is forced to stay out of both naphthyl planes thus allowing the helically-shaped conformation. Eventually and in stark contrast to **DBTXI**, in order to allow the formation of the six-membered ring, **TXAI** becomes planar again with just an experimental dihedral angle of 1° and a much lower distance **a** (from 2.98 to 2.44 Å).

The crystallographic arrangements of the four blocks, i.e., **BTXI** and **TXAI** (orthorhombic), **TCCI** (monoclinic) and **DBTXI** (triclinic), showed a clear π-π stacking between the molecules. In addition, in the stacking arrangements found for all of them (Figure 4.23), i.e., head-to-tail (**BTXI** and **DBTXI**), head-to-head (**TCCI**) and rotated (**TXAI**), no short S-S intermolecular distances below the sum of the van der Waals radii of two sulfur atoms (< 3.60 Å) were observed, suggesting the absence of intermolecular S-S interactions.

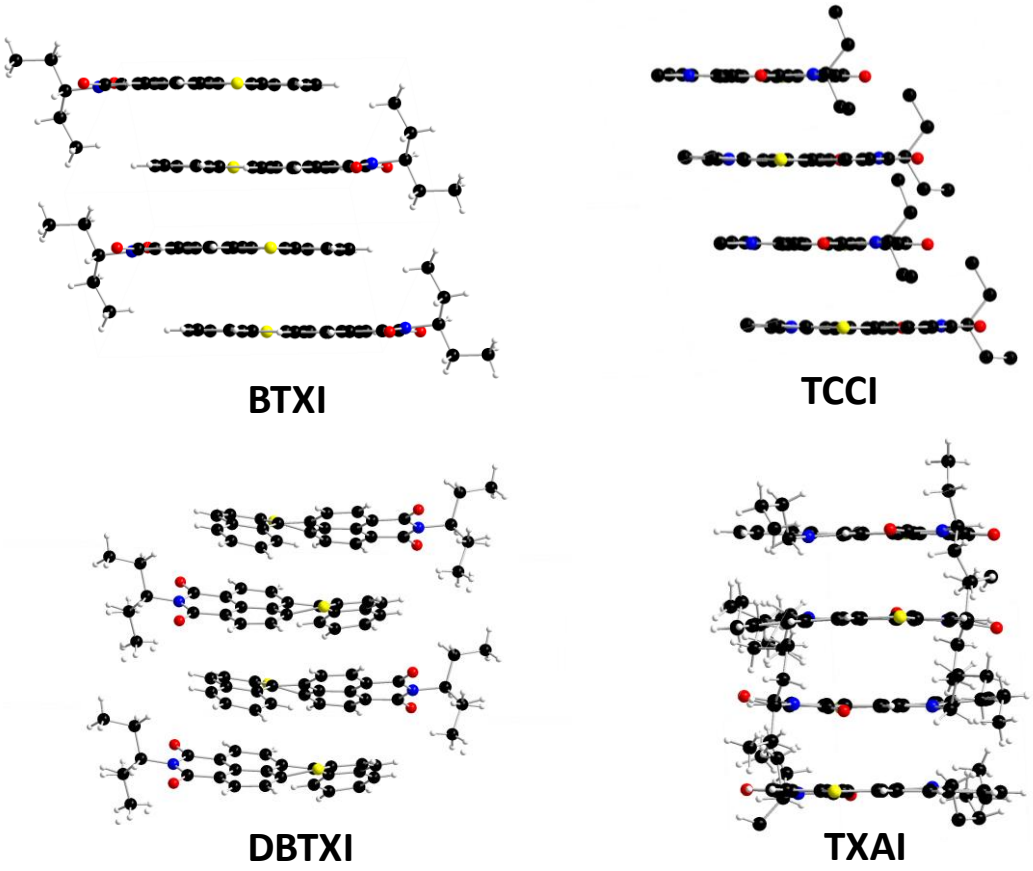

*Figure 4.23. Stacking arrangements found for **BTXI**, **DBTXI**, the methylated **TCCI** and **TXAI** by X-ray diffraction.*

In addition, the electron density and energy levels of the frontier orbitals of the four blocks were also calculated at the DFT/OT-ωB97-XD/6-31G(d,p) level of theory (Figure 4.24).

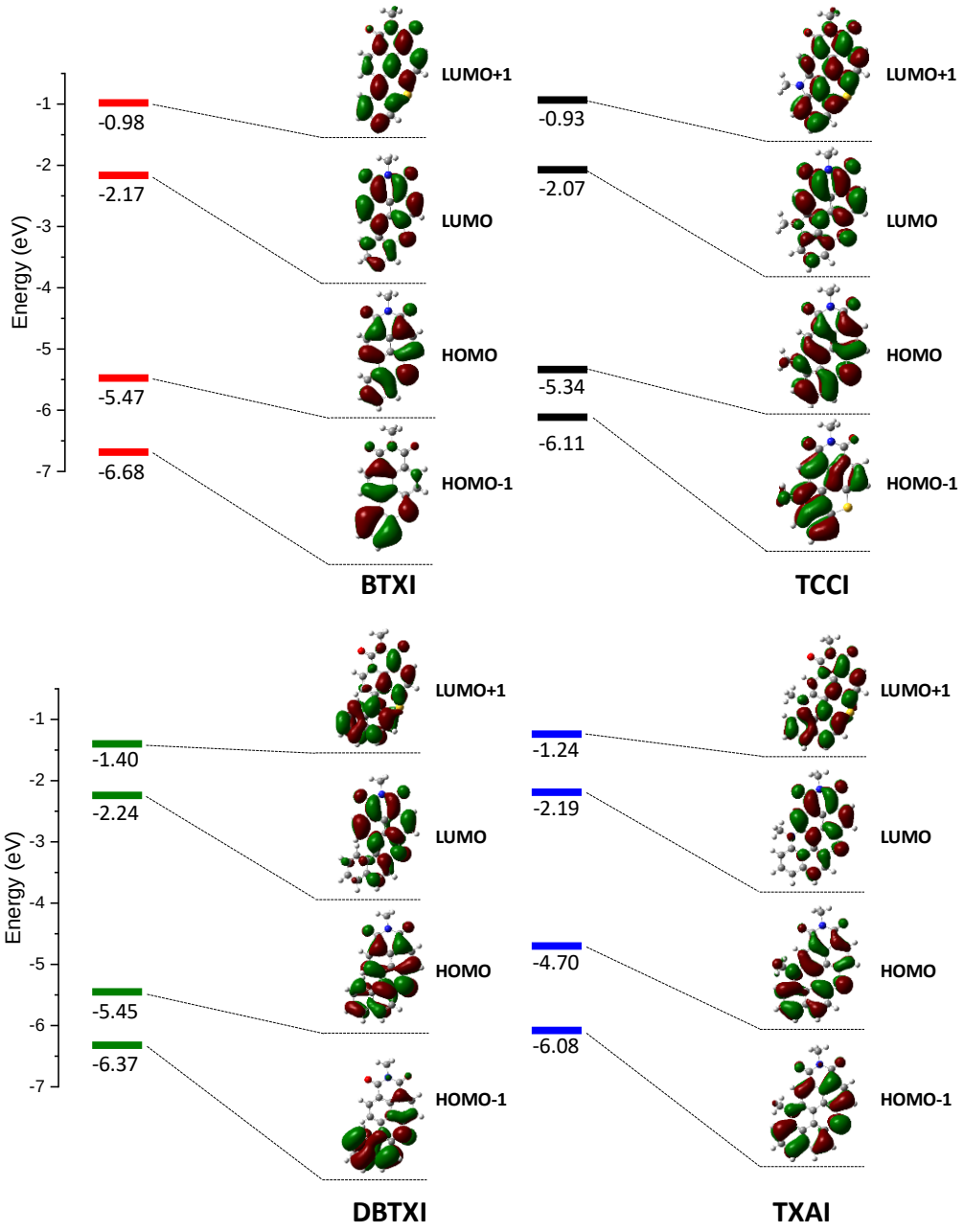

*Figure 4.24. HOMO-1, HOMO, LUMO and LUMO+1 electron density and energy levels of **BTXI**, **TCCI**, **DBTXI** and **TXAI** after optimization with Gaussian 09 at the DFT/OT-ωB97-XD/6-31G(d,p) level of theory.*

These calculations highlight that whereas the HOMO densities are regularly distributed along the whole conjugated backbone, the electronic density tends to migrate towards the imide group in the LUMOs. This behavior is in agreement with the relatively close values of LUMO energies experimentally estimated in both solution and solid state. The case of **TXAI** is the most extreme in comparison to **BTXI**, as it presents the highest HOMO by far due to its extended conjugated structure, but its LUMO energy is close to the one of **BTXI** as both electronic distributions are almost identical. It is also noticeable that even though **BTXI** and **DBTXI** may not

look that electronically different in view of their electrochemical properties, the extra phenyl ring in **DBTXI** strongly affects the electron distribution especially in the HOMO-1 and LUMO+1 levels.

In parallel, TD-DFT simulated spectra (Figure 4.25) were investigated and turned out to match quite accurately the experimental UV-Vis absorption curves. First, the main band, placed at high wavelengths in the four cases, is ascribable to HOMO→LUMO transitions. Moreover, and according to the calculations, they all present a contribution between 330 and 380 nm resulting from a HOMO-1→LUMO transition, but it is only favored in the case of **TCCI**, thus explaining its experimental absorption spectrum. It is noteworthy that this effect was not observed in the case of **PDI** after its *N*-annulation in the bay area.[19]

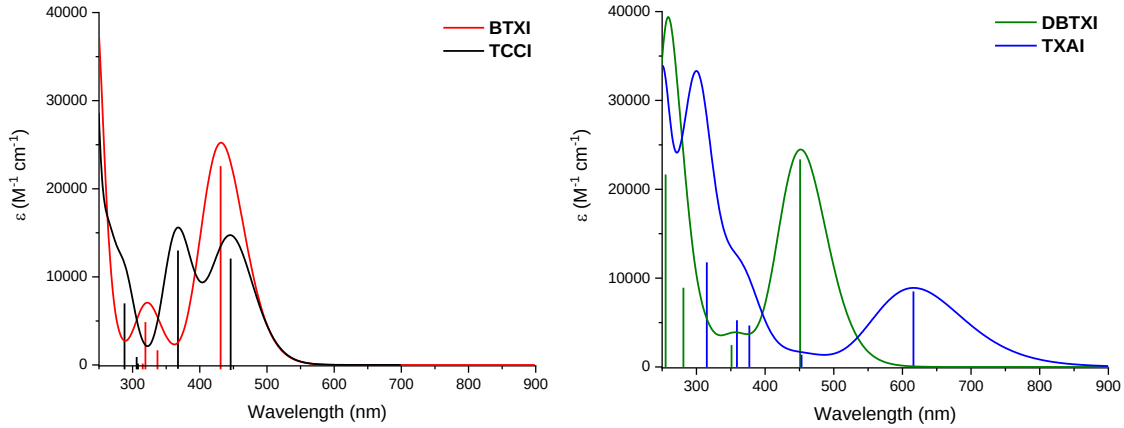

*Figure 4.25. TD-DFT simulated spectra of **BTXI** and **TCCI** (left), **DBTXI** and **TXAI** (right).*

4.5 Conclusions and perspectives

Forgotten by the community, the potential of **BTXI** for its application in organic electronics has been recently pointed out. In addition to the previously reported mono-bromination, its mono-nitration has been carried out. After the structural elucidation, the photophysical properties of the new functionalized cores have been investigated. While **BTXI** presents a high emission efficiency associated with a localized electronic transition, the introduction of D or A substituents on the naphthalene ring strongly modifies, as expected, the spectroscopic signatures. In addition, it was demonstrated that large SOC, and thus efficient singlet oxygen generation can also be efficiently achieved upon the choice of the substituents that can lead to a ground state distortion of the π-conjugated backbone. For instance, **BTXI-NPh$_2$** efficiently combined both marked CT character (redshifted luminescence with a relevant emission quantum yield) and a large singlet oxygen generation efficiency, thus becoming a potential candidate for biophotonics and theranostics applications.

Then, the nitration of the bay area was investigated in an attempt to extend the π-conjugated backbone of the dye. To do so, the most active position was first protected with a bromine atom before being engaged in a Cadogan cyclization to afford the **TCCI** derivative. In parallel, this methodology was adapted for the new **DBTXI**, whose extra phenyl ring allowed the formation of a six-membered nitrogen-containing ring resulting in the blue molecule **TXAI**. Hence, this strategy led to new blocks with diverse optical and electrochemical features allowing to take advantage of a new range of wavelengths that was previously inaccessible for BTXI-based materials.

In view of these exciting results, several ongoing projects are considered. First, with the brominated derivatives of all the new rylenes in hands, more complex materials can be easily synthesized by means of palladium-catalyzed cross-coupling reactions. Both **TCCI** and **TXAI** could also be functionalized at their carbazole positions for grafting or solubility purposes.

Finally, the properties of **BTXI** have been recently modified through two different ongoing strategies. The first one, which cannot be used in the case of other rylenes, is the direct oxidation of the sulfur atom with MPCBA to obtain its sulfone derivative **BTXI-SO_2** (Figure 4.26). This mild reaction can also be performed over most of the functionalized BTXI derivatives in high yields thus becoming an effective post-functionalizing strategy. It was found to impact the electronic character of the sulfur atom and to induce a loss of planarity, leading to considerable differences in the optical and electrochemical properties, such as blueshifted absorption and substantially lower HOMO and LUMO energies. Eventually, the oxidation of the sulfur atom also drives triplet formation unveiling the great potential of BTXI-based materials as singlet oxygen photosensitizers. This approach, combined with the halogenation of the block, recently led to BTXI derivatives with Φ_Δ= 1.[30] This photoinduced triplet state generation could pave the way for the application of these materials in many topics ranging from molecular electronics to biomedicals.

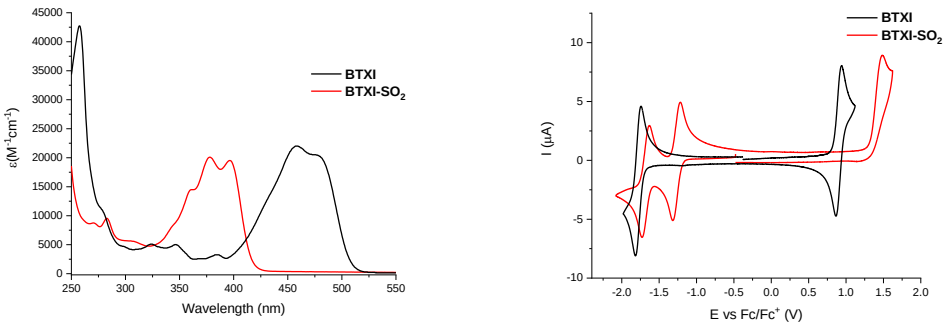

*Figure 4.26. UV-Vis spectra (left) and cyclic voltammograms in CH_2Cl_2 (right) of **BTXI** and **BTXI-SO_2**.*

The second strategy is the dimerization of the blocks. It is a well-known strategy for the synthesis of materials based on other rylenes such as **PDI**, as dimers usually exhibit better transport properties in the solid state than the monomers. Recently synthesized, the dimer illustrated in Scheme 4.11 was embedded, as a proof of concept, in solution-processed OLEDs with promising results.

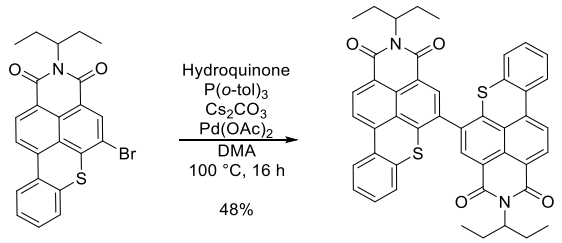

Scheme 4.11. Synthetic approach for the dimerization of BTXI-based derivatives.

References

[1] Schmidt, R., Oh, J. H., Sun, Y.-S., Deppisch, M., Krause, A.-M., Radacki, K., Braunschweig, H., Könemann, M., Erk, P., Bao, Z. and Würthner, F., *Journal of the American Chemical Society* **2009**, *131*, 6215-6228.
[2] Zhan, X., Facchetti, A., Barlow, S., Marks, T. J., Ratner, M. A., Wasielewski, M. R. and Marder, S. R., *Advanced Materials* **2011**, *23*, 268-284.
[3] Kuznetsova, L. I., Piryazev, A. A., Anokhin, D. V., Mumyatov, A. V., Susarova, D. K., Ivanov, D. A. and Troshin, P. A., *Organic Electronics* **2018**, *58*, 257-262.
[4] Zhang, K., Lv, L., Wang, X., Mi, Y., Chai, R., Liu, X., Shen, G., Peng, A. and Huang, H., *ACS Applied Materials & Interfaces* **2018**, *10*, 1917-1924.
[5] Grayshan, P. H., Kadhim, A. M. and Perters, A. T., *Journal of Heterocyclic Chemistry* **1974**, *11*, 33-38.
[6] Kadhim, A. M. and Peters, A. T., *Tetrahedron* **1974**, *30*, 2245-2249.
[7] Danko, M., Chmela, Š. and Hrdlovič, P., *Polymer Degradation and Stability* **2006**, *91*, 1045-1051.
[8] Ilčíková, M., Danko, M., Doroshenko, M., Best, A., Mrlík, M., Csomorová, K., Šlouf, M., Chorvát, D., Koynov, K. and Mosnáček, J., *European Polymer Journal* **2016**, *79*, 187-197.
[9] Li, Z.-Z., Niu, C.-G., Zeng, G.-M., Liu, Y.-G., Gao, P.-F., Huang, G.-H. and Mao, Y.-A., *Sensors and Actuators B: Chemical* **2006**, *114*, 308-315.
[10] Zhang, W., Chen, M., Ling Wu, Y., Tanaka, Y., Juan Ji, Y., Lin Zhang, S., He Wei, C. and Xu, Y., *Scientific Reports* **2015**, *5*, 13693.
[11] Nowak-Król, A. and Würthner, F., *Organic Chemistry Frontiers* **2019**, *6*, 1272-1318.
[12] Qian, X., Mao, P., Yao, W. and Guo, X., *Tetrahedron Letters* **2002**, *43*, 2995-2998.
[13] Mao, P., Qian, X., Zhang, H. and Yao, W., *Dyes and Pigments* **2004**, *60*, 9-16.
[14] Josse, P., Li, S., Dayneko, S., Joly, D., Labrunie, A., Dabos-Seignon, S., Allain, M., Siegler, B., Demadrille, R., Welch, G. C., Risko, C., Blanchard, P. and Cabanetos, C., *Journal of Materials Chemistry C* **2018**, *6*, 761-766.
[15] Payne, A.-J., Rice, N. A., McAfee, S. M., Li, S., Josse, P., Cabanetos, C., Risko, C., Lessard, B. H. and Welch, G. C., *ACS Applied Energy Materials* **2018**, *1*, 4906-4916.
[16] Josse, P. Université d'Angers, **2018**.
[17] Langhals, H. and Kirner, S., *European Journal of Organic Chemistry* **2000**, *2000*, 365-380.
[18] Ma, Y., Shi, Z., Zhang, A., Li, J., Wei, X., Jiang, T., Li, Y. and Wang, X., *Dyes and Pigments* **2016**, *135*, 41-48.

[19] Hendsbee, A. D., Sun, J.-P., Law, W. K., Yan, H., Hill, I. G., Spasyuk, D. M. and Welch, G. C., *Chemistry of Materials* **2016**, *28*, 7098-7109.
[20] Li, G., Zhao, Y., Li, J., Cao, J., Zhu, J., Sun, X. W. and Zhang, Q., *The Journal of Organic Chemistry* **2015**, *80*, 196-203.
[21] Wang, R., Li, G., Zhang, A., Wang, W., Cui, G., Zhao, J., Shi, Z. and Tang, B., *Chemical Communications* **2017**, *53*, 6918-6921.
[22] Andrés Castán, J. M., Abad Galán, L., Li, S., Dalinot, C., Simón Marqués, P., Allain, M., Risko, C., Monnereau, C., Maury, O., Blanchard, P. and Cabanetos, C., *New Journal of Chemistry* **2020**, *44*, 900-905.
[23] Penfold, T. J., Gindensperger, E., Daniel, C. and Marian, C. M., *Chemical Reviews* **2018**, *118*, 6975-7025.
[24] Zobel, J. P., Nogueira, J. J. and González, L., *Chemistry – A European Journal* **2018**, *24*, 5379-5387.
[25] Plaza-Medina, E. F., Rodríguez-Córdoba, W., Morales-Cueto, R. and Peon, J., *The Journal of Physical Chemistry A* **2011**, *115*, 577-585.
[26] Vogt, R. A., Reichardt, C. and Crespo-Hernandez, C. E., *The Journal of Physical Chemistry A* **2013**, *117*, 6580-6588.
[27] Navarro, O., Kaur, H., Mahjoor, P. and Nolan, S. P., *The Journal of Organic Chemistry* **2004**, *69*, 3173-3180.
[28] Fukata, Y., Asano, K. and Matsubara, S., *Journal of the American Chemical Society* **2015**, *137*, 5320-5323.
[29] Otani, J., Matsumura, M., Fujii, K. and Uekusa, H., *Chemistry Letters* **2015**, *44*, 662-664.
[30] Galán, L. A., Andrés Castán, J. M., Dalinot, C., Marqués, P. S., Blanchard, P., Maury, O., Cabanetos, C., Le Bahers, T. and Monnereau, C., *Physical Chemistry Chemical Physics* **2020**, *22*, 12373-12381.

General conclusions

General conclusions

The active layer of the organic solar cells is typically composed of electron-donor and -acceptor materials. Although the power conversion efficiencies of these devices are continuously getting closer to those of advanced photovoltaic technologies (silicon- and perovskite-based solar cells), it usually results from the enhancement of the synthetic complexity of both the materials and the fabrication procedure. Thus, in pursuit of a real commercialization, a compromise between the photovoltaic performances and the production cost has to be reached. That is the reason why the preparation of simpler and less expensive materials is crucial at this point.

After an introduction on OPV, the second chapter of this manuscript deals with the *N*-methyl-*N*-phenylthiophen-2-amine (MPTA) electron-donating unit, which was designed by combining the results from the literature with our background and experience. Hence, five push-pull molecules that come out from the combination of the latter with two different heterocyclic spacers and two acceptor moieties were synthesized. This strategy led to a fine tuning of the optical and the electrochemical properties of the new donor materials. Their performance was tested in solution-processed OSCs, leading to modest efficiencies due to their high crystallinity. Eventually, **MPTA-4** was selected for the preparation of vacuum-processed OSCs reaching a maximum power conversion efficiency of 4.27% in preliminary measurements with C_{70}, clearly highlighting the enormous and empirical processing dependence of this type of materials.

Although further optimizations will be carried out in the short term, the PCE reported for other similar donors from the literature probably will not be reached. Consequently, the outer phenyl of the MPTA donor was substituted by a *p*-tolyl moiety, affording two new push-pull derivatives with improved absorptivity that will be also evaluated in vacuum-processed OSCs.

In the third chapter, the synthetic procedure for the synthesis of the reference **TPA-T-DCV-Ph** has been adapted and its naphthyl analogue introduced. The substitution of the phenyl ring by a naphthyl did not impact the optical and electrochemical properties in a great manner. Then, although still unfinished, the optimization of the fabrication procedure of the vacuum-processed **TPA-T-DCV-N**-based OSCs led to a PCE value of 3.72% in the preliminary measurements with C_{70}. In addition, based on the same reference molecule, a new strategy to synthesize conjugated trimers of push-pull molecules with a phenyl moiety as a central core was designed. A first donor material was synthesized as a proof of concept, leading to slightly modified optical and electrochemical features in comparison to the monomer. Although further optimizations will be carried out in the short term to improve its modest performance in BHJ OSCs, the trimer was

sent in parallel to the laboratory of Gregory Welch in the University of Calgary to test it in OSCs with a ternary configuration.

Even though the performances of the monomers were notable, there is still room for improvements. The most evident prospect may come from the use of better electron-donating blocks, which may broaden the absorption range to make the most of the whole visible spectrum.

The fourth chapter was related to the functionalization of a sulfur-containing rylene imide, namely the benzothioxanthene imide (**BTXI**). In parallel to its bromination, the nitration of its most active position (5) was performed and then the reactivity of this nitro group was studied to obtain a series of new derivatives. According to the photophysical characterization of the new series, the introduction of substituents on the naphthalene ring strongly modified the spectroscopic signatures of the bare **BTXI**, which is associated with a localized electronic transition. It was as well demonstrated that large SOC, and thus efficient singlet oxygen generation, can also be efficiently achieved upon the choice of substituents that can lead to a ground state distortion of the π-conjugated backbone. In addition, position 11 could be functionalized when the most active position was protected. This strategy, carried out on the **BTXI** and the new **DBTXI**, enabled the cyclization in the bay area leading to their respective *N*-annulated blocks: **TCCI** and **TXAI**. The structure-property relationship highlighted how this chemical modification induced a massive impact on the features of **BTXI**.

All in all, the chemical functionalization of the **BTXI** block has been thoroughly studied leading to a huge tuning of the properties. Thus, the aim for the short term is combining all the functionalization strategies to synthesize active materials for their application in the field of organic electronics.

Experimental section

General procedures

All reagents and solvents were purchased from commercial sources and used without further purification unless otherwise stated. Reactions were carried out under an argon atmosphere unless otherwise stated. Microwave assisted reactions were performed using a Biotage initiator^{+} system. Flash chromatography was performed with analytical-grade solvents using Aldrich silica gel (technical grade, pore size 60 Å, 230–400 mesh particle size). Flexible plates ALUGRAM® XtraSIL G UV254 from MACHEREY-NAGEL were used for TLC. Compounds were detected by UV irradiation (Bioblock Scientific) or staining with I_2, unless stated otherwise. ^{1}H and ^{13}C NMR were recorded on a Bruker AVANCE III 300 (^{1}H, 300 MHz; ^{13}C, 75 MHz) or a Bruker AVANCE DRX500 (^{1}H, 500 MHz ; ^{13}C, 125 MHz). Chemical shifts are given in parts per million (ppm) relative to TMS and coupling constants *J* in Hertz (Hz). High-resolution mass spectrometry (HRMS) was performed with a JEOL JMS-700 B/E. UV-visible absorption spectra were recorded with a Shimadzu UV-1800 spectrometer. Electrochemical measurements were performed with a Biologic SP-150 potentiostat with positive feedback compensation using a conventional single-compartment three-electrode cell. The working electrode was a platinum electrode. The auxiliary was a platinum wire and the pseudo-reference electrode was a silver wire calibrated with the ferrocene potential. The supporting electrolyte was 0.1 M Bu_4NPF_6 (tetrabutylammonium hexafluorophosphate) in dichloromethane (DCM) and solutions were purged with argon prior to each experiments. All potentials are quoted relative to Fc/Fc^{+}. In all the experiments, the scan rate was 100 mV/s. Photoelectron spectroscopy in air (PESA) measurements were recorded using a Riken Keiki PESA spectrometer (Model AC-2) with a power setting of 20 nW.

X-ray single-crystal diffraction data were collected on a Rigaku Oxford Diffraction SuperNova diffractometer equipped with Atlas CCD detector and micro-focus Cu-Kα radiation (1.54184 Å). The structures were solved by direct methods and refined on F2 by full matrix least-squares techniques using SHELX programs (G. M. Sheldrick, 2018). All non-H atoms were refined anisotropically and multiscan empirical absorption was corrected using CrysAlisPro program (CrysAlisPro, Agilent Technologies, V 1.171.40.45a, 2019). The H atoms were included in the calculation without refinement.

<u>General procedure for purification with recycling preparative size exclusion HPLC:</u>

Crude compounds were solubilized in HPLC grade chloroform (stabilized with ethanol, 5 mL). Prior to injection, the solution was filtered through a 0.45 μm PTFE filter (VWR 25 mm syringe filter w/ 0.45 μm membrane). Purification was performed on a LC-9160NEXT system from the

Japan Analytical Industry Co., Ltd. (JAI) equipped with coupled UV-vis 4Ch NEXT and RI-700 II detectors at room temperature through a set of two JAIGEL-2H and 2.5H columns at an elution rate of 10 mL min^{-1}.

Synthetic procedures

_N_-methyl-_N_-phenylthiophen-2-amine (MPTA)

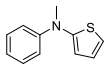

2-Dicyclohexylphosphino-2',6'-diisopropoxybiphenyl (227 mg, 0.48 mmol), sodium *tert*-butoxyde (1.62 g, 16.83 mmol), palladium acetate (27 mg, 0.12 mmol) were dissolved in dry and degassed toluene (30 mL). Then, methyl aniline (1.59 mL, 14.43 mmol) and 2-bromothiophene (1.19 mL, 12.02 mmol) were added and then the mixture was refluxed during 19 h. The reaction was quenched with brine and the organic phase was extracted with CH_2Cl_2, washed with water, dried with $MgSO_4$ and concentrated under reduced pressure. The final product was purified by column chromatography on silica gel (eluent: petroleum ether/ethyl acetate 20:1). Yield: yellowish oil (1.97 g, 86%). **^{1}H NMR** (300 MHz, $CDCl_3$): δ (ppm) 7.29 – 7.21 (m, 2H), 6.98 – 6.93 (m, 3H), 6.92 – 6.85 (m, 2H), 6.65 (dd, J = 3.6, 1.4 Hz, 1H), 3.33 (s, 3H). In accordance with literature.[1]

5-(methyl(phenyl)amino)thiophene-2-carbaldehyde (1)

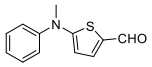

n-BuLi (1.6 M in hexanes, 0.50 mL, 0.79 mmol) was added dropwise to a solution of **MPTA** (125 mg, 0.66 mmol) in anhydrous THF (10 mL) cooled down to -78 °C. The mixture was stirred for 1 h at this temperature and then anhydrous DMF (0.12 mL, 1.58 mmol) was added. The reaction mixture was warmed up to room temperature and stirred for 16 h. The reaction was quenched with water and then the organic phase was extracted with diethyl ether, dried with $MgSO_4$ and concentrated under reduced pressure. The final product was purified by column chromatography on silica gel (eluent: CH_2Cl_2/petroleum ether/triethylamine 85:10:5). Yield: greenish solid (85 mg, 60%). **^{1}H NMR** (300 MHz, $CDCl_3$): δ (ppm) 9.53 (s, 1H), 7.49 – 7.37 (m, 3H), 7.35 – 7.29 (m, 3H), 6.09 (d, J = 4.4 Hz, 1H), 3.45 (s, 3H). **^{13}C NMR** (75 MHz, $CDCl_3$): δ (ppm) 180.8, 166.5, 146.5, 139.7, 130.0, 128.0, 126.9, 124.9, 106.1, 42.7. **HRMS** (EI): *m/z* calcd for $C_{12}H_{11}NOS$: 217.0556, found: 217.0559.

2-((5-(methyl(phenyl)amino)thiophen-2-yl)methylene)malononitrile (MPTA-1)

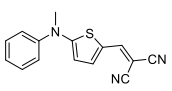

Five drops of triethylamine were added to a mixture of compound **1** (77 mg, 0.35 mmol) and malononitrile (47 mg, 0.71 mmol) in $CHCl_3$ (6 mL). The reaction mixture was refluxed for 16 h and then cooled down to room temperature. The solvent was evaporated under vacuum and the product was purified by column chromatography on silica gel (eluent: CH_2Cl_2). Yield: red solid (81 mg, 86%). **^{1}H NMR** (300 MHz, $CDCl_3$): δ (ppm) 7.52 – 7.43 (m, 3H), 7.39 – 7.29 (m, 4H), 6.11 (d, J = 4.6 Hz, 1H), 3.53 (s, 3H). **^{13}C NMR** (75 MHz, $CDCl_3$): δ (ppm)

169.0, 149.1, 145.4, 130.4, 128.1, 125.2, 121.0, 116.8, 115.9, 107.8, 107.7, 43.6. **HRMS** (CI): *m/z* calcd for $C_{15}H_{11}N_3S$: 266.0746, found: 266.0745. **IR** (neat): ν (cm^{-1}) 2196 (C≡N).

5'-(methyl(phenyl)amino)-[2,2'-bithiophene]-5-carbaldehyde (2)

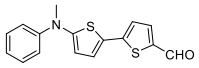

n-BuLi (1.6 M in hexanes, 0.56 mL, 0.90 mmol) was added dropwise to a solution of **MPTA** (142 mg, 0.75 mmol) in anhydrous THF (10 mL) cooled down to -78 °C. The mixture was stirred for 1 h at this temperature and then tributyltin chloride (0.27 mL, 0.94 mmol) was added. The reaction mixture was warmed up to room temperature and stirred for 16 h. The reaction was quenched with water and then the organic phase was extracted with CH_2Cl_2, dried with $MgSO_4$ and concentrated under reduced pressure.

The stannane (**MPTA-Sn**), without further purification, was dissolved together with 5-bromothiophene-2-carbaldehyde (150 mg, 0.79 mmol) and tetrakis(triphenyl-phosphine)palladium(0) (43 mg, 0.04 mmol) in 10 mL of degassed toluene and the mixture was stirred under reflux for 16 h. The reaction was quenched with water and then the organic phase was extracted with toluene, dried with $MgSO_4$ and concentrated under reduced pressure. The product was purified by column chromatography on silica gel (eluent: CH_2Cl_2). Yield: red solid (125 mg, 56%). **^{1}H NMR** (300 MHz, $CDCl_3$): δ (ppm) 9.78 (s, 1H), 7.59 (d, *J* = 4.0 Hz, 1H), 7.42 – 7.31 (m, 2H), 7.28 – 7.18 (m, 2H), 7.17 – 7.06 (m, 2H), 7.00 (d, *J* = 4.0 Hz, 1H), 6.27 (d, *J* = 4.1 Hz, 1H), 3.40 (s, 3H). **^{13}C NMR** (75 MHz, $CDCl_3$): δ (ppm) 182.2, 157.4, 148.8, 148.1, 139.9, 137.9, 129.6, 126.3, 123.9, 123.8, 122.0, 121.4, 111.6, 42.3. **HRMS** (CI): *m/z* calcd for $C_{16}H_{13}NOS_2$: 299.0433, found: 299.0436.

2-((5'-(methyl(phenyl)amino)-[2,2'-bithiophen]-5-yl)methylene)malononitrile (MPTA-2)

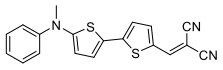

Five drops of triethylamine were added to a mixture of compound **2** (150 mg, 0.50 mmol) and malononitrile (66 mg, 1.00 mmol) in acetonitrile (30 mL). The reaction mixture was stirred for 2 h under air at room temperature and then the solvent was evaporated under vacuum. The resulting product was injected in a recycling preparative HPLC following the general procedure. Yield: purple solid (110 mg, 73%). **^{1}H NMR** (300 MHz, $CDCl_3$): δ (ppm) 7.63 (d, *J* = 0.6 Hz, 1H), 7.50 (dd, *J* = 4.2, 0.6 Hz, 1H), 7.44 – 7.37 (m, 2H), 7.32 – 7.28 (m, 2H), 7.24 – 7.18 (m, 2H), 6.97 (d, *J* = 4.2 Hz, 1H), 6.18 (d, *J* = 4.2 Hz, 1H), 3.43 (s, 3H). **^{13}C NMR** (75 MHz, $CDCl_3$): δ (ppm) 160.0, 151.9, 149.5, 147.4, 141.1, 131.2, 129.9, 128.8, 125.6, 123.3, 121.7, 120.9, 115.3, 114.4, 109.0, 72.5, 42.5. **HRMS** (FAB): *m/z* calcd for $C_{19}H_{13}N_3S_2$: 347.0545, found: 347.0550. **IR** (neat): ν (cm^{-1}) 2213 (C≡N).

2-((5'-(methyl(phenyl)amino)-[2,2'-bithiophen]-5-yl)methylene)-1*H*-indene-1,3(2*H*)-dione (MPTA-3)

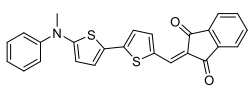

Five drops of triethylamine were added to a mixture of compound **2** (89 mg, 0.30 mmol) and 1*H*-indene-1,3(2*H*)-dione (87 mg, 0.60 mmol) in acetonitrile (20 mL). The reaction mixture was stirred for 4 h under air at room temperature and then the solvent was evaporated under vacuum. The resulting product was injected in a recycling preparative HPLC following the general procedure. Yield: purple solid (100 mg, 79%). **^{1}H NMR** (300 MHz, $CDCl_3$): δ (ppm) 7.96 – 7.89 (m, 2H), 7.88 (s, 1H), 7.78 (d, *J* = 4.2 Hz, 1H), 7.75 – 7.71 (m, 2H), 7.40 (dd, *J* = 8.5, 7.3 Hz, 2H), 7.32 – 7.27 (m, 3H), 7.21 – 7.13 (m, 1H), 7.06 (d, *J* = 4.2 Hz, 1H), 6.24 (d, *J* = 4.2 Hz, 1H), 3.43 (s, 3H). **^{13}C NMR** (75 MHz, $CDCl_3$): δ (ppm) 190.9, 190.2, 158.9, 153.1, 147.7, 144.8, 142.0, 140.6, 136.1, 134.8, 134.6, 134.2, 129.8, 127.7, 124.9, 122.9, 122.8, 122.7, 122.6, 121.8, 110.0, 42.4. **HRMS** (EI): *m/z* calcd for $C_{25}H_{17}NO_2S_2$: 427.0695, found: 427.0703. **IR** (neat): ν (cm^{-1}) 1663 (C=O).

7-(5-(methyl(phenyl)amino)thiophen-2-yl)benzo[*c*][1,2,5]thiadiazole-4-carbaldehyde (3)

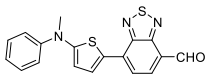

n-BuLi (1.6 M in hexanes, 1.60 mL, 2.52 mmol) was added dropwise to a solution of **MPTA** (400 mg, 2.11 mmol) in anhydrous THF (20 mL) cooled down to -78 °C. The mixture was stirred for 1 h at this temperature and then tributyltin chloride (0.75 mL, 2.63 mmol) was added. The reaction mixture was warmed up to room temperature and stirred for 16 h. The reaction was quenched with water and then the organic phase was extracted with CH_2Cl_2, dried with $MgSO_4$ and concentrated under reduced pressure.

The stannane (**MPTA-Sn**), without further purification, was dissolved together with 7-bromobenzo[*c*][1,2,5]thiadiazole-4-carbaldehyde (540 mg, 2.22 mmol) and tetrakis(triphenyl-phosphine)palladium(0) (122 mg, 0.11 mmol) in 30 mL of degassed toluene and the mixture was stirred under reflux for 16 h. The reaction was quenched with water and then the organic phase was extracted with toluene, dried with $MgSO_4$ and concentrated under reduced pressure. The product was purified by column chromatography on silica gel (eluent: petroleum ether/ethyl acetate 8:2). Yield: purple solid (650 mg, 88%). **^{1}H NMR** (300 MHz, $CDCl_3$): δ (ppm) 10.60 (s, 1H), 8.22 (d, *J* = 4.3 Hz, 1H), 8.11 (d, *J* = 7.7 Hz, 1H), 7.65 (d, *J* = 7.7 Hz, 1H), 7.46 – 7.39 (m, 2H), 7.38 – 7.33 (m, 2H), 7.24 – 7.18 (m, 1H), 6.34 (d, *J* = 4.3 Hz, 1H), 3.51 (s, 3H). **^{13}C NMR** (75 MHz, $CDCl_3$): δ (ppm) 188.4, 161.0, 154.1, 152.1, 147.5, 134.1, 133.8, 132.5, 129.8, 125.3, 124.4, 123.4, 123.3, 120.4, 109.3, 42.5. **HRMS** (FAB): *m/z* calcd for $C_{18}H_{13}N_3OS_2$: 351.0495, found: 351.0494.

2-((7-(5-(methyl(phenyl)amino)thiophen-2-yl)benzo[*c*][1,2,5]thiadiazol-4-yl)methylene)malononitrile (MPTA-4)

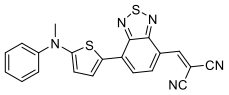

Five drops of triethylamine were added to a mixture of compound **3** (333 mg, 0.95 mmol) and malononitrile (125 mg, 1.90 mmol) in acetonitrile (60 mL). The reaction mixture was stirred for 2 h under air at room temperature and then the solvent was evaporated under vacuum. The resulting product was injected in a recycling preparative HPLC following the general procedure. Yield: dark blue solid (286 mg, 76%). **^{1}H NMR** (300 MHz, $CDCl_3$): δ (ppm) 8.67 (s, 1H), 8.64 (d, *J* = 8.2 Hz, 1H), 8.25 (d, *J* = 4.4 Hz, 1H), 7.58 (d, *J* = 8.2 Hz, 1H), 7.50 – 7.42 (m, 2H), 7.41 – 7.36 (m, 2H), 7.32 – 7.27 (m, 1H), 6.31 (d, *J* = 4.4 Hz, 1H), 3.54 (s, 3H). **^{13}C NMR** (75 MHz, $CDCl_3$): δ (ppm) 163.4, 155.1, 151.8, 150.8, 147.0, 134.6, 131.3, 130.0, 126.4, 124.3, 124.1, 120.4, 118.6, 115.1, 114.3, 109.0, 42.8. **HRMS** (FAB): *m/z* calcd for $C_{21}H_{13}N_5S_2$: 399.0607, found: 399.0610. **IR** (neat): ν (cm^{-1}) 2216 (C≡N).

2-((7-(5-(methyl(phenyl)amino)thiophen-2-yl)benzo[*c*][1,2,5]thiadiazol-4-yl)methylene)-1*H*-indene-1,3(2*H*)-dione (MPTA-5)

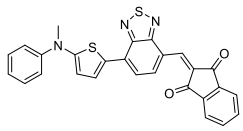

Five drops of triethylamine were added to a mixture of compound **3** (144 mg, 0.40 mmol) and 1*H*-indene-1,3(2*H*)-dione (116 mg, 0.80 mmol) in acetonitrile (30 mL). The reaction mixture was stirred for 4 h under air at room temperature and then the solvent was evaporated under vacuum. The resulting solid was dissolved in $CHCl_3$ and precipitated with pentane and washed thoroughly with pentane. Yield: blue solid (122 mg, 64%). **^{1}H NMR** (300 MHz, $CDCl_3$): δ (ppm) 9.73 (d, *J* = 8.1, 1H), 8.94 (s, 1H), 8.23 (d, *J* = 4.4 Hz, 1H), 8.04 – 7.97 (m, 2H), 7.83 – 7.75 (m, 2H), 7.72 (d, *J* = 8.1 Hz, 1H), 7.47 – 7.34 (m, 4H), 7.25 – 7.19 (m, 1H), 6.35 (d, *J* = 4.4 Hz, 1H), 3.52 (s, 3H). **HRMS** (EI): *m/z* calcd for $C_{27}H_{17}N_3O_2S_2$: 479.0757, found: 479.0754. Due to the lack of solubility of the product, we were unable to obtain a complete ^{13}C NMR spectrum. **IR** (neat): ν (cm^{-1}) 1682 (C=O).

***N*,*N*-diphenyl-4-(thiophen-2-yl)aniline (4)**

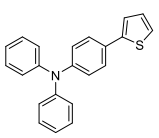

(4-(diphenylamino)phenyl)boronic acid (1.00 g, 3.46 mmol), 2-bromothiophene (5.00 mL, 5.16 mmol), K_2CO_3 (1.43 g, 10.35 mmol) and tetrakis(triphenylphosphine)palladium(0) (200 mg, 0.17 mmol) were dissolved in anhydrous and degassed DMF (15 mL) and the mixture was stirred at 100 °C for 16 h. The reaction was quenched with water and then the organic phase was extracted with CH_2Cl_2, washed with brine, dried with $MgSO_4$ and concentrated in vacuo. The product was purified by column chromatography on silica gel (eluent: petroleum ether/CH_2Cl_2 9:1). Yield: pale yellow solid (1.01 g, 88%). **^{1}H NMR**

(300 MHz, $CDCl_3$): δ (ppm) 7.50 – 7.44 (m, 2H), 7.30 – 7.20 (m, 6H), 7.15 – 6.99 (m, 9H). In accordance with literature.[2]

(5-(4-(diphenylamino)phenyl)thiophen-2-yl)(phenyl)methanone (5)

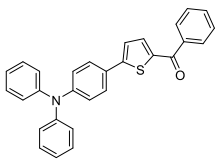

n-BuLi (2.5 M in hexanes, 0.26 mL, 0.64 mmol) was added dropwise to a solution of compound **4** (200 mg, 0.61 mmol) in anhydrous THF (3.5 mL) cooled down to -78 °C. The mixture was stirred for 1 h and then benzoyl chloride (86 mg, 0.61 mmol) was added in one portion. The reaction mixture was warmed up to room temperature and stirred for 16 h. The reaction was quenched with a mixture of brine and a 1 M aqueous solution of HCl (1 mL) and then the organic phase was extracted with CH_2Cl_2, dried with $MgSO_4$ and concentrated under reduced pressure. The product was purified by column chromatography on silica gel (eluent: CH_2Cl_2) to give pure compound **5** (107 mg, 41%) as a yellow solid. **^{1}H NMR** (300 MHz, $CDCl_3$): δ (ppm) 7.90 – 7.85 (m, 2H), 7.62 – 7.47 (m, 6H), 7.38 – 7.23 (m, 5H), 7.17 – 7.04 (m, 8H). In accordance with literature.[3]

(5-(4-(diphenylamino)phenyl)thiophen-2-yl)(phenyl)methanethione (6)

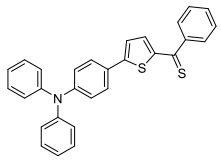

To a stirred solution of **5** (107 mg, 0.25 mmol) in toluene (10 mL) was added Lawesson's reagent (60 mg, 0.15 mmol) and the mixture was refluxed for 4 h. The reaction was then cooled down to room temperature and concentrated in vacuo. The crude was purified by column chromatography on silica gel (eluent: petroleum ether/CH_2Cl_2 6:4) yielding compound **6** (81 mg, 74%) as a red solid. **^{1}H NMR** (300 MHz, $CDCl_3$): δ (ppm) 7.71 – 7.66 (m, 2H), 7.60 – 7.52 (m, 2H), 7.52 – 7.47 (m, 1H), 7.44 – 7.36 (m, 2H), 7.35 – 7.27 (m, 6H), 7.19 – 7.02 (m, 8H). **^{13}C NMR** (75 MHz, $CDCl_3$): δ (ppm) 220.8, 158.8, 153.1, 149.4, 147.1, 147.0, 133.4, 130.9, 129.6, 128.7, 128.1, 127.2, 126.5, 125.4, 124.1, 124.1, 122.2. **HRMS** (EI): *m/z* calcd for $C_{29}H_{21}NS_2$: 447.1110, found: 447.1112.

2-((5-(4-(diphenylamino)phenyl)thiophen-2-yl)(phenyl)methylene)malononitrile (TPA-T-DCV-Ph)

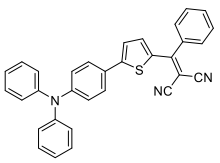

Tetracyanoethylene oxide (26 mg, 0.18 mmol) was dissolved in acetonitrile (10 mL) and then this mixture was added dropwise to a solution of **6** (81 mg, 0.18 mmol) in toluene (25 mL) under stirring. The reaction mixture was stirred at room temperature for 40 min. Then, a second amount of tetracyanoethylene oxide (26 mg, 0.18 mmol) dissolved in acetonitrile (10 mL) was added and the reaction mixture was further stirred at room temperature for 16 h and

concentrated in vacuo. The crude was purified by column chromatography on silica gel (eluent: CH_2Cl_2/petroleum ether 6:4) yielding **TPA-T-DCV-Ph** (81 mg, 93%) as a red powder. **^{1}H NMR** (300 MHz, $CDCl_3$): δ (ppm) 7.65 (d, J = 4.3 Hz, 1H), 7.62 – 7.44 (m, 7H), 7.34 – 7.27 (m, 5H), 7.17 – 7.06 (m, 6H), 7.06 – 6.99 (m, 2H). **HRMS** (FAB): *m/z* calcd for $C_{32}H_{21}N_3S$: 479.1451, found: 479.1453. In accordance with literature.[3]

(5-(4-(diphenylamino)phenyl)thiophen-2-yl)(naphthalen-2-yl)methanone (7)

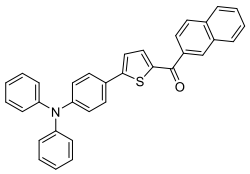

n-BuLi (2.5 M in hexanes, 0.68 mL, 1.70 mmol) was added dropwise to a solution of compound **4** (530 mg, 1.62 mmol) in anhydrous THF (6 mL) cooled down to -78 °C. The mixture was stirred for 1 h and then it was added dropwise (during ca. 1 h) over a solution of naphthoyl chloride (432 mg, 1.70 mmol) in dry THF at -78 °C. After 1h, the reaction mixture was warmed up to room temperature and stirred for 16 h. The reaction was quenched with a mixture of brine and 1 N HCl (1 mL) and then the organic phase was extracted with CH_2Cl_2, dried over $MgSO_4$ and concentrated under reduced pressure. The crude was purified by column chromatography on silica gel (eluent: CH_2Cl_2/petroleum ether 6:4) and was eventually injected in a recycling preparative HPLC following the general procedure. Yield: yellow solid (370 mg, 47%). **^{1}H NMR** (300 MHz, $CDCl_3$): δ (ppm) 8.40 (s, 1H), 8.00 – 7.90 (m, 4H), 7.67 (d, J = 4.0 Hz, 1H), 7.65 – 7.53 (m, 4H), 7.34 – 7.27 (m, 5H), 7.18 – 7.05 (m, 8H). **^{13}C NMR** (75 MHz, $CDCl_3$): δ (ppm) 188.0, 153.6, 149.0, 147.2, 141.5, 136.4, 135.7, 135.2, 132.5, 130.3, 129.6, 129.4, 128.5, 128.2, 128.0, 127.3, 127.0, 126.7, 125.5, 125.2, 123.9, 122.9, 122.7. **HRMS** (EI): *m/z* calcd for $C_{33}H_{23}NOS$: 481.1495, found: 481.1501.

(5-(4-(diphenylamino)phenyl)thiophen-2-yl)(naphthalen-2-yl)methanethione (8)

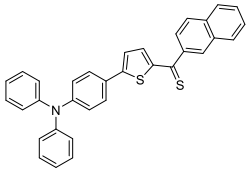

To a stirred solution of **7** (112 mg, 0.23 mmol) in toluene (10 mL) was added Lawesson's reagent (56 mg, 0.14 mmol) and the mixture was refluxed for 4 h. The reaction was then cooled down to room temperature and concentrated in vacuo. The crude was purified by column chromatography on silica gel (eluent: petroleum ether/CH_2Cl_2 7:3) yielding compound **8** (88 mg, 77%) as a red solid. **^{1}H NMR** (300 MHz, $CDCl_3$): δ (ppm) 8.16 (s, 1H), 7.96 – 7.82 (m, 4H), 7.62 – 7.50 (m, 4H), 7.39 (d, J = 4.2 Hz, 1H), 7.35 – 7.27 (m, 5H), 7.19 – 7.02 (m, 8H). **^{13}C NMR** (125 MHz, $CDCl_3$): δ (ppm) 220.2, 158.6, 153.3, 149.4, 147.0, 144.3, 134.6, 133.5, 132.4, 129.6, 129.3, 128.2, 127.9, 127.7, 127.2, 126.9, 126.7, 126.5, 125.4, 124.1, 122.2. **HRMS** (EI): *m/z* calcd for $C_{33}H_{23}NS_2$: 497.1266, found: 497.1267.

2-((5-(4-(diphenylamino)phenyl)thiophen-2-yl)(naphthalen-2-yl)methylene)malononitrile (TPA-T-DCV-N)

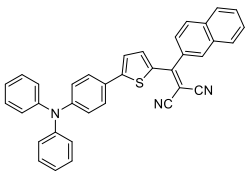

Tetracyanoethylene oxide (90 mg, 0.62 mmol) was dissolved in acetonitrile (30 mL). This mixture was added dropwise to a solution of compound **8** (300 mg, 0.60 mmol) in toluene (85 mL) under stirring. The reaction mixture was stirred at room temperature for 40 min. A second amount of tetracyanoethylene oxide (75 mg, 0.52 mmol) dissolved in acetonitrile (30 mL) was added and the reaction mixture was further stirred 16 h at room temperature and concentrated in vacuo. The crude was purified by column chromatography on silica gel (eluent: CH_2Cl_2/petroleum ether 7:3) yielding **TPA-T-DCV-N** (270 mg, 85%) as a red powder. **^{1}H NMR** (300 MHz, $CDCl_3$): δ (ppm) 8.02 – 7.91 (m, 4H), 7.70 (d, J = 4.3 Hz, 1H), 7.68 – 7.57 (m, 2H), 7.52 (dd, J = 8.5, 1.9 Hz, 1H), 7.50 – 7.44 (m, 2H), 7.35 – 7.27 (m, 5H), 7.18 – 7.08 (m, 6H), 7.06 – 7.00 (m, 2H). **^{13}C NMR** (75 MHz, $CDCl_3$): δ (ppm) 164.1, 156.4, 149.7, 146.8, 138.9, 136.2, 134.5, 133.5, 132.5, 130.2, 129.6, 128.9, 128.7, 128.3, 128.0, 127.4, 127.4, 126.0, 125.4, 125.2, 124.3, 123.7, 122.0, 115.2, 114.6, 75.5. **HRMS** (EI): *m/z* calcd for $C_{36}H_{23}N_3S$: 529.1607, found: 529.1615.

(*E*)-1-(5-bromothiophen-2-yl)-3-(dimethylamino)prop-2-en-1-one (9)

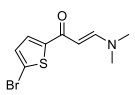

A mixture of 1-(5-bromothiophen-2-yl)ethan-1-one (2.00 g, 9.61 mmol) and *N*,*N*-dimethylformamide dimethyl acetal (1.97 mL, 14.41 mmol) was subjected to microwave irradiation under solvent-free conditions at 160 °C for 15 min. The mixture was cooled down to room temperature and then the solvent was removed in vacuo. Yield: brown solid (2.39 g, 96%). **^{1}H NMR** (300 MHz, $CDCl_3$): δ (ppm) 7.76 (d, J = 12.2 Hz, 1H), 7.34 (d, J = 3.9 Hz, 1H), 7.02 (d, J = 3.9 Hz, 1H), 5.49 (d, J = 12.2 Hz, 1H), 3.21 – 2.84 (m, 6H). In accordance with literature.[4]

Benzene-1,3,5-triyltris((5-bromothiophen-2-yl)methanone) (10)

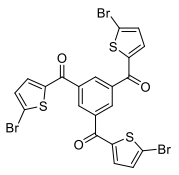

To a mixture of enaminone **9** (1.00 g, 3.84 mmol) and D-(-)-lactic acid (0.43 mL, 5.13 mmol), H_2O (40 mL) was added under air before heating at 90 °C for 16 h. Ethanol (15 mL) was added and then the mixture was cooled down to 0 °C. The precipitate was filtered off, washed with water and a mixture H_2O/EtOH 6:4 yielding compound **10** (660 mg, 81%) as a brownish solid. **^{1}H NMR** (300 MHz, $CDCl_3$): δ (ppm) 8.44 (s, 1H), 7.43 (d, J = 4.1 Hz, 1H), 7.18 (d, J = 4.1 Hz, 1H). **^{13}C NMR** (75 MHz, $CDCl_3$): δ (ppm) 184.9, 144.0, 138.4, 135.8, 132.6, 131.8, 125.1. **HRMS** (EI): *m/z* calcd for $C_{21}H_9Br_3O_3S_3$: 641.7258, found: 641.7260.

Benzene-1,3,5-triyltris((5-(4-(diphenylamino)phenyl)thiophen-2-yl)methanone) (11)

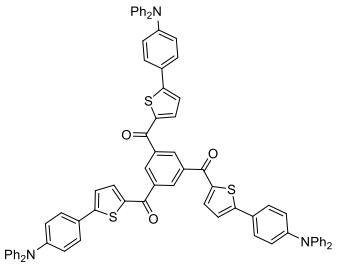

(4-(diphenylamino)phenyl)boronic acid (592 mg, 2.05 mmol), **10** (400 mg, 0.62 mmol), $NaHCO_3$ (469 mg, 5.58 mmol) and tetrakis(triphenyl-phosphine)palladium(0) (93 mg, 0.09 mmol) were dissolved in a mixture of H_2O/DMF 8:5 (13 mL) under air and then heated under microwave irradiation for 1 h at a pre-selected temperature of 150 °C. The organic phase was extracted with CH_2Cl_2, dried with $MgSO_4$ and concentrated under reduced pressure. The crude was purified by column chromatography on silica gel (eluent: CH_2Cl_2). The resulting product was injected in a recycling preparative HPLC following the general procedure yielding **11** (400 mg, 57%) as an orange powder. **^{1}H NMR** (300 MHz, $CDCl_3$): δ (ppm) 8.52 (s, 3H), 7.66 (d, J = 4.0 Hz, 3H), 7.56 – 7.50 (m, 6H), 7.33 – 7.24 (m, 15H), 7.16 – 7.03 (m, 24H). **^{13}C NMR** (75 MHz, $CDCl_3$): δ (ppm) 186.0, 154.9, 149.2, 147.1, 140.2, 139.0, 137.0, 132.3, 129.6, 127.4, 126.2, 125.3, 124.0, 123.2, 122.5. **HRMS** (MALDI): *m/z* calcd for $C_{75}H_{51}N_3O_3S_3$: 1137.3087, found: 1137.3066.

Benzene-1,3,5-triyltris((5-(4-(diphenylamino)phenyl)thiophen-2-yl)methanethione) (12)

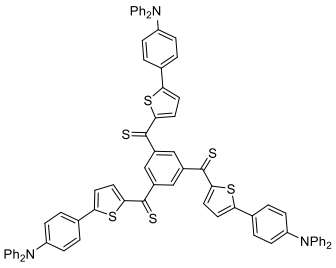

To a stirred solution of **11** (97 mg, 0.08 mmol) in toluene (20 mL) was added Lawesson's reagent (62 mg, 0.15 mmol) and the mixture was refluxed for 16 h. The reaction was then cooled down to room temperature and concentrated in vacuo. The crude was purified by column chromatography on silica gel (eluent: petroleum ether/CH_2Cl_2 1:1) yielding **12** (81 mg, 80%) as a purple solid. **^{1}H NMR** (300 MHz, $CDCl_3$): δ (ppm) 8.08 (s, 3H), 7.59 – 7.53 (m, 6H), 7.46 – 7.42 (m, 3H), 7.35 – 7.27 (m, 15H), 7.18 – 7.07 (m, 18H), 7.06 – 7.00 (m, 6H). It was immediately used in the next reaction due to stability issues in solution.

2,2',2''-(benzene-1,3,5-triyltris((5-(4-(diphenylamino)phenyl)thiophen-2-yl)methaneylylidene))trimalononitrile ((TPA-T-DCV)$_3$-Ph)

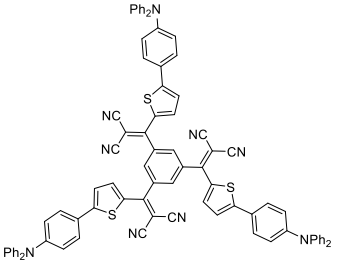

Tetracyanoethylene oxide (29 mg, 0.20 mmol) was dissolved in acetonitrile (4 mL). This mixture was added dropwise to a solution of **12** (82 mg, 0.07 mmol) in toluene (9 mL) under stirring. The reaction mixture was stirred at room temperature for 40 min. Then, a second amount of tetracyanoethylene oxide (25 mg, 0.17 mmol) dissolved in acetonitrile (4 mL) was added and the mixture was further stirred 16 h at room temperature and concentrated in vacuo.

The resulting crude was injected in a recycling preparative HPLC following the general procedure yielding **(TPA-T-DCV)$_3$-Ph** (42 mg, 47%) as a violet powder. **^{1}H NMR** (300 MHz, $CDCl_3$): δ (ppm) 7.72 (s, 3H), 7.63 (d, *J* = 4.3 Hz, 3H), 7.52 – 7.45 (m, 6H), 7.36 – 7.27 (m, 15H), 7.17 – 7.10 (m, 18H), 7.03 – 6.97 (m, 6H). **^{13}C NMR** (75 MHz, $CDCl_3$): δ (ppm) 160.4, 158.2, 150.2, 146.7, 140.4, 138.0, 134.8, 131.7, 129.7, 127.8, 125.7, 124.7, 124.5, 124.3, 121.7, 114.4, 114.2, 75.8. **HRMS** (EI): *m/z* calcd for $C_{84}H_{51}N_9S_3$: 1281.3424, found: 1281.3439.

5-nitro-2-(pentan-3-yl)-1*H*-thioxantheno[2,1,9-*def*]isoquinoline-1,3(2*H*)-dione (BTXI-NO$_2$)

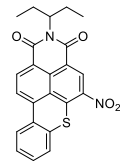

Fuming HNO_3 (≥99%, 10 μL, 0.24 mmol) was added dropwise under air over a stirred solution of **BTXI** (50 mg, 0.13 mmol) in CH_2Cl_2 (5 mL). After 5 minutes, a powder precipitated and the reaction was quenched with water. The powder was filtered and washed with water. The rest of the product was obtained by recrystallization from CH_2Cl_2 yielding **BTXI-NO$_2$** as an orange solid (30 mg, 54%). **^{1}H NMR** (500 MHz, $CDCl_3$): δ (ppm) 9.43 (s, 1H), 8.84 (d, *J* = 8.4 Hz, 1H), 8.53 (d, *J* = 8.4 Hz, 1H), 8.42 – 8.36 (m, 1H), 7.74 – 7.69 (m, 1H), 7.63 – 7.56 (m, 2H), 5.10 – 5.01 (m, 1H), 2.31 – 2.19 (m, 2H), 1.99 – 1.88 (m, 2H), 0.91 (t, *J* = 7.5 Hz, 6H). **^{13}C NMR** (125 MHz, $CDCl_3$): δ (ppm) 141.5, 139.0, 138.1, 131.7, 131.6, 130.7, 129.2, 127.4, 127.2, 126.2, 125.8, 121.2, 58.1, 25.0, 11.5. **HRMS** (EI): *m/z* calcd for $C_{23}H_{18}N_2O_4S$: 418.0982, found: 418.0986.

5,11-dinitro-2-(pentan-3-yl)-1*H*-thioxantheno[2,1,9-*def*]isoquinoline-1,3(2*H*)-dione (NO$_2$-BTXI-NO$_2$)

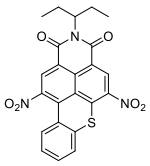

Fuming HNO_3 (≥99%, 34 μL, 0.80 mmol) was added under air over a stirred solution of **BTXI** (30 mg, 0.08 mmol) in CH_2Cl_2 (3 mL). After 20 minutes, the reaction was quenched with water and the organic phase was extracted with CH_2Cl_2, dried with $MgSO_4$ and concentrated under reduced pressure yielding **NO$_2$-BTXI-NO$_2$** (33 mg, 100%) as an orange powder. **^{1}H NMR** (300 MHz, $CDCl_3$): δ (ppm) 9.46 (s, 1H), 9.09 (s, 1H), 7.85 (dd, *J* = 8.1, 1.2 Hz, 1H), 7.76 (dd, *J* = 8.3, 1.0 Hz, 1H), 7.66 (ddd, *J* = 8.1, 7.5, 1.0 Hz, 1H), 7.54 (ddd, *J* = 8.3, 7.5, 1.2 Hz, 1H), 5.11 – 4.97 (m, 1H), 2.33 – 2.14 (m, 2H), 2.02 – 1.85 (m, 2H), 0.90 (t, *J* = 7.5 Hz, 6H). **^{13}C NMR** (75 MHz, $CDCl_3$): δ (ppm) 147.0, 140.5, 140.5, 133.1, 132.7, 131.9, 131.8, 129.8, 129.6, 129.3, 129.1, 128.4, 127.7, 124.2, 122.1, 58.7, 24.9, 11.4. **HRMS** (FAB): *m/z* calcd for $C_{23}H_{17}N_3O_6S$: 463.0833, found: 463.0838.

5-amino-2-(pentan-3-yl)-1*H*-thioxantheno[2,1,9-*def*]isoquinoline-1,3(2*H*)-dione (BTXI-NH$_2$)

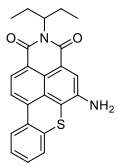

THF (60 mL) was added to a solid mixture of compound **BTXI-NO$_2$** (500 mg, 1.20 mmol) and powdered iron (467 mg, 8.40 mmol). HCl (5.00 mL, 37%) was added and the mixture was heated at 65 °C for 40 minutes. Water was added to quench the reaction and the obtained solid was filtered and washed thoroughly with water. The crude was filtered through a plug of neutral alumina (eluent: $CHCl_3$) yielding **BTXI-NH$_2$** (411 mg, 89%) as a red powder. **^{1}H NMR** (300 MHz, $CDCl_3$): δ (ppm) 8.41 (d, J = 8.0 Hz, 1H), 8.22 – 8.09 (m, 2H), 8.05 (s, 1H), 7.48 – 7.34 (m, 3H), 5.12 – 4.98 (m, 1H), 4.04 (s, 2H), 2.43 – 2.11 (m, 2H), 2.02 – 1.78 (m, 2H), 0.89 (t, J = 7.5 Hz, 6H). **^{13}C NMR** (125 MHz, $CDCl_3$): δ (ppm) 137.3, 134.8, 130.4, 129.7, 128.7, 127.9, 127.3, 126.8, 126.2, 125.3, 119.8, 57.5, 25.1, 11.5. **HRMS** (FAB): *m/z* calcd for $C_{23}H_{20}N_2O_2S$: 388.1240, found: 388.1250.

5-(diphenylamino)-2-(pentan-3-yl)-1*H*-thioxantheno[2,1,9-*def*]isoquinoline-1,3(2*H*)-dione (BTXI-NPh$_2$)

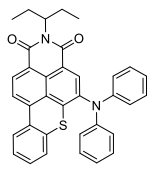

(a) Sodium *tert*-butoxyde (27 mg, 0.28 mmol), $Pd_2(dba)_3$ (10 mg, 0.01 mmol), diphenylamine (39 mg, 0.23 mmol) and **BTXI-Br** (100 mg, 0.22 mmol) were dissolved in dry and degassed toluene (5 mL). Then, 1M tri-*tert*-butylphosphine in toluene (220 μL, 0.22 mmol) was added and then the mixture was refluxed for 16 h and the reaction was filtered through a plug of silica (eluent: ethyl acetate). The solution was concentrated under reduced pressure and the final product was purified by column chromatography on silica gel (eluent: CH_2Cl_2/petroleum ether 7:3). Yield: orange solid (53 mg, 45%). **^{1}H NMR** (300 MHz, CD_2Cl_2): δ (ppm) 8.59 (d, J = 8.2 Hz, 1H), 8.33 (s, 1H), 8.31 – 8.22 (m, 2H), 7.43 – 7.32 (m, 3H), 7.31 – 7.23 (m, 4H), 7.11 – 7.01 (m, 6H), 5.07 – 4.93 (m, 1H), 2.31 – 2.12 (m, 2H), 1.94 – 1.76 (m, 2H), 0.88 (t, J = 7.5 Hz, 6H). **^{13}C NMR** (75 MHz, CD_2Cl_2): δ (ppm) 146.1, 139.9, 137.6, 136.8, 132.5, 130.3, 129.9, 129.5, 128.2, 128.1, 127.8, 127.5, 126.4, 123.6, 122.3, 120.1, 57.8, 25.4, 11.7. **HRMS** (EI): *m/z* calcd for $C_{35}H_{28}N_2O_2S$: 540.1866, found: 540.1864.

(b) Sodium *tert*-butoxyde (36 mg, 0.37 mmol), $Pd_2(dba)_3$ (14 mg, 0.02 mmol) and **BTXI-NH$_2$** (60 mg, 0.15 mmol) were dissolved in dry and degassed toluene (2.5 mL). Then, iodobenzene (87 μL, 0.77 mmol) and 1M tri-*tert*-butylphosphine in toluene (310 μL, 0.31 mmol) were added and the mixture was refluxed during 16 h and the reaction was filtered through a plug of silica (eluent: CH_2Cl_2). The solution was concentrated under reduced pressure and the final product was purified by column chromatography on silica gel (eluent: CH_2Cl_2/petroleum ether 7:3). Yield: orange solid (52 mg, 62%). Spectral data matched those previously obtained.

5-bromo-11-nitro-2-(pentan-3-yl)-1*H*-thioxantheno[2,1,9-*def*]isoquinoline-1,3(2*H*)-dione (NO_2-BTXI-Br)

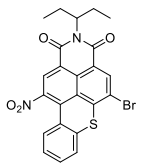

Fuming HNO_3 (≥99%, 0.19 mL, 4.42 mmol) was added over a stirred solution of **BTXI-Br** (1.00 g, 2.21 mmol) in CH_2Cl_2 (120 mL) under air. After 20 minutes, the reaction was quenched with water and the organic phase was extracted with CH_2Cl_2, dried with $MgSO_4$ and concentrated under reduced pressure. The crude was purified by column chromatography on silica gel (eluent: CH_2Cl_2) yielding **NO_2-BTXI-Br** (994 mg, 90%) as a red powder. **^{1}H NMR** (300 MHz, $CDCl_3$): *δ* (ppm) 8.89 (s, 1H), 8.76 (s, 1H), 7.71 – 7.62 (m, 2H), 7.55 (ddd, *J* = 8.0, 7.4, 1.2 Hz, 1H), 7.43 (ddd, *J* = 8.5, 7.4, 1.3 Hz, 1H), 5.09 – 4.89 (m, 1H), 2.33 – 2.11 (m, 2H), 2.02 – 1.82 (m, 2H), 0.88 (t, *J* = 7.5 Hz, 6H). **^{13}C NMR** (75 MHz, $CDCl_3$): *δ* (ppm) 146.4, 141.0, 136.1, 133.5, 131.4, 129.7, 129.4, 129.2, 128.7, 128.7, 128.4, 127.6, 125.4, 124.6, 116.7, 58.1, 24.9, 11.4. **HRMS** (FAB): *m/z* calcd for $C_{23}H_{17}BrN_2O_4S$: 496.0087, found: 496.0083.

5-bromo-2-(pentan-3-yl)indolo[4',3',2':3,4,5]isothiochromeno[7,8,1-*def*]isoquinoline-1,3(2*H*,10*H*)-dione (13)

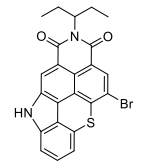

NO_2-BTXI-Br (115 mg, 0.23 mmol) and triphenylphosphine (194 mg, 0.74 mmol) were dissolved in DMF (3 mL) under argon. The mixture was refluxed for 40 h and then the solvent was removed in vacuo. The resulting crude was filtered through a plug of neutral alumina (eluent: chloroform). After removing the solvent, the crude was slurried in CH_2Cl_2 and filtered to obtain compound **13** (75 mg, 70%) as a reddish powder. **^{1}H NMR** (300 MHz, DMSO-d_6): *δ* (ppm) 11.87 (s, 1H), 8.51 (s, 1H), 8.14 (s, 1H), 7.46 (t, *J* = 8.2 Hz, 1H), 7.34 (d, *J* = 8.2 Hz, 1H), 7.20 – 7.11 (m, 1H), 5.06 – 4.91 (m, 1H), 2.28 – 2.07 (m, 2H), 1.94 – 1.78 (m, 2H), 0.83 (t, *J* = 7.4 Hz, 6H). **HRMS** (FAB): *m/z* calcd for $C_{23}H_{17}BrN_2O_2S$: 464.0189, found: 464.0159. Due to the lack of solubility of the product, we were unable to obtain a complete ^{13}C NMR spectrum.

5-bromo-10-hexyl-2-(pentan-3-yl)indolo[4',3',2':3,4,5]isothiochromeno[7,8,1-*def*]isoquinoline-1,3(2*H*,10*H*)-dione (TCCI-Br)

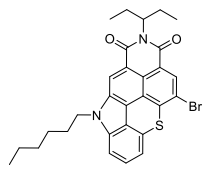

Compound **13** (60 mg, 0.13 mmol) and K_2CO_3 (35 mg, 0.25 mmol) were dissolved in DMF (3 mL) and then 1-bromohexane (33 μL, 0.24 mmol) was added. The mixture was heated at 120 °C for 16 h. Water was added to quench the reaction and the precipitate was filtered off and washed with water and methanol yielding **TCCI-Br** (53 mg, 75%) as an orange powder. **^{1}H NMR** (300 MHz, $CDCl_3$): *δ* (ppm) 8.56 (s, 1H), 8.33 (s, 1H), 7.40 (dd, *J* = 8.2, 7.5 Hz, 1H), 7.11 (d, *J* = 8.2 Hz, 1H),

7.02 (d, *J* = 7.5 Hz, 1H), 5.11 – 4.97 (m, 1H), 4.31 (t, *J* = 7.2 Hz, 2H), 2.28 – 2.11 (m, 2H), 1.95 – 1.77 (m, 4H), 1.36 – 1.15 (m, 6H), 0.90 – 0.73 (m, 9H). **^{13}C NMR** (75 MHz, $CDCl_3$): *δ* (ppm) 141.5, 140.9, 134.2, 132.5, 130.2, 129.8, 123.1, 121.9, 121.9, 118.9, 114.0, 113.9, 107.4, 57.7, 45.1, 31.6, 29.9, 26.9, 25.2, 22.6, 14.1, 11.5. **HRMS** (FAB): *m/z* calcd for $C_{29}H_{29}BrN_2O_2S$: 548.1128, found: 548.1116.

10-hexyl-2-(pentan-3-yl)indolo[4',3',2':3,4,5]isothiochromeno[7,8,1-*def*]isoquinoline-1,3(2*H*,10*H*)-dione (TCCl)

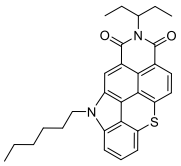

TCCl-Br (60 mg, 0.11 mmol), sodium *tert*-butoxyde (11 mg, 0.11 mmol) and (NHC)Pd(allyl)Cl (2 mg, 3.3 μmol) were dissolved in isopropyl alcohol (3 mL) and stirred at 60 °C for 2 hours. Then, the solvent was removed in vacuo and the product was purified by column chromatography on silica gel (eluent: CH_2Cl_2) yielding **TCCl** (44 mg, 86%) as an orange powder. **^{1}H NMR** (300 MHz, $CDCl_3$): *δ* (ppm) 8.50 (s, 1H), 8.18 (d, *J* = 8.1 Hz, 1H), 7.39 – 7.30 (m, 2H), 7.01 (d, *J* = 8.1 Hz, 1H), 6.89 (d, *J* = 7.5 Hz, 1H), 5.23 – 5.05 (m, 1H), 4.24 (t, *J* = 7.2 Hz, 2H), 2.40 – 2.20 (m, 2H), 2.04 – 1.80 (m, 4H), 1.41 – 1.21 (m, 6H), 0.94 (t, *J* = 7.5 Hz, 6H), 0.85 (t, *J* = 7.0 Hz, 3H). **^{13}C NMR** (75 MHz, $CDCl_3$): *δ* (ppm) 165.3, 141.5, 140.9, 133.7, 130.1, 129.5, 129.0, 123.5, 122.1, 121.4, 120.3, 119.4, 118.8, 116.2, 113.5, 107.0, 57.5, 44.8, 31.6, 29.9, 26.9, 25.2, 22.6, 14.1, 11.6. **HRMS** (EI): *m/z* calcd for $C_{29}H_{30}N_2O_2S$: 470.2022, found: 470.2031.

5-bromo-10-methyl-2-(pentan-3-yl)indolo[4',3',2':3,4,5]isothiochromeno[7,8,1-*def*]isoquinoline-1,3(2*H*,10*H*)-dione (14)

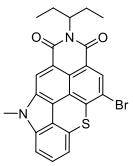

Compound **13** (160 mg, 0.34 mmol) and K_2CO_3 (93 mg, 0.67 mmol) were dissolved in DMF (7 mL) and then methyl iodide (128 μL, 2.06 mmol) was added. The mixture was heated at 60 °C for 16 h. Water was added to quench the reaction and the precipitate was filtered off and washed with water and methanol yielding compound **14** (157 mg, 95%) as an orange powder. **^{1}H NMR** (300 MHz, $CDCl_3$): *δ* (ppm) 8.59 (s, 1H), 8.35 (s, 1H), 7.44 (t, *J* = 7.9 Hz, 1H), 7.13 (d, *J* = 7.9 Hz, 1H), 7.03 (d, *J* = 7.9 Hz, 1H), 5.20 – 5.00 (m, 1H), 3.96 (s, 3H), 2.39 – 2.17 (m, 2H), 2.05 – 1.83 (m, 2H), 0.92 (t, *J* = 7.5 Hz, 6H). **^{13}C NMR** (125 MHz, $CDCl_3$): *δ* (ppm) 141.4, 134.7, 130.2, 129.9, 123.0, 121.9, 118.9, 114.0, 107.1, 57.7, 30.8, 25.2, 11.5. **HRMS** (EI): *m/z* calcd for $C_{24}H_{19}BrN_2O_2S$: 478.0345, found: 478.0347.

10-methyl-2-(pentan-3-yl)indolo[4',3',2':3,4,5]isothiochromeno[7,8,1-*def*]isoquinoline-1,3(2*H*,10*H*)-dione (15)

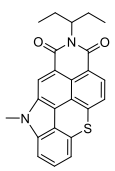

Compound **14** (60 mg, 0.12 mmol), sodium *tert*-butoxyde (13 mg, 0.13 mmol) and (NHC)Pd(allyl)Cl (2 mg, 3.8 μmol) were dissolved in isopropyl alcohol (3 mL) and stirred at 60 °C for 2 hours. Then, the solvent was removed in vacuo and the product was purified by column chromatography on silica gel (eluent: CH_2Cl_2). To reach a higher degree of purity, it was purified by HPLC, yielding compound **15** (25 mg, 51%) as a yellow solid. **^{1}H NMR** (300 MHz, $CDCl_3$): *δ* (ppm) 8.60 (s, 1H), 8.24 (d, *J* = 7.9 Hz, 1H), 7.50 – 7.38 (m, 2H), 7.11 (d, *J* = 7.9 Hz, 1H), 7.00 (d, *J* = 7.9 Hz, 1H), 5.20 – 5.07 (m, 1H), 3.96 (s, 3H), 2.38 – 2.20 (m, 2H), 1.94 (m, 2H), 0.92 (t, *J* = 7.5 Hz, 6H). **^{13}C NMR** (125 MHz, $CDCl_3$): *δ* (ppm) 141.6, 134.4, 130.2, 129.8, 123.7, 122.2, 121.5, 120.5, 119.0, 113.8, 106.8, 57.5, 30.6, 25.2, 11.5. **HRMS** (EI): *m/z* calcd for $C_{24}H_{20}N_2O_2S$: 400.1240, found: 400.1237.

2-(pentan-3-yl)-1*H*-benzo[7,8]thioxantheno[2,1,9-*def*]isoquinoline-1,3(2*H*)-dione (DBTXI)

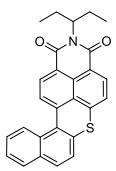

4-bromo-1,8-naphthalic anhydride (11.00 g, 39.70 mmol), 1-aminonaphthalene-2-thiol (7.65 g, 43.67 mmol) and potassium carbonate (5.49 g, 39.70 mmol) were dissolved in DMF (270 mL) under air. The solution mixture was stirred for 16 h at room temperature. Then, isopentyl nitrite (15.72 mL, 119.10 mmol) was added and the mixture was stirred for 24 h at 60 °C. The orange precipitate that appeared was filtrated and washed with water and methanol. Then, the obtained solid, 3-aminopentane (5.33 mL, 45.71 mmol) and imidazole (77 g) were mixed and heated at 100 °C for 16 h. After cooling down to room temperature, a 1 M aqueous solution of HCl was added, the mixture was extracted with CH_2Cl_2 and the organic layer was dried with $MgSO_4$ and concentrated under reduced pressure. The final product was purified by column chromatography on silica gel (eluent: CH_2Cl_2). Yield: orange solid (2.20 g, 13%). **^{1}H NMR** (300 MHz, $CDCl_3$): *δ* (ppm) 8.72 – 8.58 (m, 2H), 8.45 – 8.38 (m, 2H), 7.90 – 7.83 (m, 1H), 7.80 (d, *J* = 8.6 Hz, 1H), 7.59 – 7.50 (m, 3H), 7.39 (d, *J* = 8.6 Hz, 1H), 5.15 – 5.02 (m, 1H), 2.36 – 2.20 (m, 2H), 2.00 – 1.84 (m, 2H), 0.91 (t, *J* = 7.5 Hz, 6H). **^{13}C NMR** (75 MHz, $CDCl_3$): *δ* (ppm) 139.1, 136.8, 134.0, 133.5, 131.6, 130.4, 130.4, 129.2, 129.1, 127.5, 126.7, 125.9, 125.7, 124.0, 123.1, 121.1, 120.0, 118.6, 57.5, 25.1, 11.5. **HRMS** (MALDI): *m/z* calcd for $C_{27}H_{21}NO_2S$: 423.1288, found: 423.1293.

5-bromo-2-(pentan-3-yl)-1*H*-benzo[7,8]thioxantheno[2,1,9-*def*]isoquinoline-1,3(2*H*)-dione (DBTXI-Br)

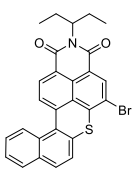

To a solution of **DBTXI** (500 mg, 1.18 mmol) in CH_2Cl_2 (90 mL) was added dropwise a 1 M solution of bromine in CH_2Cl_2 (190 mg, 1.18 mmol). The reaction mixture was refluxed for 16 h before being quenched with a saturated aqueous solution of $Na_2S_2O_3$. Then, the organic phase was washed with water and brine. After drying it over $MgSO_4$, the solution was concentrated under reduced pressure and the crude was purified by column chromatography on silica gel (eluent: CH_2Cl_2). Yield: orange solid (416 mg, 70%). **^{1}H NMR** (300 MHz, $CDCl_3$): δ (ppm) 8.70 – 8.58 (m, 3H), 8.47 (d, J = 8.1 Hz, 1H), 7.90 – 7.81 (m, 2H), 7.58 – 7.50 (m, 2H), 7.46 (d, J = 8.6 Hz, 1H), 5.16 – 5.01 (m, 1H), 2.35 – 2.18 (m, 2H), 2.00 – 1.84 (m, 2H), 0.91 (t, J = 7.5 Hz, 6H). **^{13}C NMR** (75 MHz, $CDCl_3$): δ (ppm) 136.7, 134.2, 133.0, 131.4, 130.8, 130.2, 129.2, 129.0, 127.7, 127.0, 126.5, 125.1, 124.0, 123.2, 114.1, 77.6, 57.7, 25.0, 11.5. **HRMS** (MALDI): *m/z* calcd for $C_{27}H_{20}BrNO_2S$: 501.0393, found: 501.0390.

5-bromo-13-nitro-2-(pentan-3-yl)-1*H*-benzo[7,8]thioxantheno[2,1,9-*def*]isoquinoline-1,3(2*H*)-dione (NO_2-DBTXI-Br)

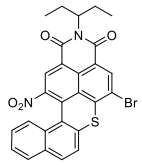

Fuming HNO_3 (≥99%, 50 μL, 1.19 mmol) was added under air over a stirred solution of **DBTXI-Br** (300 mg, 0.60 mmol) in CH_2Cl_2 (45 mL). After 20 minutes, the reaction was quenched with water and the organic phase was extracted with CH_2Cl_2, dried with $MgSO_4$ and concentrated under reduced pressure. The crude was purified by column chromatography on silica gel (eluent: CH_2Cl_2) yielding **NO_2-DBTXI-Br** (290 mg, 89%) as a pink powder. **^{1}H NMR** (300 MHz, $CDCl_3$): δ (ppm) 9.20 (s, 1H), 8.78 (s, 1H), 8.01 (d, J = 8.7 Hz, 1H), 7.95 – 7.87 (m, 2H), 7.66 (d, J = 8.7 Hz, 1H), 7.62 – 7.55 (m, 1H), 7.55 – 7.48 (m, 1H), 5.13 – 5.00 (m, 1H), 2.34 – 2.18 (m, 2H), 2.01 – 1.85 (m, 2H), 0.91 (t, J = 7.5 Hz, 6H). **^{13}C NMR** (75 MHz, $CDCl_3$): δ (ppm) 147.1, 140.6, 135.1, 132.8, 132.7, 131.7, 131.4, 131.3, 129.8, 129.3, 128.7, 127.8, 123.2, 122.0, 120.6, 116.1, 58.3, 25.0, 11.4. **HRMS** (MALDI): *m/z* calcd for $C_{27}H_{19}BrN_2O_4S$: 546.0243, found: 546.0231.

1-bromo-4-(pentan-3-yl)benzo[8,1]isoquinolino[5,4,3-*cde*]isoquinolino[4,5,6-*hij*]isothiochromene-3,5(4*H*,7*H*)-dione (16)

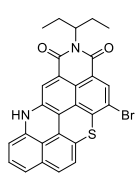

NO_2-DBTXI-Br (220 mg, 0.37 mmol) and triphenylphosphine (307 mg, 1.17 mmol) were dissolved in DMF (5 mL) under argon. The mixture was refluxed for 40 h and then water was added to quench the reaction, the precipitate was filtered off and washed with water and methanol yielding compound **16** (165 mg, 88%) as a blue powder. **HRMS** (MALDI): *m/z* calcd for $C_{27}H_{19}BrN_2O_2S$: 514.0345, found:

514.0335. Due to the lack of solubility of the product, we were unable to obtain complete ^{1}H NMR and ^{13}C NMR spectra.

1-bromo-7-hexyl-4-(pentan-3-yl)benzo[8,1]isoquinolino[5,4,3-*cde*]isoquinolino[4,5,6-*hij*]isothiochromene-3,5(4*H*,7*H*)-dione (TXAI-Br)

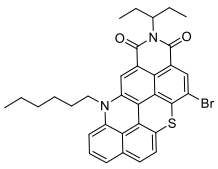

Compound **16** (120 mg, 0.23 mmol) and K_2CO_3 (63 mg, 0.45 mmol) were dissolved in DMF (8 mL) and then 1-bromohexane (60 μL, 0.43 mmol) was added. The mixture was heated at 120 °C for 16 h. Water was added to quench the reaction, the precipitate was filtered off and washed with water and methanol yielding **TXAI-Br** (121 mg, 87%) as a blue powder. **^{1}H NMR** (500 MHz, $CDCl_3$): *δ* (ppm) 7.92 (s, 1H), 7.61 (s, 1H), 6.97 – 6.84 (m, 2H), 6.59 – 6.50 (m, 2H), 5.96 – 5.88 (m, 1H), 4.99 – 4.89 (m, 1H), 3.41 – 3.30 (m, 2H), 2.23 – 2.11 (m, 2H), 1.96 – 1.85 (m, 2H), 1.50 – 1.35 (m, 8H), 0.95 (t, *J* = 7.0 Hz, 3H), 0.90 (t, *J* = 7.4 Hz, 6H). **^{13}C NMR** (125 MHz, $CDCl_3$): *δ* (ppm) 163.1, 141.2, 141.1, 138.7, 134.6, 133.6, 129.1, 128.8, 127.0, 126.4, 124.8, 123.8, 123.6, 123.4, 121.2, 118.3, 114.7, 105.0, 57.7, 47.1, 31.6, 26.6, 25.0, 24.6, 22.9, 14.2, 11.6. **HRMS** (MALDI): *m/z* calcd for $C_{33}H_{31}BrN_2O_2S$: 598.1284, found: 598.1282.

7-hexyl-4-(pentan-3-yl)benzo[8,1]isoquinolino[5,4,3-*cde*]isoquinolino[4,5,6-*hij*]isothiochromene-3,5(4*H*,7*H*)-dione (TXAI)

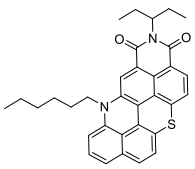

TXAI-Br (90 mg, 0.15 mmol), sodium *tert*-butoxyde (15 mg, 0.16 mmol) and (NHC)Pd(allyl)Cl (3 mg, 4.5 μmol) were dissolved in isopropyl alcohol (4 mL) and stirred at 60 °C for 2 hours. Then, the solvent was removed in vacuo and the product was purified by column chromatography on silica gel (eluent: CH_2Cl_2) yielding **TXAI** (44 mg, 56%) as a blue powder. **^{1}H NMR** (500 MHz, $CDCl_3$): *δ* (ppm) 7.59 – 7.51 (m, 1H), 7.40 (s, 1H), 6.74 (t, *J* = 7.9 Hz, 1H), 6.69 – 6.63 (m, 1H), 6.42 – 6.32 (m, 2H), 6.17 (d, *J* = 8.5 Hz, 1H), 5.75 – 5.64 (m, 1H), 5.00 – 4.87 (m, 1H), 3.23 – 2.96 (m, 2H), 2.21 – 2.09 (m, 2H), 1.99 – 1.87 (m, 2H), 1.50 – 1.41 (m, 2H), 1.40 – 1.32 (m, 6H), 1.00 – 0.88 (m, 9H). **^{13}C NMR** (125 MHz, $CDCl_3$): *δ* (ppm) 164.2, 163.4, 140.9, 137.9, 134.3, 129.9, 128.6, 126.8, 126.5, 125.0, 124.7, 123.3, 123.0, 122.2, 120.7, 120.2, 117.9, 104.5, 57.4, 46.9, 31.5, 26.5, 25.0, 24.5, 22.9, 14.2, 11.7. **HRMS** (MALDI): *m/z* calcd for $C_{33}H_{32}N_2O_2S$: 520.2179, found: 520.2180.

Additional methods

Devices fabrication and measurement

Substrate cleaning: Indium-tin oxide pre-coated glass slides of 24 x 25 x 1.1 mm with a sheet resistance of 7 Ω/sq were purchased from Visiontek Systems LTD. The substrates were washed with a diluted Deconex® 12 PA-x solution (2% in water) before being cleaned by a series of ultrasonic treatments in distilled water, acetone and isopropanol for 15 min each. Once dried under a steam of nitrogen, a UV-ozone plasma treatment (UV/Ozone ProCleaner Plus, Bioforce Nanosciences) was performed for 15 min.

Solution-processed OSC with a direct structure: A filtered aqueous solution of poly(3,4-ethylenedioxy-thiophene)-poly(styrenesulfonate) (PEDOT:PSS; Ossila Al 4083) through a 0.45 µm RC membrane (Minisart® RC 15) was spun-cast onto the ITO surface at 5000 rpm for 40 s before being baked at 120 °C for 30 min. For PHJ, the donor was deposited via spin coating from chloroform solutions and then the accepting material and the cathode were thermally deposited in vacuum. For BHJ, the bulk was deposited via spin coating from chloroform solutions before thermally depositing the cathode in vacuum. Device architecture: ITO/PEDOT:PSS (24 nm)/BHJ or (D/A (30 nm))/LiF (1 nm)/Al (100 nm).

Device characterization: *J-V* curves were recorded in the dark and under illumination using a Keithley 236 source-measure unit and a homemade acquisition program. The light source is an AM1.5 Solar Constant 575 PV simulator (Steuernagel Lichttecknik, equipped with a metal halogen lamp, 80 $mW.cm^{-2}$). The light intensity was measured by a broad-band power meter (13PEM001, Melles Griot). EQE were measured under ambient atmosphere using a halogen lamp (Osram) with an Action Spectra Pro 150 monochromator, a lock-in amplifier (Perkin-Elmer 7225) and a S2281 photodiode (Hamamatsu).

Vacuum-processed OSCs from Heliatek: Devices were prepared by thermal vapour deposition onto room temperature on tin-doped indium oxide (ITO) coated substrates (Thin Film Devices, USA, sheet resistance of 30 Ω sq^{-1}) in an ultra-high vacuum chamber with a base pressure of 10^{-7}mbar. Layer thicknesses were determined during evaporation by using quartz crystal monitors calibrated for the respective material. Solar cells were prepared layer by layer with-out breaking the vacuum as follows: ITO; 15 nm C_{60}; 6 or 10 nm **MPTA-4**; 10 nm BPAPF; 45 nm BPAPF doped with NDP9 (purchased from Novaled AG Germany, 10 wt%); 1 nm NDP9; 100 nm Al. Device characterization: *J–V* and *EQE* measurements were carried out in a solvent-free N_2 filled glovebox (O_2 and H_20 levels <1ppm). *J–V* characteristics were measured using a source-measure

unit (Keithley SMU 2400) and an AM 1.5G sun simulator (KHS Technical Lighting SC1200). The intensity was monitored with a silicon photodiode (Hamamatsu S1337), which was calibrated at Fraunhofer ISE. The mismatch between the spectrum of the sun simulator and the solar AM 1.5G spectrum was taken into account for the calculation of current density. Aperture masks (2.76 mm^2) were used to obtain well-defined active solar cell areas.

Vacuum-processed OSCs from TUD: Devices were prepared by Vacuum Thermal Evaporation (VTE) in a high vacuum system with a base pressure of $<10^{-7}$ mbar (Kurt J. Lesker). All layers of materials were evaporated onto a glass substrate with a pre-structured ITO contact (Thin Film Devices), cleaned in subsequent ultrasonic baths with NMP, Deionized water and ethanol and ultraviolet ozone cleaning system. Prior to evaporation, all materials were purified by vacuum gradient sublimation. Metal contacts were deposited through a shadow mask, to form a top contact, overlapping with the bottom ITO contact thus defining the device are (A = 6.44 mm^2). To avoid degradation due to external conditions, all devices were encapsulated with a glass cavity glued to the substrate with a moisture getter.

Standard devices: ITO/MoO_3 (3 nm)/BHJ or (D/A*)/BPhen (8 nm)/Ag (100 nm).

Inverted devices: ITO/Bis-HFl-NTCDI:$W_2(hpp)_4$ (5 nm)/BHJ or (D/A*)/MoO_3 (3 nm)/Ag (100 nm).

*In PHJ OSCs, the thickness of the layer of fullerene acceptor was 15 nm unless otherwise specified.

Device characterization: External Quantum Efficiency (EQE) spectra are taken using light from a xenon lamp (Apex 150 W Xenon Arc Lamp, Newport Oriel) and a monochromator (Cornerstone 260 Newport Oriel). Signal from the device was amplified and recorded with a lock-in amplifier (SR 7265 Lock-In Amplifier, Signal Recovery). The reference spectrum was taken with a Silicon reference diode (S1337, Hamamatsu, calibrated by Fraunhofer ISE). Current-density-Voltage (J-V) characteristics were measured with Keithley 2400 SMU source meter. The sample is illuminated by a sum simulator (16S-150V.3, Solar Light Co.) with intensity adjusted such as to duplicate the Am1.5G spectrum (100 mW/cm^2), calibrated with Silicon photodiode (S1337, Hamamatsu, calibrated by Fraunhofer ISE).

Photophysical measurements

Absorption spectra were recorded on a JASCO V-650 spectrophotometer in diluted solution (ca. 10^{-5} or 10^{-6} mol L^{-1}), using spectrophotometric grade solvents. Emission spectra were measured using Horiba-Jobin–Yvon Fluorolog-3 fluorimeter. The steady-state luminescence was excited by unpolarised light from a 450 W xenon continuous wave (CW) lamp and detected at an angle of

90° for measurements of dilute solutions (10 mm quartz cuvette) by using a Hamamatsu R928. Spectra were corrected for both excitation source light-intensity variation and emission spectral responses. Luminescence quantum yields Q were measured in diluted solutions with an absorbance lower than 0.1, by using the following equation:

$$\frac{Q_x}{Q_r} = \left[\frac{A_r(\lambda)}{A_x(\lambda)}\right] \cdot \left[\frac{n_x^2}{n_r^2}\right] \cdot \left[\frac{D_x}{D_r}\right]$$

where A(λ) is the absorbance (or optical density) at the excitation wavelength, n the refractive index of the solvent and D the integrated luminescence intensity. “r“ and “x“ stand for reference and sample, respectively. Here, the reference is coumarine-153 in methanol (Qr = 0.45). Excitations of reference and sample compounds were performed at the same wavelength. The reported results are the average of 4–5 independent measurements at various absorbances (comprised between 0.01–0.1) for both sample and reference. The plot of the integrated luminescence intensity vs. absorbance gives straight line with excellent correlation coefficients and the slope S can be determined for both sample (x) and reference (r). Then, the previous equation becomes the following:

$$\frac{Q_x}{Q_r} = \left[\frac{S_x}{S_r}\right] \cdot \left[\frac{n_x^2}{n_r^2}\right]$$

For singlet oxygen quantum yield determination ϕΔ, the principle is exactly the same except that the singlet oxygen luminescence emission band (D) is integrated for both sample (x) and reference (r) compounds. A(λ) is the absorbance (or optical density) at the excitation wavelength. In this case it is very important that both experiments are conducted in the same solvent at exactly the same excitation wavelength (nx = nr). The reported results are the average of 4–5 independent measurements at various absorbances (comprised between 0.01–0.1) for both sample and reference. The plot of the integrated singlet oxygen luminescence intensity vs. absorbance gives straight line with excellent correlation coefficients and the slope S can be determined for both sample (x) and reference (r). In the present case, the reference is phenalenone (ϕΔr = 0.98 in DCM).

Excited state lifetime analyses were measured at the maximum emission wavelength using a 390 nm nanoLED by means of the time correlated single photon counting (TCSPC) method of diluted dichloromethane solutions at room temperature.

The relationship between Stokes shift and the polarizability of solvent can be described following the Lippert–Mataga equation:

$$\Delta\nu = \frac{2\Delta f}{4\pi\varepsilon_0\hbar c a^3}(\mu_e - \mu_g)^2 + b$$

$$\Delta f = \frac{\varepsilon - 1}{2\varepsilon + 1} - \frac{n^2 - 1}{2n^2 + 1}$$

where Δv is the Stokes shift, $\hbar$ is the Planck constant, c is the light speed, a is the Onsager cavity radius, and μe, μg are the excited and ground-state dipole moments, respectively. Δf, is known as the solvent polarizability and can be calculated using the dielectric constants (ε) and refractive indices (n).

Crystallographic data

Table S1. Crystal Data Collection and Refinement Parameters of **NO_2-BTXI-NO_2** and **NO_2-BTXI-Br**.

Molecule	**NO_2-BTXI-NO_2**	**NO_2-BTXI-Br**
Empirical formula	$C_{23}H_{17}N_3O_6S$, C_7H_8	$C_{23}H_{17}BrN_2O_4S$, C_7H_8
Formula weight	555.59	589.49
Temperature (K)	150.0(1)	150.0(1)
Wavelength(Å)	1.54184	1.54184
Crystal system, space group	Monoclinic, P 21/n	Monoclinic, P 21/c
a(Å)	17.1645(2)	17.2992(3)
b(Å)	7.20880(10)	7.13370(10)
c(Å)	21.1257(3)	22.0936(4)
α(deg)	90	90
β(deg)	101.8510(10)	109.488(2)
γ(deg)	90	90
Z	4	4
Volume ($Å^3$)	2558.28(6)	2570.31(8)
Calculated density (Mg/m^3)	1.442	1.523
Absorption coefficient (mm^{-1})	1.568	3.275
θ range (deg)	3.030 to 76.167	2.709 to 72.003
Completeness to θ = 70.000	98.4%	98.0%
GOF	1.030	1.042
Largest diff. peak & hole ($e/Å^3$)	0.282 & -0.343	1.481 & -0.702

Table S2. Crystal Data Collection and Refinement Parameters of **DBTXI-Br** and **NO_2-DBTXI-Br**.

Molecule	**DBTXI-Br**	**NO_2-DBTXI-Br**
Empirical formula	$C_{27}H_{20}BrNO_2S$	$C_{27}H_{19}BrN_2O_4S$
Formula weight	502.41	547.41
Temperature (K)	150.0(1)	150.0(1)
Wavelength(Å)	1.54184	1.54184
Crystal system, space group	Monoclinic, P 21/n	Monoclinic, P 21/c
a(Å)	13.8628(8)	12.0181(3)
b(Å)	7.4278(4)	14.6961(3)
c(Å)	20.6317(10)	13.1169(4)
α(deg)	90	90
β(deg)	96.880(5)	109.850(3)
γ(deg)	90	90
Z	4	4
Volume ($Å^3$)	2109.2(2)	2179.05(10)
Calculated density (Mg/m^3)	1.582	1.669
Absorption coefficient (mm^{-1})	3.791	3.813
θ range (deg)	3.648 to 73.869	3.911 to 75.813
Completeness to θ = 70.000	98.2%	98.4%
GOF	0.997	1.060
Largest diff. peak & hole ($e/Å^3$)	0.743 & -0.501	0.642 & -0.491

Table S3. Crystal Data Collection and Refinement Parameters of **BTXI** and **TCCI** (**15**).

Molecule	**BTXI**	**TCCI (15)**
Empirical formula	$C_{23}H_{19}NO_2S$	$8(C_{24}H_{20}N_2O_2S),3(CH_2Cl_2)$
Formula weight	373.45	3458.61
Temperature (K)	150.0(1)	150.0(1)
Wavelength(Å)	1.54184	1.54184
Crystal system, space group	Triclinic, P -1	Monoclinic, P 21/n
a(Å)	7.4198(5)	7.3447(3)
b(Å)	8.8854(5)	25.3472(11)
c(Å)	15.1195(9)	22.0821(8)
α(deg)	101.609(5)	90
β(deg)	90.283(5)	96.839(4)
γ(deg)	111.324(5)	90
Z	2	1
Volume ($Å^3$)	906.22(10)	4081.7(3)
Calculated density (Mg/m^3)	1.369	1.407
Absorption coefficient (mm^{-1})	1.728	2.510
θ range (deg)	5.476 to 76.310	2.665 to 72.331
Completeness to θ = 70.000	98.0%	98.1%
GOF	1.032	1.103
Largest diff. peak & hole ($e/Å^3$)	0.551 and -0.300	1.025 & -0.591

Table S4. Crystal Data Collection and Refinement Parameters of **DBTXI** and **TXAI**.

Molecule	**DBTXI**	**TXAI**
Empirical formula	$C_{27}H_{21}NO_2S$	$C_{33}H_{32}N_2O_2S$
Formula weight	423.51	520.66
Temperature (K)	150.0(1)	150.0(1)
Wavelength(Å)	1.54184	1.54184
Crystal system, space group	Orthorhombic, P 21 21 21	Triclinic, P -1
a(Å)	7.4412(2)	13.8024(4)
b(Å)	8.0589(3)	14.1157(4)
c(Å)	33.5265(13)	14.9672(5)
α(deg)	90	81.003(3)
β(deg)	90	64.157(3)
γ(deg)	90	83.063(2)
Z	4	4
Volume ($Å^3$)	2010.51(12)	2587.60(15)
Calculated density (Mg/m^3)	1.399	1.337
Absorption coefficient (mm^{-1})	1.630	1.378
θ range (deg)	2.636 to 72.412	3.175 to 75.036
Completeness to θ = 70.000	98.5%	98.1%
GOF	1.130	1.040
Largest diff. peak & hole ($e/Å^3$)	0.486 & -0.400	0.971 & -0.625

References

[1] Charles, M. D., Schultz, P. and Buchwald, S. L., *Organic Letters* **2005**, *7*, 3965-3968.
[2] Leliège, A., Blanchard, P., Rousseau, T. and Roncali, J., *Organic Letters* **2011**, *13*, 3098-3101.
[3] Kozlov, O. V., Luponosov, Y. N., Solodukhin, A. N., Flament, B., Douhéret, O., Viville, P., Beljonne, D., Lazzaroni, R., Cornil, J., Ponomarenko, S. A. and Pshenichnikov, M. S., *Organic Electronics* **2018**, *53*, 185-190.
[4] Baraldi, P. G., Fruttarolo, F., Tabrizi, M. A., Romagnoli, R., Preti, D., Ongini, E., El-Kashef, H., Carrión, M. D. and Borea, P. A., *Journal of Heterocyclic Chemistry* **2007**, *44*, 355-361.

List of publications

- Synthesis, characterization and use of benzothioxanthene imide based dimers. **J.M. Andrés Castán**, C. Dalinot, S. Dayneko, L. Abad Galan, P. Simón Marqués, O. Alévêque, M. Allain, O. Maury, L. Favereau, P. Blanchard, G. Welch, C. Cabanetos. *Chemical Communications*, **2020**, 56, 10131.

- Triphenylamine/Tetracyanobutadiene-based π-Conjugated Push-Pull Molecules End-capped with Arene Platforms: Synthesis, Photophysics, and Photovoltaic Response. P. Simón Marqués, **J.M. Andrés Castán**, M. Blais, M. Allain, B. A. L. Raul, M. S. Pshenichnikov, G. Londi, D. Beljonne, I. Ramirez, K. Walzer, C. Cabanetos, P. Blanchard. *Chemistry - A European Journal*, 10.1002/chem.202002810.

- Effect of 4-biphenyl groups on the charge transport and photovoltaic properties of arylamine based push-pull systems. P. Simón Marqués, **J.M. Andrés Castán**, P. Josse, M. Blais, A, Habibi, I. Ramirez, K. Walzer, J. Roncali, P. Blanchard, C. Cabanetos. *New Journal of Chemistry*, **2020**, 44, 11441**.**

- Theoretical and experimental investigation on the intersystem crossing kinetics in benzothioxanthene imide luminophores, and their dependence on substituents effects. L. Abad Galán, **J.M. Andrés Castán**, C. Dalinot, P. Simón Marqués, P. Blanchard, O. Maury, C. Cabanetos, T. Le Bahers, C. Monnereau. *Physical Chemistry Chemical Physics*, **2020**, 22, 12373.

- Regioselective Monohalogenation and Homo/Hetero Dihalogenation of Benzothioxanthene Monoimide. C. Dalinot, P. Simón Marqués, **J.M. Andrés Castán**, P. Josse, M. Allain, L. Abad Galán, C. Monnereau, O. Maury, P. Blanchard, C. Cabanetos. *European Journal of Organic Chemistry*, **2020**, 2140.

- Indeno[1,2-*b*]thiophene End-capped Perylene Diimide: Should the 1,6-Regioisomers be systematically considered as a byproduct? P. Simón Marqués, F. Tintori, **J.M. Andrés Castán**, P. Josse, C. Dalinot, M. Allain, G. Welch, P. Blanchard, C. Cabanetos. *Scientific Reports*, **2020**, 10, 3262.

- Nitration of the benzothioxanthene: towards a new class of dyes with versatile photophyscial properties. **J.M. Andrés Castán**, L. Abad Galán, S. Li, C. Dalinot, P. Simón Marqués, C. Risko, C. Monnereau, O. Maury, P. Blanchard, C. Cabanetos. *New Journal of Chemistry*, **2020**, 44, 900.

UNIVERSITE MATIERE BRETAGNE MOLECULES LOIRE ET MATERIAUX

université angers

Matériaux à base de molécules push-pull pour le photovoltaïque organique

Mots clés : Photovoltaïque organique, systèmes π-conjugués, synthèse organique, push-pull, électronique organique, benzothioxanthène imide.

Résumé : Les efforts continus développés dans le domaine du photovoltaïque organique (OPV) ont permis d'améliorer les rendements de photoconversion jusqu'à 18%. Cependant, une vision critique des publications met en évidence que les rendements les plus élevés sont généralement associés à une augmentation de la complexité synthétique des matériaux (donneur et accepteur) et de la procédure de fabrication. C'est la raison pour laquelle la préparation de matériaux plus simples et moins chers est si cruciale. Après un premier chapitre examinant les progrès récents en OPV, un deuxième chapitre traite de la synthèse des molécules D-π-A dérivées du *N*-méthyl-*N*-phénylthiophène-2-amine (MPTA), un groupe donneur d'électron D encore non utilisé auparavant en OPV. Une série de dérivés a été synthétisée en modulant l'espaceur π-conjugué et le groupe attracteur d'électrons A, et l'impact sur leurs propriétés optiques, électrochimiques et photovoltaïques a naturellement été étudié. Un troisième chapitre porte sur différentes approches de modification structurale d'une molécule push-pull récemment décrite dans la littérature, à savoir le TPA-T-DCV-Ph. La présence du groupe phényle (Ph) terminal a conduit à une longueur de diffusion d'exciton plus élevée et ainsi à un meilleur rendement de photoconversion par rapport à la molécule push-pull de référence TPA-T-DCV. Finalement, un quatrième chapitre se focalise sur la fonctionnalisation d'un bloc prometteur et très peu exploré, le benzothioxanthène (BTXI). Ainsi, sa réactivité a été étudiée et les propriétés des nouveaux dérivés sont discutées.

Push-pull-based materials for organic photovoltaics

Keywords : Organic photovoltaics, π-conjugated systems, organic synthesis, push-pull, organic electronics, benzothioxanthene imide.

Abstract : The continuous efforts devoted to improving the performances in organic photovoltaics (OPV) have enhanced the photoconversion efficiencies over 18% so far. However, a critical vision of the state-of-the-art publications highlights that the highest efficiencies are generally paired with an enhancement of the synthetic complexity of both the materials (donor and acceptor) and the fabrication procedure. That is the reason why the preparation of simpler and less expensive materials is that crucial. In this regard, after a first chapter reviewing the recent progress in OPV, a second chapter is focused on the synthesis of D-π-A molecules based on the *N*-methyl-*N*-phenylthiophen-2-amine (MPTA) electron-donor unit, which was not previously used in the field. A series of derivatives is synthesized by modulating the π-spacer and the electron-withdrawing group A and the impact on their optical, electrochemical and photovoltaic properties is naturally investigated.
A third chapter is related to the structural modification of a recently reported push-pull molecule, namely TPA-T-DCV-Ph. Its additional phenyl ring in the accepting moiety led to a higher exciton diffusion length and therefore photoconversion efficiency in comparison to the well-known TPA-T-DCV. Hence, two different structural modifications of this donor are reported. Eventually, a fourth chapter is related to the functionalization of a promising and unexplored rylene, namely the benzothioxanthene (BTXI) whose most attractive features are its low synthetic cost and outstanding optical and electrochemical properties. Thus, its reactivity is explored in a deeper level and the properties of the new derivatives are studied.